

**MODELING OF MATERIAL JETTING ADDITIVE
MANUFACTURING WITH APPLICATIONS TO PAPER MACHINE
FABRICS**

A Dissertation
Presented to
The Academic Faculty

by

Chad Albert Hume

In Partial Fulfillment
of the Requirements for the Degree
Doctor of Philosophy in the
School of Mechanical Engineering

Georgia Institute of Technology

May 2022

COPYRIGHT © 2022 BY CHAD HUME

MODELING OF MATERIAL JETTING ADDITIVE MANUFACTURING WITH APPLICATIONS TO PAPER MACHINE FABRICS

Approved by:

Dr. David W. Rosen, Advisor
School of Mechanical Engineering
Georgia Institute of Technology

Dr. Meisha Shofner
School of Materials Science and
Engineering
Georgia Institute of Technology

Dr. Yan Wang
School of Mechanical Engineering
Georgia Institute of Technology

Dr. Christopher Luetgen
Chemical and Biomolecular
Engineering
Georgia Institute of Technology

Dr. H. Jerry Qi
School of Mechanical Engineering
Georgia Institute of Technology

Date Approved: April 25th, 2022

To my family.

ACKNOWLEDGEMENTS

This work would not have been possible without the support and patience of many great people and organizations.

I would like to express my sincerest gratitude to my advisor, Dr. David W. Rosen, for his guidance and patience throughout this long journey. His invaluable inputs and suggestions always pushed me to grow in my thinking and improve as a researcher. I am very fortunate to have had such a great role model during my tenure at Georgia Tech.

I would also like to extend my deep appreciation to my reading committee members, Dr. Chris Luetzgen, Dr. Jerry Qi, Dr. Meisha Shofner, and Dr. Yan Wang. It is a great gift to have so many talented professors give their time to improving my research. This resulting work is a direct result of their feedback and advice.

I would like to acknowledge Georgia Tech's Renewable Bioproducts Institute for the generous financial support given through the PSE Fellowship. This fellowship opened an entirely new direction for me and provided so many wonderful opportunities to learn and grow.

I would like to thank my fellow lab members: Dr. Amit Jariwala, Dr. Wenchao Zhou, Dr. Jane Kang, Dr. Namin Jeong, Dr. Sang-in Park, Dr. Xiayun Zhao, Jonathan Holmes, Narumi Watanabe, Jason Nguyen, Patrick Chang, and Yeming Xian. To have such a diverse, warm hearted, and brilliant set of peers is a true testament to the special place that is Georgia Tech and Dr. Rosen's lab.

Finally, I would like to thank my family. No words can fully express my love and appreciation for their endless support and encouragement. My wife, Amy Cheng, has stood as an eternal light throughout this journey. Her unwavering support knew no end, and without her continued belief in me and steady encouragement I would not be where I am today. Thank you to my son, Finn Hume, who became my greatest source of motivation, providing purpose and clarity to all that I now know. Thank you to David Hume, my brother, for being the greatest friend and encourager a little brother could ask for. Lastly, I would like to especially thank my parents, David and Linda Hume, to whom I owe everything. They have devoted their life to ensuring my happiness and success. Without them, I would not have become the person I am today.

TABLE OF CONTENTS

ACKNOWLEDGEMENTS	iv
LIST OF TABLES	viii
LIST OF FIGURES	ix
LIST OF SYMBOLS AND ABBREVIATIONS	xvii
SUMMARY	xix
CHAPTER 1. Introduction	1
1.1 Additive Manufacturing	1
1.2 Material Jetting AM	3
1.3 Applications	4
1.4 MJ Challenges	6
1.5 Research Objective and Questions	7
1.6 Summary	9
CHAPTER 2. Investigation into Mesoscale Feature Fabrication via Material jetting	11
2.1 MJ Printing Process	12
2.2 Review of MJ Characterization	14
2.3 Investigation into mesoscale feature fabrication	17
2.3.1 Benchmark Model Design	17
2.3.2 Experimental Methods	19
2.3.3 1D Features – Gaps	21
2.3.4 1D Features – Ribs	28
2.3.5 2D Features	35
2.4 Discussion	44
2.5 Summary	53
CHAPTER 3. Literature review – Material Jetting Deposition from droplet impact to Part Fabrication	55
3.1 Printing of Droplets	55
3.2 Printing of Lines	60
3.3 Printing of Layers	68
3.4 Part Fabrication	74
3.5 Summary	77
CHAPTER 4. modeling of the layer deposition process	79
4.1 Numerical Modeling	79
4.1.1 Governing Equations	79
4.1.2 Level Set Method	80
4.2 Model Implementation	83
4.3 Validation	84

4.3.1	Static Equilibrium	84
4.3.2	Dynamic Spreading	86
4.4	Modeling Droplet Deposition near the layer edge	88
4.5	Modeling of Layer Deposition	94
4.6	Discussion on computational expense	109
4.7	Summary	110
CHAPTER 5.	Quasi-static Boundary Method	113
5.1	Introduction	113
5.2	Quasi-static Boundary-based Model	115
5.2.1	Theoretical Underpinnings	115
5.2.2	Finite Element Model	118
5.2.3	Computational Modelling Procedure	118
5.2.4	Validation	125
5.3	Comparison with Existing Modeling Approaches	131
5.4	Improvements to the Model	135
5.5	Modeling Features	140
5.6	Summary	147
CHAPTER 6.	Design and manufacturability of novel press fabric membranes	149
6.1	Review of Paper Machine Pressing and Press Fabric Design	149
6.1.1	Introduction	149
6.1.2	Design and Characterization of Press Fabrics	150
6.2	Press Fabric Design Exploration	155
6.2.1	Objective	155
6.2.2	Method	155
6.2.3	Results	157
6.2.4	Active Press Fabrics	168
6.3	Summary	173
CHAPTER 7.	Closing Remarks and Contributions	176
7.1	Answering the Research Questions	177
7.1.1	Research Question One	177
7.1.2	Research Question Two	178
7.1.3	Research Question Three	180
7.2	Contributions	182
7.3	Recommendations for Future Work	184
REFERENCES		187

LIST OF TABLES

Table 1: Companies using Additive Manufacturing	2
Table 2: Minimum manufacturable gap (μm) varying thickness and orientation	21
Table 3: Average dimensional error over feature profile.....	25
Table 4: Minimum manufacturable rib size (μm).....	30
Table 5: Average dimensional error over profile.....	34
Table 6: Minimum manufacturable hole size for varied thickness (μm).....	36
Table 7: Average dimensional error over profile for 1000 μm thick Square Hole.....	37
Table 8: Material properties and printing conditions for model	88
Table 9: Time scales of droplet spreading	115
Table 10: Effects of mesh size and order on simulation time and accuracy	127
Table 11: Comparison of Mean average error for the different modeling methods	135
Table 12: Count of droplets and deposition line for example features and simulation times for linear and non-linear QSB method.....	142
Table 13: Review of press fabric patent literature	154
Table 14: QSB simulation time for check valve design	172

LIST OF FIGURES

Figure 1: Material jetting process schematic [5].....	4
Figure 2: Applications of inkjet based fabrication: a) electronic devices, b) microfluidics, c) 4D active materials, and d) consumer products	5
Figure 3: a) Traditional base weave construction; b) proposed design with an adaptive layer; c) the check valve design that closes when the pressure is low and opens when the pressure is high.	6
Figure 4: Comparison of designed mesoscale features with as fabricated parts: a) positive feature, b) negative feature	7
Figure 5: Material jetting process schematic [5].....	13
Figure 6: Illustration of multiple printing passes required to complete a single layer	13
Figure 7: Close up of 500x500 micron rectangle with angled walls and corner rounding [29].....	16
Figure 8: Three primitive features used for process benchmarking: a) 1D rib feature (thin wall), b) 1D gap feature, and c) 2D hole feature	17
Figure 9: Benchmarking specimens a) 1D ribs and gaps (at 0°, 45°, 90° orientation), b) 2D hole features (circular, square, diamond).....	18
Figure 10: Gap feature cross-section for 1mm part in 0° orientation	21
Figure 11: Cross-sectional measurement of 1mm part, 0.500mm gap	22
Figure 12: Gap width at bottom with varying orientation angle - a) 250 μm, b) 500 μm, c) 1000 μm	23
Figure 13: Gap width at bottom with varying thickness - a) 0°, b) 45°, c) 90°	24

Figure 14: Gap width measured at bottom, middle, and top of feature profile with orientation angle of 0° and 90°	25
Figure 15: Comparison of desired profile with as fabricated cross-sectional profile	26
Figure 16: Cross section profile evolution for gap feature	27
Figure 17: Overlay of feature profile for gap at different thicknesses.....	27
Figure 18: Rib feature cross-section for 1mm part	28
Figure 19: Rib height with varying orientation angle - a) 250 μm , b) 500 μm , c) 1000 μm	29
Figure 20: Rib width at bottom with varying orientation angle - a) 250 μm , b) 500 μm , c) 1000 μm	32
Figure 21: Rib width at bottom with varying thickness - a) 0° , b) 45° , c) 90°	33
Figure 22: Rib width measured at bottom, middle, and top of feature profile with orientation angle of 0° and 90°	34
Figure 23: Comparison of rib feature desired profile with as fabricated cross-sectional profile	35
Figure 24: Schematic of measurement directions and naming convention	37
Figure 25: Microscope images of fabricated 2D features from the top and bottom	38
Figure 26: Circular hole measurement at bottom - a) 250 μm , b) 500 μm , c) 1000 μm ..	39
Figure 27: Square hole measurement at bottom - a) 250 μm , b) 500 μm , c) 1000 μm	40
Figure 28: Diamond hole measurement at bottom - a) 250 μm , b) 500 μm , c) 1000 μm ...	41
Figure 29: 1000 μm thick square hole measured at bottom, middle and top.....	42
Figure 30: Cross-sectional profiles of square hole with different thicknesses	42

Figure 31: Comparison as fabricated feature with desired shape, and observed corner rounding: a) square, b) diamond	43
Figure 32: Boundary uncertainty for a deposited line	47
Figure 33: Illustration of impact of droplet spread and position uncertainty on printing gaps, a) gap feature on pixelated build platform, b) 250 μm gap which fails to print, c) 300 μm gap which successfully prints	48
Figure 34: Schematic diagram of droplet impacting at edge of previous layer and overflowing previous boundary	49
Figure 35: Corner rounding on the top edge of printed feature	51
Figure 36: Illustration of single droplet spread on an inclined surface [38]	52
Figure 37: Regime map of droplet behavior at impact, image from [45]	58
Figure 38: Phases of droplet impact and spreading [40]	59
Figure 39: Regimes of printed line behavior [48]	61
Figure 40: Diagram of deposited drop and bead [48]	62
Figure 41: Regime map for deposited line morphologies [48]	64
Figure 42: Comparison of top and side views with experimental results. Model I represents a surface tension limited case, Model II included viscosity [58]	68
Figure 43: Deposited films at various line spacings: a) desired shape is 500 μm square, b) desired shape is 1 mm square (right) [61]	70
Figure 44: Square layers printed of substrates of different roughness [63]	72
Figure 45: Surface evolver simulated film shape [63]	73
Figure 46: Contact angle around the film perimeter based on surface evolver solution [63]	73

Figure 47: Height change at center point depending on neighbors [67]	75
Figure 48: Simulation results for a 400 um tall printed cylinder with 20% process uncertainty: open-loop (top), closed-loop (bottom) [67]	76
Figure 49: Schematic of model computational domain and boundary conditions.....	84
Figure 50: Simulated equilibrium droplet shape for different contact angles	85
Figure 51: Comparison of equilibrium spread factor between Comsol simulation and theoretical model.....	85
Figure 52: Simulation results of droplet impact on solid surface	86
Figure 53: Experimental results of droplet impact from Dong [76]	87
Figure 54: Validation of dynamic spread factor evolution	87
Figure 55: Droplet impacting at the first layer edge: a) a flat leveled surface, b) a ribbed non-leveled surface	89
Figure 56: Ribbed surface topology.....	89
Figure 57: Simulation of droplet deposition at layer edge with a flat surface (Time units = 10^{-5} second).....	91
Figure 58: Simulation of droplet deposition at layer edge with ribbed surface (Time units = 10^{-5} second).....	92
Figure 59: Comparison of effect of droplet inaccuracy on deposition	93
Figure 60: Side view comparison of max impact spread and max capillary spread for offsets of 0, 10, 20, 30 μm	94
Figure 61: Illustration of target feature, 9x9 pixel, 3 layers thick	95
Figure 62: Simulation results for a single line deposition: a) final shape, b) cross-sectional profile.....	97

Figure 63: Deposition pattern for the first two passes of layer 1, showing that deposited beads do not intersect.....	98
Figure 64: Simulation of Pass 3 and/or Pass 4. Deposition between two previously deposited lines.....	99
Figure 65: Final shape of completed Layer 1	100
Figure 66: Layer 2 Pass 1 at the edge	101
Figure 67: Layer 2 Pass 1 or 2 at the interior.....	101
Figure 68: Layer 3 Pass 3 or 4 near the edge.....	102
Figure 69: Layer 2 Pass 3 or 4 Central	102
Figure 70: Final shape of completed Layer 2	103
Figure 71: Layer 3 Pass 1: a) edge pass, b) interior central pass	104
Figure 72: Layer 3 Pass 2.....	105
Figure 73: Layer 3 Pass 3 or 4 near the edge.....	105
Figure 74: Layer 3 Pass 3 or 4 Central	106
Figure 75: Final shape of completed Layer 3	107
Figure 76: XZ and YZ plane cross-section through middle of feature, plotting evolution of 3 layers vs target.....	108
Figure 77: Comparison of cross-sectional shape of Layer 2 with a layer that had an extra edge pass, YZ plane	109
Figure 78: Phases of droplet impact and spreading, image from [45]	114
Figure 79: Line deposited at edge of previous layer.....	118
Figure 80: Predict droplet spread.....	119
Figure 81: A) Domain boundary, B) boundary condition values	120

Figure 82: Linear and quadratic triangular elements	121
Figure 83: Problem domain discretized with a linear triangular mesh	122
Figure 84: Volume optimization problem formulation.....	122
Figure 85: Process flow to solve for fluid deposition surface	124
Figure 86: Solution for 3d fluid interface	125
Figure 87: Spherical Cap	126
Figure 88: a) Simulation results from [52], b) Boundary-based results, c) Comparison of surface profile at $Y=0$	128
Figure 89: Simulation results for 9x9 pixel square, a) Layer 1, b) Layer 2, c) Layer 3 .	129
Figure 90: XZ and YZ plane cross-section through middle of feature, comparing with CFD results	130
Figure 91: Simulation of 3 rd layer only, using CFD results as input	131
Figure 92: a) Surface profile of as fabricated 12 layer, 8mm-by-8mm square feature, b) cap profile for deposited droplet, c) four-layer deposition pattern	133
Figure 93: a) 12-layer 8mm-by-8mm square predicted feature using QSB model, b) height map of difference between QSB surface and as-fabricated feature.....	134
Figure 94: Asymmetric spreading as a combination of radial spreading and tangential translation.....	136
Figure 95: Implementation of asymmetric spreading and boundary determination	137
Figure 96: Non-physical solution results due to steep incline relative to solution plane	138
Figure 97: Process for converting to local coordinate system to solve for fluid surface	139
Figure 98: 9x9 pixel feature, XZ and YZ plane cross-section through middle of feature, comparing Improved QSB with CFD results.....	140

Figure 99: Illustration of features, a) extruded square, b) square with circular hole, c) square with square hole, d) rectangle with gap	141
Figure 100: Feature simulation process steps	142
Figure 101: Simulation results for 1x1mm extruded square.....	143
Figure 102: Simulation results for extruded square with a 0.3 mm circular hole.....	143
Figure 103: Simulation results for extruded square with a 0.3 mm square hole	144
Figure 104: Simulation results for 1x2mm extruded rectangle with a 0.3x1.5mm gap..	144
Figure 105: XZ-plane cross-sectional profiles through: a) the middle of the extruded square, b) the middle of the gap feature.....	146
Figure 106: XY-Plane Cross-sectional profile of square hole at: a) bottom of feature (middle of layer 1), b) top of feature (middle of layer 10)	147
Figure 107: Overview of paper machine	150
Figure 108: Examples of conventional press fabrics	151
Figure 109: Press fabrics with polymer layers, a) Albany AperTech, b) Voith Evolution, c) Voith Revolution.....	153
Figure 110: Simulation domain and boundary conditions	156
Figure 111: Overview of proposed design variations	158
Figure 112: Simulation results for varying hole shape and membrane thickness.....	159
Figure 113: Investigation into effect of edge rounding and edge undercut	160
Figure 114: Investigation into effect of batt layer on membrane performance	161
Figure 115: Simulation results comparing a traditional base weave with a tuned hole featuring a rounded forward edge and undercut reverse edge	163
Figure 116: Effect of conical hole structure compared with circular hole	165

Figure 117: Investigation into conical hole with rounded forward edge and undercut reverse edge	166
Figure 118: Tesla Design, cone with internal cutback.....	167
Figure 119: Active fabric design, check valves	168
Figure 120: Actuation of the check valve, valve opens under compression.....	169
Figure 121: Simulation results for check valve design: forward flow with open valve, reverse flow with closed valve.....	169
Figure 122: Simulation of the upper region of the check valve design	170
Figure 123: Simulation of the lower region of the check valve design	170
Figure 124: Voxelated representation of the QSB simulated check valve: a) full geometry, b) closeup sectional of a single cell	171
Figure 125: a) Prototype check valve membrane printed at 2X scale, b) demonstration of valve opening under compression.....	173

LIST OF SYMBOLS AND ABBREVIATIONS

AM	Additive Manufacturing	–
MJ	Material Jetting	–
dpi	dots per inch	–
D_0	Droplet Diameter	m
U	Deposition Velocity	m/s
ρ	Fluid Density	kg/m ³
μ	Dynamic Viscosity	cP
σ	Surface Tension	N/m
θ	Contact Angle	°
Re	Reynolds Number	–
We	Weber Number	–
Oh	Ohnesorge Number	–
Bo	Bond Number	–
D_{cap}	Deposited droplet cap diameter	m
V_{drop}	Droplet volume	m ³
Δx	Droplet spacing	m
β	Spread factor	–
β_{eqm}	Equilibrium Spread Factor	–
t_{spread}	Impact driven spread time	s
t_{osc}	Oscillation spread time	s
t_{visc}	Capillary driven spread time	s
t_{relax}	Relaxation spread time	s
t_{dep}	Time between droplet deposition	s

QSB	Quasi-static Boundary-based Method	–
Δp	Pressure drop across fluid interface	Pa
Ω	Droplet wetted region	–

SUMMARY

Material jetting-based (MJ) additive manufacturing (AM) is a promising manufacturing technology uniquely suited to enable new innovation, especially at the mesoscale, like novel paper machine press fabrics. The objective of this research is to improve the understanding of mesoscale feature fabrication via material jetting AM and improve our understanding of how to model the material jetting fabrication process. Additionally, we seek expand the state of the art for paper machine press fabrics through the design and analysis of novel membrane layers.

To begin, a series of benchmark test specimens with parametrically varying mesoscale features were designed and fabricated using an industry leading material jetting machine. These specimens were characterized to explore the printing fidelity with respect to minimum manufacturable feature size, dimensional accuracy, and shape accuracy, as well as any respective dependencies on design variables (i.e., feature shape, size, orientation, and thickness). Geometric deformations affecting the feature accuracy as well as shape accuracy were revealed to be of significant degree. While the ultimate impact on any proposed design would depend on the application, the presented methods can be leveraged to define DfAM guidelines and provide clarity on expected feature outcome.

Next, high-fidelity multiphase droplet models are developed to explore how deposition dynamics affect feature formation. What makes this work novel is the exploration of deposition on non-uniform surfaces near a layer edge. Results showed that local deposition dynamics will result in material flow beyond the layer boundary, which will expand the layer boundary, reducing deposition height and lead to feature deformation.

Additionally, the developed models were used to simulate multiple droplet deposition and coalescence, as would be seen during the printing process, to form a multi-line, 3-layer feature. In doing so, the material overflow was observed to form the edge rounding seen during physical characterization. By better understanding this effect process control improvements can be made to improve feature resolution and fidelity, and a preliminary example showing an extra edge pass was demonstrated.

A novel Quasi-static Boundary-based method for rapidly modeling the material jetting process was developed and demonstrated. The key assumption of this approach is that for the material properties and timescales of interest for the MJ process, with a reasonable prediction of the droplet footprint after the spreading phase, the final fluid surface can be determined without having to solve the full fluid problem which is both time consuming and complex. The general framework was developed, then validated through comparison with prior literature as well as the modeling presented in this work. Additionally, the method was compared with other MJ modeling approaches found in literature and shown to predict the as-fabricated surface most accurately. The model was then used to explore representative mesoscale features which consisted of thousands of simulated droplets. These simulated mesoscale features showed similar deformations to the physical features printed, like rounded edge deformations, suggesting that the driving cause is likely the asymmetric deposition spread near the edge.

Finally, a simulation-based investigation is undertaken to look specifically at the ideal design for novel press fabric membrane layers. The results showed that rather simple designs can promote one directional flow. To further improve the one directional flow, an active “check-valve” design is developed. Flow simulations showed significant promise

for promoting one directional flow. A physical specimen of the “check-valve” design was fabricated at 2X scale. Simulated compression of the prototype showed opening of the area as intended. These simulations and findings should guide future development of press fabric constructions and merit physical testing to validate their performance.

CHAPTER 1. INTRODUCTION

As an emerging technology, additive manufacturing (AM) and its subprocesses like material jetting (MJ), have the potential to enable significant innovations in the way we imagine, design, and realize solutions to the many challenges we face. To ensure these solutions succeed, it is essential to develop a deep understanding of how AM processes work and how they can best be utilized. This dissertation offers a step towards that understanding.

The following sections introduce the fundamental background and motivation for this work, and then present the research questions and hypotheses to be answered.

1.1 Additive Manufacturing

Additive manufacturing (AM), often referred to as 3D printing or rapid prototyping, is a class of processes which fabricate 3D objects directly from digital CAD models through selective material joining, usually layer upon layer [1]. This is in contrast with more traditional approaches such as subtractive manufacturing where material is removed from a larger bulk workpiece by milling, turning, or drilling until the final form is created. One of the key advantages of such additive processes is the geometric freedom to produce parts of near infinite complexity with the same efficiency and cost as building a simple block.

Since the first commercial machines entered the market in the 1980's, additive manufacturing has experienced significant expansion in investment, development and use. Today there are well over one hundred different companies providing AM machines

and services, leveraging a host of underlying technologies such as powder bed fusion (e.g., selective laser melting (SLS)), material extrusion (e.g., fused deposition modeling (FDM)), printing-based systems (e.g., material jetting), beam deposition processes (e.g., Laser Engineered Net Shaping (LENS)), etc. [2]. The main differentiators of these technologies are the types of materials that can be processed and how the material is processed to ensure the layers are joined together. For example, FDM is a polymer-based technology that extrudes a plastic filament through a heated nozzle in much the same manner as a baker extrudes icing onto a cake, whereas SLS uses a high-power laser to selectively melt and join powdered metal to form full density metal parts.

With so many technologies, and near infinite design potential, it should come as no surprise that AM is growing at a rapid rate, fueling innovations in many industries including aerospace, automotive, medical devices and beyond. In 2018 the AM market grew by 18% to \$9.3 billion in generated revenue from hardware, software, materials and services [3]. Furthermore, in a 2016 survey PWC found that more than two-thirds of US manufacturers are leveraging AM in some way [4]. Table 1 shows a small sample of companies currently applying AM.

Table 1: Companies using Additive Manufacturing

Align Technology (Invisalign)	Ford	Boeing
General Electric	Shell	Hasbro
SpaceX	Nike	Hershey

Still, like its more traditional manufacturing counterparts, AM is not without its manufacturing constraints. These constraints vary between different AM processes, requiring a detailed understanding of the effects of geometric and process parameters for each specific process. Of particular interest in this work is the material jetting process.

1.2 Material Jetting AM

Material jetting-based (MJ) processes are a promising approach for AM, benefiting from the significant process development achieved by commercial 2D inkjet printing. To fabricate parts, banks of print heads selectively eject streams of droplets onto a build platform positioned below, see Figure 1. These droplets then coalesce to form the deposited layer, which solidifies based on the principles of the material being used. Subsequent layers are deposited in the same fashion, one on top of the other, to form the desired 3D geometry. Ejected droplets can be molten material (such as wax or low melting temperature metal), particle suspensions, or photocurable polymers. The discrete nature of the process, with multiple nozzles and printheads, enables simultaneous deposition of multiple materials such as sacrificial support material or different functional build materials for multi-material parts. No other AM technology offers as much material flexibility as MJ nor the ability to deposit different materials on a pixel-by-pixel basis. MJ machines are also among the highest resolution AM processes, with the added benefit of scalability in both size and speed.

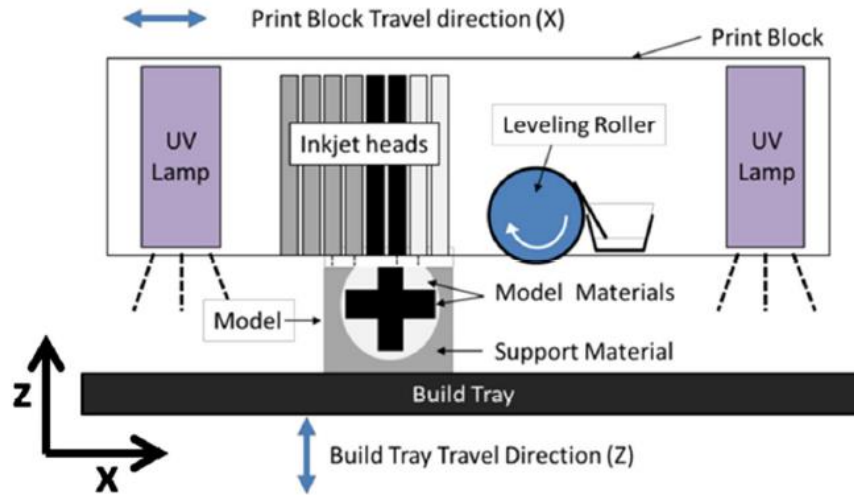


Figure 1: Material jetting process schematic [5]

Commercially, MJ platforms have been available since the mid-1990's beginning with the ModelMaker from Sanders Prototype (now Solidscape) printing molten wax. Other dominant platforms include Stratasys' Polyjet line (after acquiring Objet in 2012), and 3D Systems' MultiJet lines, printing an impressive variety of photocurable polymers with a range of physical properties. Still, newcomers continue to emerge like Nano Dimension Ltd with its Dragonfly Pro machine capable of printing 3D electronics [6].

1.3 Applications

With the advantages of multiple materials, high resolution, scalability and speed, material jetting-based technologies have attracted significant research and development efforts as a novel fabrication technique with particular focus on mesoscale applications. Active areas of interest include printed electronics [7], microfluidics [8], "4D" printing [9], and more broadly additive manufacturing as a whole [10], as shown in Figure 2.

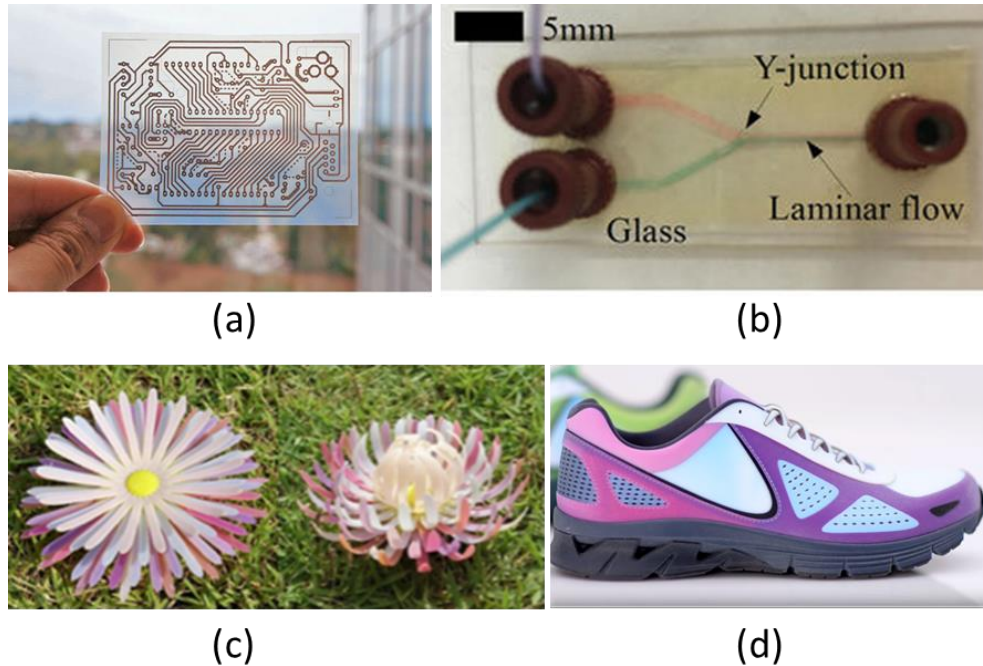


Figure 2: Applications of inkjet based fabrication: a) electronic devices, b) microfluidics, c) 4D active materials, and d) consumer products

One application motivating this work is the paper machine press fabric. Press fabrics are a critical element of the modern paper machine serving as a microporous filtration fabric, and case studies have shown that changes in machine fabrics can result in substantial energy and cost savings for paper mills [11]. Exploring new fabric designs is a critical research need for the paper community, as described by Agenda 2020, an industry partnership, in a recently released technology roadmap [12]. Traditionally, press fabrics are woven fiber structures which greatly restrict the resulting geometry, as shown in Figure 3a. By fabricating fabrics using MJ, the goal is to increase design freedom and enable novel designs that improve performance, see Figure 3b,c. Understanding how different feature shapes and constructions of these designs impact flow performance is a critical area for further investigation.

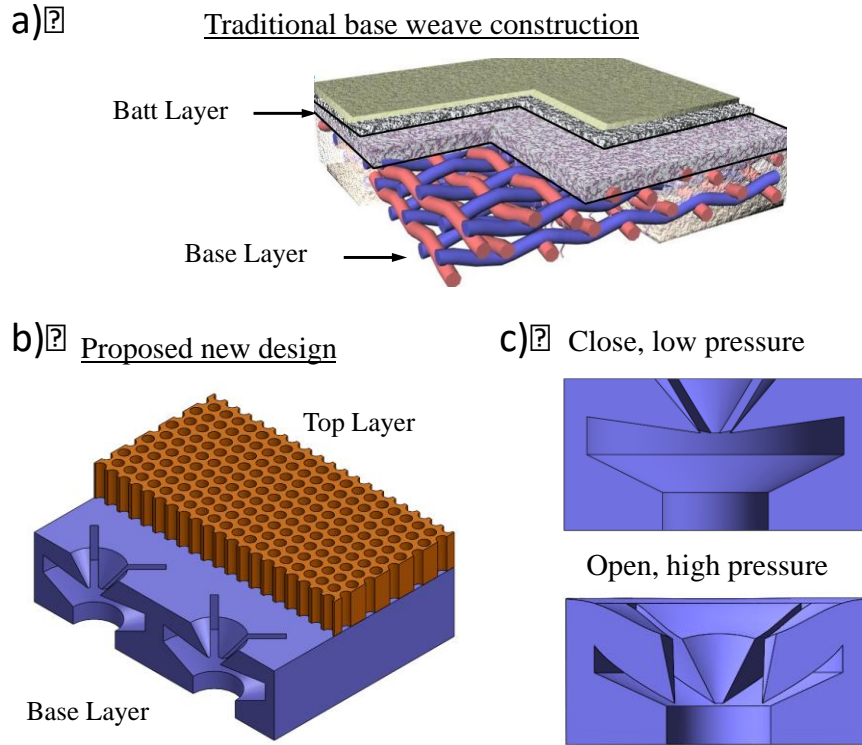


Figure 3: a) Traditional base weave construction; b) proposed design with an adaptive layer; c) the check valve design that closes when the pressure is low and opens when the pressure is high.

1.4 MJ Challenges

As these new applications develop, MJ systems are increasingly pushing into new frontiers of size, complexity, and functionality, testing the limits of current machines. In fact, characterizations of existing machines have shown significant geometric deformities at the mesoscale, such as sloped walls and rounded corners [13]. Similar deformations are found in this work, as shown in Figure 4.

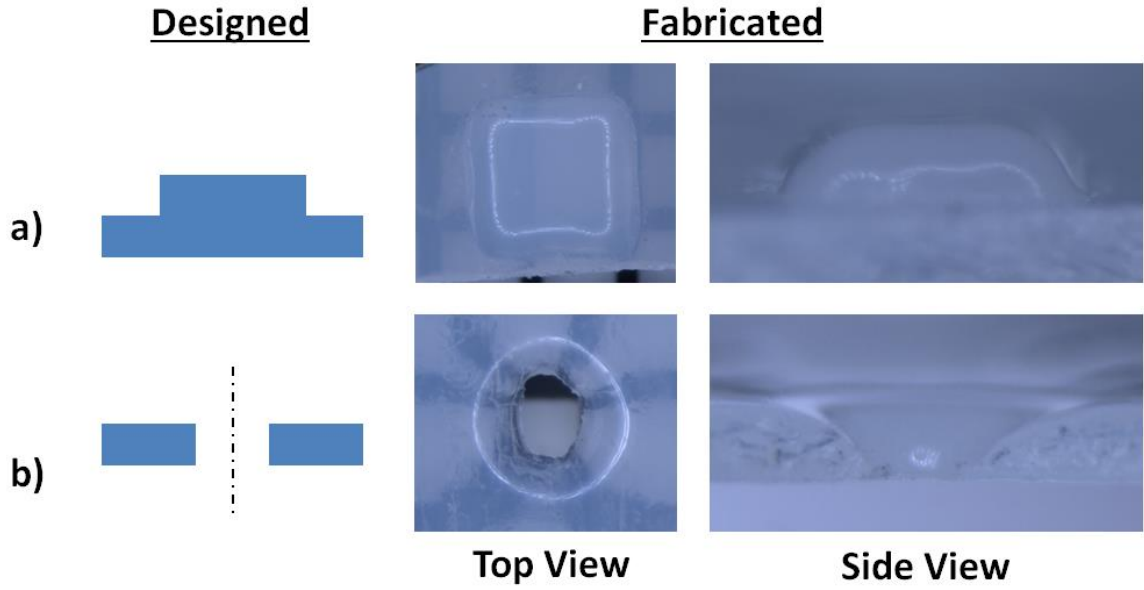


Figure 4: Comparison of designed mesoscale features with as fabricated parts: a) positive feature, b) negative feature

It is critical to develop a strong understanding of the underlying physical process along with models capable of accurately and efficiently predicting the fabricated geometry. Due to the inherent complexity and multiscale nature of the process, robust physics-based modeling from individual drop through to final part is virtually unseen in literature due to the computational burden and has resulted in a gap between small scale, but high-fidelity modeling, and simplistic process planning models that cannot predict local feature errors found in mesoscale parts.

1.5 Research Objective and Questions

The objective of this research is to improve the understanding of mesoscale feature fabrication via material jetting AM and improve our understanding of how to model the material jetting fabrication process, to enable the design exploration of novel mesoscale applications such as the paper machine press fabric.

Specifically, this research seeks to address the following research questions:

Research Question 1: What is the minimum size of primitive mesoscale features fabricated using commercial MJ processes, what are the effects of geometric parameters (i.e., shape, size, orientation, and feature thickness), and how does this relate to machine resolution?

Hypothesis 1: A parametric study of representative features (square holes, circular holes, thin walls, gaps, etc.) with varying orientations, and transverse thicknesses can be used to determine minimum feature size, shape accuracy, and comparative effects.

Research Question 2.1: How can local material flow near previously jetted lines and boundary edges be modeled and how does such flow affect feature resolution?

Hypothesis 2.1: Deposition near an existing edge can be modeled using a series of high-fidelity 3D CFD simulations that explore droplet deposition with respect to edge, or line boundaries. Additionally, these simulations can be further expanded to explore line and layer deposition.

Research Question 2.2: How can the material jetting process be modeled to rapidly predict the as-manufactured shape of mesoscale features?

Hypothesis 2.2: A reduced order model based on a quasi-static boundary-based approach can accurately predict the as fabricated feature shape with reduced computational expense.

Research Question 3: How can paper machine press fabrics be designed to increase dewatering efficiency? Specifically, can the traditional filament-based press fabric layout be augmented to promote unidirectional flow and resist rewet?

Hypothesis 3: A systematic investigation of hole shapes, sizes, behaviors, can identify membrane geometries which promote one directional flow to promote dewatering flow, and restrict rewetting flow. Press fabrics which incorporate a membrane with active, one-way, structures that open under roller nip pressure and close upon exit can be designed to further increase one directional flow and dewatering efficiency.

1.6 Summary

This research investigates material jetting-based additive manufacturing, how the process can be modeled, and a novel application. The thesis is organized as follows. Chapter 1 provides the motivation and context of this work, along with the guiding research questions to be answered. In Chapter 2, mesoscale feature fabrication is explored using a commercially available material jetting machine. Chapter 3 presents a detailed literature survey on existing modeling efforts and approaches. In Chapter 4, the initial layer deposition process is investigated using high fidelity 3D numerical models. Due to the high computational burden of traditional modeling approaches a more efficient method must be developed. In Chapter 5, a quasi-static boundary-based approach is proposed to efficiently model the line-by-line, layer-by-layer shape evolution of the material jetting process. Simulation results are compared with the high-fidelity simulations of Chapter 4, as well as physical specimens from Chapter 2. Chapter 6 leverages CFD modeling to explore the design of novel membrane layers for paper machine press fabrics, which

could in the future be fabricated with MJ AM, to understand how membrane features impact flow performance. Chapter 7 concludes this work, providing analysis of the methods and results presented, along with recommendations for future work.

CHAPTER 2. INVESTIGATION INTO MESOSCALE FEATURE FABRICATION VIA MATERIAL JETTING

Additive manufacturing has the potential to enable exciting innovations; this notion is bolstered by the continuously expanding footprint of AM into new industries and applications. Still, for each of these new applications, designers and manufactures quickly realize that much like traditional manufacturing approaches AM is not without manufacturing constraints. Therefore, to enable these and future applications it is important to understand and characterize AM constraints and identify areas for process improvements.

It is widely recognized that AM limitations are highly process and material dependent. Therefore, it is generally necessary to study and establish specific constraints for individual processes and specific applications. Benchmarking parts are used as a reproducible way of establishing machine constraints. Many benchmark specimens have been proposed [14]; some are used for general comparison between different processes, while others have focused on specific processes. Due to the wide set of AM processes, and wider set of applications, there is no general consensus on benchmarking. Therefore, in many cases, specific benchmarks are designed based on the process and application of interest.

In this study, specifically designed benchmark parts are used with the objective to better understand the material jetting process and characterize mesoscale feature fabrication. The designed test specimens consist of representative features and shapes such as thin

walls, gaps, and holes, which serve as the most basic feature elements for applications at this scale, such as novel press fabrics.

In Section 2.1, an overview of the material jetting process is presented, followed by a review of existing characterization literature in Section 2.2. The detailed study of mesoscale fabrication is presented in Section 2.3 along with a detailed discussion of the results.

2.1 MJ Printing Process

While several commercial MJ systems exist, the Stratasys Polyjet process is one of the most well-established commercial material jetting systems and has therefore been selected for use herein. Polyjet printers are known for their high resolution and small layer thickness. For most systems, maximum reported resolution in the X-Y plane is 600x600 dpi (42x42 μm), with layer thicknesses of 16 or 30 μm depending on the printer option selected. They are also unique in their ability to print multiple materials in a single build (e.g., rigid and flexible), and additionally mix these materials to form an expanded set of digital materials enabling a wide array of properties.

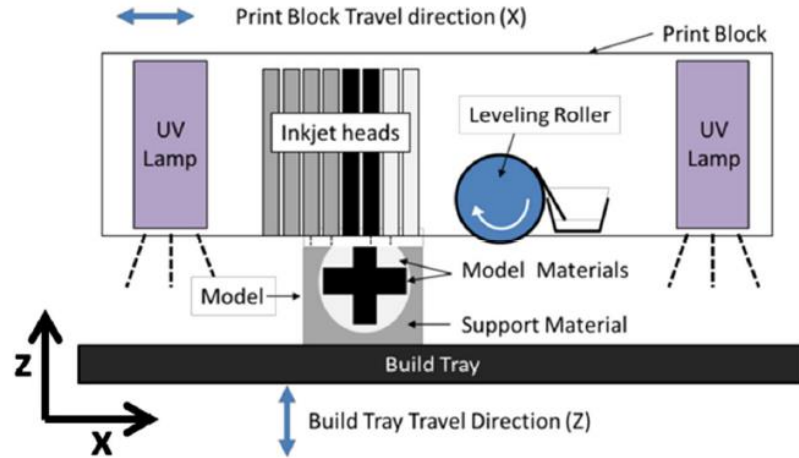


Figure 5: Material jetting process schematic [5]

To fabricate parts, banks of print heads, each containing build or support material, selectively eject streams of photocurable droplets onto a build platform positioned below, Figure 5. These droplets coalesce to form lines of deposited material. Due to the spacing of printhead nozzles, multiple printhead passes are typically required to form a complete layer, Figure 6.

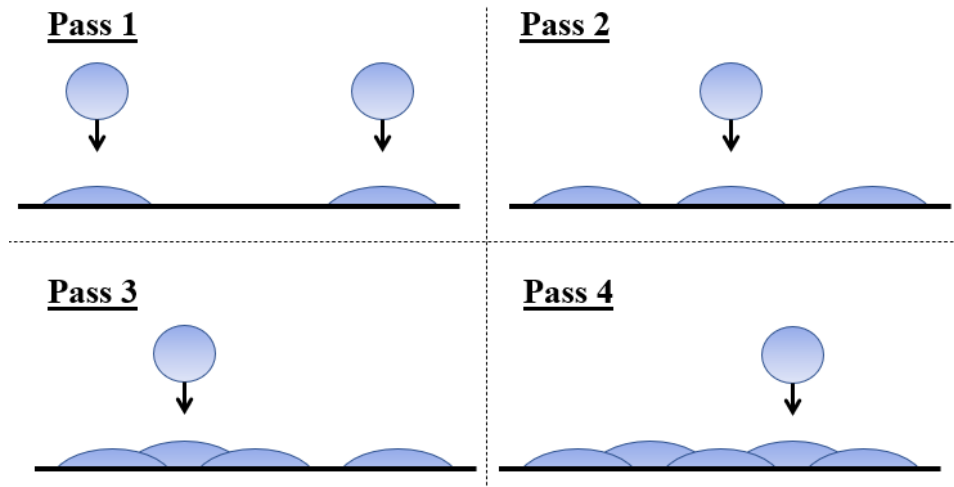


Figure 6: Illustration of multiple printing passes required to complete a single layer

With each pass of the printhead, UV lamps irradiate the build platform and cure the deposited material. To control any unevenness of the layer, a leveling roller is used to

skim the surface of the layer at the preset layer height. All deposition occurs during x-direction passes. If the part width is larger than a single swath width, the printhead will translate in the y-direction and continue printing the next layer section as described above. After the full layer is complete, the build platform will lower one-layer thickness in the z-direction, and the next layer will begin.

2.2 Review of MJ Characterization

Several authors have explored the Stratasys/Object Polyjet process, to characterize material and geometric performance. Barclift and Williams, along with several others, studied the effects of process parameters on strength of Polyjet printed parts, concluding that parameters like build location and orientation are significant factors for part performance [15]–[17]. UV exposure is also quite significant. Vieira et al. found that the flexural modulus can be improved through UV or thermal postprocessing, though this also has a negative effect on fatigue life [18]. Others explored the effects of aging on part properties, as well as shielding effects that occur when a part is printed with support material surrounding the exterior [7],[8]. Moore and Williams investigated the fatigue life of the elastomeric material, TangoBlack, and created an experimental curve relating the percent elongation to the expected life of the specimen along with several design rules [20]. More recent investigations have begun to look at performance of multi-material printing, useful for functionally graded materials and printed composites, and how material combinations and interface effect impact performance [21], [22].

Of more relevance to the present study are the works exploring final part geometric quality. Singh studied dimensional accuracy of Polyjet parts for features on the order of

10-60mm, finding average error of less than $\pm 0.1\text{mm}$ [23]. Several authors investigated surface roughness, finding that surface roughness increases with orientation angle, and the “glossy” setting (no support material) provided the best surface finish [17], [24]–[26]. Meisel and Williams expanded upon these works with the goal of establishing a set of design for additive manufacturing guidelines (DfAM) for material jetting [27], [28]. They investigated minimum feature size, removal of support material, survivability of small features, and self-supporting angles in the absence of support material using the Objet Connex 350 in digital material mode. While not specifically investigating mesoscale features, they did report a mean resolvable feature size of 0.897 mm in diameter under the worst printing scenarios, and a “best-case” minimum printable feature of 0.372 mm if a designer is able to account for all the significant variables. Yap et al. proposed several benchmark artifacts for investigating the process capabilities of material jetting. Using these artifacts, they studied the effect of various process conditions on dimensional accuracy, as well as investigated special features such as thin walls and clearance gaps for assembly-free parts [29].

Most of these works are focused on macroscale parts, with little usefulness for the sub-millimeter resolution needed for press fabric manufacture. Lee et al. explored material jetting for microfluidic applications [13]. Results showed that submillimeter rectangular channels printed without support material tend to have angled walls and rounded corners if fabricated at all, as shown in Figure 7.

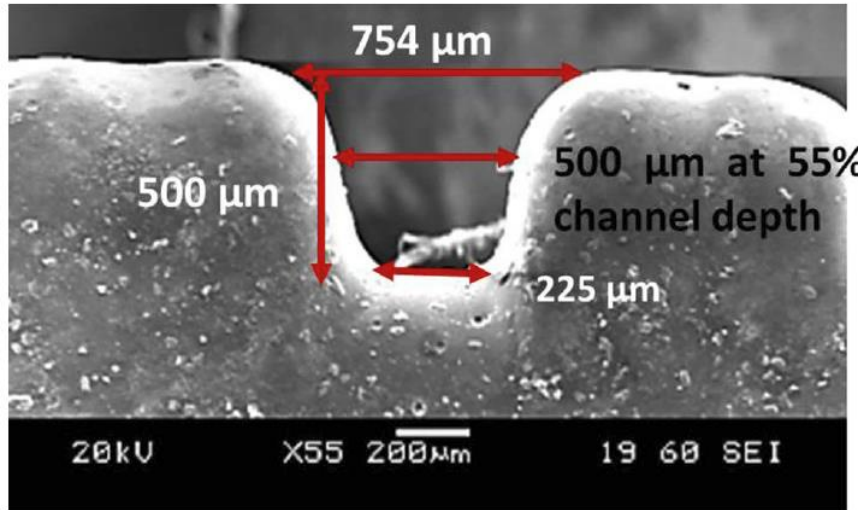


Figure 7: Close up of 500x500 micron rectangle with angled walls and corner rounding [13]

MacDonald et al. evaluated several AM technologies, including material jetting (Polyjet), for their potential use fabricating microfluidic mixers [30]. For the Polyjet machine, they found that channels tended to be slightly smaller than designed ($-40 \pm 36 \mu\text{m}$) and the smallest successfully printed channel had a width of $205 \pm 13 \mu\text{m}$ (designed width of $250 \mu\text{m}$). Walczak and Adamski, also evaluating applications in microfluids, looked solely at material jetting machines, comparing between both Polyjet and ProJet technologies. After a general comparison of the four different machines, most of their analysis focused on the ProJet technology, which was selected as their preferred machine of choice, and featured easier to remove support material. Dimensional fidelity, shape conformity and surface roughness were studied, and results matched those previously discussed with the smallest successfully printed channel having a width measuring $\sim 200 \mu\text{m}$. The work additionally noted deformations such as corner rounding, and sloped walls as seen in Lee et al.

With the limited studies to date, it is not fully clear what the performance limits are regarding mesoscale features; whether errors are linear, or scale with size, or how

deviations develop. Therefore, to enable applications such as microfluidics or press fabrics, more characterization is needed to develop specific design guidelines.

2.3 Investigation into mesoscale feature fabrication

2.3.1 Benchmark Model Design

To explore the feasibility of press fabric manufacture and characterize the material jetting process, simple benchmark parts are designed incorporating basic features relevant to mesoscale fabric-like applications. Specifically, these features are gaps, ribs, and holes as shown in Figure 8.

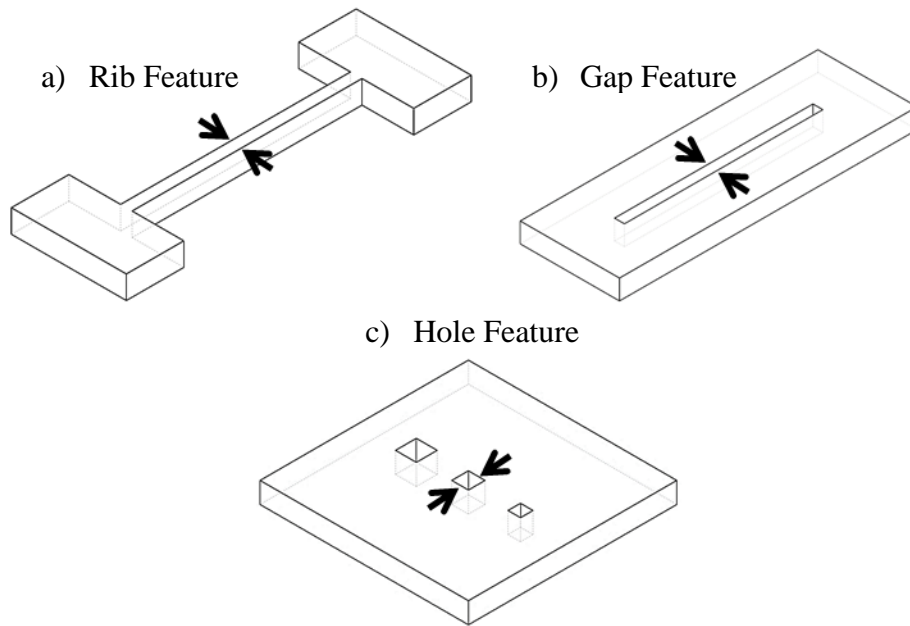
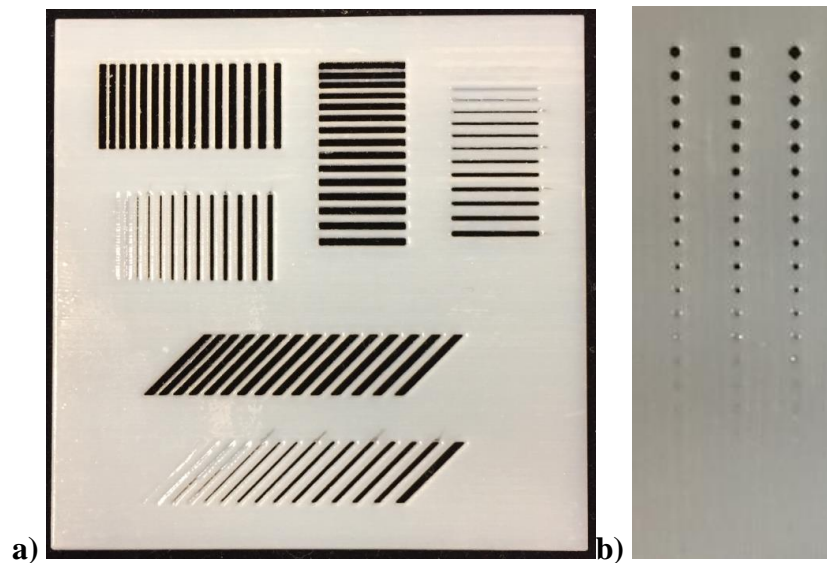


Figure 8: Three primitive features used for process benchmarking: a) 1D rib feature (thin wall), b) 1D gap feature, and c) 2D hole feature

The objective is to investigate minimum manufacturable feature size, dimensional accuracy, and feature shape, along with any variations associated with feature orientation or thickness of the part. Minimum manufacturable feature size is the minimum designed feature size that results in a successfully built feature. In the case of a gap or hole, this

means the feature is open all the way through the part, and for ribs it means the rib built to full height. Dimensional accuracy is defined as how closely the measured critical dimension (e.g., gap width) matches the designed dimension. Feature shape explores any deviations from the ideal shape (e.g., slanted walls and edge rounding).

Two benchmark parts are used. Part A (as shown in Figure 9a) consists of 1D gap and rib features at 0° , 45° , and 90° orientations with respect to the printing direction. Dimensions of the gaps and ribs vary from $50\ \mu\text{m}$ to $750\ \mu\text{m}$ in increments of $50\ \mu\text{m}$. Part B (as shown in Figure 9b) consists of an array of 3 different hole features (circular, square, diamond), each varying from $100\ \mu\text{m}$ to $1000\ \mu\text{m}$ in increments of $50\ \mu\text{m}$. Each part is built with three different thicknesses: 0.25, 0.5, and 1.0 mm.



**Figure 9: Benchmarking specimens a) 1D ribs and gaps (at 0° , 45° , 90° orientation),
b) 2D hole features (circular, square, diamond)**

2.3.2 *Experimental Methods*

2.3.2.1 Printer Description and Settings

The benchmark parts were manufactured using an Objet260 Connex Polyjet printer [31]. The Objet260 Connex machine is a high resolution, multi-material printer with a moderate size build area (255 x 252 x 200 mm XYZ). The printhead bank assembly consists of eight printheads, each including 96 nozzles spaced 0.6809 mm (~1/37.5 inch) apart, with a nozzle diameter of 50 microns [32]. In total, the machine can support up to three distinct materials. Four of the printheads are allocated for support material, and the remaining four are allocated for build materials, either a single build material in all four printheads or two build materials with two printheads each. The printer has three printing modes depending on how the build materials are loaded. When using a single build material in all four printheads, one can print using either High Quality Mode or High-Speed Mode. If two build materials are loaded, then the Digital Material Mode is used. As the names suggest, the key differences relate to build resolution, build speed, and printing with more than one material. High Quality Mode provides the machine's best resolution, reported as 600x600 DPI (X and Y axes), and a 16 μm layer thickness. The High-Speed Mode maintains the X and Y axis resolution, but has an increased layer thickness of 30 μm , and is stated to be roughly half the build time of the High-Quality Mode. Digital Material Mode is a bit of a hybrid, where Stratasys literature reports a 30 μm layer thickness, but "near-high quality" resolution and print times. Stratasys highlights that the Digital Material Mode is often preferred, as having two available build materials eliminates the need to swap materials for different builds, which reduces setup times and the amount of wasted model material, all with a minimal impact on quality.

The next critical setting is the selection of surface finish: Matte or Glossy. A Matte finish encases the full build with support material, which textures the surface. A Glossy finish excludes support material, except for the base or when required for an overhang, resulting in a smooth surface.

For the specimens printed in this study, two build materials were loaded into the machine, and were therefore printed using the Digital Material Mode. All parts were assigned to be a single material, VeroWhite, which is one of Stratasys' proprietary materials that is rigid and opaque. The surface finish was selected to be Glossy, such that no extra support material was used.

2.3.2.2 Measurement Process

Three duplicate specimens were built for each benchmark part at each thickness (e.g., 3x Benchmark A at 0.250mm thickness, 3x Benchmark A at 0.5mm thickness, and 3x Benchmark A at 1.0mm thickness). All Polyjet parts use a base layer of support material which must be removed. Therefore, after printing, the base support material was manually removed with a scraper and then parts were cleaned using isopropanol and a soft bristle brush. Features were imaged using a Nikon SMZ800 stereomicroscope, equipped with a PixeLink camera (PL-B686CF), and measured using image analysis software with a measurement resolution of 1.5 μ m, as well as a 0.001 mm digital micrometer.

2.3.3 1D Features – Gaps

Figure 10 shows a representative cross-sectional view of the fabricated gap features, specifically the 0° orientation gap of the 1mm thickness part.

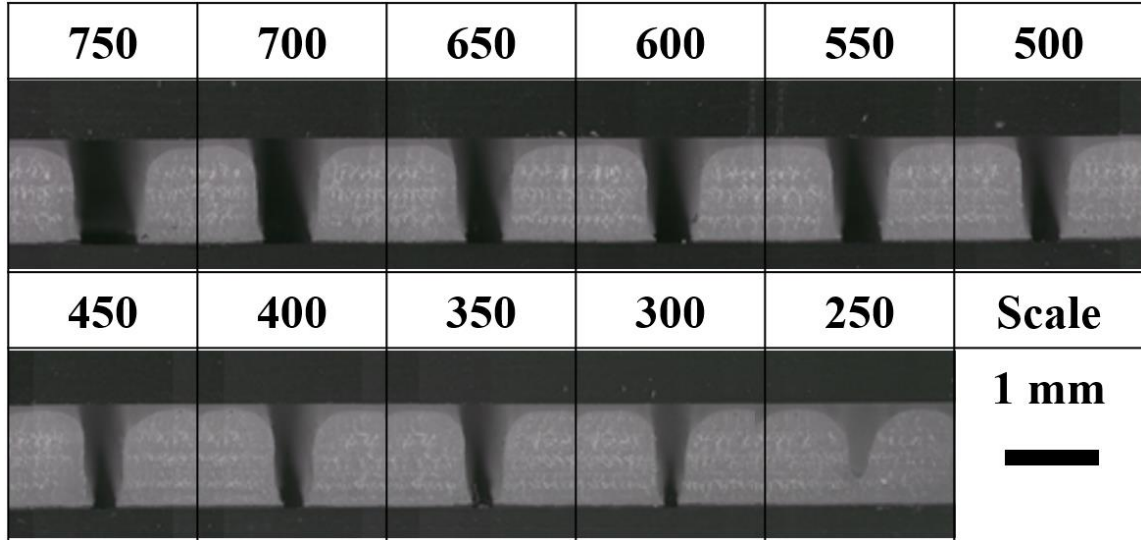


Figure 10: Gap feature cross-section for 1mm part in 0° orientation

First, parts were inspected to determine minimum manufacturable feature size, which for gaps is determined to be a minimum designed gap dimension that is open all the way through the part. Table 2 shows the minimum manufacturable feature for each thickness and orientation. The minimum manufacturable gap is found to be 300 μm irrespective of thickness and orientation. One gap with a width of 250 μm was successfully printed for the 250 μm thick part, in the 90° orientation, but was not successful for all specimens.

Table 2: Minimum manufacturable gap (μm) varying thickness and orientation

Gaps	0	45	90
250	300	300	300
500	300	300	300
1000	300	300	300

Second, fabricated features were measured to evaluate dimensional accuracy. Measurements were taken at the bottom opening of the gap and results are shown in Figure 12 and Figure 13. Measured dimensions are consistently smaller than the designed dimension for all thicknesses and orientations. Additionally, thickness has no discernible impact on the measured gap dimension, which is especially evident for 45° and 90° orientations. The observed independence from thickness is significant, as others have hypothesized that the closure of thin gaps results from extra material being pushed over the edge by the roller [29]. If this is true, any effects are localized within $250\mu\text{m}$ of thickness and do not scale with height. Additionally, the 45° and 90° orientations produce very smooth increments in size, tracking with the designed dimension. The 0° orientation, however, has discrete plateaus and jumps likely resulting from the fixed nozzle spacing in the y-direction.

It is apparent from the cross-sectional images that significant rounding and deformation results in a wider opening at the top of the printed features and a smaller opening at the bottom. To better understand the gap profile, measurements of gap width at the bottom, middle, and top of the features is presented in Figure 14, with a representative example shown in Figure 11.

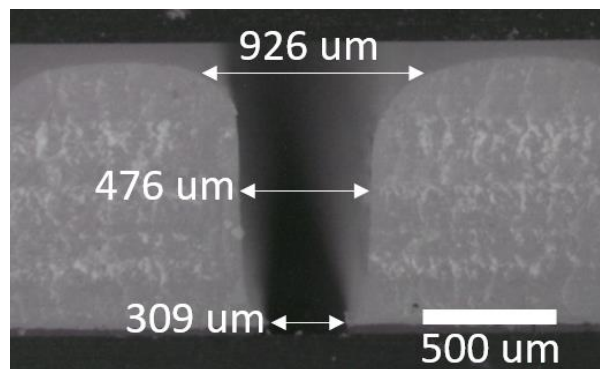
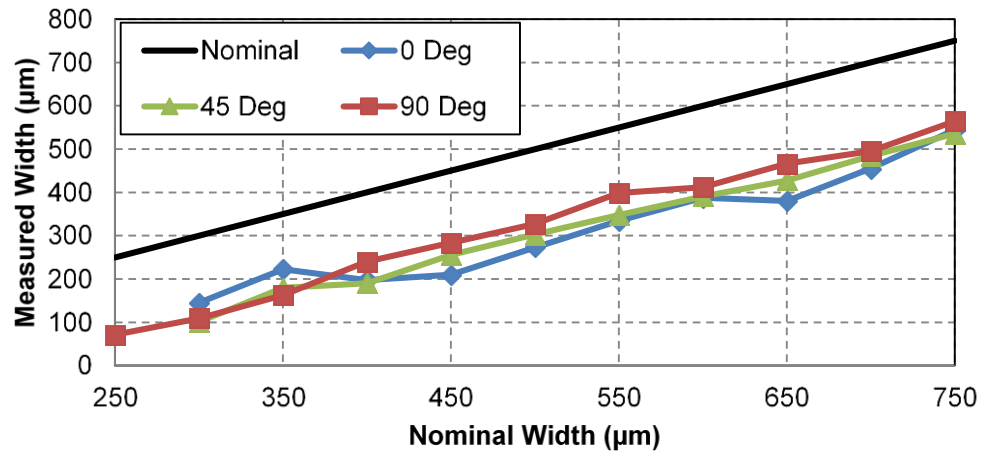
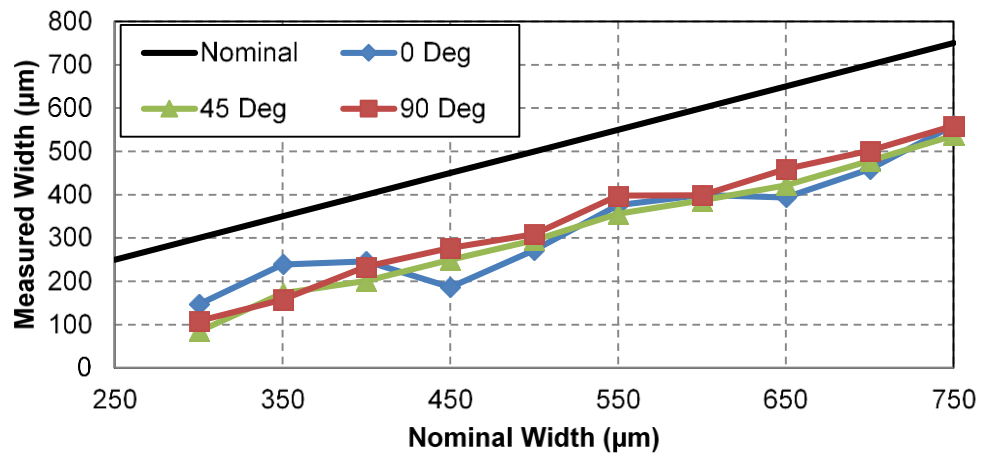


Figure 11: Cross-sectional measurement of 1mm part, 0.500mm gap

a) 250 μm



b) 500 μm



c) 1000 μm

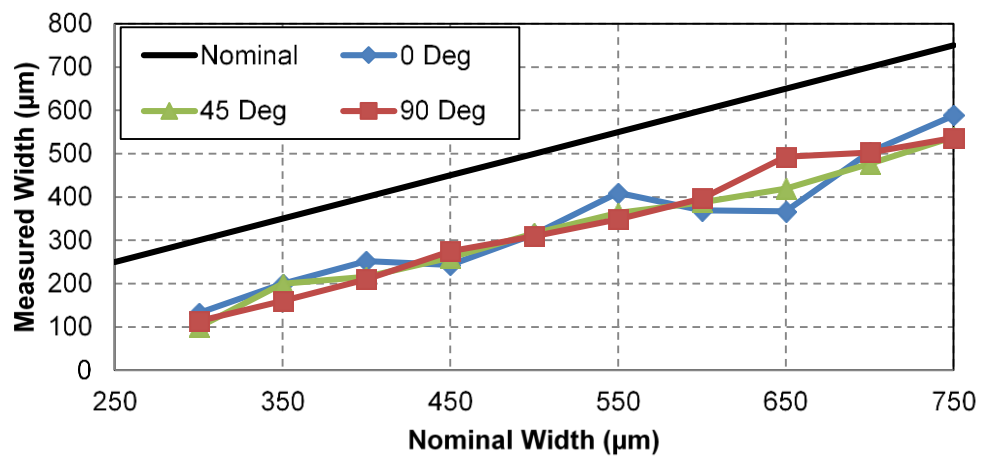
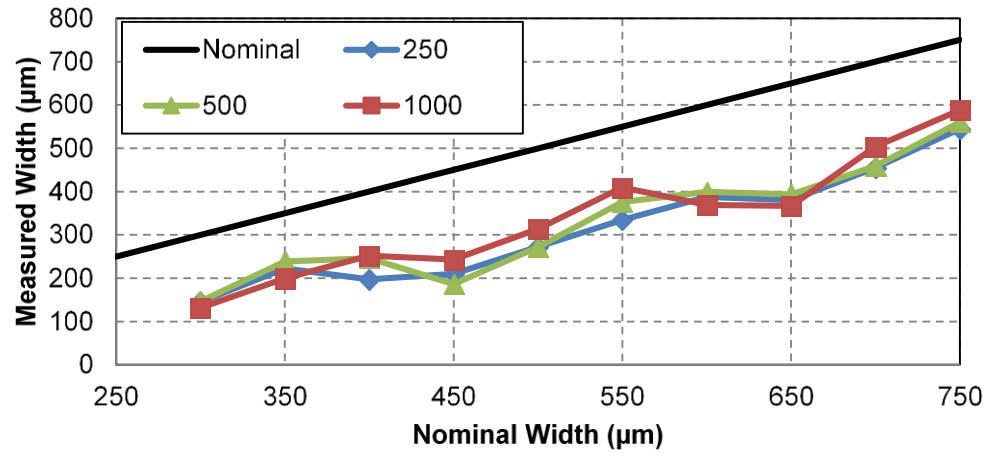
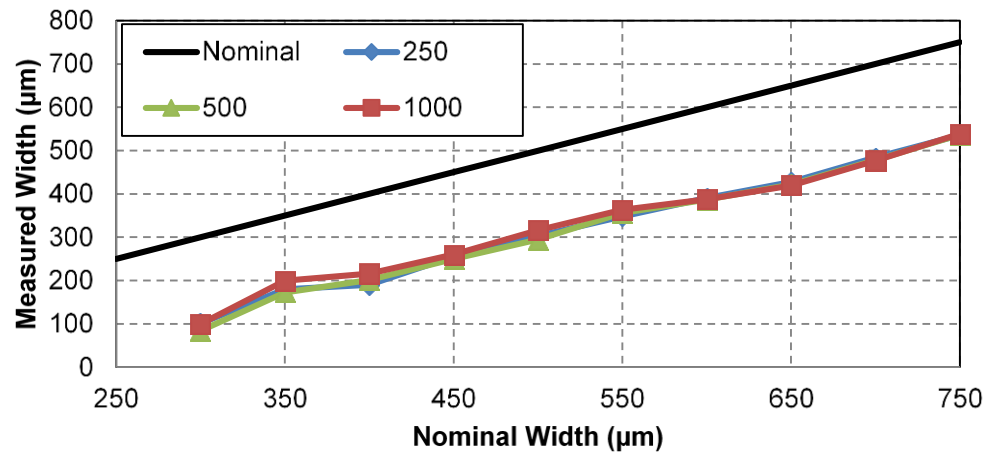


Figure 12: Gap width at bottom with varying orientation angle - a) 250 μm , b) 500 μm , c) 1000 μm

a) 0 Degree



b) 45 Degree



c) 90 Degree

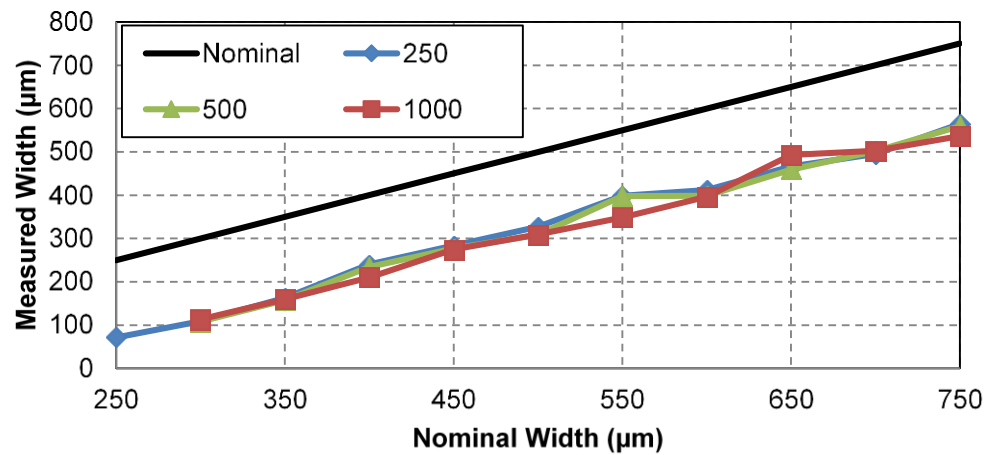


Figure 13: Gap width at bottom with varying thickness - a) 0°, b) 45°, c) 90°

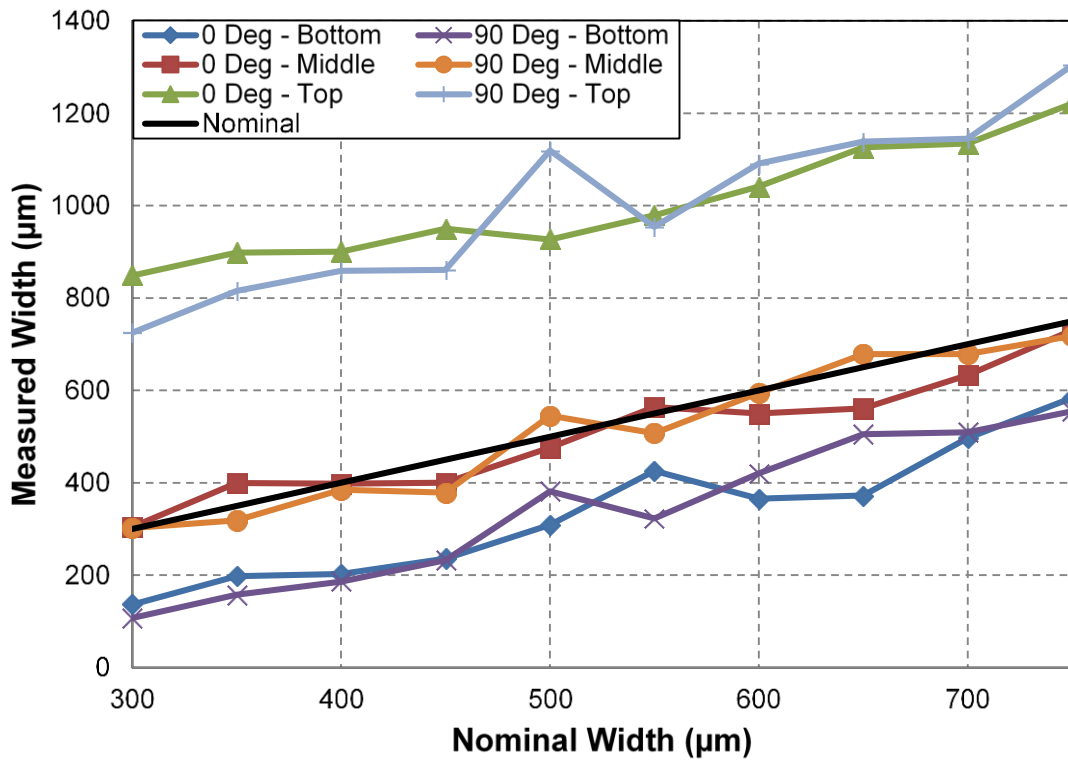


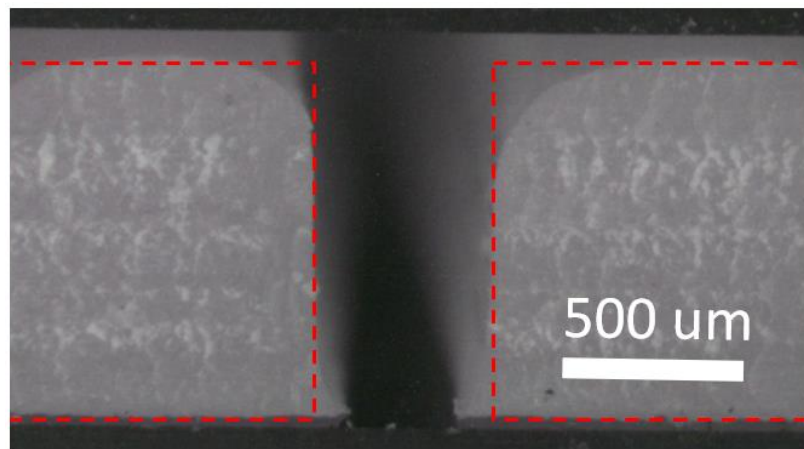
Figure 14: Gap width measured at bottom, middle, and top of feature profile with orientation angle of 0° and 90°

As previously mentioned, the width at the bottom is consistently smaller than the designed dimension. At the top of the gap, the measured dimension is significantly larger than the designed dimension. At the middle, however, the measured dimension tracks the designed dimension very well. The average dimensional error is shown in Table 3, below:

Table 3: Average dimensional error over feature profile

	Bottom	Middle	Top
0°	-192 μm	-23 μm	477 μm
90°	-187 μm	-14 μm	476 μm

The dimensional errors presented above are a result of shape deformations at the exterior and interior corners, specifically convex and concave rounding. As shown in Figure 15, the interior rounding results in a protrusion past the desired profile whereas the exterior rounding underfills the profile by a considerable degree. These deformations are of critical concern for the suggested applications, where such deviations from the designed feature could alter the flow characteristics and thus device performance.



----- Designed Profile

Figure 15: Comparison of desired profile with as fabricated cross-sectional profile

An additional complexity of the above deformations is their variations with size. Figure 16 illustrates the shape evolution as a gap feature grows thicker. The profile starts convex but then an inflection point appears as the vertical wall emerges. This growth can be seen in Figure 17, where the gap profiles have been extracted and overlaid. While some have suggested the curvature results from material overflowing the edge, and this may be true for the first few layers, it appears more likely that the edge is actually receding relative to the initial layer deposits, as there is a longer arc length to cover compared with the initial flat surface. This process continues progressively until a vertical wall is formed and a steady state condition is achieved.

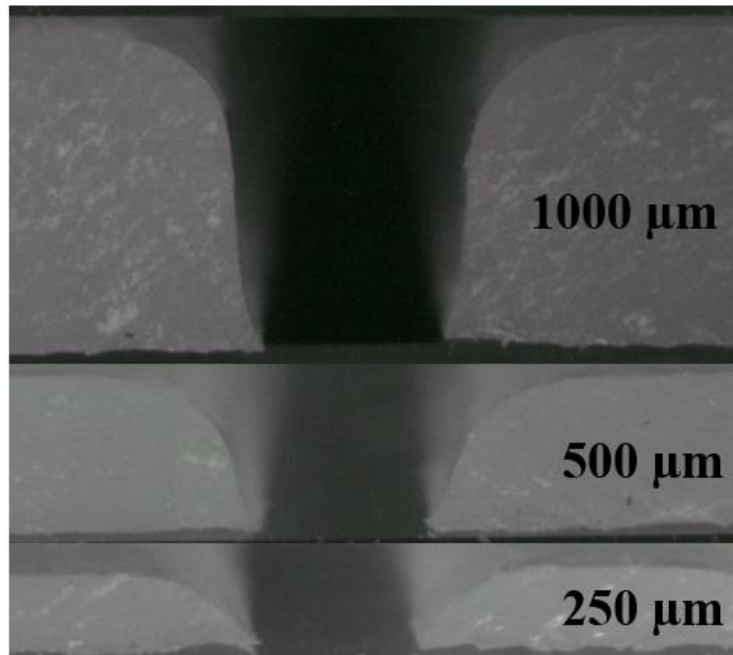


Figure 16: Cross section profile evolution for gap feature

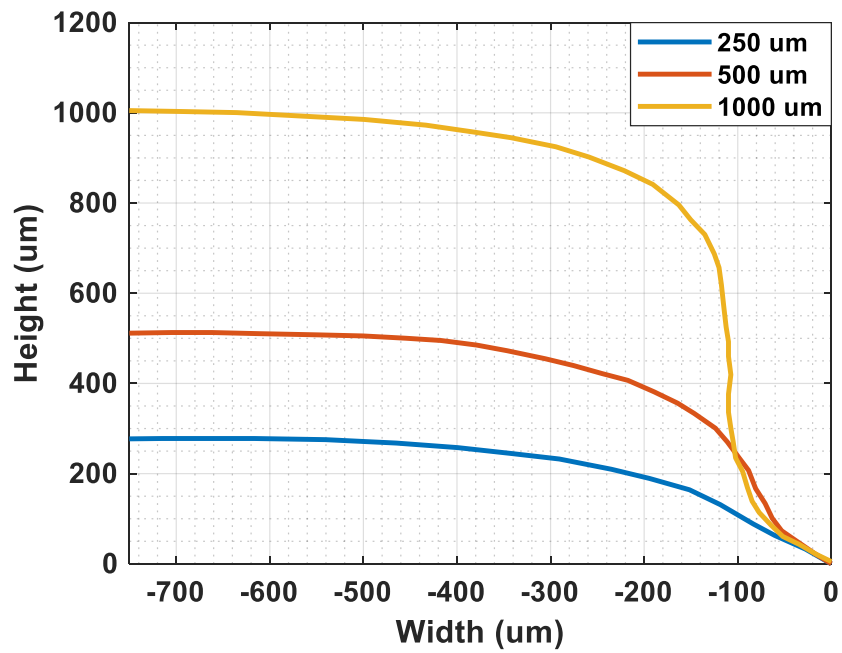


Figure 17: Overlay of feature profile for gap at different thicknesses

2.3.4 1D Features – Ribs

Continuing with the analysis of primitive mesoscale features, an investigation into rib fabrication is now presented. Figure 18 shows a representative cross-sectional view of the fabricated rib features, specifically the 90° orientation gap of the 1mm thickness part.

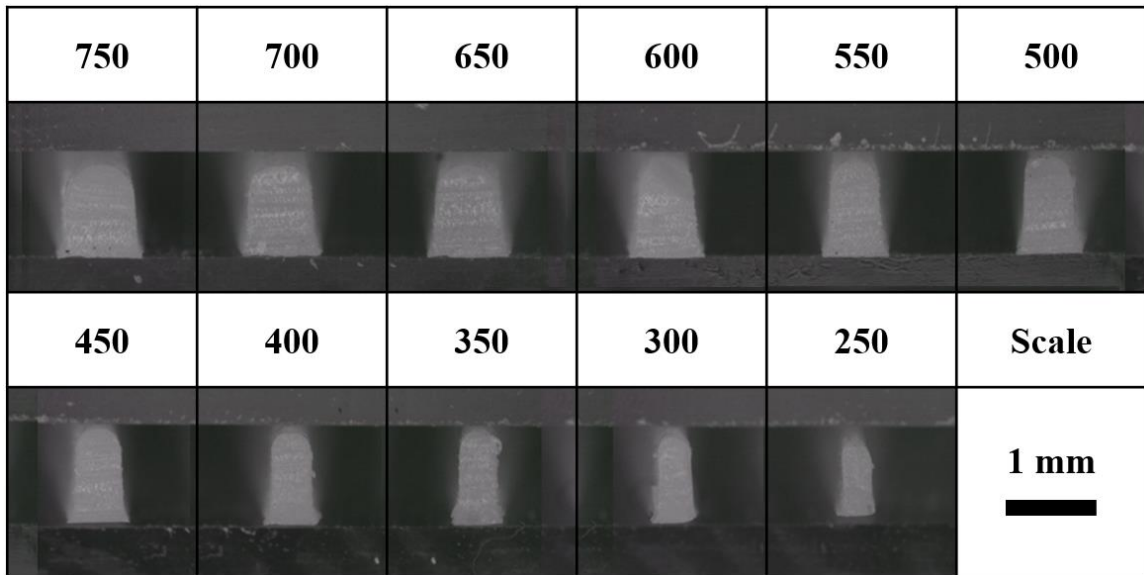
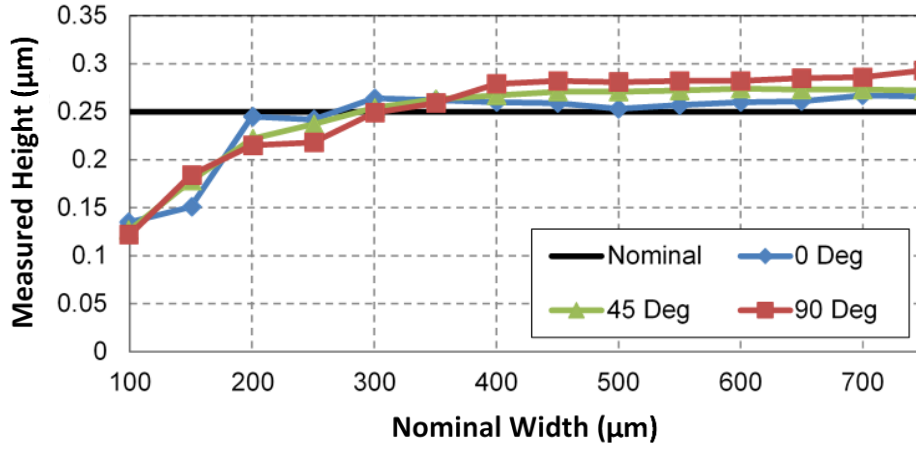


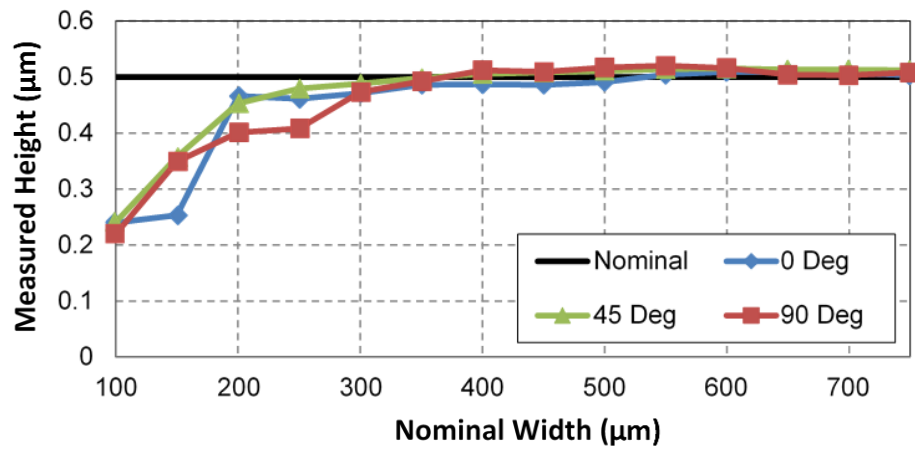
Figure 18: Rib feature cross-section for 1mm part

While determining success for gap features is relatively straight forward, as light will pass through the gap during inspection, rib feature success is less obvious as some form of feature is present for even the thinnest designed rib. Therefore, rib heights were measured using a ten-thousandth micrometer, shown in Figure 19, and the minimum manufacturable feature size is established as the minimum designed rib that is built to full height.

a) 250 μm



b) 500 μm



c) 1000 μm

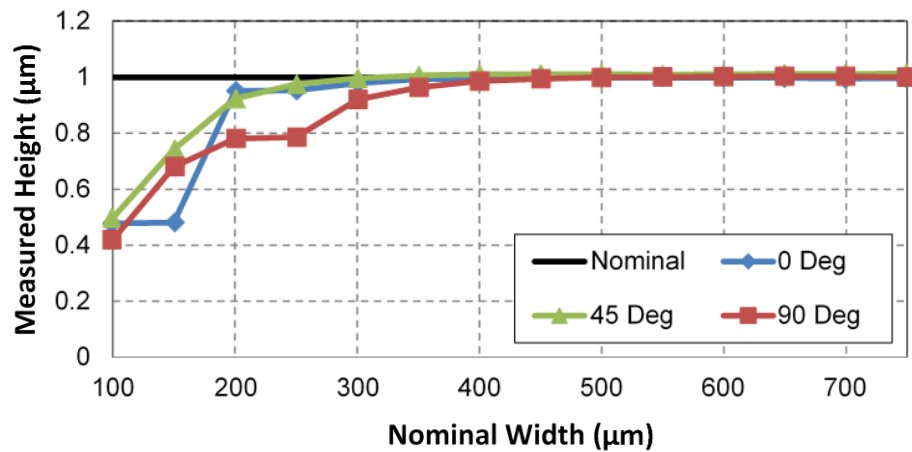


Figure 19: Rib height with varying orientation angle - a) 250 μm , b) 500 μm , c) 1000 μm

From the height measurement results shown in Figure 19, it is observed that “full height” could be a subjective evaluation based on the application tolerance, as well as consideration for discretization error resulting from the thicknesses not being a multiple of the layer thickness and potential additional support material remaining (especially for the thinnest parts that were very delicate and difficult to clean). It is also observed that a clear plateau of build height is achieved for thicker ribs of the benchmark parts, suggesting that these ribs have fully topped out. Therefore, within the context of this work, success for achieving “full height” is defined to be a height within $30\mu\text{m}$ (1 layer thickness) of the average plateau height, where plateau height was calculated as the average height of the last 6 ribs (0.500mm and greater). Using this criteria, the minimum manufacturable rib sizes are reported in Table 4.

Table 4: Minimum manufacturable rib size (μm)

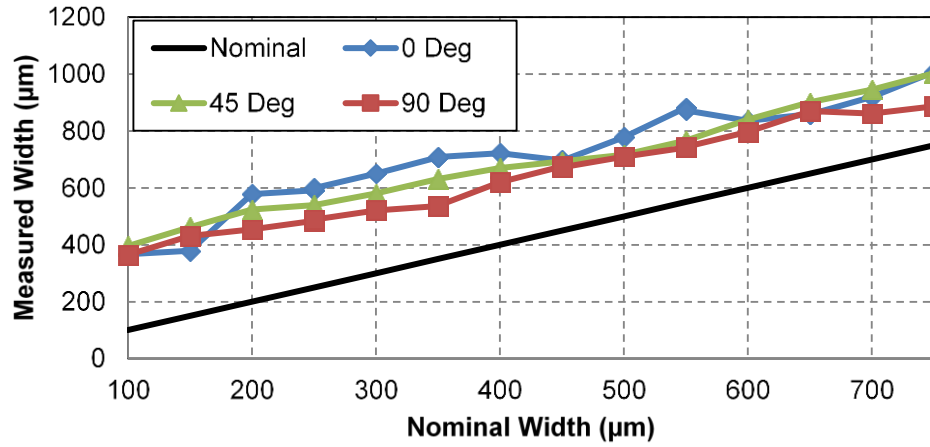
		Orientation ($^{\circ}$)		
		0	45	90
Thickness (μm)	250	200	300	350
	500	300	300	350
	1000	300	300	400

The 0° orientation produced the smallest designed ribs (0.200, 0.300, 0.300 mm minimum rib, respectively) to achieve full height, with the 45° orientation producing similar results of 0.300mm minimum rib for all thickness. The 90° orientation had a slightly larger minimum manufacturable rib size (0.350 – 0.400 mm minimum rib). Additionally, the 0° orientation still performed quite well down to 0.200mm ribs for the thicker parts, with measured height deviations within $60\mu\text{m}$ (2 layers), before the

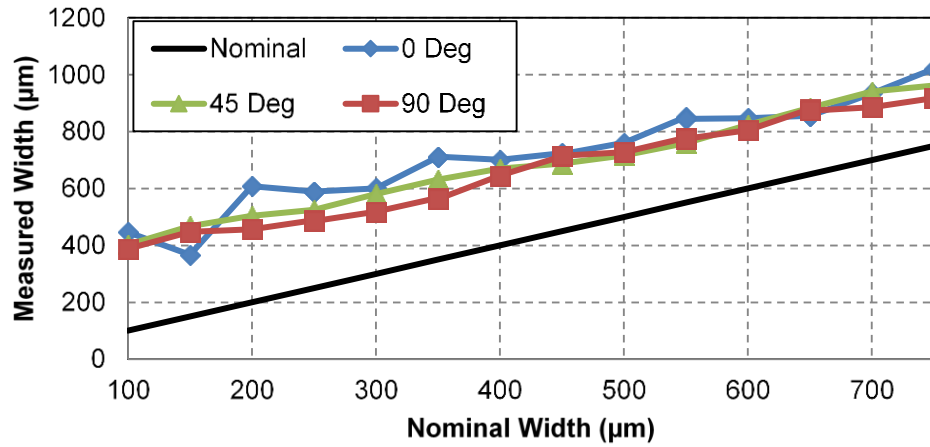
measured height dropped significantly. From these results, it is recommended to design ribs or thin wall to be 0.400 mm wide or greater when possible, and to align any smaller ribs with the 0° orientation (printing direction). One additional observation of the 0.100 mm nominal width rib, for all thicknesses, is that the measured height is consistently around half of the desired height. This is likely due to a scenario where the rib is only a few droplets wide, and as it builds, a portion of the material from the droplets at or near the edge is flowing down the edge slope and not contributing to the height.

As was done for gaps, fabricated rib features were measured to evaluate dimensional accuracy. Measurements were taken at the bottom of the rib and results are shown in Figure 20 and Figure 21. Measured dimensions are consistently larger than the designed dimension for all thicknesses and orientations. Matching the observations for gaps, thickness has no discernible impact on the measured width dimension, which is especially evident for 45° and 90° orientations. Orientation has minimal observed impact on rib features, with 0° tending to be slightly wider, 90° measuring slightly smaller, and 45° falling in between. Rounding and deformations are again observed, which results in a wider bottom of the printed features and a smaller top. To better understand the overall profile dimension, measurements of rib width at the bottom, middle, and top of the feature is presented in Figure 22. Due to the continuous round at the top of the rib features, it is difficult to take a top width measurement. Therefore, the “top” width measurement was taken one layer thickness (30 µm) below the highest point in the cross section.

a) 250 μm



b) 500 μm



c) 1000 μm

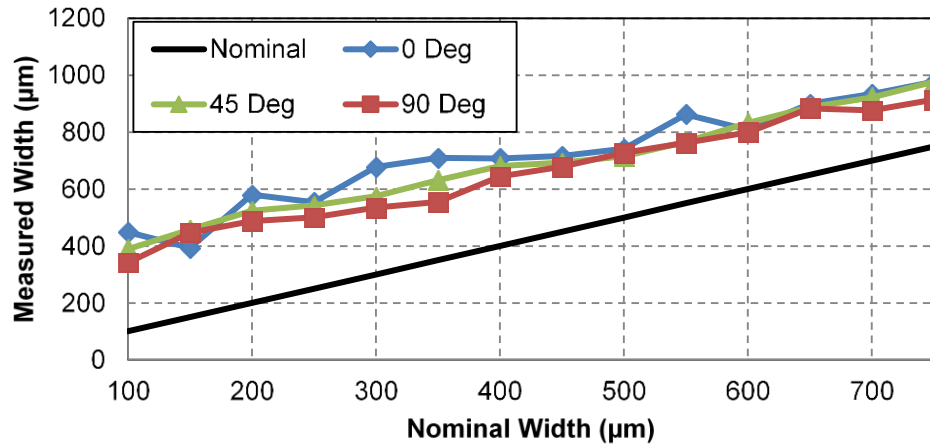
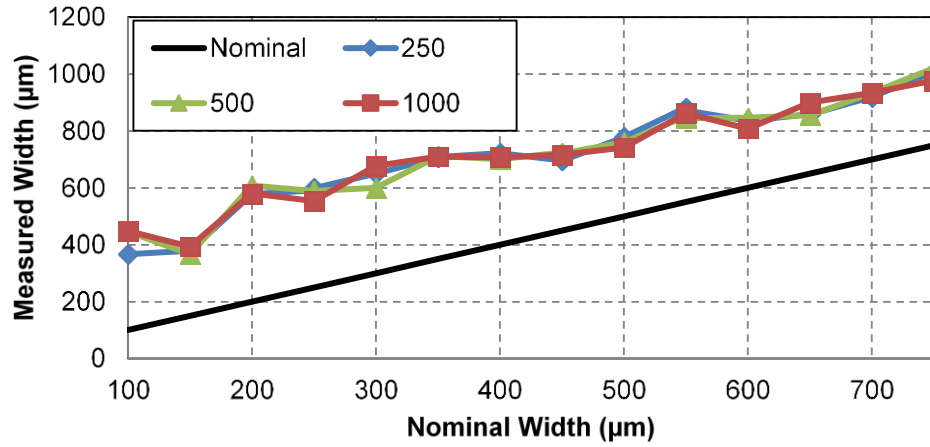
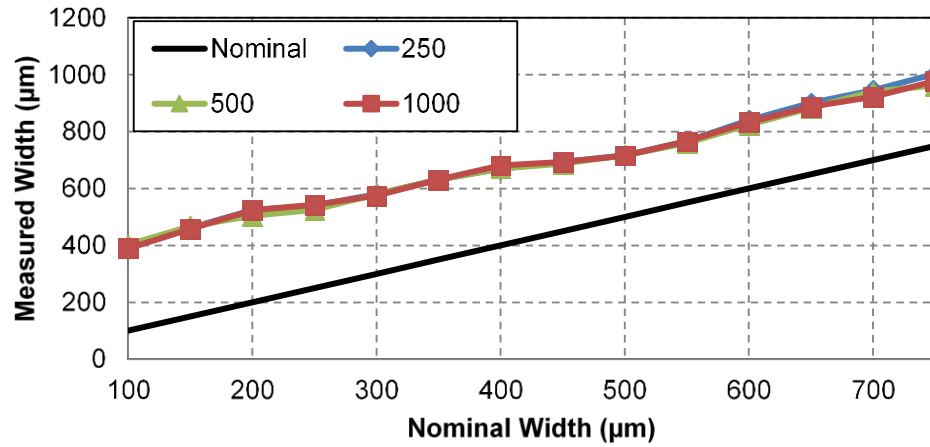


Figure 20: Rib width at bottom with varying orientation angle - a) 250 μm , b) 500 μm , c) 1000 μm

a) 0 Degree



b) 45 Degree



c) 90 Degree

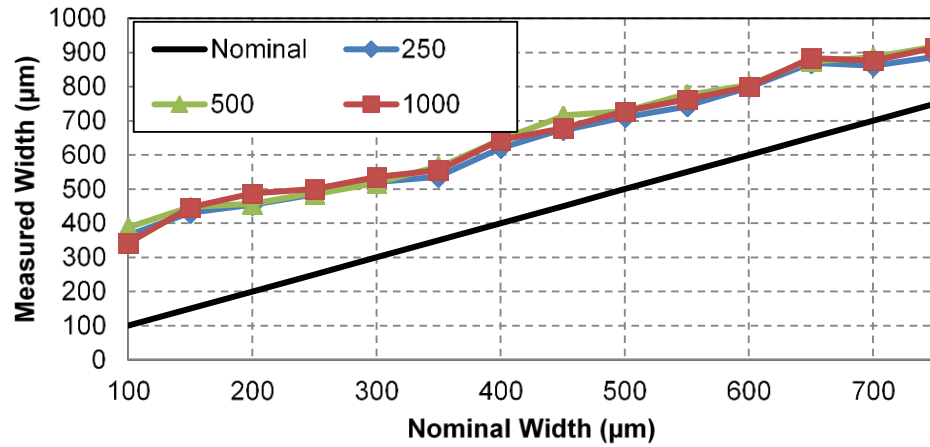


Figure 21: Rib width at bottom with varying thickness - a) 0°, b) 45°, c) 90°

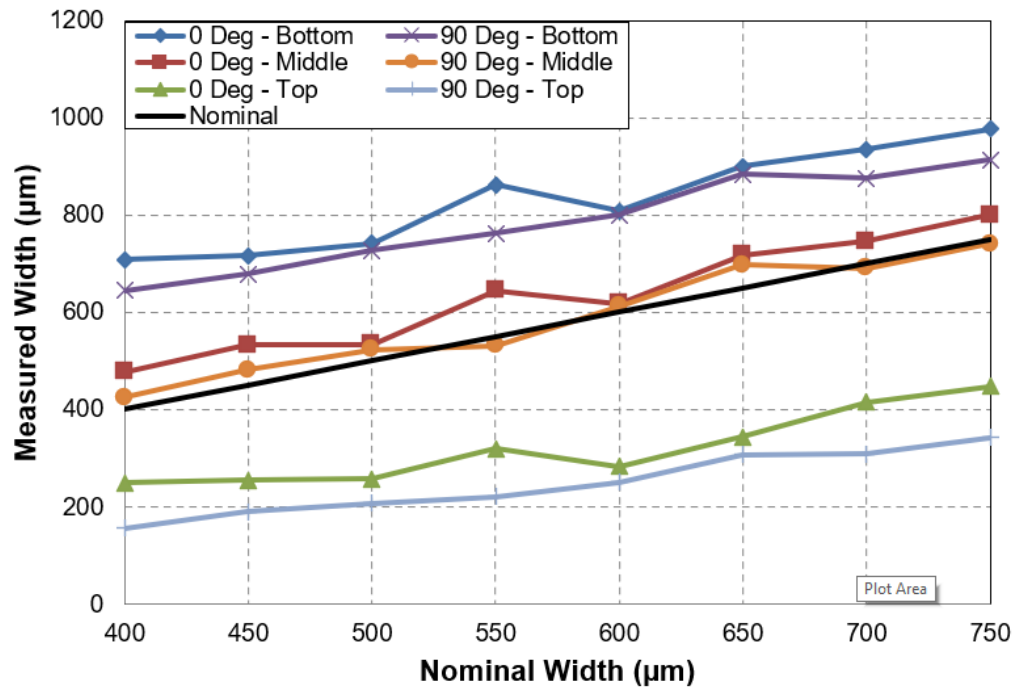


Figure 22: Rib width measured at bottom, middle, and top of feature profile with orientation angle of 0° and 90°

In terms of overall shape accuracy, the width at the bottom is consistently larger than the designed dimension. At the top of the rib, the measured dimension is significantly smaller than the designed dimension. At the middle, however, the measured dimension, again, tracks the designed dimension very well. The average dimensional error is shown in Table 5, below:

Table 5: Average dimensional error over profile

	Bottom	Middle	Top
0°	280 μm	90 μm	-193 μm
90°	216 μm	25 μm	-285 μm

These deviations track with those seen during the analysis of gaps (albeit the inverse) and are a result of the geometric deformations discussed previously. A comparison of the designed feature shape with the as fabricated shape is presented in Figure 23.

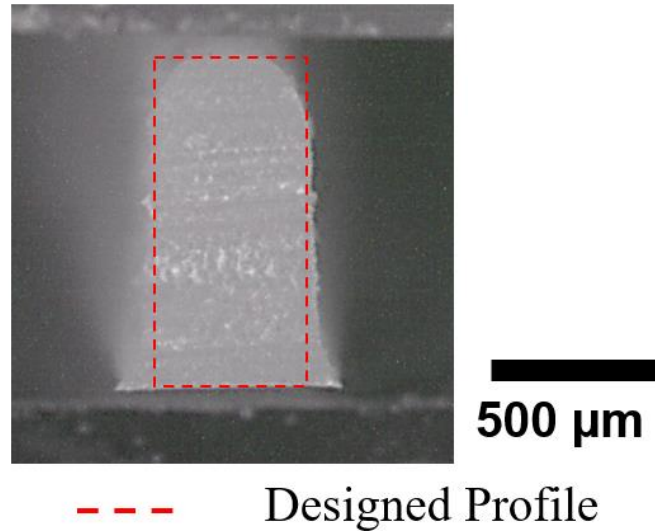


Figure 23: Comparison of rib feature desired profile with as fabricated cross-sectional profile

2.3.5 2D Features

In this section, the investigation into mesoscale feature fabrication is expanded to study two dimensional holes. Three different hole shapes are considered, circular, square, and diamond (square rotated 45°), each with a characteristic dimension varying from 100 μm to 1000 μm in increments of 50 μm . Representative top and bottom views of the three fabricated features, with 1 mm thickness, are shown in Figure 25.

To determine minimum manufacturable feature size, two criteria were considered. First, as was done for gaps, a successful build was determined to be the minimum designed hole dimension that is open all the way through the part. This dimension for each shape and thickness is shown in Table 6 under the subheading, “Through.” For square and

diamond shaped holes, the minimum manufacturable feature size is 450 μm irrespective of thickness. Whereas for circular holes, the minimum manufacturable feature size matches for the thinnest part but increases to 500 μm for a thickness of 500 μm and 1000 μm . The square and diamond shapes likely printed the smaller feature due to the increased hole area compared with the circle.

It is apparent from the images in Figure 25 that as the size decreases, squares and diamonds no longer reflect their desired shape and transition towards a circular cross section. This is due to rounding of the interior corner, similar to the rounding observed at the bottom and top edges. Therefore, the second criteria for minimum manufacturable feature size is the minimum dimension where the as fabricated shape still reflects the desired shape based on the top view. For circular holes, this naturally matches the “through” criteria. However, for square and diamond holes, it is noticeably larger at 750 μm and 650 μm , respectively. Thus, if the hole shape is of critical importance, features with straight edges would need a larger minimum edge dimension.

Table 6: Minimum manufacturable hole size for varied thickness (μm)

Holes	Circle		Square		Diamond	
	Through	Shape	Through	Shape	Through	Shape
250	450	450	450	750	450	650
500	500	500	450	750	450	650
1000	500	500	450	750	450	650

To evaluate dimensional accuracy measurements were taken at the bottom opening of the holes. As shown in Figure 24, circular holes were measured in four directions, whereas square and diamond holes were measured twice with respect to their characteristic

dimension. Measured dimensions are presented in Figure 26, Figure 27, and Figure 28, and are consistently smaller than the designed dimension for all thicknesses and measurement orientations which matches the results observed for gaps. Thickness has no significant impact on the measured gap dimension, with the exception of the 450 μm circular hole being successful at 250 μm thickness, but not at 500 μm or 1000 μm .

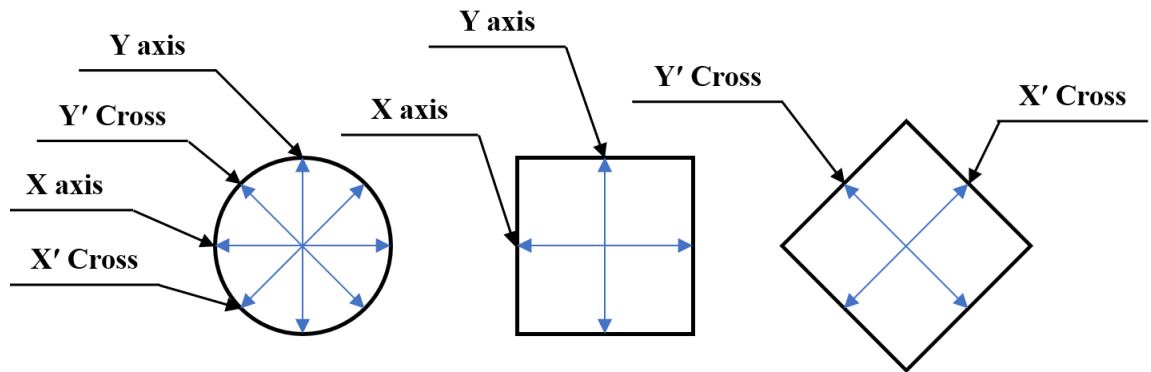


Figure 24: Schematic of measurement directions and naming convention

Measurements at the bottom, middle, and top are shown in Figure 29 for the 1000 μm thick Square Hole to evaluate accuracy along the profile. In close agreement with gap feature accuracy, the measured dimensions have a considerable offset at the bottom and top resulting from the corner rounding discussed previously. At the middle of the feature, the measured dimension tracks the desired dimension very well. Average dimensional error is shown in Table 7.

Table 7: Average dimensional error over profile for 1000 μm thick Square Hole

	Bottom	Middle	Top
X axis	-194 μm	-23 μm	439 μm
Y Axis	-180 μm	-10 μm	427 μm


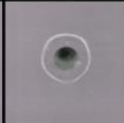
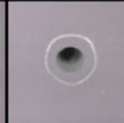
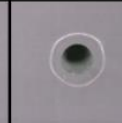
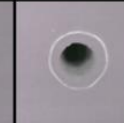

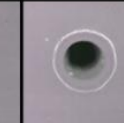
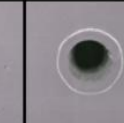
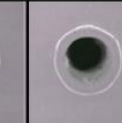

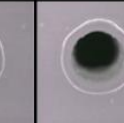
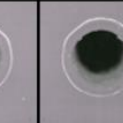
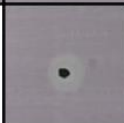




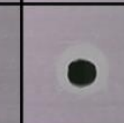
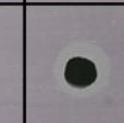
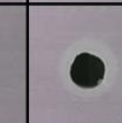


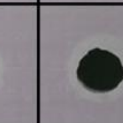

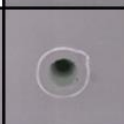


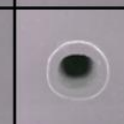






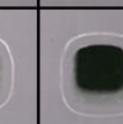

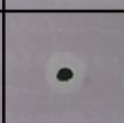



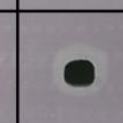


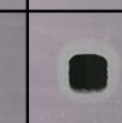

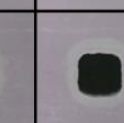
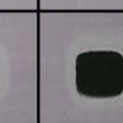









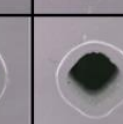


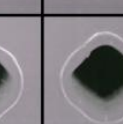




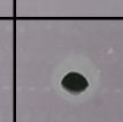


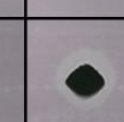

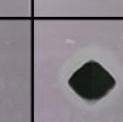




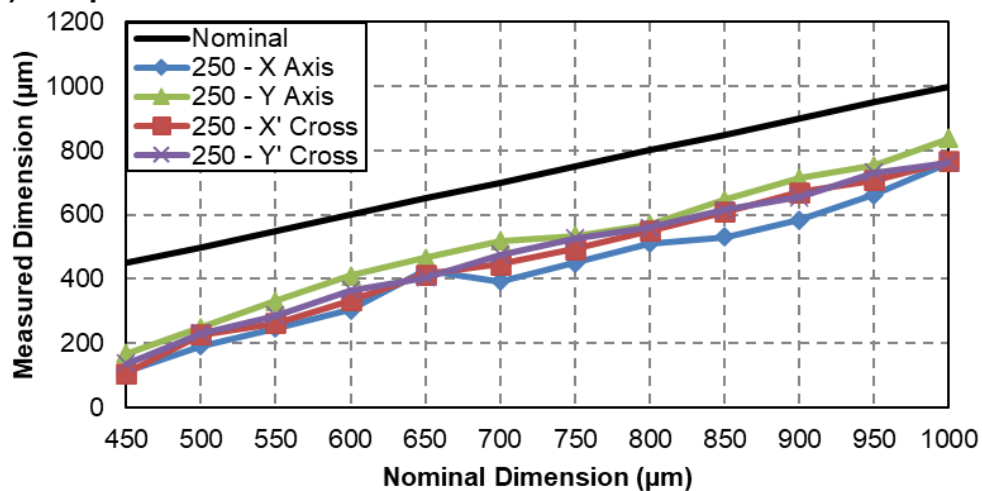
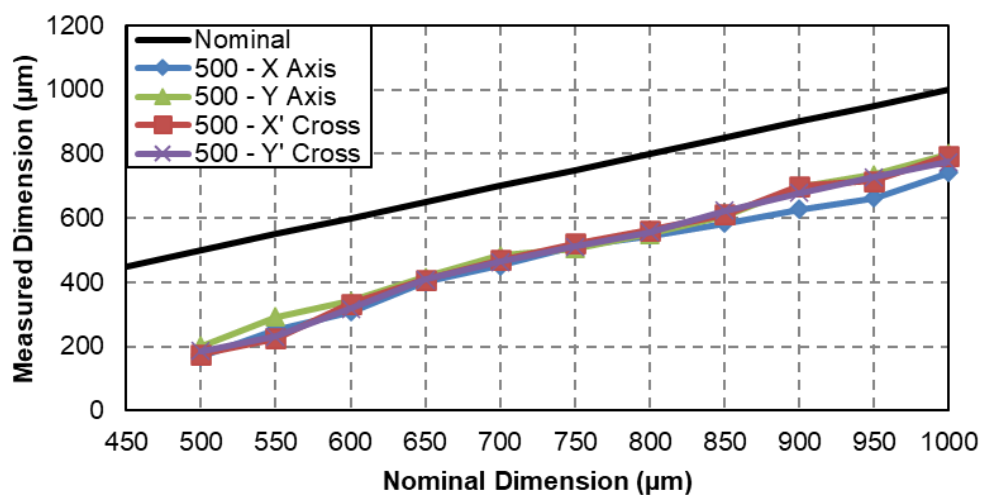
	400	450	500	550	600	650	700	750	800	850	900	950	1000
Circular	X												
	X	X											
Square	X												
	X												
Diamond													
													
X – did not print												1000 μm 	

Figure 25: Microscope images of fabricated 2D features from the top and bottom

a) 250 μm



b) 500 μm



c) 1000 μm

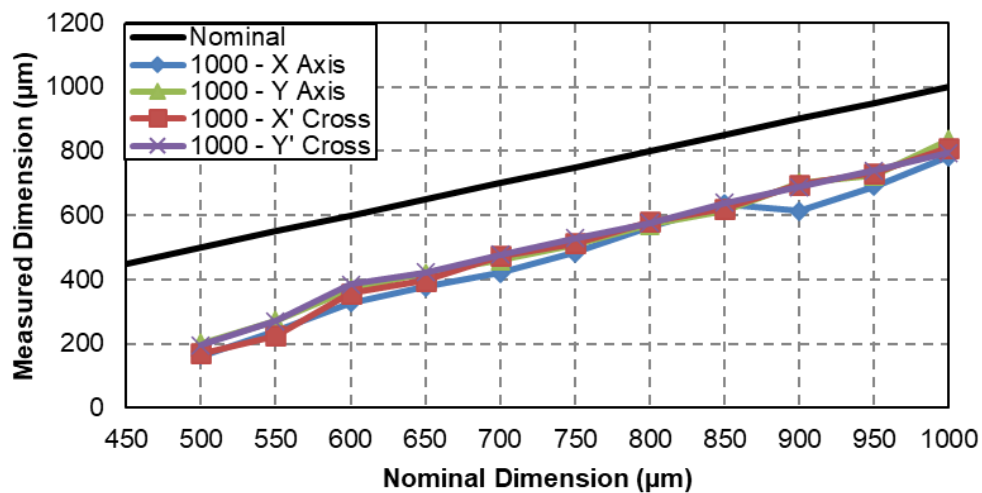
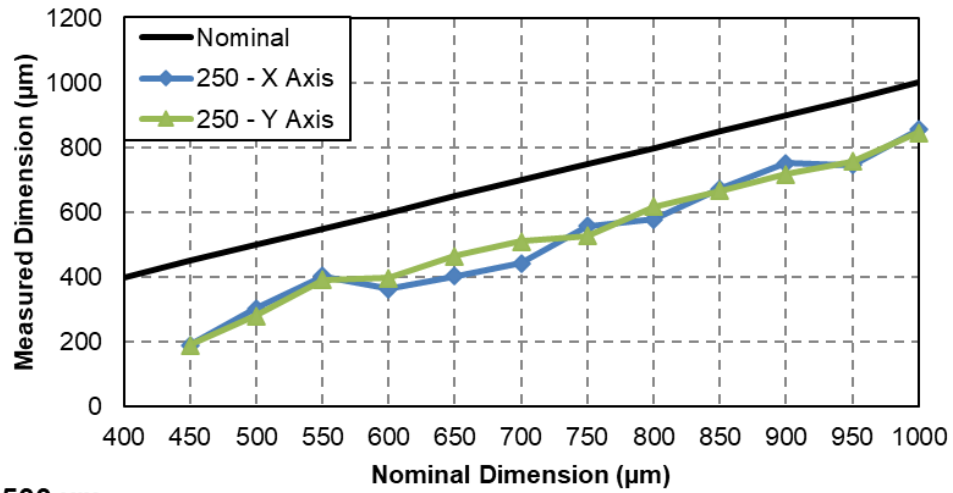
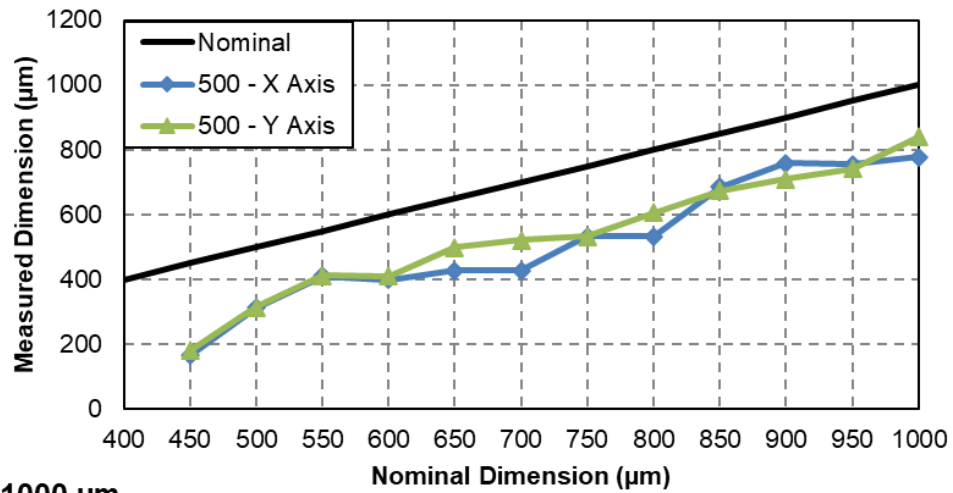


Figure 26: Circular hole measurement at bottom - a) 250 μm , b) 500 μm , c) 1000 μm

a) 250 μm



b) 500 μm



c) 1000 μm

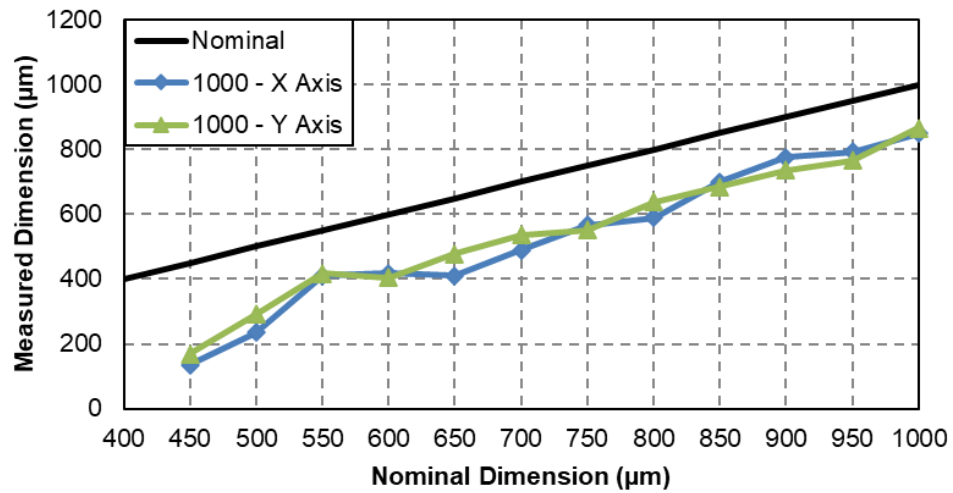
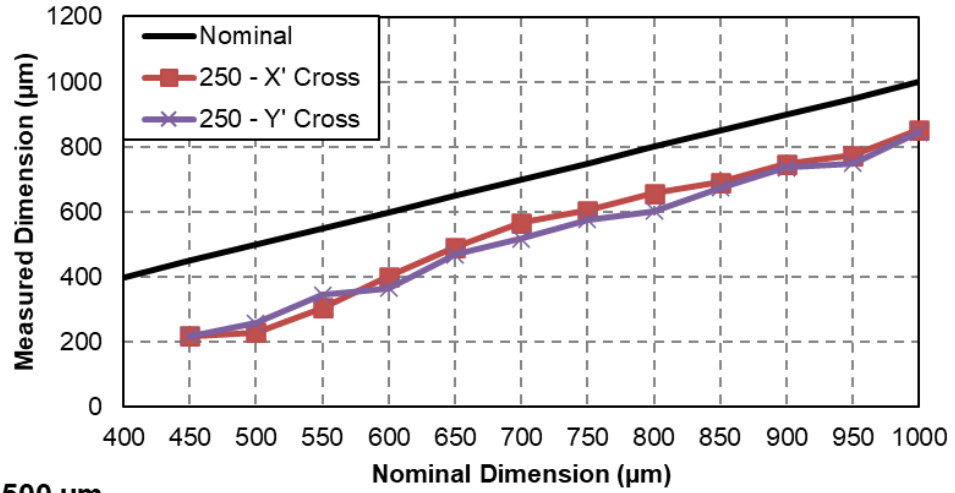
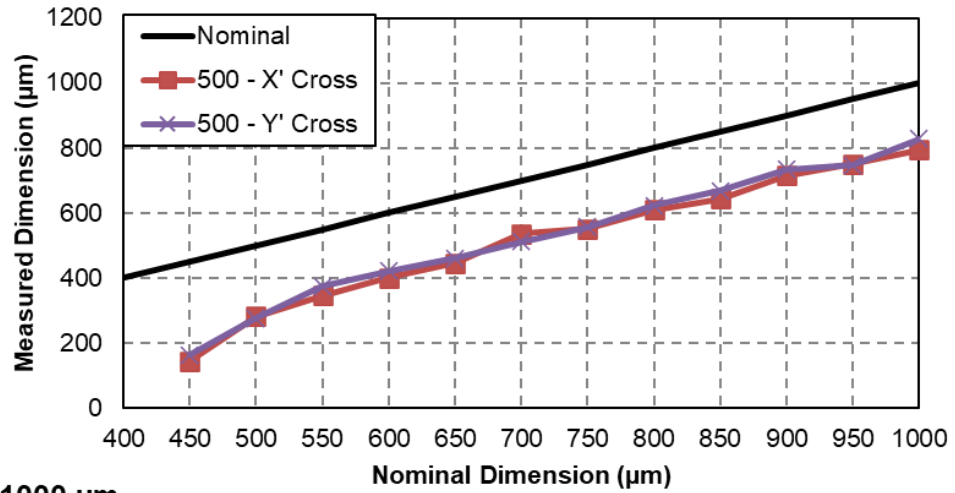


Figure 27: Square hole measurement at bottom - a) 250 μm , b) 500 μm , c) 1000 μm

a) 250 μm



b) 500 μm



c) 1000 μm

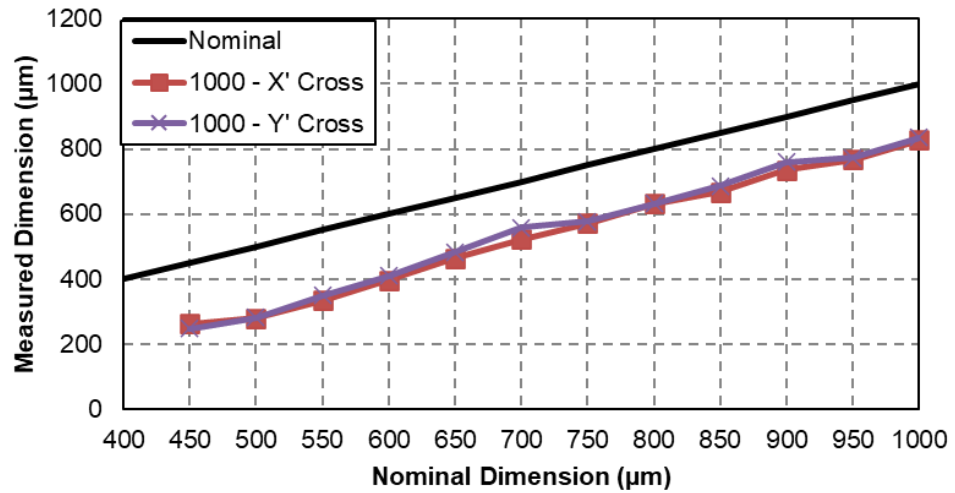


Figure 28: Diamon hole measurement at bottom - a) 250 μm , b) 500 μm , c) 1000 μm

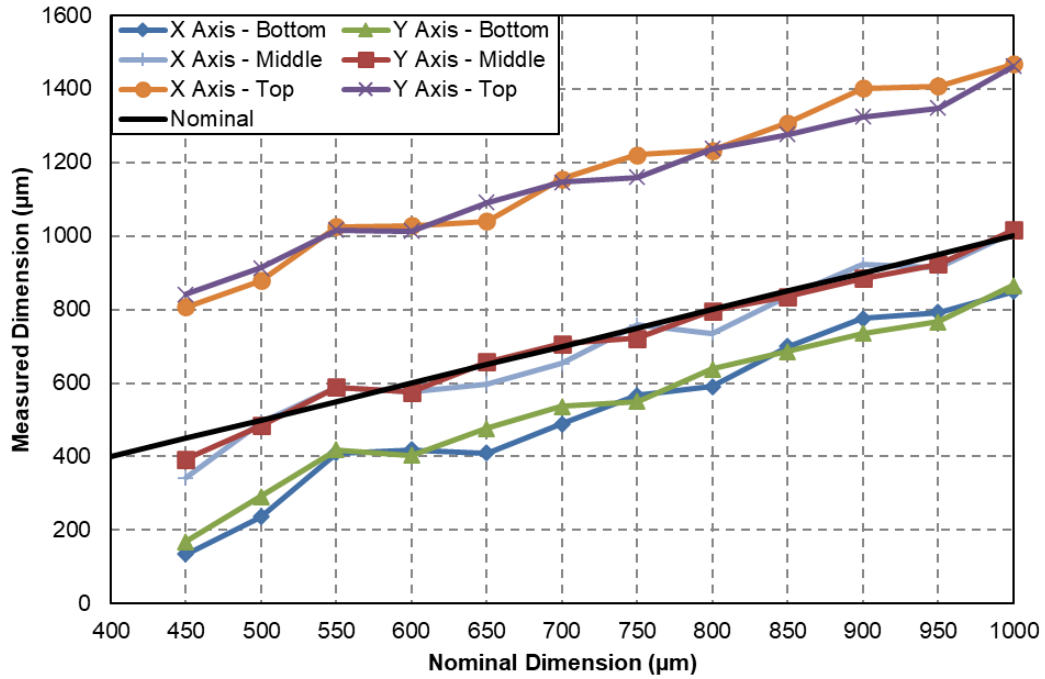


Figure 29: 1000 μm thick square hole measured at bottom, middle and top

As described in the results above, shape accuracy along the thickness (XZ and YZ plane) of the feature for 2D holes was found to match that of the 1D features, namely significant deformation at the top and bottom edges resulting from convex and concave corner rounding as well as shape profile transition as the feature grows thicker, see Figure 30.

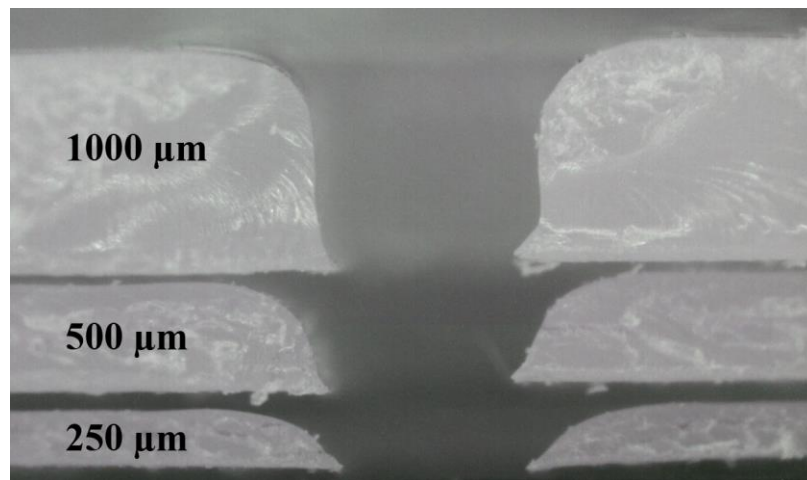


Figure 30: Cross-sectional profiles of square hole with different thicknesses

Additional shape deformation is observed in the XY plane cross-section in the form of corner rounding for the square and diamond features, which as the designed dimension decreases results in the fabricated shape converging towards circular. A comparison of the designed feature shape with the as fabricated shape for a square and diamond is presented in Figure 31. It is observed that the diamond feature has on average a slightly smaller corner radius which results in the better minimum feature shape fidelity described above.

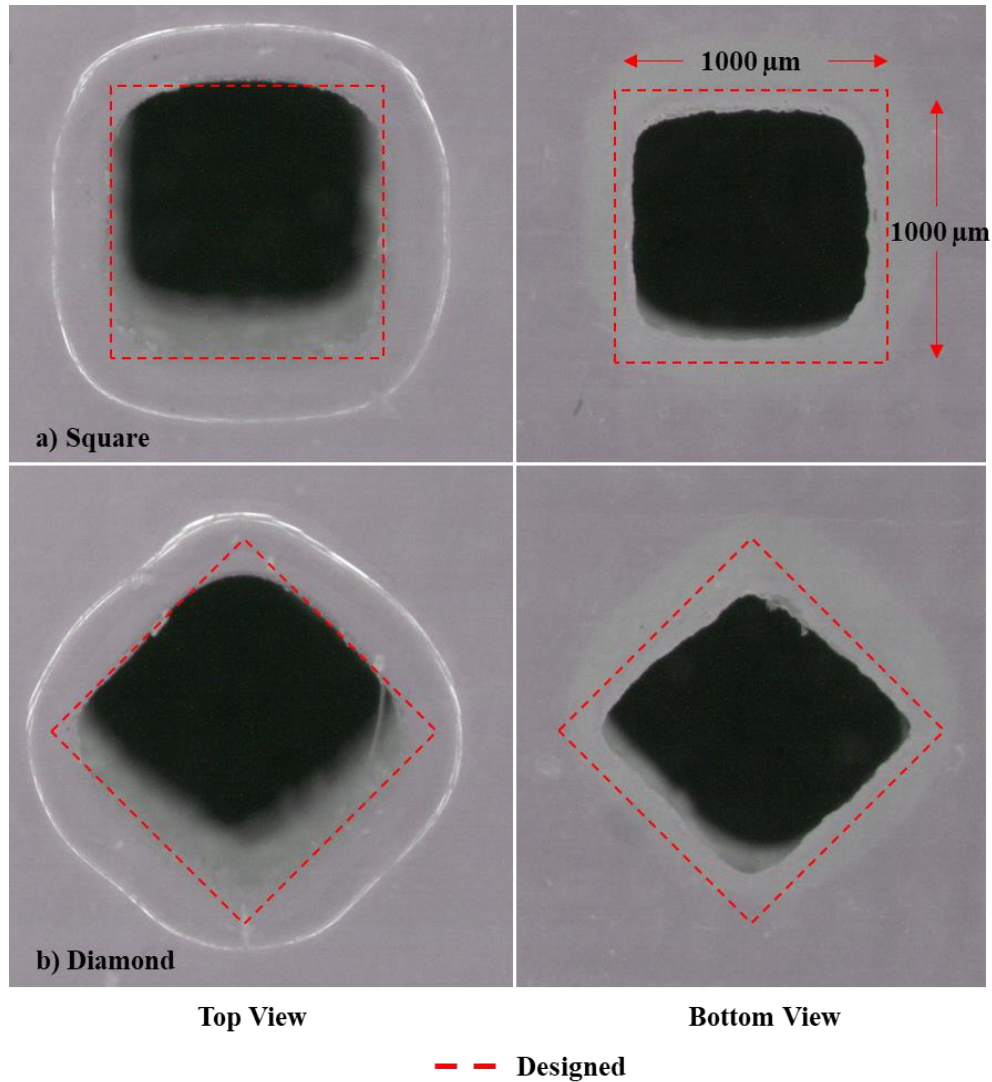


Figure 31: Comparison as fabricated feature with desired shape, and observed corner rounding: a) square, b) diamond

2.4 Discussion

In the preceding sections, a benchmark study into mesoscale feature fabrication is presented, specifically investigating minimum manufacturable feature size, dimensional accuracy, and feature shape. It is clear the inkjet machine under study is capable of fabricating sub-millimeter mesoscale features, down to a few hundred micrometers for these basic shapes. However, it is also noteworthy that the minimum feature sizes found were several times larger than the reported machine resolution of $42\mu\text{m}$ (600dpi). Additionally, while the accuracy at the middle of the feature tracked well with the desired dimension, at the top and bottom of the features deformations in the form of concave and convex rounding caused significant deviation from the desired dimension and shape. Similar rounding was seen for the interior corners of the square and diamond holes. Potential sources of these printing errors are considered hereafter, but it is also important to note that given the proprietary nature of the system, there is an inherent degree of uncertainty around how the process planning is implemented and the consequences they may have.

While the reported resolution is “near-high quality” (High Quality being 600x600 dpi) in the XY plane, a deeper investigation suggests that the Y-axis (perpendicular to the print direction) resolution under these selected print conditions is likely 300 dpi ($84.6\mu\text{m}$). This results from each model material being dispensed from only two print heads for the Digital Material Mode (rather than four printheads for single material mode), and the resolution is thus halved. This lower resolution in the Y-axis helps to explain why gap and rib features oriented in line with the print direction, 0° , had discrete plateaus and

jumps when compared with smoother increments for 45° and 90° orientations, as seen in Figure 12 and Figure 13.

Even considering the above suggested resolution reduction, the observed minimum features (e.g., 300µm for gaps) is still 3 to 4 times larger than lowest machine deposition resolution. To understand this discrepancy, one must consider the details of the deposition process, where layers are formed from lines built of individually ejected droplets, and the sources of error therein.

The above reported dots per inch (dpi) provides an indication of the density of droplets being deposited, but of equal importance with respect to MJ feature resolution is the volume of material being deposited with each drop and the shape once deposited. Several factors control the volume of material ejected (e.g., nozzle diameter, actuator type, fluid properties, etc.), and specific tuning and investigation is required when selecting machine printheads. In the machine under investigation, a Ricoh printhead is used with two tunable drop volume ranges available, 25-35 picoliter and 60-90 picoliter, and a reported volume variation of $\pm 10\%$ for each drop [33]. In the current machine, it is believed that for the High-Quality mode a 30pL droplet is used, whereas for the High Speed and Digital Material Mode a 90pL droplet is used. Upon deposition, the initially spherical droplet spreads and rebounds as kinetic energy of impact dissipates, and surface energy driven spread develops to yield a final equilibrium shape of a spherical cap, characterized by the fluid-surface contact angle and the droplet volume. Prior investigations have indicated the contact angle for the Vero class materials to be approximately $40 \pm 5^\circ$ [34]. Considering this contact angle range with a $90\text{pL} \pm 10\%$ droplet, a deposited droplet footprint would have a nominal diameter of 106.4 µm but could vary from 98 - 116 µm,

considerably higher than the 42 μm and 84 μm calculated from 600 and 300 dpi. Furthermore, as multiple droplets are deposited, coalescing into lines of material, this value represents a minimum footprint width. In fact, considering a deposition rate of 600 dpi with the above droplet characteristics, the expected line width would nominally be 138 μm and reasonably range from 128 - 147 μm , further reducing the feature resolution.

Next, consider the positional errors when placing the individual droplets. The droplet path once ejected from a printhead nozzle is not always perfectly perpendicular to the surface. For instance, the Ricoh printhead considered herein reports a jet straightness of 50 milliradian ($\sim 2.9^\circ$). If the gap is assumed to be 1mm, the error in impingement position due to ejection angle could be as high as 50 μm in any direction. Furthermore, the position of the printhead itself introduces its own errors. Typical belt drive linear actuators like those used for the X and Y direction movements of the printhead carriage have reported accuracies of around 100 μm and positional repeatability within 25 μm .

Combining these uncertainties together reveals their potential impact on resolution. Considering a deposited line, as illustrated in Figure 32, the material boundary edge position could be off by as much as 80 μm from the ideal boundary, and 107 μm beyond what a 300 dpi resolution would suggest.

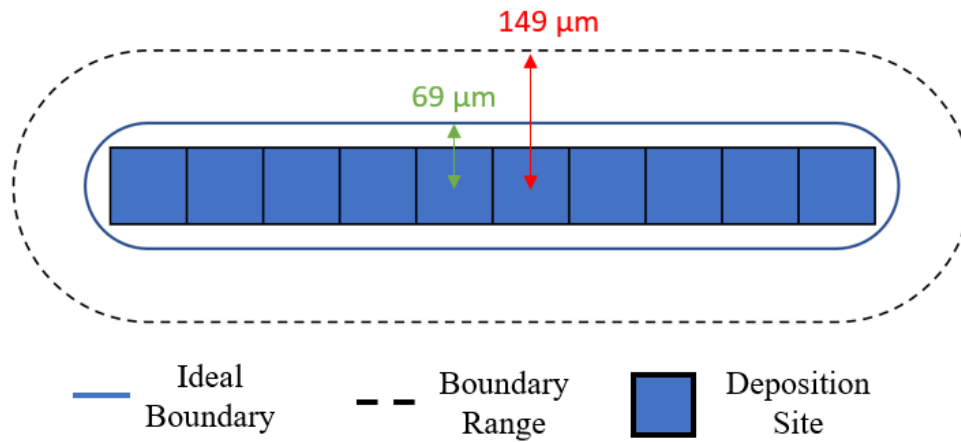
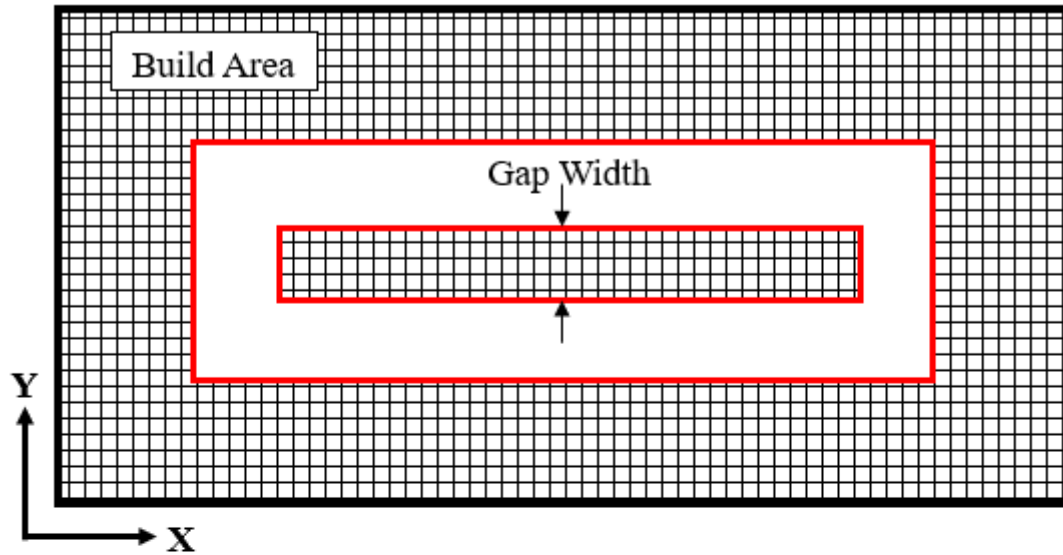


Figure 32: Boundary uncertainty for a deposited line

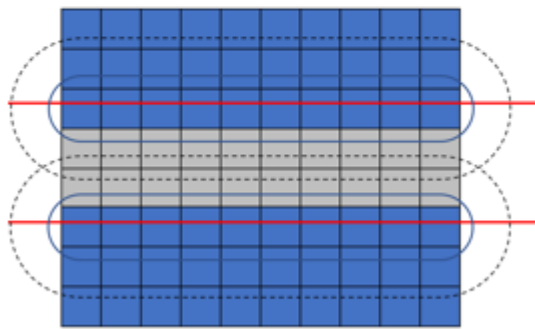
Relating the above errors and uncertainties to the minimum feature sizes observed in the preceding sections helps to explain why the observed resolution is so much lower than the printer specifications. As illustrated in Figure 33a, when a part to be fabricated is laid out on the build platform, the cross section for each layer is overlaid a pixelized printing region. In its simplest form, there is a fixed grid matching the resolution of the printer settings, and the printer processing software determines the droplet deposition sites based on the pixels that intersect the boundary or fall within the part interior similar to a binary image. Figure 33 (b, c) shows a representative deposition grid for a 250 μm and 300 μm gap aligned with the X axis (0° orientation) assuming a 300x300 dpi grid. Sites colored blue indicate that a droplet should be deposited, whereas sites colored gray represent a blank. Notice that during this pixelization process, there is some discretization error resulting from the fixed grid not aligning perfectly with the cross-section boundary. The ideal deposition boundary and the boundary range considering uncertainties are included as well. For a designed gap with a nominal width of 250 μm , it is observed that the gap opening is equivalent to two blank sites, and that the boundary range for the edge depositions overlap explaining why this size gap generally failed to print. For the 300 μm

gap, we see the gap opening is three sites wide, separating the edges enough that the boundary ranges do not overlap, explaining why at this designed dimension the feature successfully printed.

a) Gap Layer Cross-Section



b) 250 μm Gap



c) 300 μm Gap

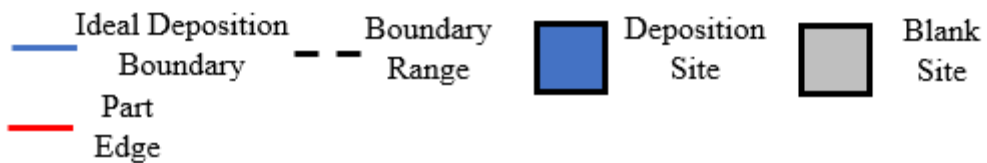
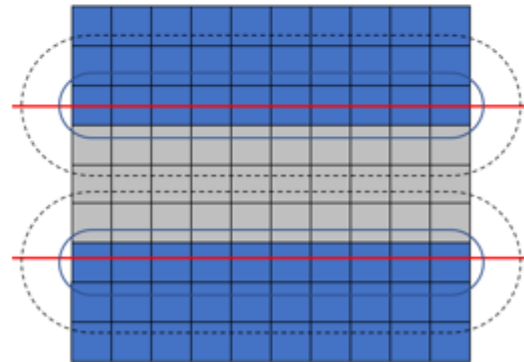


Figure 33: Illustration of impact of droplet spread and position uncertainty on printing gaps, a) gap feature on pixelated build platform, b) 250 μm gap which fails to print, c) 300 μm gap which successfully prints

Additionally, the droplet and line spread discussed above only considers deposition on the initial ideal surface present for the first layer. After that, droplet and lines deposited at the edge are impacting on a more complex surface as shown in Figure 34. As the second layer of droplets impact this edge, it is likely to flow down and past the first layer boundary, expanding the part footprint. Additionally, any positional error described above could offset the impact down the curved edge increasing the angle of incline at impingement and increasing the spread down the incline. The magnitude of this overflow is unknown as no AM literature appears to have explored this phenomenon. Even in the broader inkjet/droplet deposition literature, similar boundary conditions are relatively unexplored; thus, further investigation is certainly warranted. Some works investigating printed electronics have sought to leverage the deposition flow next to pre-deposited and solidified beads showing that under certain surface conditions the newly deposited material could flow fully down to the base surface [35], [36].

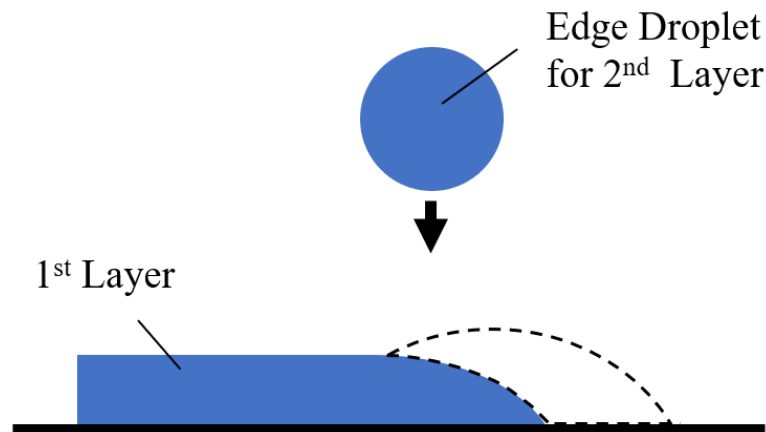


Figure 34: Schematic diagram of droplet impacting at edge of previous layer and overflowing previous boundary

A critical observation of the above discussion is that determining material jetting minimum feature resolution goes far beyond the “dots per inch” at which droplets are

deposited as is often highlighted. Other key factors include volume of ejected droplets, contact angle and spreading, droplet coalescence into lines, droplet flow on an incline, ejection angle uncertainty, as well as machine positional accuracy. In fact, given the magnitude of effect caused by machine accuracy and ejection angle uncertainty cited above, the general accuracy of the machine could significantly outweigh the deviations in volume of material deposition. Running a similar boundary range analysis using the highest resolution setting which has droplets roughly one-third the volume used above (now 30 pL), the anticipated improvement for gaps using this benchmark part would be successfully printing of one size down, 250 μm , but likely struggling to print a 200 μm wide gap.

Another important factor affecting the fabricated feature accuracy is the shape deformations observed, particularly the edge rounding, sloped walls, and corner rounding. We observed that such deformation resulted in variations along the feature profile causing errors at the top and bottom of the feature.

Of particular note for the observed shape deviations is the magnitude of rounding observed at the top edge of fabricated features, shown in Figure 35. Which, on review of the cross-sectional images shown above, range from 200-400 μm (approximately 5-10 times the reported resolution and droplet size).

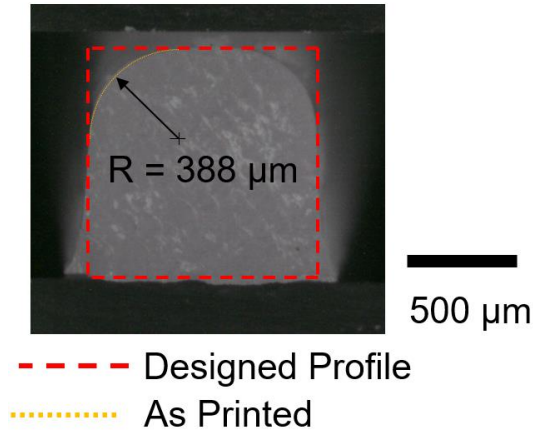


Figure 35: Corner rounding on the top edge of printed feature

There are several possible explanations for this deformation. Other works observing similar deformation have suggested excess flow of material down the feature wall due to gravity before the UV light had passed or the leveling roller pushing material over the edge [29], [37]. Shrinkage due to the UV curing process is known in other AM processes and could apply here. It is also possible that Stratasys in their planning process recognizes some challenge with deposition near the edge, such as overflowing or missing the edge and closing feature gaps, and they adjust for this by backing off deposition near the edge as the feature height increases. However, due to the limited insights into the processing software this suggestion is unrealistic to explore. Another consideration is the role of droplet level impact, as discussed above, spreading at the layer edge, and resulting in accumulated deviations in height.

If the deposited material were indeed flowing down the wall to the base of the feature, we would expect to see some feature width dependency on part thickness. As shown in Figure 13 and Figure 21, there was no dependency on part thickness and would suggest if such flow existed, it is limited to only a few layers of relative influence. Additionally, at the size scales and fluid properties of interest for inkjet applications, the relative effects

of gravity are negligible compared with the surface energy and viscous forces at play, as described by Bond Number later in this work. Therefore, while it is certainly realistic that a droplet impacting an incline will spread asymmetrically “downhill” compared with symmetric radial spread on a flat surface, as seen in Figure 36, this would be very localized to the impact location, and after completing the droplet would in effect be “stuck” in that location and would not slide down due to gravity.

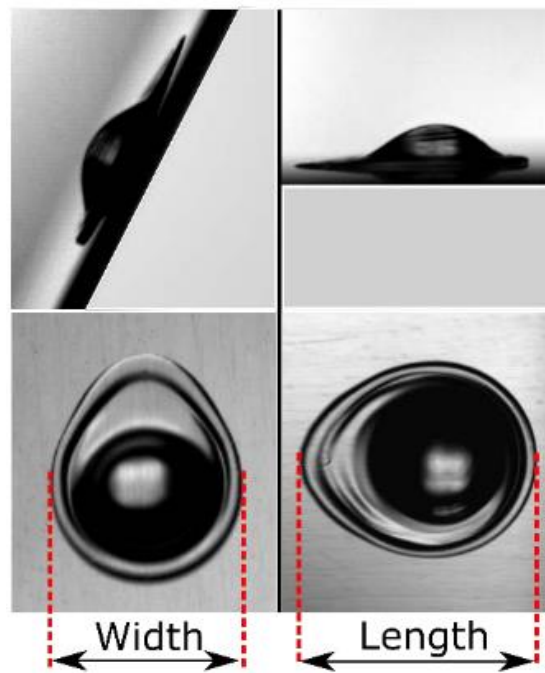


Figure 36: Illustration of single droplet spread on an inclined surface [38]

As for the leveling roller pushing material over the edge, we would again expect this effect to present itself as a change in feature size with increasing thickness which did not occur. Furthermore, an investigation into roller leveling found no evidence of the roller blurring material across a multicolor layer, suggesting that the roller is not moving material in a manner necessary to cause the observed edge deformations [39].

Shrinkage is a more plausible concern, as it is known to occur for UV cured polymers and cause residual stress in parts. Additionally, the repeated passes of the UV lamp do provide excess exposure time. The specific shrinkage characteristics for this material are unknown to the author and little other discussion of shrinkage or shape deviation is found in the characterization literature. If shrinkage were to cause such a large relative deformation, one would expect the effect to scale with size and be more prominent in larger parts as is often seen with FDM prints.

While the reality is that each of the above considerations likely play some part in the observed deformations, this work's hypothesis is that the deformations are better explained by looking at the basic droplet deposition phenomenon, focusing on the changing surface conditions encountered by the boundary droplets as successive layers are deposited (as shown in Figure 34), and their cumulative impact on the profile. If such hypothesis proves true, modeling just the droplet deposition and coalescence of lines will yield a good prediction of the feature shape without the need to include the additional physics of the roller or curing.

2.5 Summary

In this chapter, an investigation into mesoscale feature fabrication via material jetting-based additive manufacturing is presented, exploring the first research question and hypothesis. Key attributes, such as minimum manufacturable feature size, dimensional accuracy, and shape accuracy are studied using specifically designed benchmark specimens which vary feature type, size, and thickness. The process is shown to successfully fabricate features down to a few hundred microns, which is notably larger

than the machine's reported resolution. Differences in minimum manufacturable feature size are observed for different feature types; however, it is concluded that feature orientation and feature thickness have negligible effects on minimum feature size. Significant geometric deformations are observed in the form of edge and corner rounding. These deformations affect the feature accuracy as well as shape accuracy; thus, their potential impact on end use performance must be closely considered. A detailed discussion into sources of error during the fabrication process, as well as causes for the feature deformation, is presented. Through this work, an improved understanding of the material jetting process and its limitations at the mesoscale is developed, along with a general framework with benchmark specimens for evaluating other machines.

CHAPTER 3. LITERATURE REVIEW – MATERIAL JETTING DEPOSITION FROM DROPLET IMPACT TO PART FABRICATION

In the previous chapter, mesoscale feature fabrication was explored and limiting deformations shown. To improve process resolution and eliminate dimensional errors requires a deep process understanding, along with the development of models to predict and ultimately control the deposition process.

In this chapter, existing research relevant to material jetting deposition and process modeling is reviewed. A full consideration of material jetting feature fabrication spans scales from single droplet deposition to line and layer deposition, to ultimately multilayer feature formation. Many approaches over these size scales have been explored including analytical, numerical, and stochastic methods.

3.1 Printing of Droplets

The ejection, impact, and spreading of inkjet printed droplets has been well studied and reviewed [40]–[42]. While the inkjet process begins with printhead and methods of achieving droplet ejection, for this work we have limited the scope of review to matters most related to deposition and feature development, and point those interested in upstream processes to the references above.

A number of physical parameters are significant to characterize droplet deposition and the relative significance of inertial forces, capillary forces, and gravitational forces. These parameters include droplet size (D_0), deposition velocity (U), fluid density (ρ), viscosity (μ), surface tension (σ), and material-surface interaction like contact angle (θ). To relate these parameters and forces, dimensionless numbers such as the Reynolds (Re), Weber (We), Ohnesorge (Oh), and Bond numbers (Bo) are helpful and enable comparison between different studies.

The Reynolds number is the ratio of the inertial force to the viscous force and is defined as:

$$Re = \frac{\rho U D_0}{\mu} \quad (1)$$

The Weber number is the ratio of the inertial force to surface tension, and is defined as:

$$We = \frac{\rho U^2 D_0}{\sigma} \quad (2)$$

The Ohnesorge number is independent of velocity and relates the viscous force to the initial and surface forces, and is defined as:

$$Oh = \frac{(We)^{1/2}}{Re} = \frac{\mu}{\sqrt{\rho \sigma D_0}} \quad (3)$$

The Bond number the ratio of gravitational forces to surface tension and is defined as:

$$Bo = \frac{\rho g D_0^2}{\sigma} \quad (4)$$

One additional parameter of note is the “printing indicator”, Z :

$$Z = \frac{Re}{(We)^{1/2}} = \frac{1}{Oh} \quad (5)$$

The printing indicator has been developed as a useful guide to capture the relative fluid characteristics that allow for stable droplet ejection and formation. At low values of Z viscous forces prevent droplet ejection, whereas at high values surface tension becomes dominant causing fluid breakup and satellite droplets. Several works have explored ideal values, with the range, $1 < Z < 10$, proposed for successful ejection [40]. Furthermore, MicroFab outlines the following ranges of viscosity and surface tension as suitable for ejection, 0.5-40 mPa · s and 20-70 mN/m, respectively for fluids with a specific gravity near 1 [43].

Similar to ejection, the Weber and Ohnesorge numbers are also particularly important for characterizing droplet impact, where the Weber number describes driving force for spreading and the Ohnesorge number describes the resisting force. Using these numbers, Schiaffino and Sonin proposed a deposition map which identified four regimes of droplet deposition, shown in Figure 37 [44]. Most inkjet printing applications fall in Region I, characterized by impact driven spreading dominated by inertial forces and weak viscous forces.

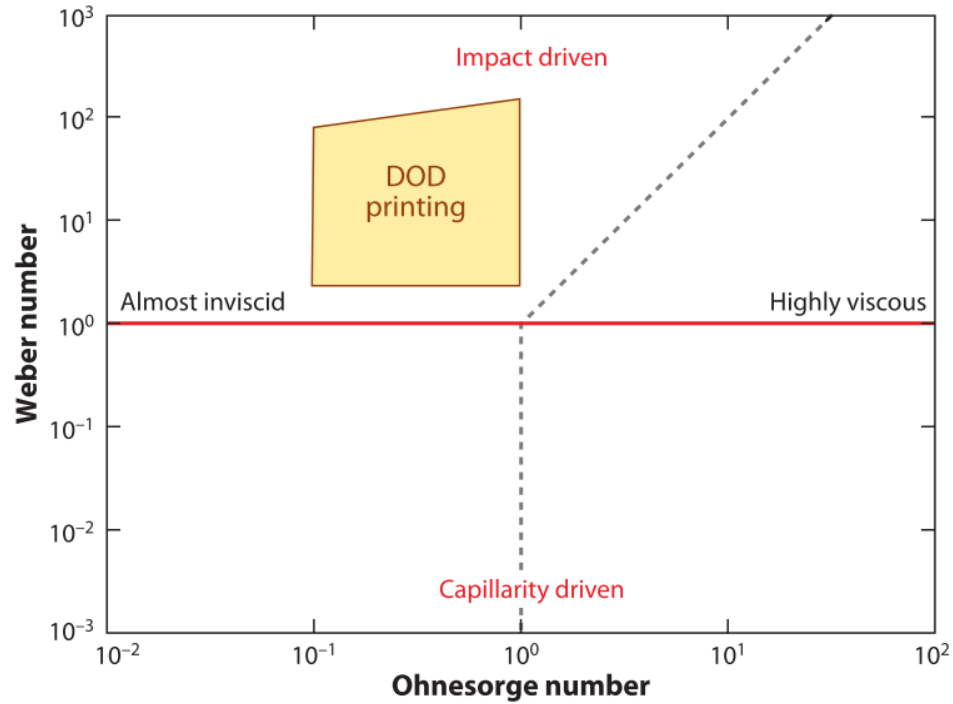


Figure 37: Regime map of droplet behavior at impact, image from [45]

Due to the constraints on drop-on-demand ejection, most printing can be considered almost inviscid, and a balance between inertial and capillary forces dominate. To describe this balance, droplet evolution is typically divided into three phases, Figure 38. The initial impact phase is dominated by kinetic behavior determined by the impact velocity. During the second phase, the droplet will relax back from expansion with any oscillations being damped by viscous forces. Finally, in the last phase, capillary forces dominate as the fluid spreads to its final sessile shape.

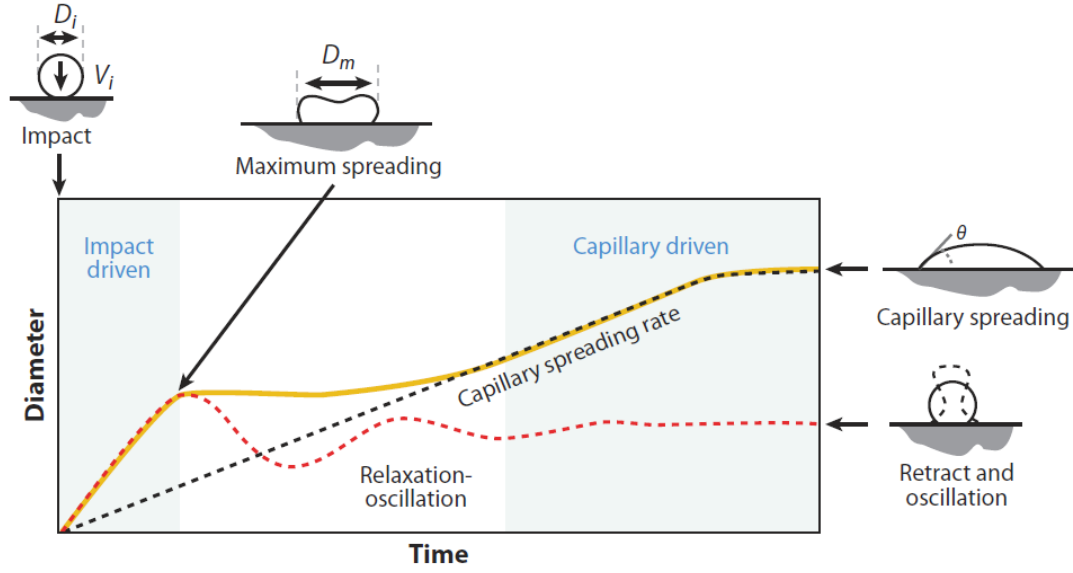


Figure 38: Phases of droplet impact and spreading [40]

The final shape of a deposited drop will depend on its volume and contact angle, θ . For droplets typical of inkjet printing where gravitational forces can be neglected (Bond number $\ll 1$), this shape is assumed to be a spherical cap with a diameter:

$$D_{cap} = d_o * \sqrt[3]{\frac{8}{\tan \frac{\theta}{2} \left(3 + \left(\tan \frac{\theta}{2} \right)^2 \right)}} \quad (6)$$

where d_o is the falling droplet diameter [40].

The contact angle of a fluid with a substrate is an important and complex parameter, defined as the angle between the liquid-vapor interface and the solid surface. Often, a contact angle is listed based on the equilibrium value; however, in many situations, it turns out that the contact angle is able to change. This phenomenon is known as contact angle hysteresis and occurs because there are many different meta-stable states on non-ideal surfaces due to surface roughness, impurities, and inhomogeneity in general.

Contact angle will then be characterized by an advancing and receding contact angle. Contact line dynamics are a continuing area of research, especially in terms of the best means of modeling the phenomenon and its relative impact on the impingement dynamics.

3.2 Printing of Lines

It is well documented that printing continuous, uniform lines or tracks is quite challenging. Davis presented the early theory on bead stability using linear hydrodynamic analysis, and examined the influence of contact line boundary conditions [46]. For deposited beads where the contact line is free to move, but the contact angle is a fixed value, the bead will always be unstable. Beads whose contact angles vary with contact line speed but return to an equilibrium angle at zero speed will also be unstable. The case studied beads whose contact lines are pinned in a parallel state while the contact angle is free to change. This phenomenon is known as contact angle hysteresis. Davis found that under this condition, the bead will be stable for contact angles less than $\frac{1}{2}\pi$ and unstable when greater than $\frac{1}{2}\pi$.

Schiaffino and Sonin confirmed this theory experimentally, studying the deposition of liquid water and molten wax droplets on a flat surface [47]. As expected, water beads were inherently unstable and would break up into individual sessile droplets. Wax depositions experience contact line pinning due to solidification but produce smooth uniform lines for only a small range of deposition rates and sweep speeds. Outside of this range, non-uniformities persist in the form of periodic bulges. A quasi-one-dimensional

model to predict the wavelength associate with the bulges is presented and agrees well with the observed wavelength in the experiments.

Soltman and Subramanian further characterized printed line morphologies for solution based inks, observing five line patterns: individual droplets, a scalloped line, a uniform line, a bulging line, and stacked coins [48]. Resulting morphologies are shown in Figure 39. Individual droplets intuitively occur at large droplet spacing where no overlap of the expanding drop occurs. As the droplet spacing decreases and the deposited drop footprints begin to overlap, the resulting liquid bead will produce the “scalloped” shape. At smaller spacing, a sweet spot is achieved forming a stable liquid bead with smooth parallel sides. Beneath this spacing, bulging instabilities will occur. The fifth pattern is referred to as “stacked coins” and occurs when the deposition rate is slowed, such that deposited drops dry individually before the next droplet is deposited.

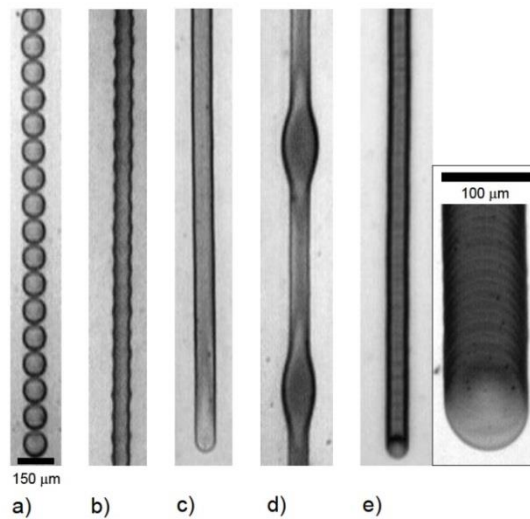


Figure 39: Regimes of printed line behavior [48]

To aid in understanding the different morphologies, Soltman and Subramanian developed a simple geometric model for a deposited bead and impacting drop. Their analysis assumes zero receding contact angle, meaning the contact line cannot recede, as well as

the assumption that once a deposited drop overlaps with the existing bead, all expansion is halted as it is energetically favorable for the fluid to flow into the pre-existing bead.

As mentioned above, for small droplets with a Bond number, Bo , less than 1 the deposited shape can be approximated as a spherical cap. Similarly, as a series of droplets impinge and coalesce, the ideal deposition will flow into the shape of a cylindrical cross section with an equilibrium contact angle, as shown below.

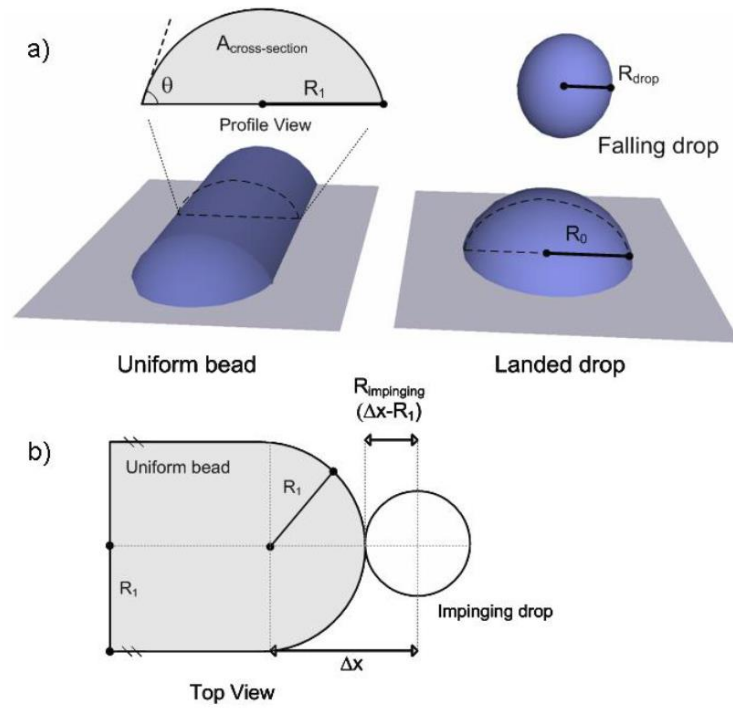


Figure 40: Diagram of deposited drop and bead [48]

The deposited radius of this bead can then be determined by considering the volume of fluid deposited per unit length:

$$\frac{V_{drop}}{\Delta x} = \text{Area Cylinder Cross Section} \quad (7)$$

which gives the radius as an inverse square root function of the drop spacing, Δx ,

$$R_1 = \sqrt{\frac{2V_{drop}}{\pi \cdot \Delta x \cdot f(\theta)}} \quad (8)$$

where,

$$f(\theta) = \frac{2}{\pi} \left(\frac{\theta}{\sin^2 \theta} - \frac{\cos \theta}{\sin \theta} \right) \quad (9)$$

Assuming the end of the bead is a semi-circle of radius R_1 , the maximum expansion of a deposited drop before interacting with the bead is

$$R_{imp} = \Delta x - R_1 \quad (10)$$

Evaluating the above equations, we see that as Δx increases, R_1 decreases and R_{imp} increases. Thus, the bead gets thinner, and the impinging drop is able to expand farther. When R_{imp} is able to expand farther than the theoretical bead radius, R_1 , a scalloped line is possible since it is assumed the contact line cannot recede. As Δx increases further and R_{imp} approaches its maximum value of R_0 , landed drops will start to merge in pairs before finally forming individual isolated deposits. Soltman and Subramanian went on to plot dimensionless values $\frac{R_1}{R_0}$ and $\frac{R_{imp}}{R_0}$ against the non-dimensional drop spacing $y = \frac{\Delta x}{R_0}$ to identify four theoretical regimes: continuous line with straight edges, scalloped line, pairwise bead formation, and isolated drop deposition. These are shown below in Figure 41. A uniform stable bead is expected to form along the red line between the blue and green lines. Also, note that within this region it is possible to have a tunable bead radius from a maximum to minimum value. Overall, the regime corresponded reasonably well to

their experimental data. Additionally, simple simulation models (VOF using Flow3D) were used to help with validation, though their fidelity was limited. It should also be noted that similar geometric analysis was conducted by Stringer and Derby [49].

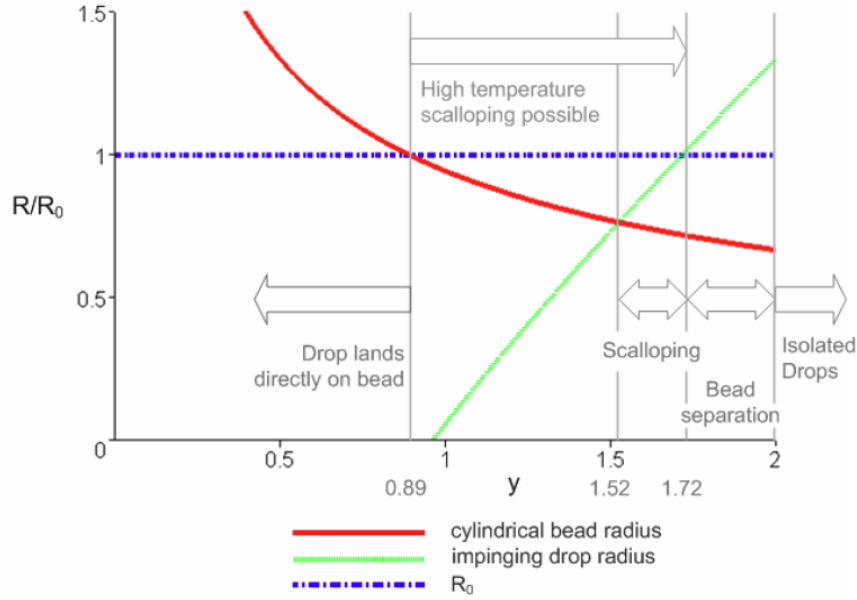


Figure 41: Regime map for deposited line morphologies [48]

A significant assumption of the above model is the fluid's zero receding contact line. Some papers have suggested that this may be a necessary condition for stable printing. Others disagree. Hsiao et al. experimentally investigated line formation with nonzero receding contact angles and compared with Soltman's model [50]. For small drop spacing, they saw good agreement with the track morphology predicted by Soltman's model. They also confirmed the preferential drop-to-bead fluid flow and the predicted drop spreading variation in the scalloped line. However, they found that Soltman's model underestimated the maximum spreading radius and line width due to not including the droplet impact inertia. High speed imaging also revealed instabilities such as a bulging head as fluid is preferentially pulled toward the first deposited droplet.

As shown above, printing of a single uniform line is far from simple and depends on a wide range of factors including printing properties (i.e., drop size, drop spacing, impact speed), material properties of the liquid, and the properties describing the surface-fluid interactions. Additionally, due to the significant experimental challenges surrounding the relevant size and timescale, many of the relevant governing mechanisms are still poorly understood. Numerical simulations offer an appealing alternative to better understand the complexities and interactions of these many factors, over different size and time scales.

Lee and Son investigated line deposition and coalescence using a sharp-interface level set method developed in house [51]. A dynamic contact angle was implemented, and the contact line allowed to move when outside the advancing and receding contact angles. Simulations explored coalescence of two drops as well as line deposition up to four drops. Contact angles as well as drop spacing were varied. Their results showed that drop impact and resulting deposition morphology depends significantly on the advancing and receding contact angle values. In general, better line quality was observed at lower values of advancing and receding contact angles, though a more thorough investigation would be needed to understand if there is an optimal range.

Li et al. performed numerical simulation using the volume of fluid method (VOF) to investigate sequential deposition of molten aluminum droplets [52]. Fluid motion and heat transfer are calculated by solving Navier-Stokes coupled with the energy equation, but a temperature dependent source term is added to the momentum equation such that when the temperature fall below the solidification point the source term will dominate any diffusive and convective components. The problem was implemented in a commercial solver, Flow3D. In their implementation, they ignored any of the contact

line/angle complexities, and there is very little coalescence dynamics due to the previous drops being solidified before the next drop is deposited. Still, the different stages of the molten droplet fusion process were identified which is important for future control of the process. A very similar study appears to have been done using Fluent though the specific software used is not mentioned [53].

Simulation of sequential droplet deposition in 3D using conventional methods and commercial codes is very difficult, and often computationally prohibitive, due to the size and serial nature of the problem. Recent studies have sought to overcome these limitations using the Lattice Boltzmann method. Zhou et al. developed a numerical solver based on a combination of LBM and phase field to investigate the interface evolution during multi-droplet interactions [54]. Throughout the evolution of droplet impingement and coalescence, Zhou compared the interface shape with a desired shape using a derived shape coefficient. An array of droplets forming a film is simulated, and the optimal spacing to prevent air bubbles is presented. Later work went on to incorporate the effect of contact angle hysteresis, such that line deposition could be studied [55]. A maximum of six droplets were simulated.

Zhang et al. also used the lattice Boltzmann method to study deposited line morphology [56]. Their investigation included the study of the effects of droplet spacing, value of advancing contact angle, and viscosity, with optimal values presented.

While the above modeling approaches show continuing progress in terms of both fidelity and efficiency, the computational cost to explore wide ranges of process parameters or increasing numbers of droplets continues to be prohibitive.

Considering that challenge, Thompson et al. developed reduced dimensional models capable of predicting the evolution of complex line morphology drop by drop with surprising accuracy, see Figure 42 [57]. Model I represented a surface tension limited case, while Model II incorporated how viscosity regulated fluid redistribution. Their work simulated up to 20 droplets on a flat substrate, more than any other publication, and compared with high-speed imaging of sequential droplet deposition. The developed models implement only a few physical mechanisms: surface tension through the Young-Laplace equation, contact angle hysteresis, and viscous effects through the thin film lubrication equations. Impact dynamics are included through an experimentally determined parameter, and contact line motion complexities are replaced with a quasi-static spreading law. The resulting problem is effectively a 2D footprint where the height profile is solved using FEM and a volume constraint. Based on the resulting profile, the contact angle around the perimeter is calculated. If the resulting contact angle is greater than the measured advancing contact angle, the perimeter is expanded in the normal direction using the quasi-static spreading rate. An additional assumption of this method is the arrival rate of new droplets must be much slower than the contact line speed, resulting in full equilibrium before the next deposition, which may not always hold true. Their experimental deposition occurred at a rate of 540 Hz, which is significantly lower than most commercial systems, ~8-12 kHz. Droplet diameter in their study is 20.6 μm .

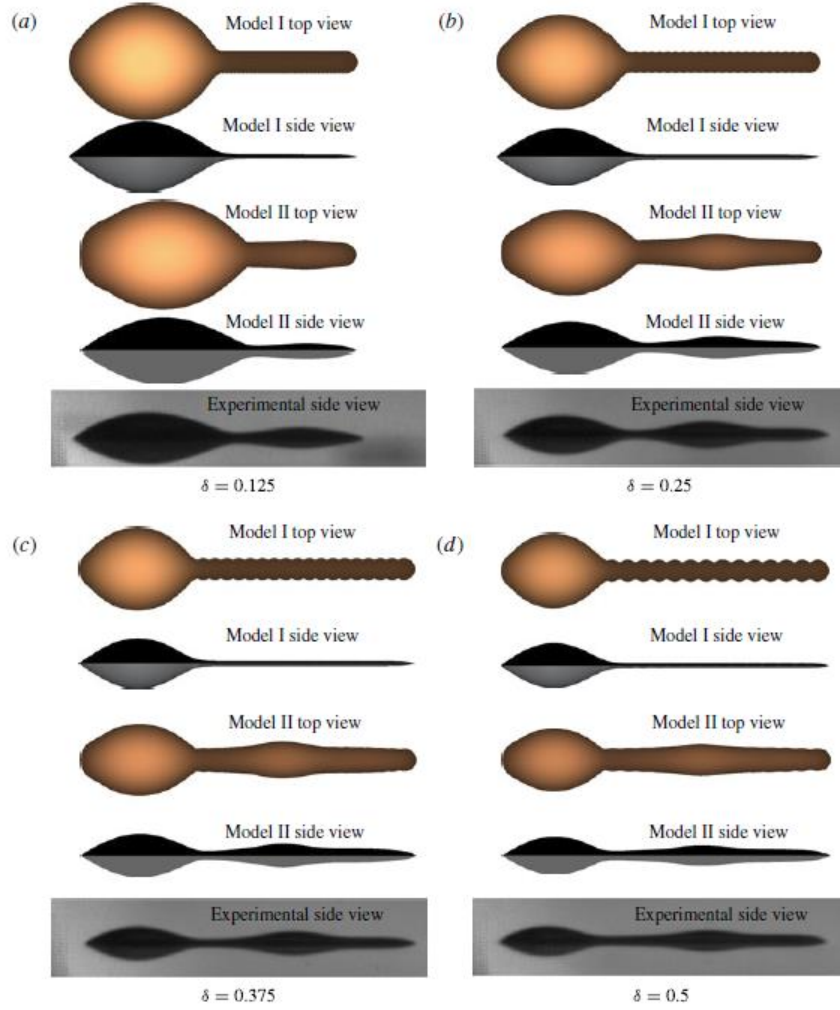


Figure 42: Comparison of top and side views with experimental results. Model I represents a surface tension limited case, Model II included viscosity [57]

Kant et al. followed up Thompson's work by applying the surface tension limited model to deposition of a single droplet into a topologically varying well [58]. Results indicate that this simplified model is effective at predicting the resulting capillary spreading, though the time evolution does not match due to the exclusion of viscous effects.

3.3 Printing of Layers

Moving beyond line formation, in this section, work relating to film and layer formation is reviewed. While obviously important to additive manufacturing, much of the relevant

work investigating inkjet-based layer deposition has focused on electronics applications. Tekin et al. presented an early experimental investigation into inkjet deposition of solution-based polymer films. Primarily, this work was focused on film uniformities after the solvent evaporation and methods to control quality. Zhang et al. also experimentally explored deposition of solvent based polymer films and the resulting morphologies, investigating several relevant process parameters including: droplet spacing, line overlap, and substrate temperature [59].

Kang, Soltman, and Subramanian conducted a more detailed investigation of a fluid film formation developing a simple analytical framework to describe the observed morphologies similar to the line model presented above [60]. Their investigation studied the effects of solution concentration, droplet spacing, and film size on the quality of the resulting film. Films were printed via single nozzle deposition in a raster-scan pattern onto substrates which produce contact angle hysteresis. Film thickness after evaporation was observed to decrease monotonically as droplet spacing increased, and any increase in polymer concentration resulted in a linear increase in thickness as expected. The effect of droplet spacing and film size on the resulting quality is more interesting. For smaller films, 500 μm squares, decreasing the droplet spacing resulted in bulging around the perimeter and reduced resolution, Figure 43a. Whereas, for larger films, 1 mm squares, the film began to separate and break into smaller sections at the optimal spacing taken from 500 μm squares, as shown in Figure 43b.

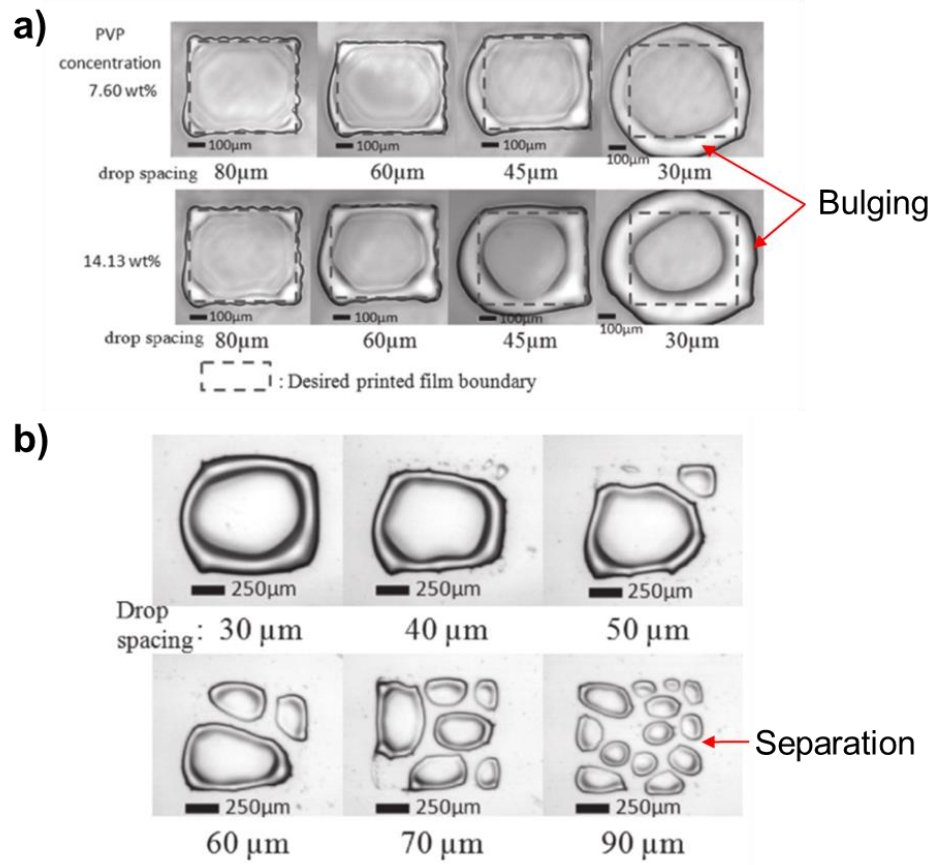


Figure 43: Deposited films at various line spacings: a) desired shape is 500 μm square, b) desired shape is 1 mm square (right) [60]

These phenomena were explained with a simple analytical model of the equilibrium line width for a given volume and contact angle. We previously described the cylindrical shape of a uniformly deposited line, such that the deposited radius is a function of the drop volume, drop spacing and contact angle. W_{single} is thus $2 * R_1$. When the second line is deposited at a spacing, d , the new merged width will be:

$$W_{merged} = W_{single} + 2 \left(d - \frac{W_{single}}{2} \right) = 2d \quad (11)$$

If the merged line width is smaller than the line width calculated using the advancing contact angle, then the merged bead's current contact angle is greater than the advancing

contact angle and will flow until the contact angle is reduced to the advancing contact angle. Using this relationship, it is possible to calculate if bulging will occur given the number of lines, n , and the line spacing.

$$\frac{d}{W_{single}} \geq \frac{1}{\sqrt{n}} \quad (12)$$

If this inequality is satisfied, the printed bead will not bulge. A similar approach is applied to film separation but is not reproduced here. In some cases, these models fail to predict separation and the observed error stems from the 1D assumption of an infinite bead, which is not true for a square or rectangular film.

In a follow up work, Soltman et al. further explored the 2D nature of film printing, and how to prevent bulging and separation [61]. Based on a merged line contact angle model, a variable line spacing approach is employed to adjust as a film size grows. Additionally, preprinted perimeter drops are shown to improve quality by creating pinning sites to inhibit fluid withdrawal. All experimental work was done in a raster scan pattern, and the deposited fluid was only subject to evaporation with no viscosity changes or curing.

Their most recent work explored the impact of contact angle hysteresis on film external corner resolution using experimental results and numerical modeling [62]. Varying substrate surface roughness, Rz 6-16nm, was used to control the resulting receding contact angle. Square patterns were printed with nominal size ranging from 0.5mm to 2 mm. Printed droplet diameter equaled approximately 66 μm with in-line spacing of 70

μm . As surface roughness increased, relating to greater contact angle hysteresis and a lower value for the receding contact angle, less corner rounding was observed.

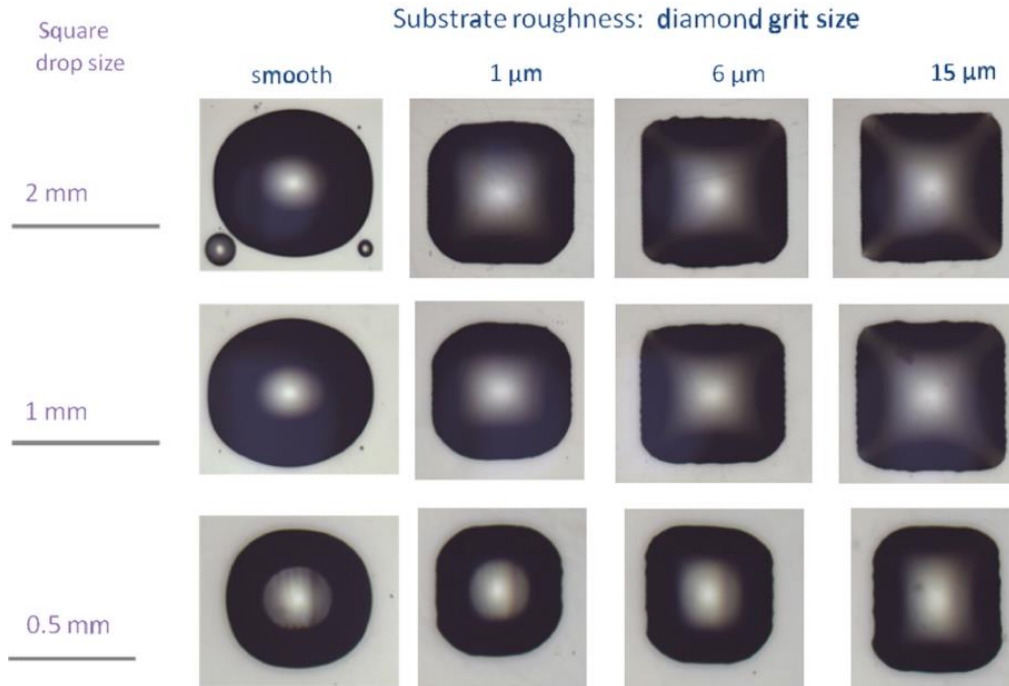


Figure 44: Square layers printed of substrates of different roughness [62]

Numerical modeling was used to better understand how the contact angle varies around the perimeter and explain why the corner radius varies. The open-source Surface Evolver program was used, which calculates a fluid surface via surface energy minimization for a given volume of fluid and fluid footprint, Figure 45. For a prescribed footprint, they could then predict the resulting contact angle variation around the perimeter, Figure 46, with a maximum contact angle occurring at the middle of an edge (closest boundary point) and the minimum contact angle occurring at the corner (farthest boundary point). If the contact angle at the edge is less than the fluids receding contact angle, it is expected to recede towards the center resulting in greater rounding. Thus, it is advantageous to have a minimum receding contact angle or contact line pinning. At that point, exterior

corner radius is determined by deposited droplet radius or fluid bulging if droplets are too closely spaced.

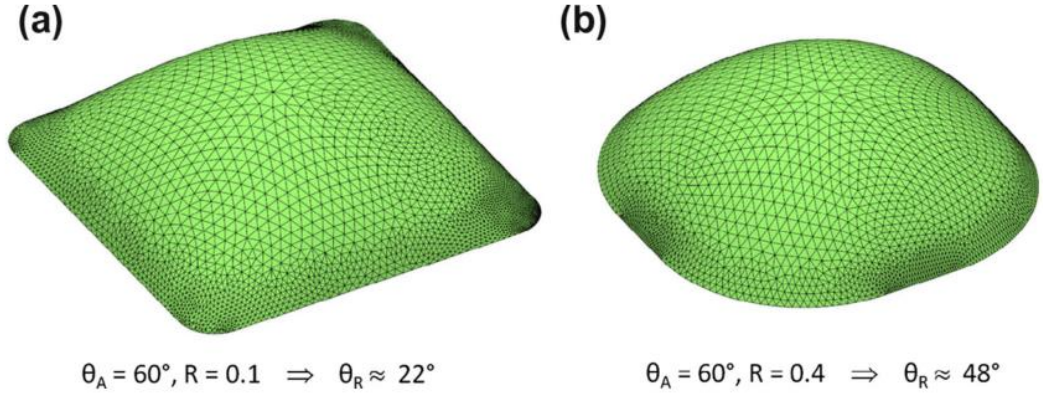


Figure 45: Surface evolver simulated film shape [62]

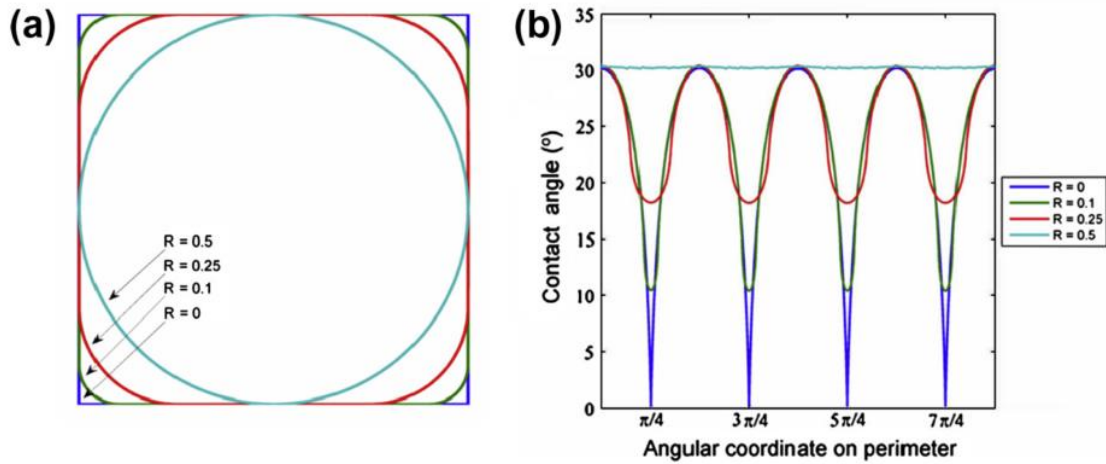


Figure 46: Contact angle around the film perimeter based on surface evolver solution [62]

These results are noteworthy from an AM perspective given that a leveling process is traditionally employed. It could be possible to improve the feature resolution by changing the roughness of the roller and the resulting top surface of each layer. Reported roughness of the top of Polyjet printed parts is generally a few microns, compared to nanometer roughness for the Soltman substrate, so such benefits may already be effectively built in.

3.4 Part Fabrication

Several works have sought a global model for MJ part accuracy and control, ignoring the complex physics of individual droplet deposition. Huang et al. in a series of works investigates accuracy control for AM generally (not specifically for MJ) [63], [64]. This work seeks to quickly predict final product shape or shrinkage, as well as take a desired design and generate a compensated model that when fabricated results in the correct shape. Their method incorporates no process physics into their representation, but rather uses a small set of learning specimens to develop a shrinkage model and compensation model. Slices are modeled in polar coordinates, to create a phase diagram of deformation, and then test specimens of different sizes allow additional data sets as a function of radius. This method has only been implemented for 2D uniform cross sections and has not been demonstrated for freeform 3D objects. Furthermore, since this approach is mainly focused on capturing bulk shrinkage, it does not appear that it can be used to model the droplet-level effects of fluid flow, varied deposition patterns, or mesoscale feature formation.

Other works have sought to develop closed-loop control methods for the MJ process, utilizing droplet-level deposition models in their feedback loop. Cohen and Lipson estimate the deposition field height by assuming each droplet can be approximated as a spherical cap, where the resulting height is simply a linear addition of the an overlapping regions [65]. This height map is then within the feedback loop of their “greedy geometric feedback” control algorithm along with real-time measurements. Performance of their method is evaluated using a Matlab simulator as well as an experimental platform. Their technique outperformed open-loop control.

In several works, Mishra et al. developed a model-based feedback control algorithm using an empirical height change model for the deposition of one droplet next to its neighbors [66], [67]. Given a uniform printing grid, it is assumed that the height at a given point on that grid is affected by the center droplet, side droplets, and corner droplets. The height change is then the resulting summation of all the contributions of these droplets. These height changes are determined by experimental deposition studies. Next to account for any existing topology from a previous layer, a modification factor is included based on the height difference between the deposition center point and its surrounding neighbors. Therefore, if the side neighbor is lower than the center height, more height contribution will go to the side than the center, as shown in Figure 47. Similarly, if the side neighbor is much higher than the center height no fluid is expected to flow to the side, and all of the height change is contributed to the center point. This height model is incorporated into their feedback algorithm to control droplet deposition position such that height deviation is minimized.

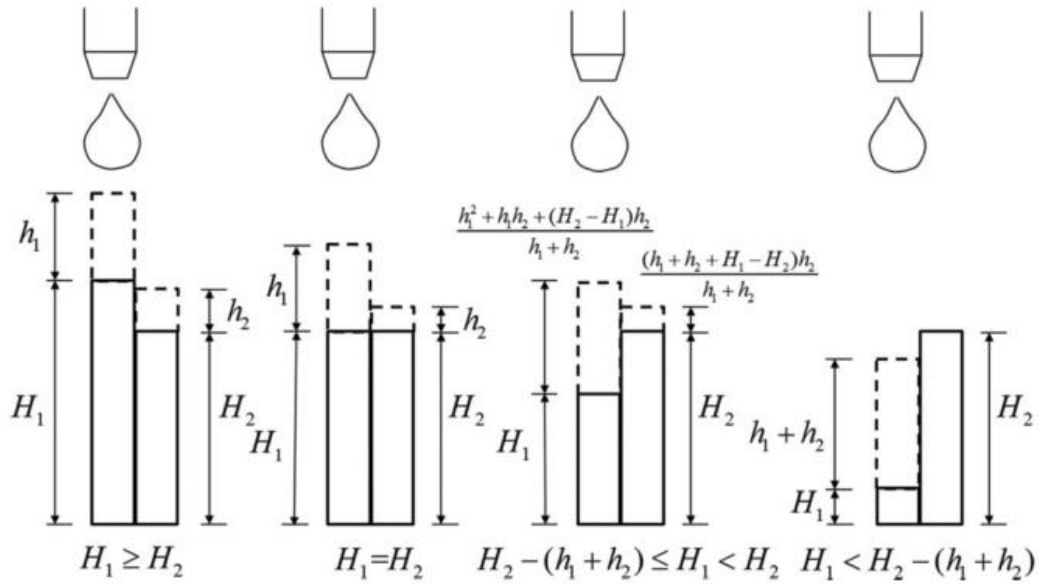


Figure 47: Height change at center point depending on neighbors [66]

Performance of their method is primarily confirmed via Matlab simulation, though in one work a four-layer thick square is printed for validation. Overall, the simulation and experimental results indicate effectiveness at improving height accuracy, especially in the case where process uncertainty is added to the simulation, see Figure 48. One paper does note significant computational concerns due to the large scale of the optimization problem.

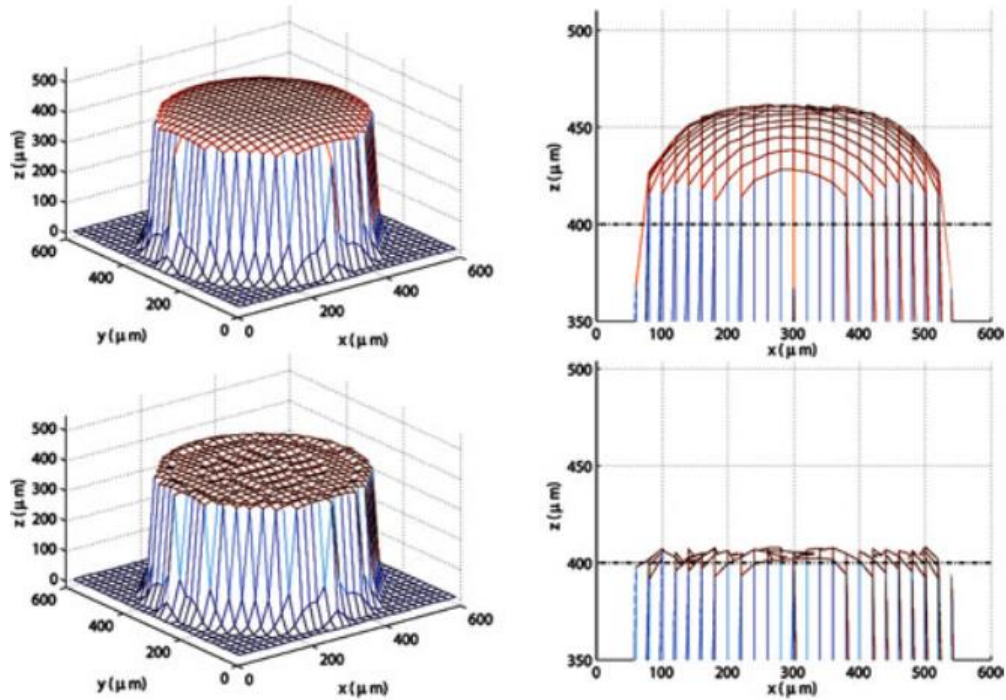


Figure 48: Simulation results for a 400 um tall printed cylinder with 20% process uncertainty: open-loop (top), closed-loop (bottom) [66]

In more recent works, the layer-to-layer height model is further developed by Mishra et al. using a graph-based approach to capture the influence of droplet flow [68]. Their work proposes that the material flow is proportional to the height difference between grid points around the deposition site, and the resulting flow can be represented and solved for as a directed graph. This approach is reported to improve accuracy by 5-14% when

compared to the prior height change model, and the cap model, respectively. This model is then leveraged in multiple works investigating the development of control algorithm for improved process performance [69], [70]. Wu and Chiu take a similar approach to Mishra looking at the basic flow as a function of the height difference between adjacent grid points. However, they represent the problem as an area and volume propagation, then use volume conservation to determine height. So far the model has only been demonstrated for single layer 2D patterns [71].

In another control algorithm focused work, Pannier et al. investigates several methods for representing the heightmap evolution during droplet deposition [72]. The “direct” method leverages *Surface Evolver* to solve for droplet height within the model. Noting that the computational expense of this method is likely to limit online application of such an approach, the model is used to construct a deposition dataset that is then used for height approximation through linear regression but is shown to result in a significant reduction in accuracy.

3.5 Summary

The review presented in this chapter surveys the existing droplet deposition and material jetting literature spanning from single droplet to full feature modeling. While there has been a substantial volume and variety of existing research, both in terms of printing conditions and modeling methods, most work to date has focused on ideal, flat surfaces. There is little investigation into modeling specific conditions of MJ AM and the 3D nature of the surface boundary as it develops. Thus, there is substantial opportunity to explore these conditions and better understand the MJ process, particularly conditions

relevant to the feature and deformations observed in Chapter 2. It is additionally important to leverage these learnings to develop modeling approaches that can rapidly predict fabricated features and evaluate the impact of different printing parameters or strategies. A couple works have developed simplistic models to be used within closed loop control algorithms, but they are mainly empirical and have limited flexibility without additional experiments and could benefit from an approach that incorporates some elements of the deposition physics.

CHAPTER 4. MODELING OF THE LAYER DEPOSITION PROCESS

Despite the significant research efforts investigating droplet deposition discussed in the previous chapter, much of the prior work has been focused on single droplet or line deposition on an ideal flat surface. While certainly foundational, for AM applications only the very first layer is deposited onto a flat surface, further work is needed to understand and predict how features develop when droplets are deposited on uneven prior layers and near the edge of a feature. In this Chapter, after development and validation of a high-fidelity 3d droplet model, deposition near a layer edge is studied to understand how a droplet spreads as well as the impact of positional error on overflow. Additionally, the model is further extended to simulate the multi-droplet, multi-pass, multi-layer process of fabrication.

4.1 Numerical Modeling

4.1.1 Governing Equations

The dynamics of droplet deposition represent a complex two-phase flow problem governed by the Navier-Stokes equations. To make this problem more tractable, the following assumptions are made:

- 1) The fluids are assumed to be incompressible as the impact velocities of interest are much less than the speed of sound in the fluid.
- 2) Flow is assumed to be laminar for both fluids based on the magnitude of the Reynolds number.

- 3) The fluids are assumed to be Newtonian, with densities, viscosities, and surface tension remaining constant.

With these assumptions, the Navier-Stokes equations for conservation of mass and conservation of momentum are as follows:

$$\nabla \mathbf{u} = 0 \quad (13)$$

$$\rho \frac{\partial \mathbf{u}}{\partial t} + \rho \mathbf{u} \cdot \nabla \mathbf{u} = \nabla \cdot [-p\mathbf{I} + \mu(\nabla \mathbf{u} + (\nabla \mathbf{u})^T)] + \mathbf{F} + \mathbf{F}_{ST} \quad (14)$$

where \mathbf{u} is the velocity vector (m/s), t is time (s), ρ is the fluid density (kg/m³), p is the fluid pressure, μ is the dynamic viscosity (Pa·s), \mathbf{F} is the body force, \mathbf{F}_{ST} is the surface tension force, and \mathbf{I} is the identity matrix.

4.1.2 Level Set Method

In addition to the equations of fluid motion, it is also critical to accurately resolve the boundary interface, ϕ , separating the two phases. There are two general approaches for modeling these interfaces: explicit and implicit. As the name suggests explicit approaches directly track the moving interface using particle markers along the interface surface. Implicit methods, such as level-set, represent the interface using an auxiliary function and the interface is set by a certain level set or isocontour of the globally defined function. While explicitly defining the interface has its appeal, in practice, such methods are quite difficult to implement and struggle to handle sharp corners and topological changes. Implicit methods bear no such burden, as well as enabling the domain to use a fixed

mesh, which has resulted in their more widespread use. For that reason, this work elected to use an implicit approach, the level-set method, which is implemented in COMSOL.

As described above, the level-set method represents the interface as a specific level set of a smooth function defined throughout the domain. Early implementations used a signed distance function, defining the interface as the 0 level set, whereas modern approaches utilize a smeared Heaviside function which varies smoothly from 0 in Fluid 1 to 1 in Fluid 2. In this case, $\phi = 0$ in air, $\phi = 1$ within droplet material, and $\phi = 0.5$ defines the interface.

The motion of the boundary is convected from the fluid velocity field, \mathbf{u} , using the following equation:

$$\frac{\partial \phi}{\partial t} + \mathbf{u} \cdot \nabla \phi = \gamma \nabla \cdot \left[\varepsilon \nabla \phi - \phi(1 - \phi) \frac{\nabla \phi}{|\nabla \phi|} \right] \quad (15)$$

where the left-hand side governs the motion of the interface, while the right-hand side controls numerical stability. The parameter ε controls the thickness of the transition layer and should be set on the same order of magnitude as the mesh size in the deposition region. The parameter γ determines the degree of numerical stabilization. It is recommended to set γ as the maximum magnitude of the velocity within the domain.

Equation 15 is known as the non-conservative form of the level-set equation as it only conserves the integral of the level-set function approximately. A conservative form has been presented by Olsson and Kreiss which obtains exact numerical conservation [73], shown in Equation 16:

$$\frac{\partial \phi}{\partial t} + \nabla \cdot (\mathbf{u}\phi) = \gamma \nabla \cdot \left[\varepsilon \nabla \phi - \phi(1 - \phi) \frac{\nabla \phi}{|\nabla \phi|} \right] \quad (16)$$

Unfortunately, solution of this formulation generally suffers from convergence issues and is not broadly recommended. Furthermore, similar droplet impingement studies comparing the two forms showed negligible difference in results [74]. For these reasons, the non-conservative form is used in this work.

Discontinuity of fluid properties across the interface, e.g., density and viscosity, is smoothed by the level-set function using the following equations:

$$\rho = \rho_a + (\rho_l - \rho_a)\phi \quad (17)$$

$$\mu = \mu_a + (\mu_l - \mu_a)\phi \quad (18)$$

where $\rho_a, \rho_l, \mu_a, \mu_l$, are the densities and viscosities of the air and liquid, respectively.

The surface tension force in Equation 14 is calculated using Equation 19.

$$\mathbf{F}_{ST} = \nabla \cdot [(\sigma(\mathbf{I} - \mathbf{nn}^T))\delta] \quad (19)$$

where σ is the surface tension, \mathbf{I} is the identity matrix, δ is the Dirac delta function, and \mathbf{n} is the normal to the interface. The unit normal is determined using Equation 20:

$$\mathbf{n} = \frac{\nabla \phi}{|\nabla \phi|} \Big|_{\phi=0.5} \quad (20)$$

Lastly, before the first step can be solved for, the level set function must be initialized such that it varies smoothly from 0 to 1 across the interface. This is done by setting ϕ_0 equal to 0 on one side of the interface and 1 on the other then solving Equation 21.

$$\frac{\partial \phi}{\partial t} = \gamma \nabla \cdot \left[\varepsilon \nabla \phi - \phi(1 - \phi) \frac{\nabla \phi}{|\nabla \phi|} \right] \quad (21)$$

4.2 Model Implementation

The numerical model to solve the two-phase flow problem is implemented in COMSOL 5.2 building from their Laminar Two-Phase Flow Level Set interface. An exemplary 3D simulation domain is shown in Figure 49. A droplet, or droplets, is placed in the domain above the substrate and assigned an initial velocity corresponding to the desired impact velocity to be studied. The top and sides of the domain in free air are set as open boundary conditions, and whenever possible symmetry boundary conditions are used to reduce the computational scale. The substrate surface is modeled as a rigid wall and uses the wetted wall boundary condition to control fluid surface flow, as well as set the contact angle, θ .

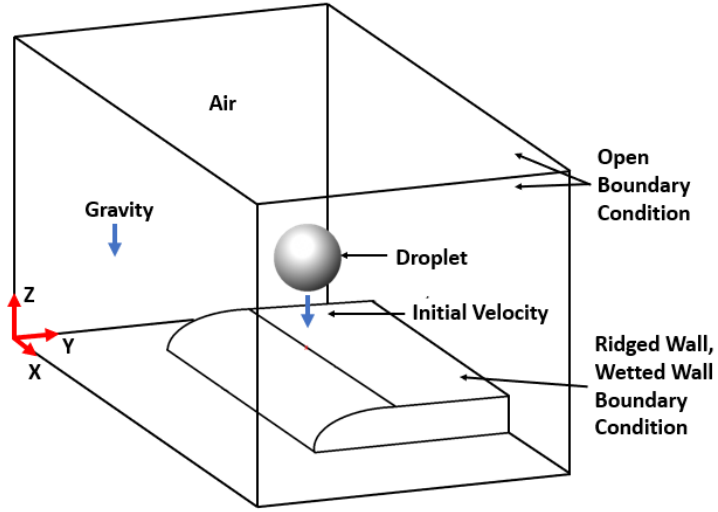


Figure 49: Schematic of model computational domain and boundary conditions

4.3 Validation

To validate the proper implementation of the model, simulation results for both static and dynamics cases are compared with analytical models and experimental results.

4.3.1 Static Equilibrium

As discussed in Chapter 3, the final equilibrium shape of a deposited microdroplet takes the form of a spherical cap. The non-dimensional equilibrium spread factor, β_{eqm} , the ratio of cap footprint diameter to initial droplet diameter, is calculated using volume conservation and the equilibrium contact angle [49]:

$$\beta_{eqm} = \frac{d_{eqm}}{d_o} = \sqrt[3]{\frac{8}{\tan \frac{\theta}{2} \left(3 + \left(\tan \frac{\theta}{2} \right)^2 \right)}} \quad (22)$$

To validate proper static equilibrium solutions, four cases are simulated using contact angles of 30°, 60°, 90°, and 120°, respectively, and an initial droplet diameter, $d_o =$

40 μ m. Simulation results for the four cases are shown in Figure 50, along with a comparison of the equilibrium spread factor with the theoretical model shown in Figure 51. Simulated results are in good agreement with theoretical values and expected shape.

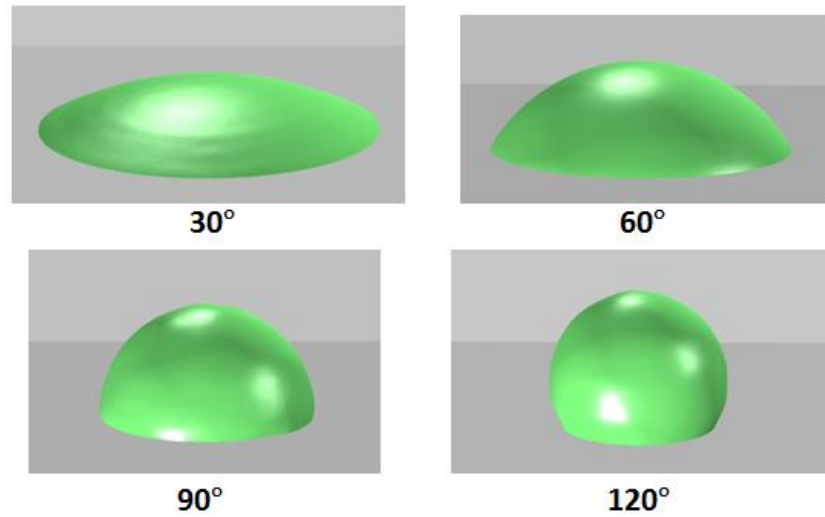


Figure 50: Simulated equilibrium droplet shape for different contact angles

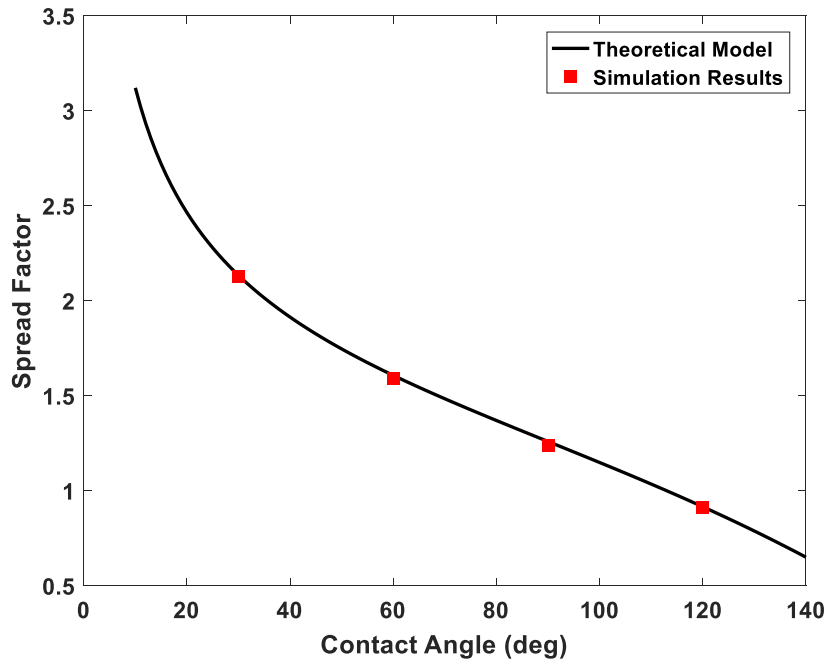


Figure 51: Comparison of equilibrium spread factor between Comsol simulation and theoretical model

4.3.2 Dynamic Spreading

Next, the dynamic performance of the level set formulation is compared with the experimental study of Dong et al, which investigated micrometer scale droplet deposition under conditions appropriate for AM [75]. The studied droplet has a diameter of $48.8\text{ }\mu\text{m}$ with an impact velocity of 4.36 m/s . The fluid used for the experiment was distilled water, therefore fluid properties used for the droplet simulation are taken as the standard properties of water and air at 1 atm and 25° C . The resulting Weber, Ohnesorge, and Reynolds numbers are $We = 12.8$, $Oh = 0.0151$, and $Re = 238$, respectively. The measured equilibrium contact angle of 88° is used.

Sequential snapshots of the droplet development are shown in Figure 52, along with images of the experimental deposition shown in Figure 53, for comparison.

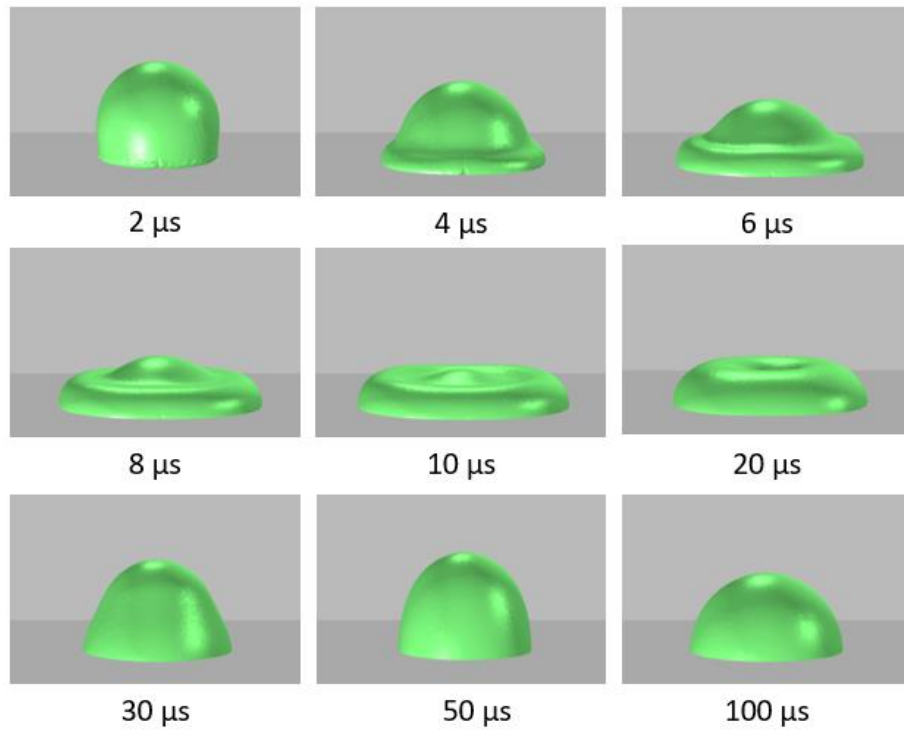


Figure 52: Simulation results of droplet impact on solid surface

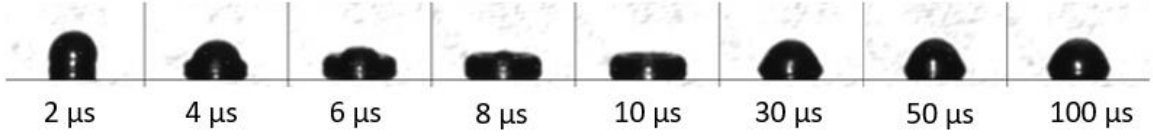


Figure 53: Experimental results of droplet impact from Dong [75]

The temporal evolution of the droplet spread factor is compared with the experimental data in Figure 54 . Overall, there is good agreement with the experimental results particularly with respect to the temporal evolution of the initial spreading, and the maximum spread factor observed. The main differences observed are the retraction of the simulated droplet, resulting in the valley seen near 40 μs , and the slightly lower final equilibrium spread factor. These discrepancies are likely related to physical contact line pinning for the experimental droplet, which retards the movement of the fluid contact line during retraction and resulted in a final spread factor greater than the theoretical equilibrium. Since the simulation uses a constant contact angle value as reported by Dong, such pinning effects are not captured. Similar differences were observed in other simulation studies [76], [77].

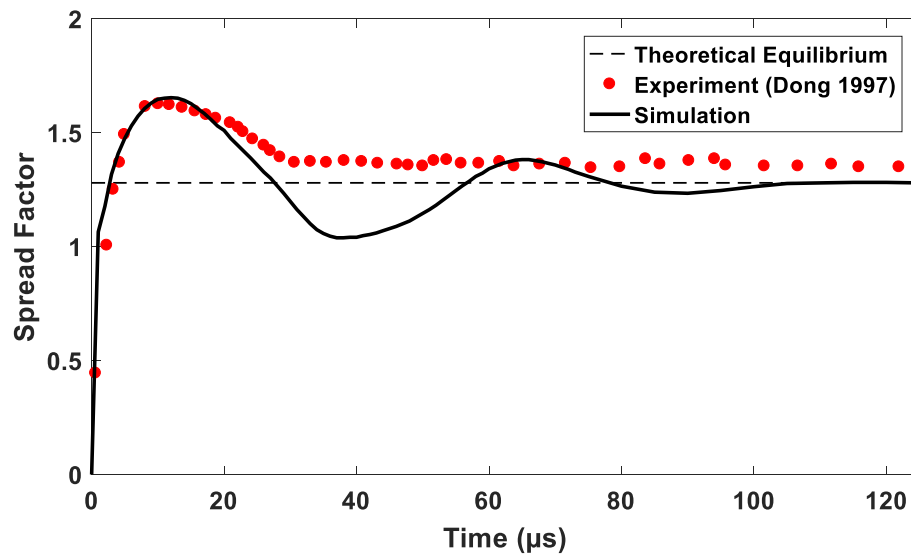


Figure 54: Validation of dynamic spread factor evolution

4.4 Modeling Droplet Deposition near the layer edge

With the modeling approach validated, several cases of droplet deposition at the layer edge are now studied. Printing conditions and material properties used in the simulations are listed in Table 8. These conditions are taken from comparable AM jetting literature and are representative of the conditions found in the Objet machine evaluated in Chapter 2 [78], [79]. The droplet size of 30 picoliter ($D_0 \approx 40 \mu\text{m}$) is selected to match the highest resolution setting available. Like the validation cases, the surrounding bulk fluid is set to match the properties of air at 1 atm and 25° C.

Table 8: Material properties and printing conditions for model

ρ (kg/m ³)	μ (Pa·s)	σ (N/m)	θ_{eq} (°)	D_0 (μm)	U (m/s)
1000	0.010	0.025	45	40	4-5
Re	We	Oh	Bo		
16	25.6	0.32	0.0006		

We consider the condition where a first layer has been deposited and cured and is a rigid solid surface. For the deposition of the second layer, a droplet at the edge is no longer impacting on an ideal flat surface. Rather, the surface is half flat and half sloped down as shown in Figure 55a, which represents an idealized vision of layer leveling, or will be ribbed due to the multiple line passes and the edge sloped down, see Figure 55b. The ribbed surface could result from a leveling strategy that levels at only certain intervals, or due to ineffective leveling. This phenomenon as was observed during the mesoscale

characterization, see Figure 56, where ribbing on the surface was oriented in the direction of deposition.

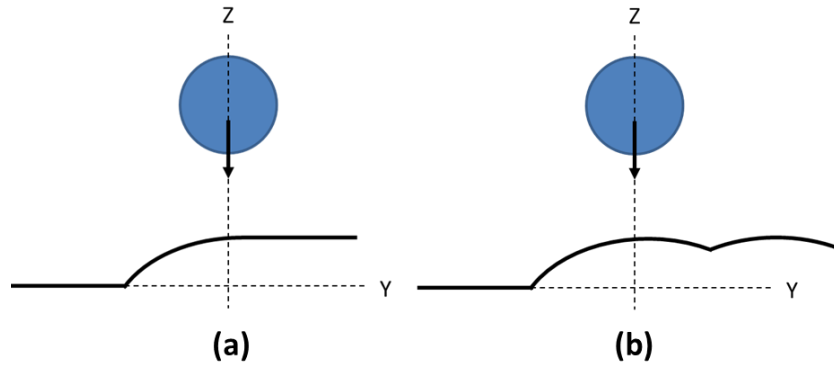


Figure 55: Droplet impacting at the first layer edge: a) a flat leveled surface, b) a ribbed non-leveled surface

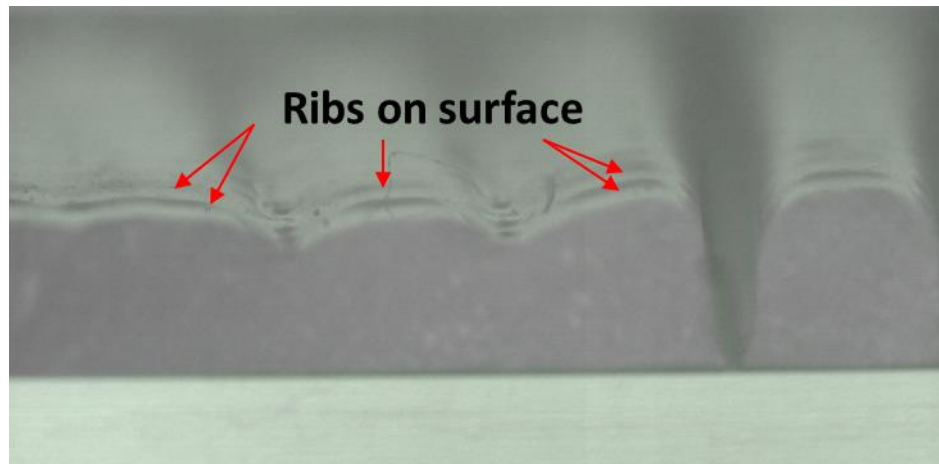


Figure 56: Ribbed surface topology

Simulation results for the flat and ribbed layers are shown in Figure 57 and Figure 58, respectively. As was discussed in Chapter 3, Figure 38, upon impact the droplet rapidly expands its footprint due to impact driven spread. This phase extends to about $2e-5$ seconds. At this point, the kinetic energy of impact is mostly dissipated by viscous forces and the impact transitions to a relaxation phase through approximately $5e-5$ seconds, due to the moderate viscosity, low surface tension and low contact angle no oscillations are

observed. After, capillary spread becomes dominant on a longer time scale, and the droplet boundary creeps towards a surface tension driven equilibrium.

It is important to note the present study does not include contact angle hysteresis, contact line pinning, or the viscosity changes likely to occur as a result of fluid cooling and photopolymerization. While these factors would likely have minimal effect on the initial impact driven spread, they would certainly be significant on the capillary driven phase and the extent of spread therein [80]. Thus, the results at max impact driven spread and capillary spread are viewed together as bounds for the final deposited shape.

For both the flat and ribbed cases, the droplet is observed to fully flow down the layer edge, extending past the prior layer boundary. Such overflow, as discussed in Chapter 2, suggests that even in the most ideal case of droplet deposition, without some compensation scheme or support material, there will be a reduction in feature resolution resulting from basic droplet spread dynamics and the non-flat edge conditions, beginning with the 2nd layer. For the flat surface simulation, the extent of this overflow observed during the impact driven phase is 10 μm and extended to 16.5 μm during the capillary spread. Similar results were recorded for the ribbed surface and the overall difference between the two surface topologies was minimal, except for a slight difference in the final capillary shape where the droplet spread some into the rib seam. Additionally, as material has extended down into the first layer zone there is also a reduction in height contribution to the second layer at the edge. The added height at the deposition site was 6.7 μm at the point of max impact spread and recovered back to 12 μm in the capillary zone as the uphill edge and sides receded. The observed overflow and height reduction are quite significant considering this is only the second layer with ideal conditions.

Comparing with the reported resolution of 600 dpi ($\sim 42\text{ }\mu\text{m}$), the overflow falls in the 20-40% of the resolution, and since a single drop on a flat surface would have a height of $15\text{ }\mu\text{m}$, the second layer would be a reduction to 45-80% of ideal.

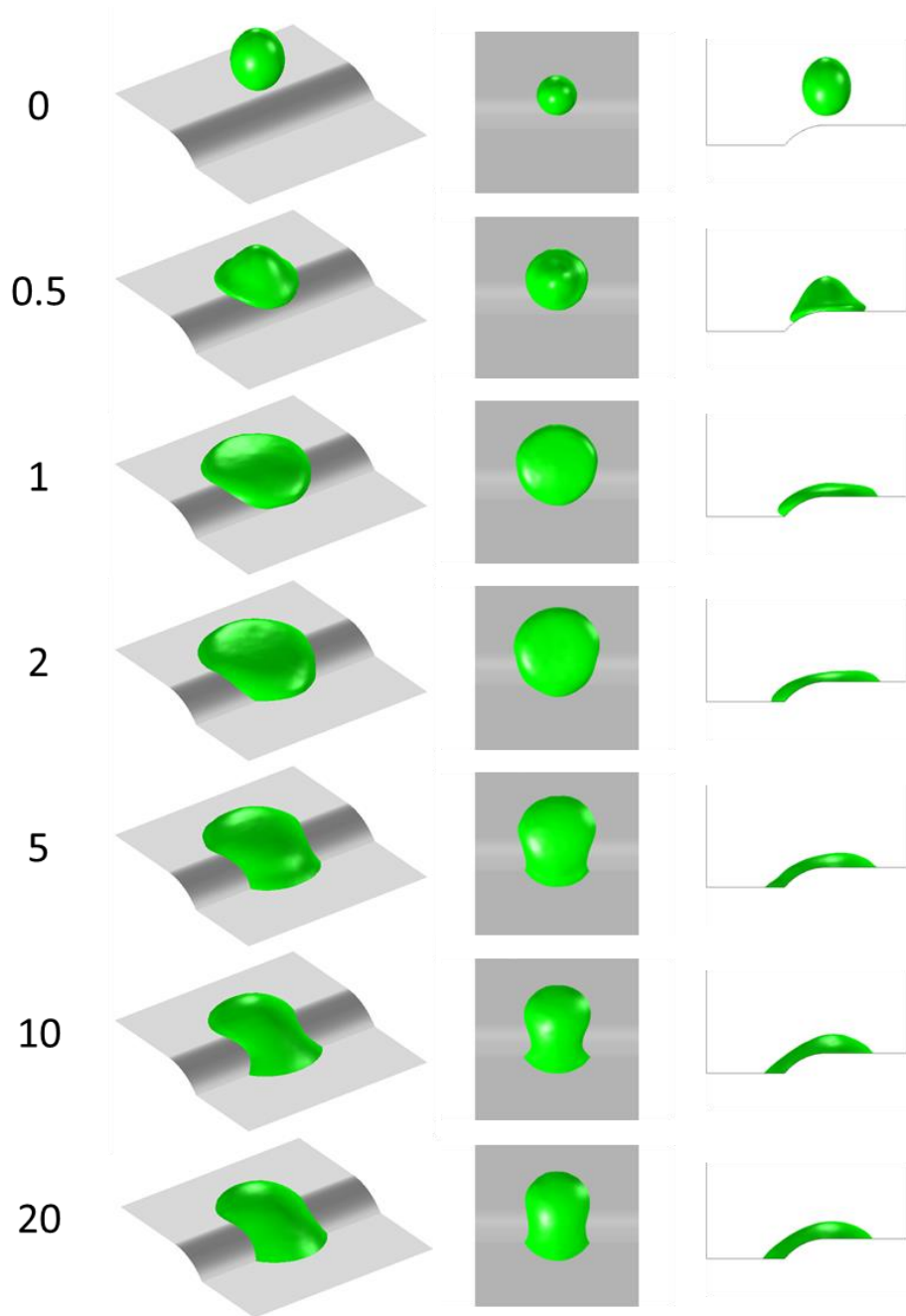


Figure 57: Simulation of droplet deposition at layer edge with a flat surface
(Time units = 10^{-5} second)

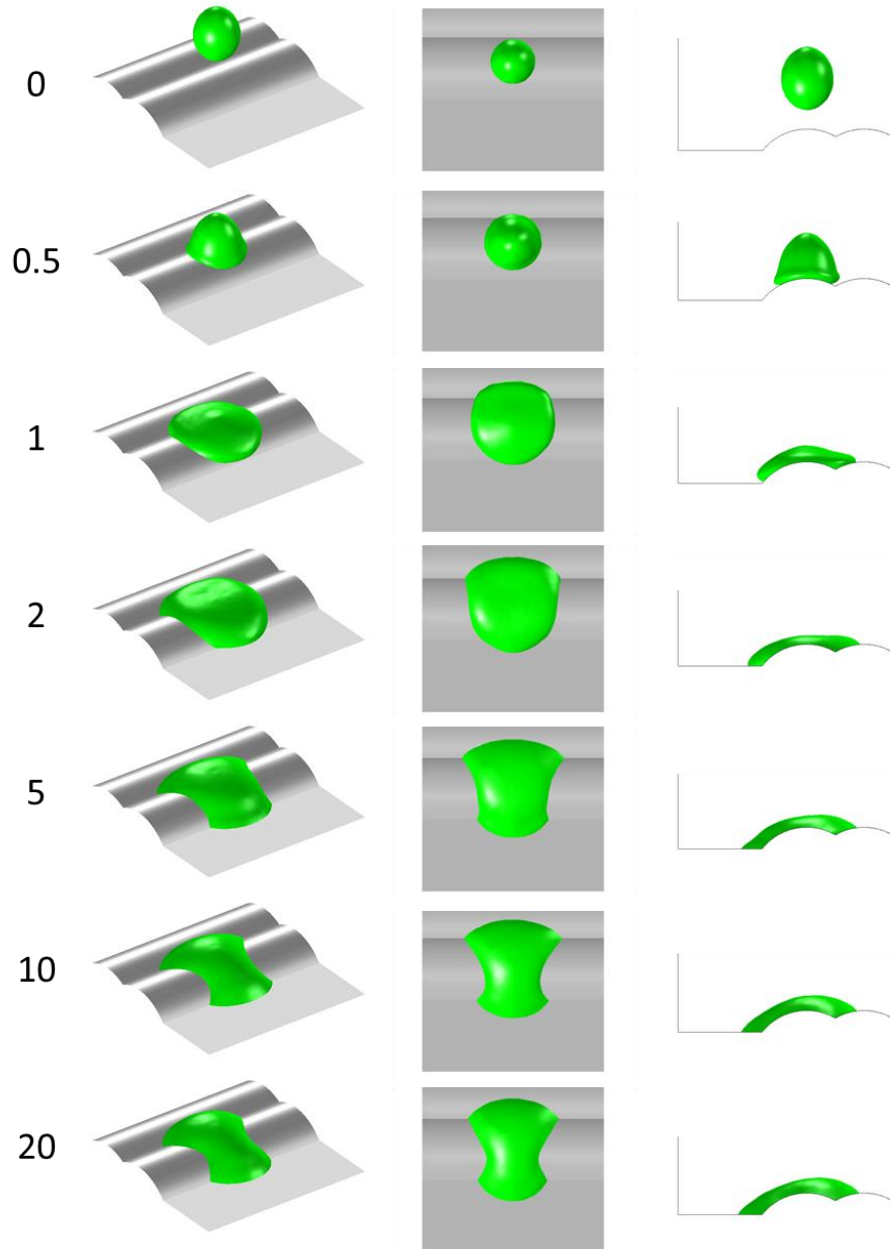


Figure 58: Simulation of droplet deposition at layer edge with ribbed surface
 (Time units = 10^{-5} second)

The prior simulations consider a deposition site that is exactly in line with the deposition site of the prior layer edge droplet. Next, we consider the influence of impact position inaccuracy, as presented in Chapter 2, on the resulting overflow. All simulation conditions are kept constant with the prior simulations apart from the droplet impact position respect to the edge. Three new cases are studied where the droplet is positioned beyond the edge center by 10 μm , 20 μm , and 30 μm , which is well within the positional errors discussed in Chapter 2. The resulting deposition evolutions are shown in Figure 59 and the side profile at max impact spread and max capillary spread are shown in Figure 60.

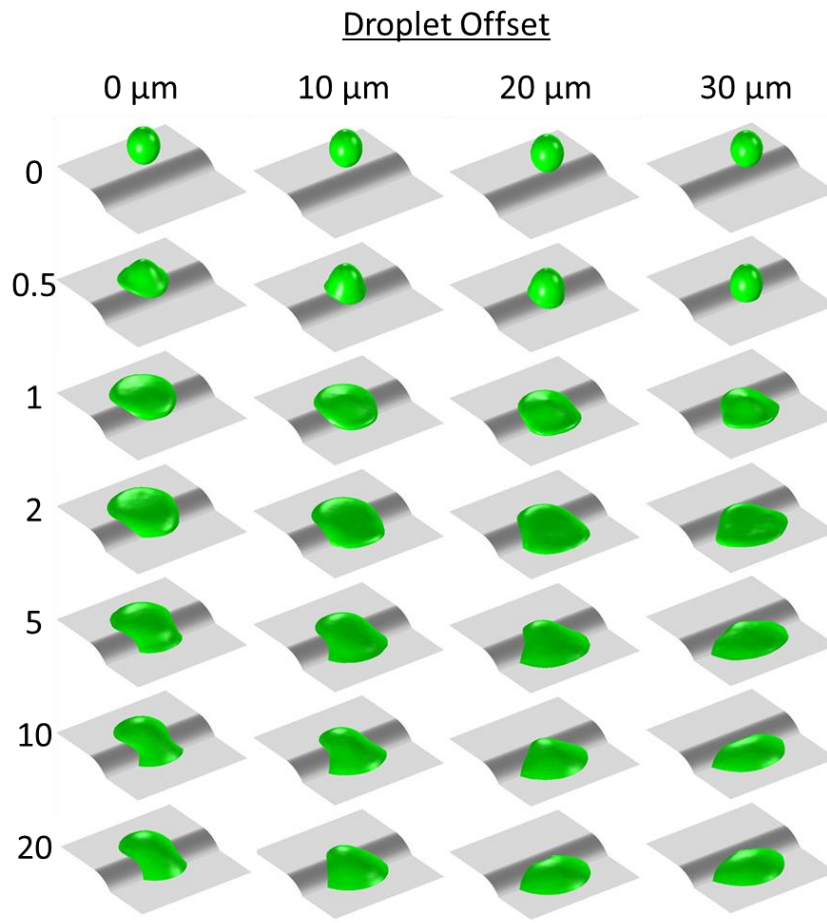


Figure 59: Comparison of effect of droplet inaccuracy on deposition

It makes intuitive sense that as the impingement site is moved so too would the spread, and that is indeed observed. During the impact driven spread, the boundary extended an additional 15, 25, and 33 μm beyond the ideal deposition case, respectively, for offsets of 10, 20, and 30 μm . Also of interest is the effect the positional error had on the max capillary spread, where there is little distinction between the 20 μm and 30 μm offset cases since both were pulled fully down the edge to the base substrate surface. Such flow results in no material contribution to the height for layer two at the edge and a significant expansion in the part boundary and illustrates the impact of single droplet accuracy.

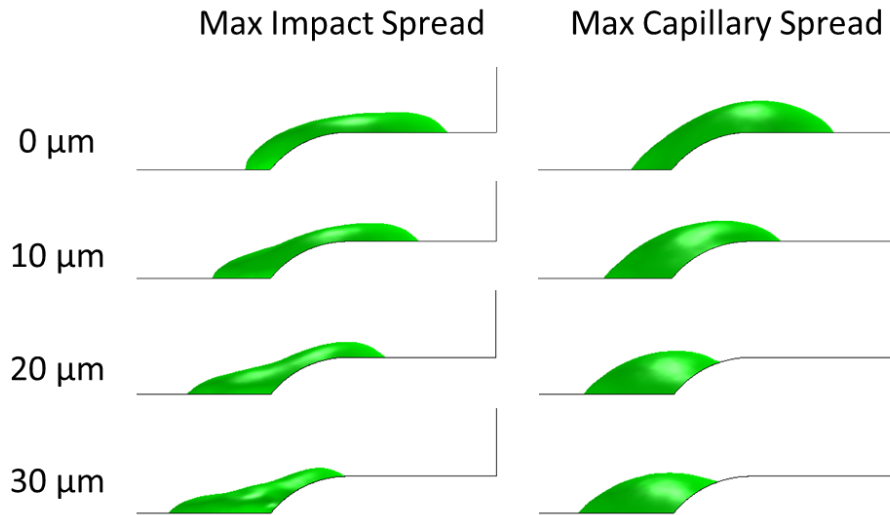


Figure 60: Side view comparison of max impact spread and max capillary spread for offsets of 0, 10, 20, 30 μm

4.5 Modeling of Layer Deposition

In the previous section, we showed the impact of single droplets near a first layer edge and the resulting overflow and height reduction that can occur under ideal circumstances. In this section, we will expand these studies to simulate multiple droplets and multiple layer evolution. Specifically, we will consider the fabrication of an extruded square that is 9 pixels by 9 pixels, and 3 layers high, as shown in Figure 61. The simulation domain

is set up to approximate the operations of commercially available MJ printers based on observations of the printing process, related research, and patents [81]. To that end, the same droplet parameters listed in Table 8 are used, along with a target deposition spacing of 600 dpi in both the X and Y axis, based on the Objet 260 system. This yields a pixel size of roughly $42.3\mu\text{m}$, giving a square side length of $\sim 380\mu\text{m}$. The Objet machine states a layer thickness for the high-resolution setting of $16\mu\text{m}$, which is assumed to incorporate the leveling process. No leveling is incorporated into the current study, however, for reference purposes a target layer thickness of $16\mu\text{m}$ is used.

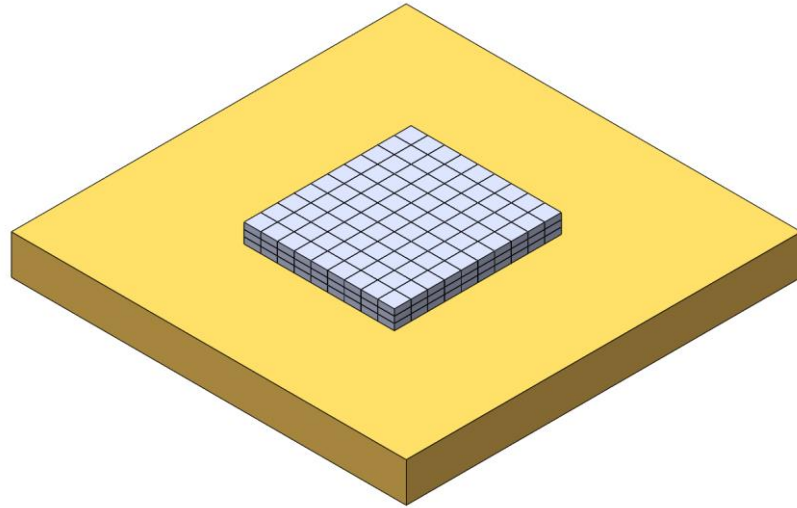


Figure 61: Illustration of target feature, 9x9 pixel, 3 layers thick

A critical element of the process operation is the multi-pass deposition pattern needed to fully cover a printing area at the desired resolution. Consider a printer, such as the Objet 260, which features 8 printheads (4 for build material and 4 for support material). If each printhead has a nozzle spacing of $1/37.5$ inch (based on Ricoh MH 1900 printhead), and the printheads are spaced to provide equal distance between all nozzles, as seen on the machine and patent literature. Then, for each pass of the printhead bank, lines will be deposited with a 150 dpi spacing. Therefore, to reach the target resolution of 600 dpi, 4

passes are required, which is what is observed on the system used in Chapter 2 and will be modeled in this work. Given the deposition parameters stated and a multi-pass system, this work makes several assumptions. First, no two adjacent lines will interact during a given pass and can therefore be modeled independently, as will be shown in the next section. Second, for each pass, the deposited beads will have received a full pass of the UV lamps, and it is assumed that all material is fully cured before the next pass is deposited and is treated as a rigid solid surface. Lastly, this work also assumes that the droplets closest to the edge during line deposition are most significant in terms of the edge shape. As such, it was determined that the computational domain will include two and a half droplets for each line to effectively predict the feature shape development. Doing so provides a reasonable approximation of the deposition and keeps the significant computational cost and scale inherent to these types of 3D multiphase models manageable.

Layer 1

To begin modeling Pass 1 of the printhead, let us start with a single nozzle depositing a line of material, where the deposited droplets will impact and coalesce into a semi-cylindrical bead as shown in Figure 62a. The resulting 2D cross section of deposited bead is shown in Figure 62b and has a base width of 70.5 μm and a height of 14.6 μm . These results match closely with the analytical model described by Equation 8 using the droplet volume, spacing, and contact angle [40].

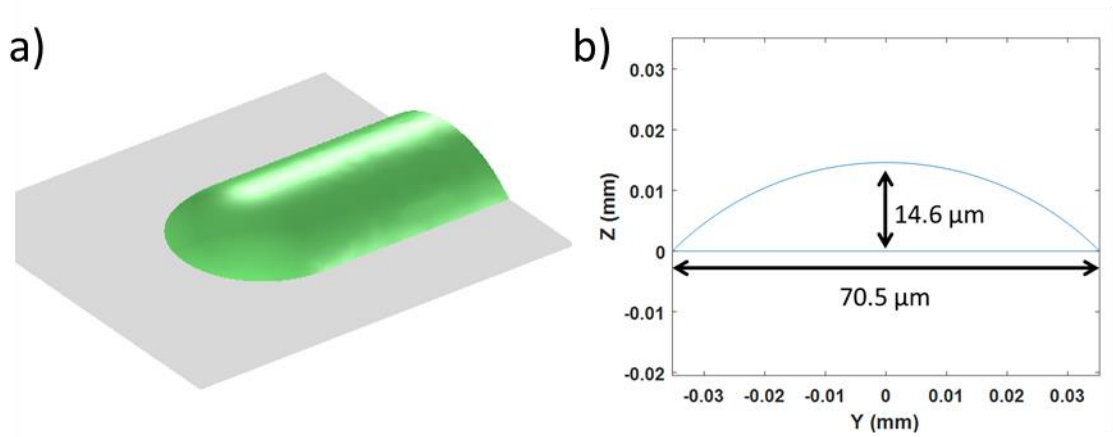


Figure 62: Simulation results for a single line deposition: a) final shape, b) cross-sectional profile

For this deposited bead width, given a 150 dpi line spacing ($\sim 169.3 \mu\text{m}$) fixed by the printhead bank, the assumption that no two adjacent lines will interact during the first pass is validated, and will all be single beads on an ideal flat surface. Additionally, we see that these conditions hold for Pass 2 as well, as the second pass will not interact with the first pass bead under ideal conditions. Figure 63 illustrates this point, where for the first pass there is ample space between the deposited cross-sections, which are colored to match the corresponding printhead and nozzle within the bank. Then, for the second pass the printheads have been shifted over half a step and still will not intersect the first pass deposition, now shown in black.

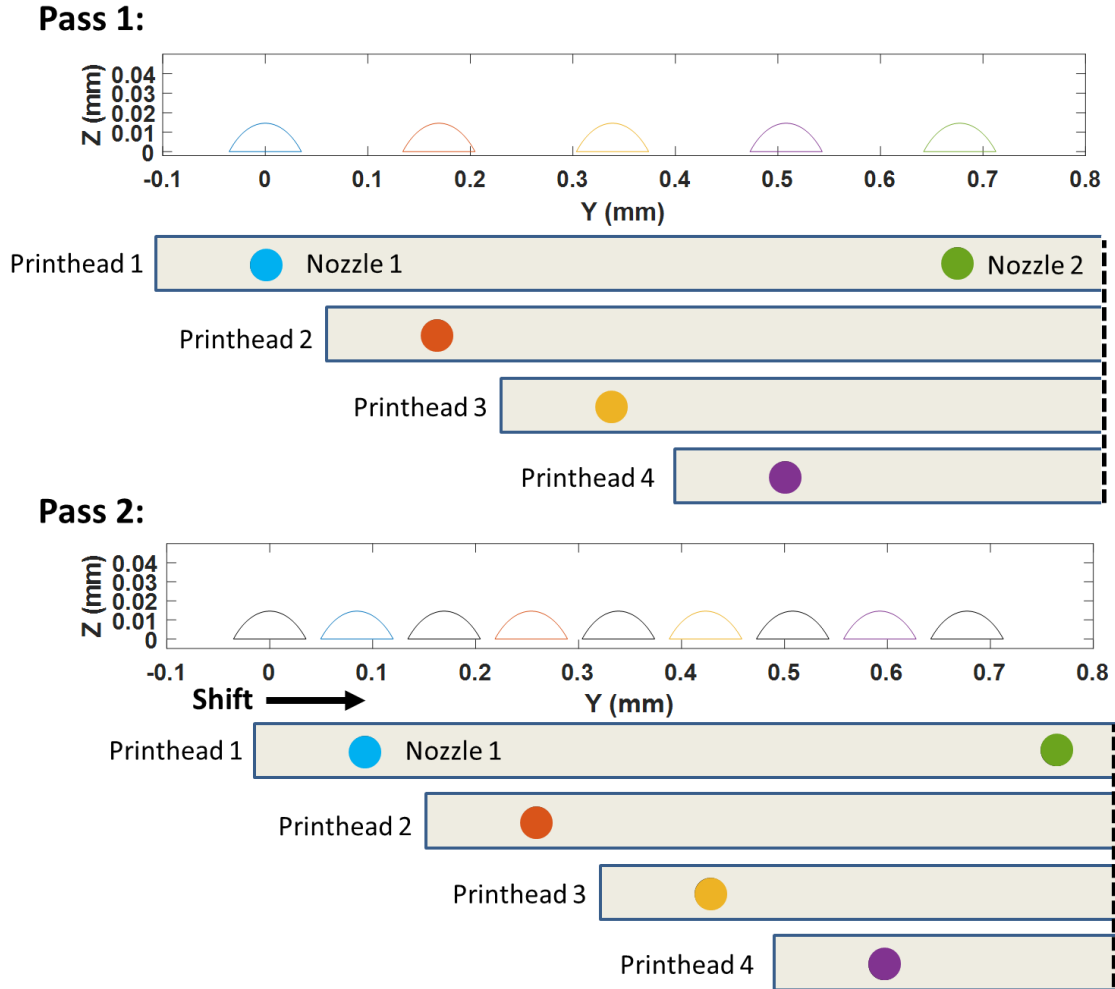


Figure 63: Deposition pattern for the first two passes of layer 1, showing that deposited beads do not intersect

Beginning with Pass 3 of Layer 1 the deposited droplets and bead will impinge into the groove formed by the prior passes, a non-flat surface, changing the deposition shape. The resulting bead formation is shown in Figure 64. For this pass, as a result of depositing between the two existing lines, there is a bulge in layer height, where the height of the Pass 3 bead at the center peak is over 20 μm . It is additionally observed that deposition of the final droplet at the edge results in a footprint expansion that is $\sim 10 \mu\text{m}$ beyond the furthest extent of the first or second pass.

On a longer time scale, capillary withdrawal could negate this expansion, pulling the bead toward the interior and shrinking the boundary if no pinning or curing occurs. For this study, the “final” shape was selected between the two extents at a point that extend $\sim 4\text{ }\mu\text{m}$ beyond the beads of Pass1 and 2.

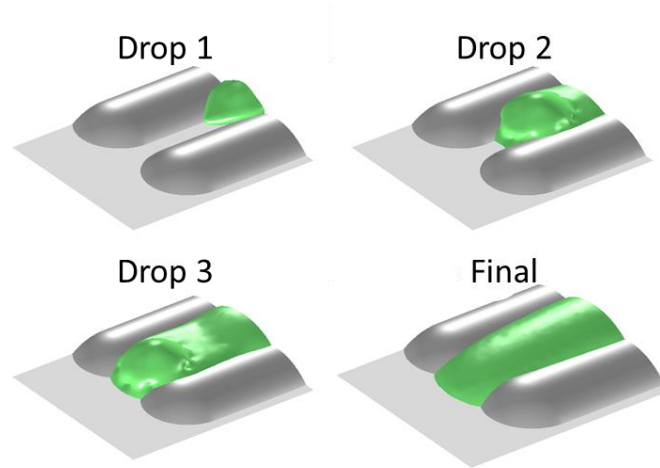


Figure 64: Simulation of Pass 3 and/or Pass 4. Deposition between two previously deposited lines

The fourth pass of the printhead encounters the same surface conditions as the third pass, namely deposition into a groove formed by Pass1 and 2 lines, and finishes filling in the layer. The completed layer is shown in Figure 65 below.

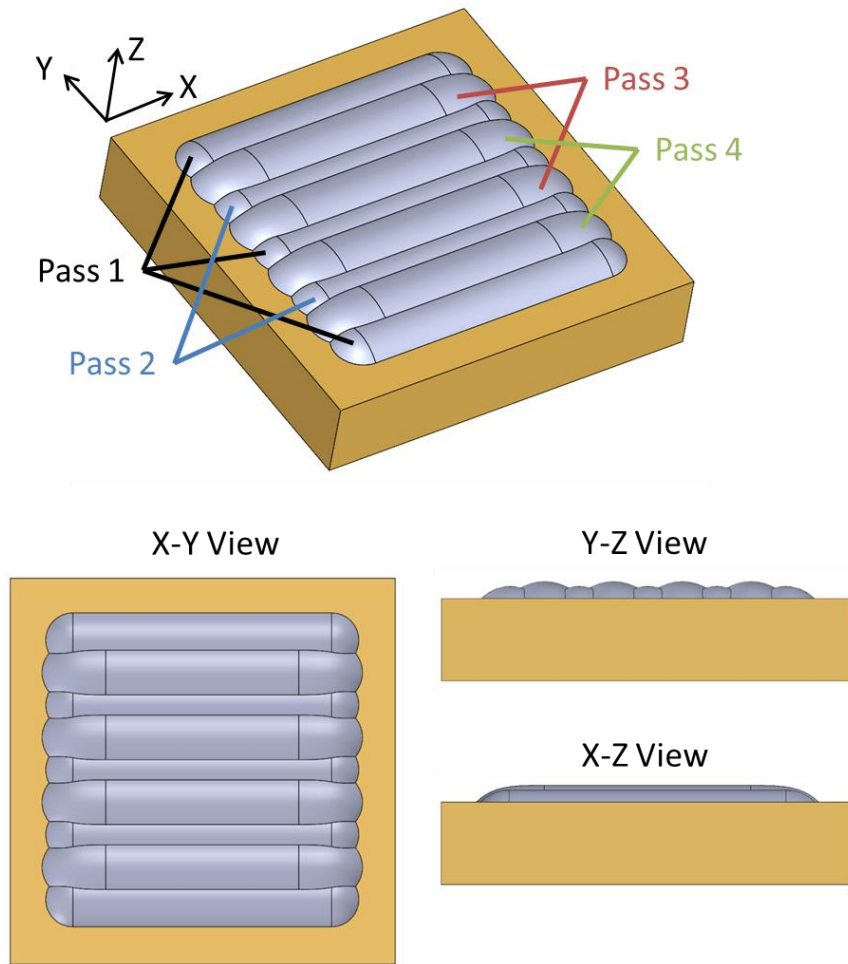


Figure 65: Final shape of completed Layer 1

Layer 2

From the result above, we see that deposition for Layer 2 will occur on a much more complex surface than Layer 1, particularly near the layer edge. Unlike Layer 1 for the three beads to be deposited during the first pass of Layer 2 there are two different surface conditions that a line will encounter: a line entirely on the edge of the part or one that passes through the interior. For the deposition along the edge, shown in Figure 66, the bead spreads fully down to the initial surface, expanding the feature footprint, like what was observed with a single droplet. This expansion also reduces the height contribution

for this pass, especially near the corner, which added only half the height of the first layer.

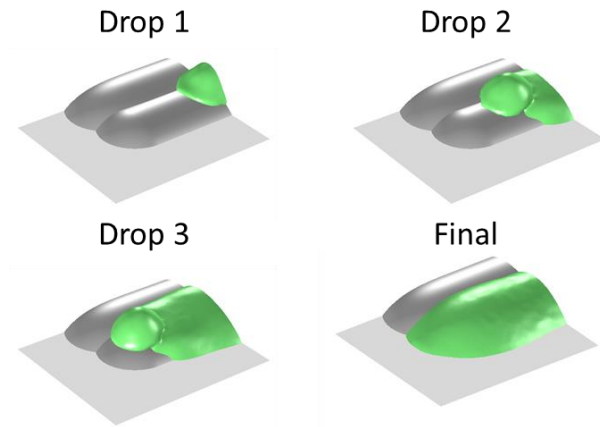


Figure 66: Layer 2 Pass 1 at the edge

In Figure 67, results for the Pass 1 central bead are shown. For this position as well, the deposited fluid expands down the edge and reaches the base surface. As the surface topology for Pass 2 is identical to the Pass 1 central line, the simulation applies for both.

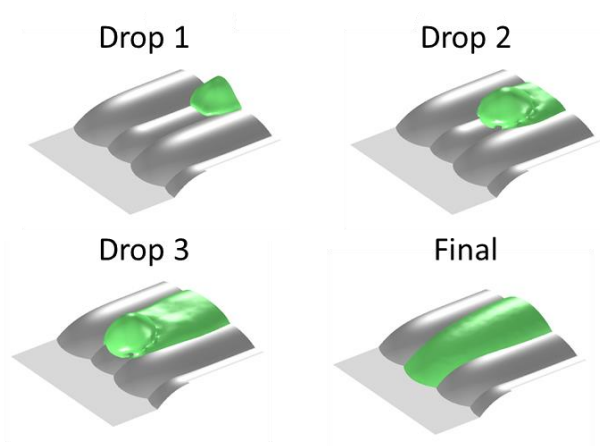


Figure 67: Layer 2 Pass 1 or 2 at the interior

Pass 3 and Pass 4 each have two unique depositions (near edge and central); however, they are mirrors of each other and can be fully considered with two simulations. As was seen with the previous passes of Layer 2 these beads also fully expand to the base surface.

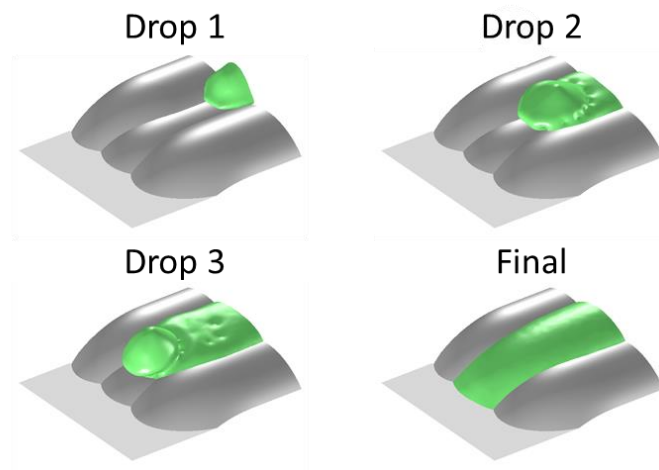


Figure 68: Layer 3 Pass 3 or 4 near the edge

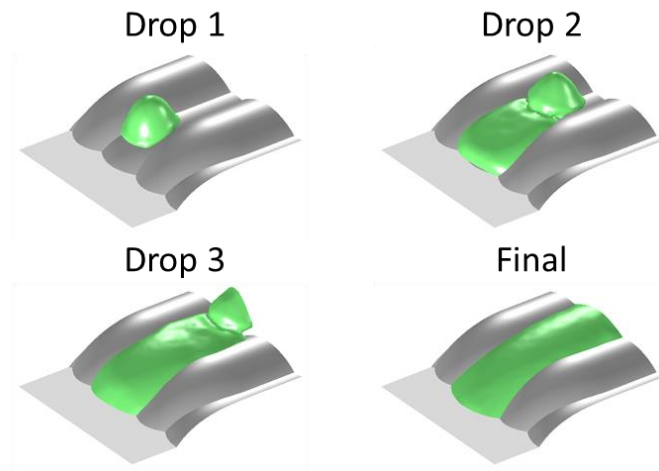


Figure 69: Layer 2 Pass 3 or 4 Central

Having completed the simulations for all scenarios of the four passes, the resulting combined geometry is shown in Figure 70. This layer has expanded the feature footprint on all four sides because of fluid overflow. There is also an increasing radius at the edges of the part, along with a corresponding reduction in height compared with the center of the plateau.

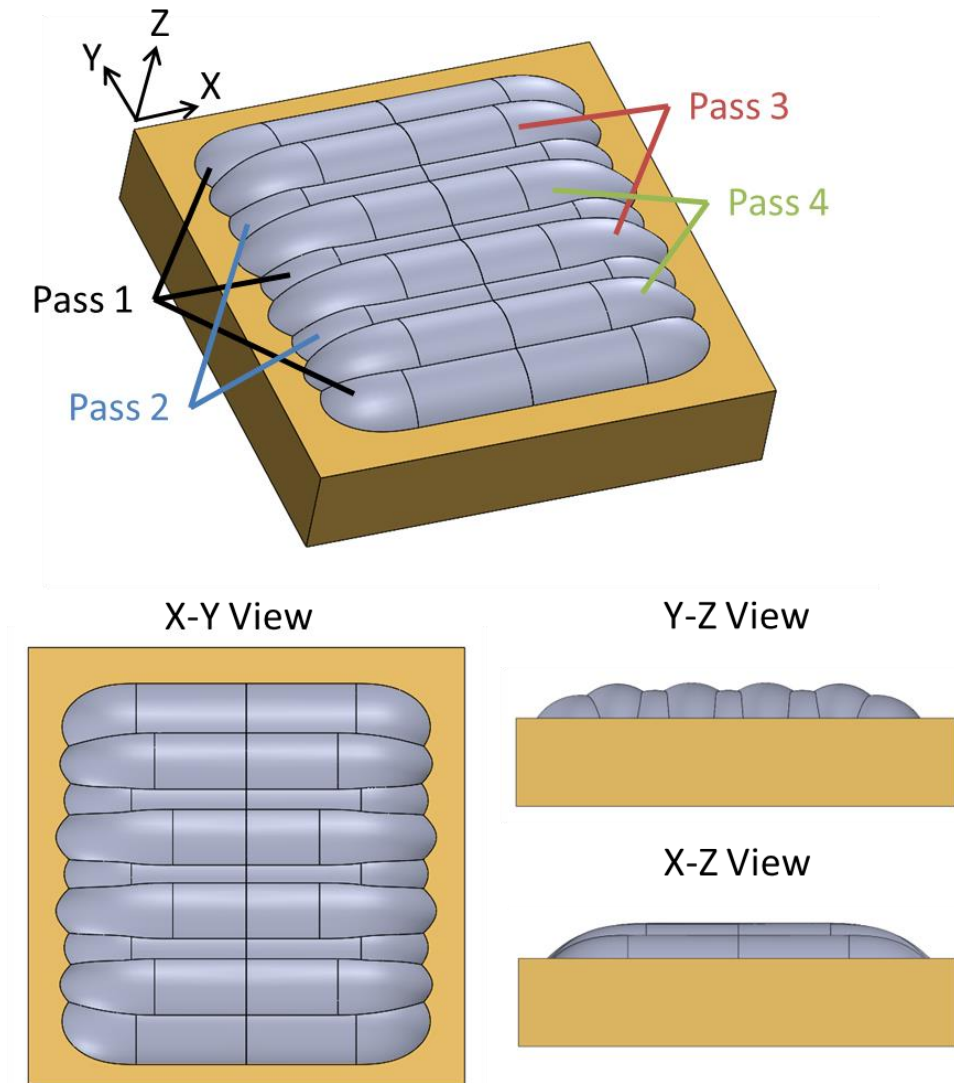


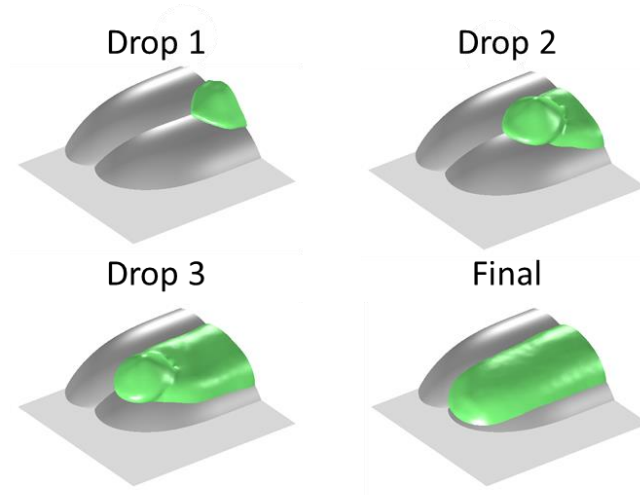
Figure 70: Final shape of completed Layer 2

Layer 3

For the third layer of the study, the simulation procedure follows in the same manner as the previous layer. For the first pass, simulations are conducted for the two unique surface topologies: along the edge and through the center. The simulation results are shown in Figure 70. Note that for the deposition at the edge, the spread no longer reaches the base surface and would likely indicate an end to the expansion of the footprint along

this edge, at least under ideal deposition. For the central pass, however, the bead just barely reaches the base surface as shown in Figure 70b.

a) Pass 1 - Edge



b) Pass 1 - Interior

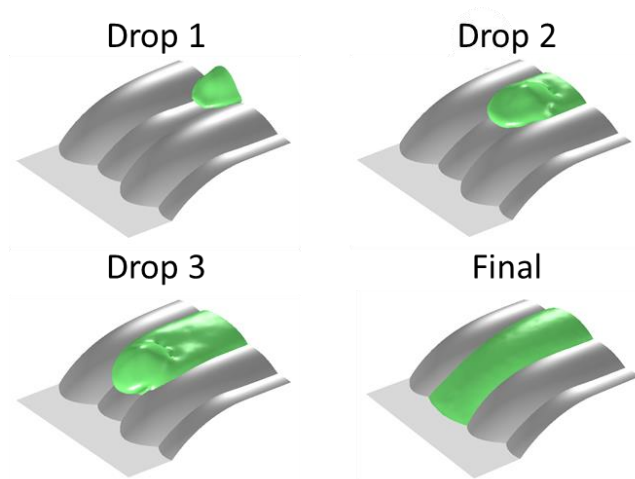


Figure 71: Layer 3 Pass 1: a) edge pass, b) interior central pass

While remarkably similar to the Pass 1 central deposition, the Pass 2 surface is unique and must be simulated. The results are shown in Figure 72 and are nearly identical to those above with the deposited bead extending to the base surface.

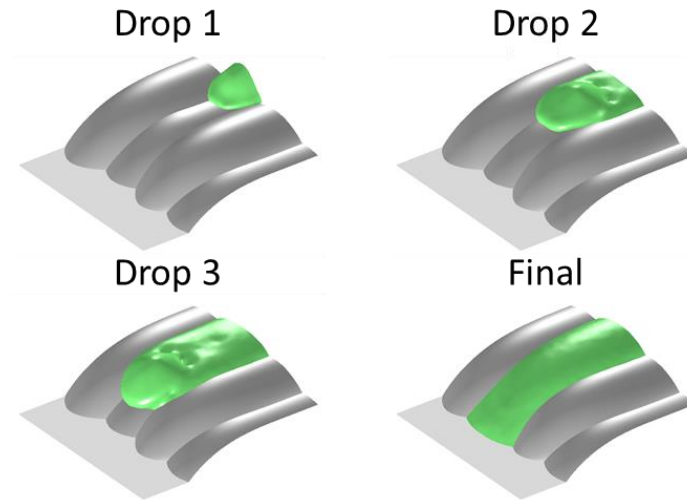


Figure 72: Layer 3 Pass 2

The final simulation results for Passes 3 or 4 are shown in Figure 73 and Figure 74. For these passes, the bead no longer reaches the bottom. While this may appear wrong given the previous pass reached the base, the extent of spread for these passes is very similar. The main difference between these beads and the Pass 2 deposition that reached the base is the surface height from the previous layer is higher and extends out farther at the base. Thus, the distance along the surface to reach the base is longer by over 10 μm .

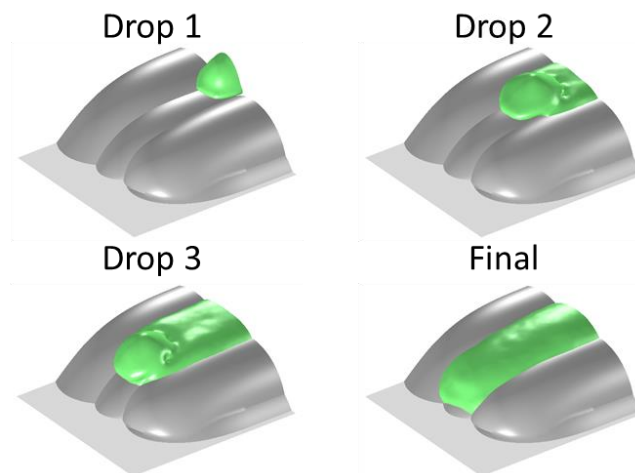


Figure 73: Layer 3 Pass 3 or 4 near the edge

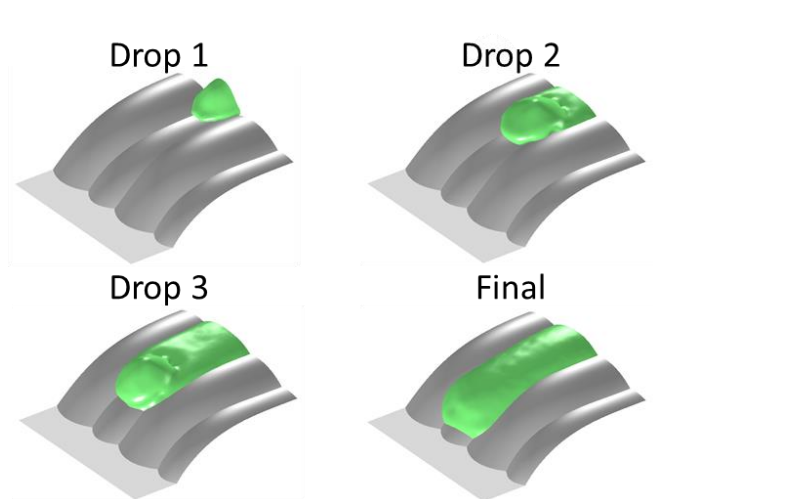


Figure 74: Layer 3 Pass 3 or 4 Central

The resulting combined geometry is shown in Figure 75. For this layer, we saw that there was no longer a general expansion of the feature footprint, except for the first and second central passes. However, the increasing radius at the edges of the part continued, along with a corresponding reduction in height compared with the center of the plateau.

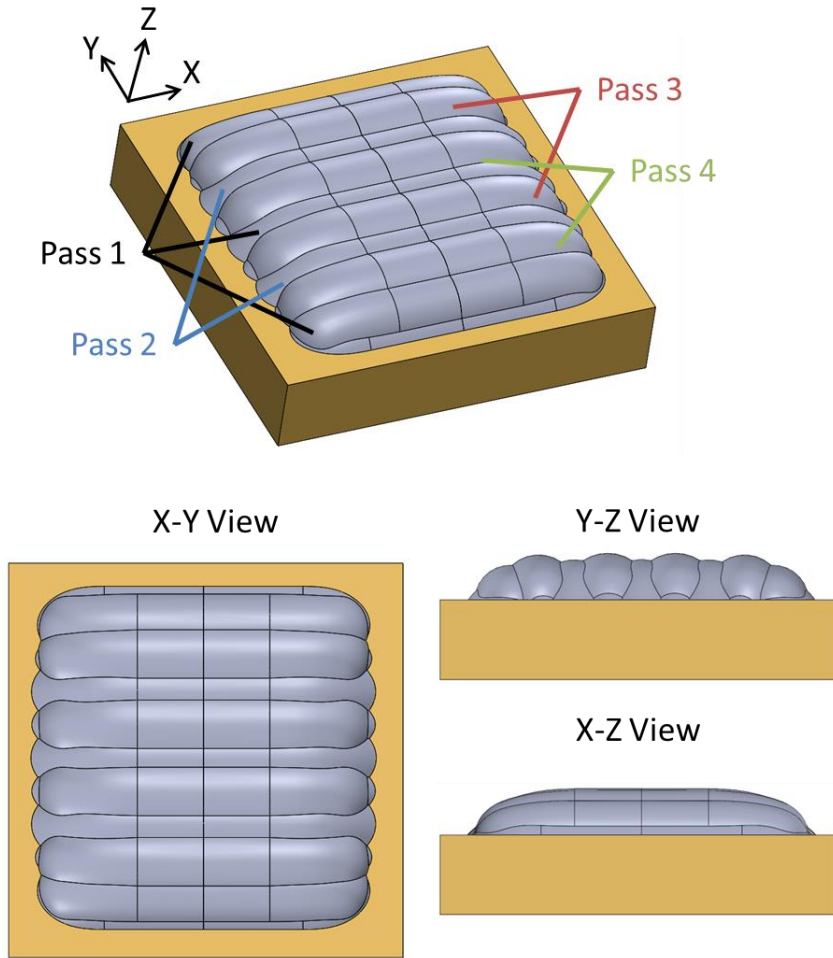


Figure 75: Final shape of completed Layer 3

With the layer simulations complete, Figure 76 compares the three-layer evolution with slices through the middle of the feature in the XZ-plane and YZ-plane. There are several key takeaways from these results. First, as was proposed in Chapter 2, droplet and line spreading at the layer edge is likely to cause overflow and extend the feature boundary even under the most ideal conditions. For the current simulations, it is observed that the extension of the boundary beyond the target edge is roughly $30\text{ }\mu\text{m}$ on each side, which is nearly 75% of the given resolution before any positional errors in deposition or variations in droplet size are considered. While significant, the simulation results also suggest that the extent of the overflow is limited to local droplet/bead spreading length scale, and the

deposited fluid will not run down the slope beyond the initial impact. This matches the result of Chapter 2 where no substantive difference in width at the bottom of a feature was seen with respect to thickness. After the first few layers, the extent of flow is likely similar, but it is no longer enough to reach the base surface and expand the footprint. One caveat is that since the effect of layer leveling has not been studied herein, it is possible this further pushes fluid down the edge. The author expects this to be limited for the reason stated above as the characterization results do not show increased width with increasing height. The second key observation is because of the fluid spread and overflow, there is a significant edge rounding observed which matches the rounding seen within the characterization results of Chapter 2. This rounding corresponds with a significant reduction in height at the edge region and shape deviation.

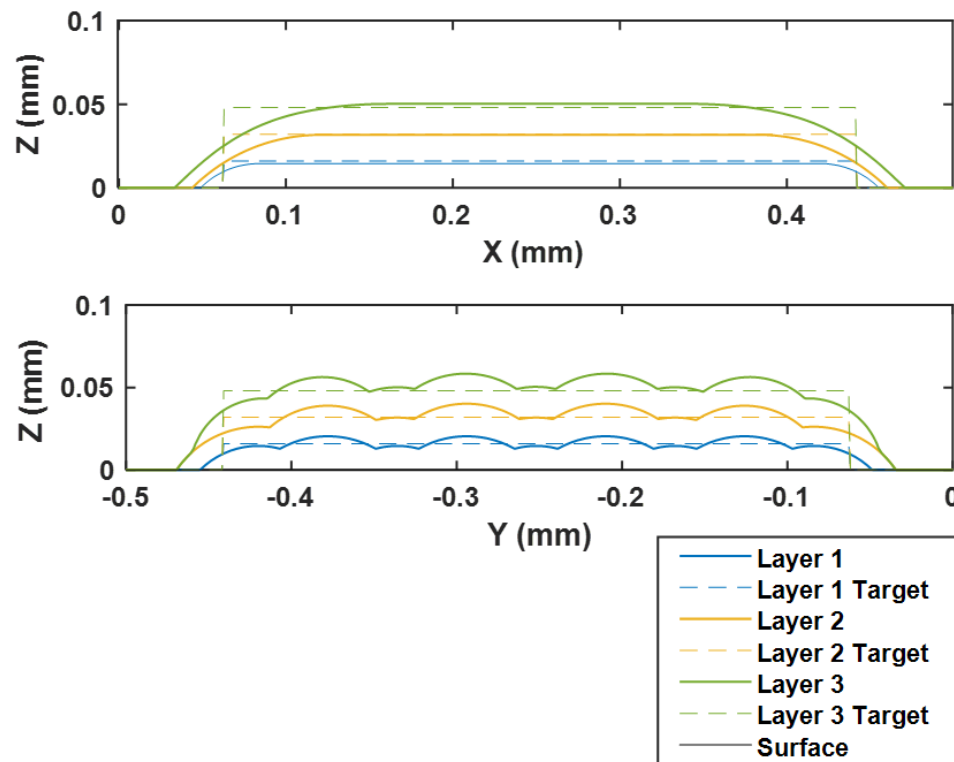
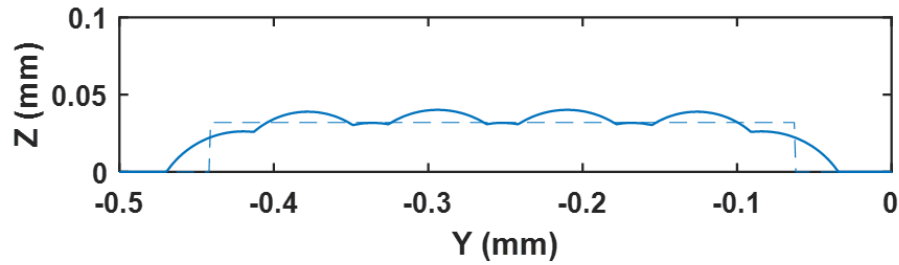


Figure 76: XZ and YZ plane cross-section through middle of feature, plotting evolution of 3 layers vs target

While the flow and shape deviation appear to be inherent to the process at the most basic droplet level, one can certainly envision a process plan where given the predicted surface deviations above would deposit additional material to close the gap. A simple example of this would be to consider the results of Layer 3 Pass 1 at the edge as if it were a corrective pass for Layer 2 as shown in Figure 77. With the extra edge pass, the entire layer is above the target height and makes for a more even layer and has a more vertical edge wall. Similar depositions could be deployed to correct for rounding in the XZ-plane as well as the deviations at the corner.

a) Pass 2 nominal



b) Pass 2 with extra edge pass

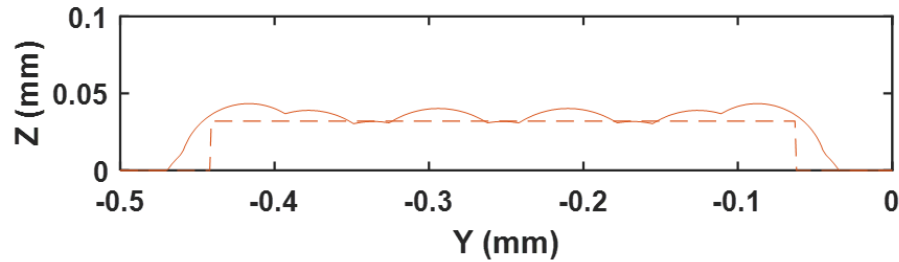


Figure 77: Comparison of cross-sectional shape of Layer 2 with a layer that had an extra edge pass, YZ plane

4.6 Discussion on computational expense

The results in the previous sections demonstrate the power of high fidelity CFD tools to study the inkjet deposition process and predict feature development on a drop-wise, line-

wise, layer-wise basis. Leveraging similar simulations to study the effects of changing process and material parameters, e.g., contact angle, viscosity, surface tension, impact speed, droplet spacing, are extremely valuable during initial process development and research, especially given the difficulty physically imaging at the relevant time and length scales. However, they are far from rapid, and the computational cost of the simulations are such that if the author expanded further than the aforementioned results, the required time to achieve results would be impractical for any general manufacturing application, whether as a control model or a tool for design evaluation. For example, the simulations involving a single droplet took multiple hours to solve and simulations involving multiple droplets took over 24 hours on a reasonably powerful desktop machine. Certainly, it is possible to make improvements on this simulation time with more powerful machines, but realistically these improvements would be quickly consumed with a minor expansion in simulation scale and thus another approach is needed. The question now becomes, what can be done to rapidly predict the relevant feature development? One observation from the above simulations is that the most important factor dictating the deposited shape is the coalesced fluid footprint and most of the complex impingement dynamics are immaterial so long as you can reasonably predict the footprint. The next chapter will explore this further.

4.7 Summary

In this chapter, the second research question is studied: How can local material flow near previously jetted lines and boundary edges be modeled and how does such flow affect feature resolution? A high-fidelity multiphase droplet impact model is developed, using the COMSOL Multiphysics platform, and validated with analytical and experimental

results. Leveraging this model, individual droplet impact at a representative layer edge is studied investigating the effects of surface topology as well as positional error on the fluid spread and overflow. It is shown that for the parameters studied, there is indeed overflow beyond the first layer boundary due to impact driven spread, on the order of 20-40% of the droplet resolution, with minimal differences between a flat topped and ribbed surface. Accompanying the overflow is a reduction in height contribution at the deposition site and resulting height deviation from target. Additionally, as is intuitively expected, it is shown that positional errors where a droplet impacts farther out the layer edge results in increased overflow and reduced resolution. However, the final extent of the spread will depend on the degree of capillary driven flow that may occur as it competes with contact line pinning and fluid curing.

Next, as single droplet impact is insufficient to draw major conclusions with respect to broader MJ feature development, the model is expanded to include multiple droplets depositing and coalescing. Then, a multi-pass line deposition scheme representative of the typical MJ system is run, simulating a portion of a 9x9 droplet square through three layers of deposition. To the best of the author's knowledge this is the first of any such study to explore full 3D CFD simulations multi-line/multilayer. The results further validated that edge overflow and resolution reduction occur because of basic droplet impact driven spread. Additionally, the results show the beginnings of corner rounding and height deviation at the edge, all in absence of other proposed culprits like roller leveling and curing. Building from the developed models and layer simulation process, future work can explore the effect of varied material and process parameters on the edge feature development and shape fidelity. Still, due to their prohibitive computational cost,

it would be unrealistic to scale to predict full mesoscale feature development. Therefore, in the next chapter, a more computationally feasible method is explored.

CHAPTER 5. QUASI-STATIC BOUNDARY METHOD

5.1 Introduction

In the previous chapter a high fidelity CFD model was shown to be a powerful tool for simulating the MJ deposition process; however, due to the significant computational expense of such methods, it is infeasible to scale beyond what is presented. Considering this limitation, this chapter proposes a new Quasi-static Boundary based method to answer Research Question 2.2: How can the material jetting process be modeled to rapidly predict the as-manufactured shape of mesoscale features?

As discussed in Chapter 3, a number of physical parameters are significant to characterize droplet deposition such as droplet size (D_0), deposition velocity (U), fluid density (ρ), viscosity (μ), surface tension (σ), and material-surface interaction like contact angle (θ). To relate these parameters and the dominate deposition forces at play, dimensionless numbers such as the Reynolds (Re), Weber (We), Ohnesorge (Oh), and Bond numbers (Bo) are helpful to classify deposition conditions and enable comparison between different studies.

While helpful in characterizing initial impact conditions, it is also important to understand the evolution of droplet impingement over time. For the deposition of interest to this work, there are three general phases, shown in Figure 78. The initial impact phase is dominated by kinetic behavior determined by the impact velocity. The expansion of the droplet is balanced by both surface tension and viscosity. During the second phase, depending on the extent of initial expansion and fluid surface interactions, the droplet

could relax back from expansion or could remain stationary experiencing contact angle hysteresis. For the fluids of interest to material jetting this phase is generally well damped, showing minimum or no oscillation. Finally, in the last phase, capillary forces dominate as the fluid spreads to its final sessile shape.

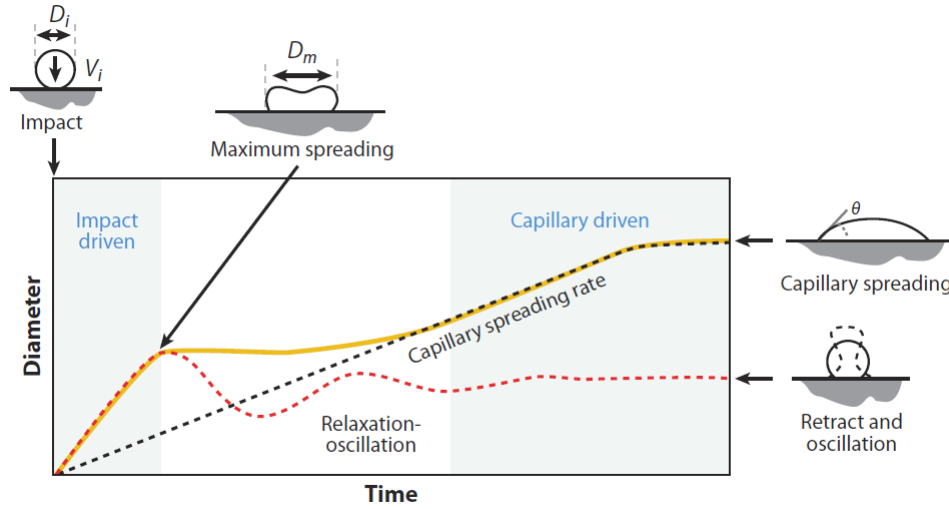


Figure 78: Phases of droplet impact and spreading, image from [45]

The relative time scales for each of these phases can be approximated using the process parameters listed in Table 8 and the following equations [44]:

$$t_{spread} \approx \frac{D_0}{U} ; t_{osc} \approx \sqrt{\frac{\rho D_0^3}{\sigma}} ; t_{visc} \approx \frac{\rho D_0^2}{\mu} \quad (23)$$

The tabulated values are listed in Table 9. As a rough order of magnitude estimate, the transition from the relaxation phase to the final capillary phase is taken as half the viscous time period.

Table 9: Time scales of droplet spreading

t_{spread} (μs)	t_{osc} (μs)	t_{visc} (μs)	t_{relax} (μs)	t_{dep} (μs)
10	50	160	80	125

To put these time scales into perspective, we will compare the printing deposition interval, t_{dep} (the time between subsequent drops). We estimate the ejection rate for an Objet machine to be ~ 8 kHz, based on speed of the printhead and know resolution, giving a deposition interval of $125 \mu\text{s}$. We can see that the initial droplet spreading and oscillation is much faster than the droplet deposition, meaning that the fluid bead fully reaches the capillary stage before subsequent deposition. This is a great benefit towards simplifying our fluid modeling. In the capillary stage for low Ohnesorge fluid, the bead evolution can be considered quasi-static such that the fluid surface can be determined based on the contact line boundary [57]. Therefore, with a reasonable prediction of the droplet footprint after the spreading phase, the final fluid surface can be determined without having to solve the full fluid problem.

5.2 Quasi-static Boundary-based Model

Herein the quasi-static boundary-based model is developed, abbreviated as the QSB model.

5.2.1 Theoretical Underpinnings

Consider a fluid wetting a surface in a quasi-static or equilibrium state. Assuming gravitational forces are negligible, $Bo \ll 1$ as is the case in this work, the pressure drop across the liquid-gas interface is described by the Young-Laplace equation:

$$\Delta p = \sigma \left(\frac{1}{R_1} + \frac{1}{R_2} \right) \quad (24)$$

where Δp is the pressure drop across the fluid interface, σ is the surface tension, and R_1 and R_2 are the principal radii of curvature.

The Young-Laplace equation assumes that on the interface the only stress applied is from external pressure and the resulting pressure drop is balanced by the surface tension forces, determined by the product of the bulk surface tension parameter, σ , and the mean curvature $\left(\frac{1}{R_1} + \frac{1}{R_2} \right)$. Since the liquid is assumed to be in a quasi-static state, tangential stresses are assumed to be negligible.

Expressing Equation 24 in terms of Cartesian coordinates, where the height of the liquid interface is $z = h(x, y)$, yields the following non-linear partial differential equation:

$$\Delta p = -\sigma \nabla \cdot \frac{\nabla h}{\sqrt{1+|\nabla h|^2}}, (x, y) \in \Omega \quad (25)$$

where Ω is the wetted region. Expanding the gradients gives:

$$\Delta p = \sigma \frac{(h_{xx} + h_{yy}) + (h_{xx}h_y^2 + h_{yy}h_x^2) - 2h_xh_yh_{xy}}{(1 + h_x^2 + h_y^2)^{3/2}} \quad (26)$$

which fully describes the fluid interface so long as $h(x, y)$ is unique for any point (x, y) .

Equation 26 is a second order nonlinear partial differential equation of the elliptic form. Given a prescribed pressure drop and associated boundary conditions, Equation 26 could be solved to determine the fluid interface height; however, typically the associate

pressure drop across the interface is not known a priori. Fortunately, since our deposited material is assumed to have a known mass and the fluid is incompressible, the volume of material is known. By adding a matching volume constraint, calculated using Equation 26, the pressure drop can be varied iteratively to solve for the interface height:

$$V = \int_{\Omega} (h(x, y) - s(x, y)) dx dy \quad (27)$$

where $s(x, y)$ is the height profile of the substrate, and the substrate height is assumed to be unique for any point (x, y) .

It should be noted that solving non-linear PDE's numerically is far from trivial and nearly impossible analytically for any complex domain. For this reason, many works seek to simplify to a linear form by adopting the thin film approximation shown in Equation 28, which drops the first derivative terms with the error vanishing as a function of the square of the slopes.

$$\Delta p = \sigma \nabla^2 h(x, y) = \sigma (h_{xx} + h_{yy}) \quad (28)$$

Equation 28 represents a second order linear partial differential equation of the elliptic form and is equivalent the commonly seen Poisson equation. As such, solving for the resulting height field is much more manageable resulting in better stability and faster solutions so long as the resulting error is acceptable. The degree of this error will be tested later during validation.

5.2.2 Finite Element Model

The above model is solved numerically using the finite element method implemented in MATLAB. The finite element method is a power tool whereby a geometric domain of interest is divided into a collection of subdomains over which approximate solutions to the governing equations are solved, and then assembled to form a piecewise solution to the problem of interest. The benefits of such an approach are far reaching, but most important are the ability to represent complex geometric domains with simple subdomains (finite elements) and the ability to reduce the solution of governing equation over these domains to much more manageable systems of algebraic equations. There are several common finite element approaches. The Matlab implementation utilizes the weighted-residual approach (also known as the Galerkin).

5.2.3 Computational Modelling Procedure

The method used consists of three steps described below and demonstrated by modeling a line consisting of five sequential droplets, deposited at the edge of a previous layer, shown in Figure 79.

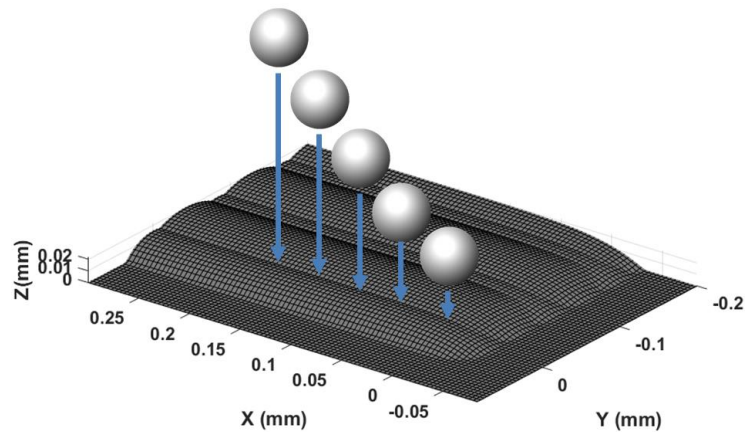


Figure 79: Line deposited at edge of previous layer

Step 1: Define the domain boundary

The first step towards defining the domain boundary is to estimate the contact line boundary of fluid in contact with the substrate. For each droplet, it is assumed that the fluid will flow outward from the deposition site, and the distance traveled can be modeled with a spreading law. For now, a simple spreading law is considered distance traveled in each radial direction and over the surface is a constant value, where the constant is determined based on a single droplet spreading on a flat surface. A more sophisticated second spreading law could consider how the slope of the substrate at each deposition site would change the spread distance in each radial direction.

An example of the predicted spread for five sequential drops at the edge of an existing layer is shown in Figure 80.

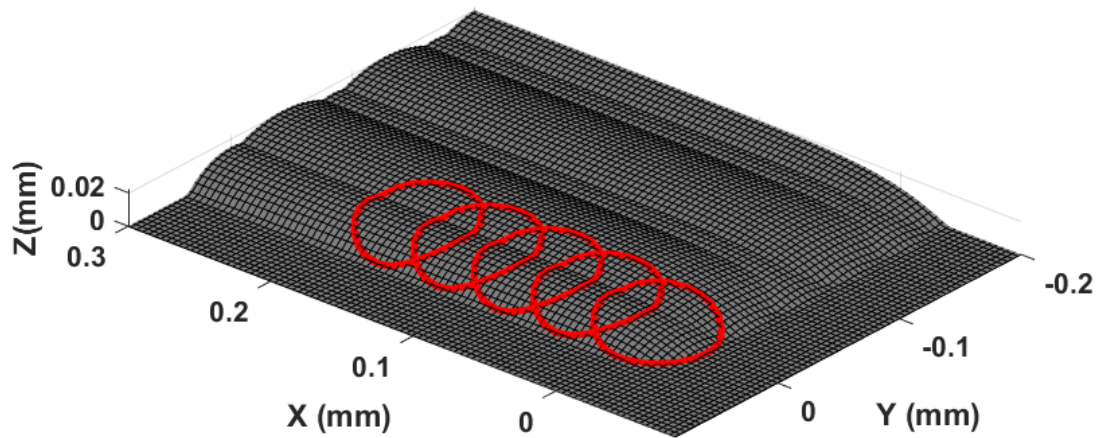


Figure 80: Predict droplet spread

Next, the individual droplet profiles are projected onto the x - y plane and convex hull of the points is determined. This represents the 2D domain boundary of the problem.

On this boundary, a Dirichlet boundary condition is used, which specifies the value of the solution at the boundary of the domain. Since the domain boundary is the point where the fluid interface meets the substrate at the contact line, the associated boundary value at each point is simply the height of the surface at that point, which is set by using the substrate height from the previous layer and interpolating for any points between the grid spacing. The domain boundary and associated boundary condition values for the five-droplet line are shown in Figure 81.

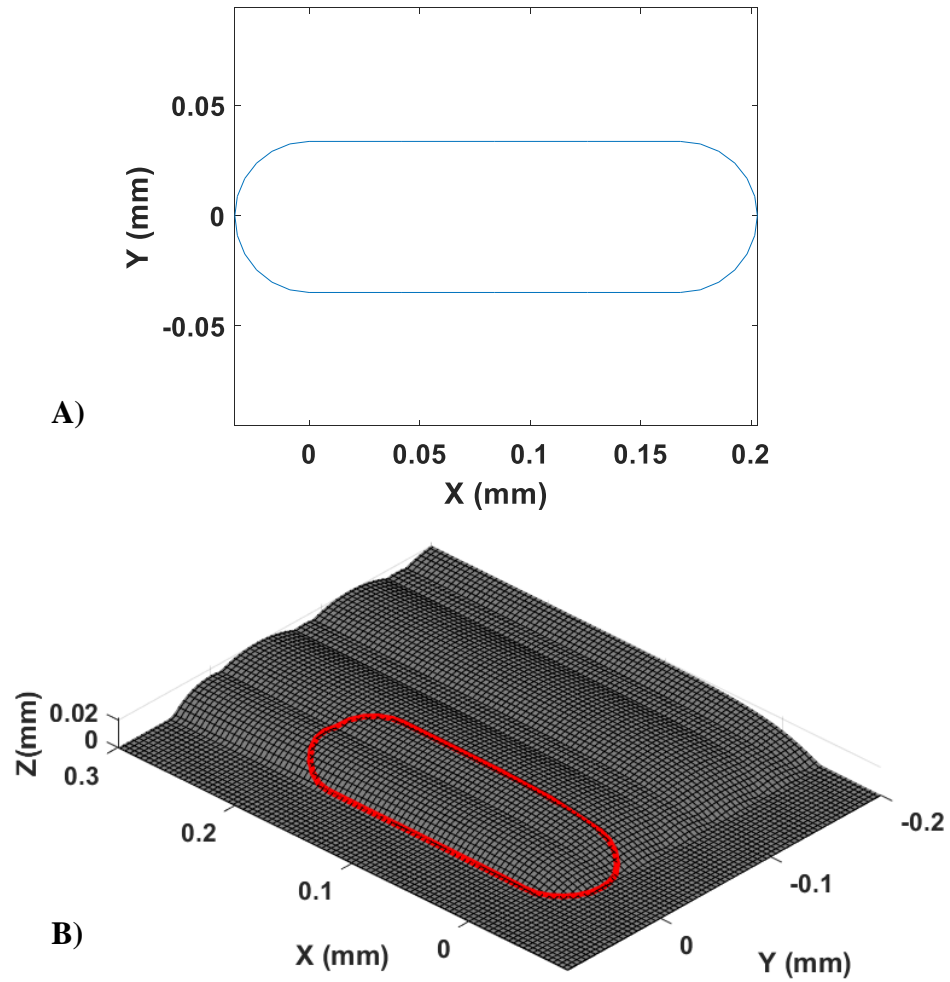


Figure 81: A) Domain boundary, B) boundary condition values

Step 2: Mesh the domain

With the domain boundary and associated boundary conditions set, the domain is now meshed with triangular elements. When meshing the domain, maximum element size and element order (linear or quadratic) is specified. The relative influence of these parameters is evaluated during validation below. A linear triangular element has three end nodes and features linear shape functions, whereas a quadratic element has the three end nodes plus three midpoint nodes leading to quadratic shape functions. Examples of these elements are shown in Figure 82.

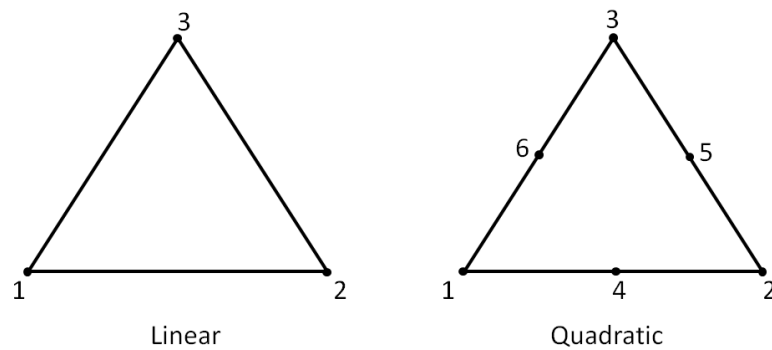


Figure 82: Linear and quadratic triangular elements

An example of the domain from Figure 81, meshed with linear elements is shown in Figure 83.

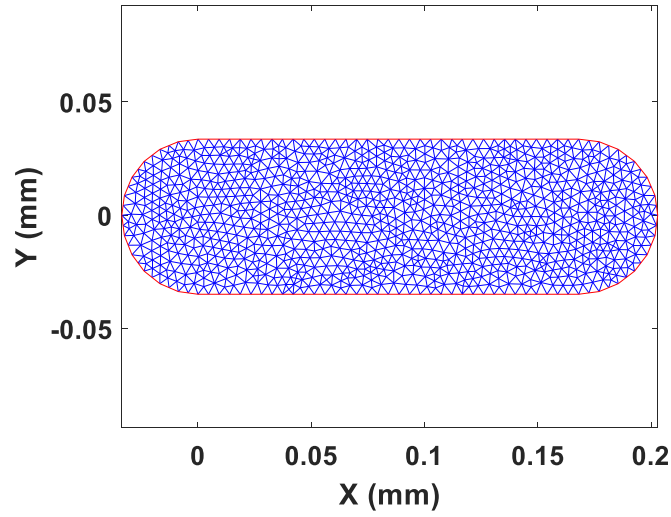


Figure 83: Problem domain discretized with a linear triangular mesh

Step 3: Solve the PDE and Volume Constraint

With the boundary conditions set and the domain meshed, the fluid surface problem is solved. Matlab's built in FEM solver is used. As was previously stated, since the specific interface pressure difference is not known a priori, a volume constraint is used. This is implemented as a bounded search, constrained optimization problem, see Figure 84, to find the associated pressure difference to satisfy the volume constraint after the surface is solved.

<p>Minimize:</p> $f(\Delta p) = \frac{(Volume_{Line\ FEA} - Volume_{Target})}{Volume_{Target}} \times 100\%$ <p>Subject to:</p> $\Delta p_{min} \leq \Delta p \leq \Delta p_{max}$ <p>Where:</p> $Volume_{Line\ FEA} = \int_{\Omega} (h(x, y) - s(x, y)) dx dy$ <p style="text-align: center;">$h(x, y)$: deposition surface height solved for using FEA</p> <p style="text-align: center;">$s(x, y)$: base surface height</p>

Figure 84: Volume optimization problem formulation

An overview of the solution process is shown in Figure 85. The volume optimization problem is solved using the Matlab optimization function, *fminbnd*. To begin the search, an initial pressure value is given and the PDE is solved over the finite element domain. The volume of the solution is calculated using the trapezoidal method, subtracting the volume of the substrate beneath the domain. The volume difference is then calculated and used to generate the next pressure value based on the gradient of the volume solutions. This is repeated iteratively until the volume constraint is met. Stopping criteria is set to a percent volume difference under 0.5. The solution of the example problem is shown in Figure 86.

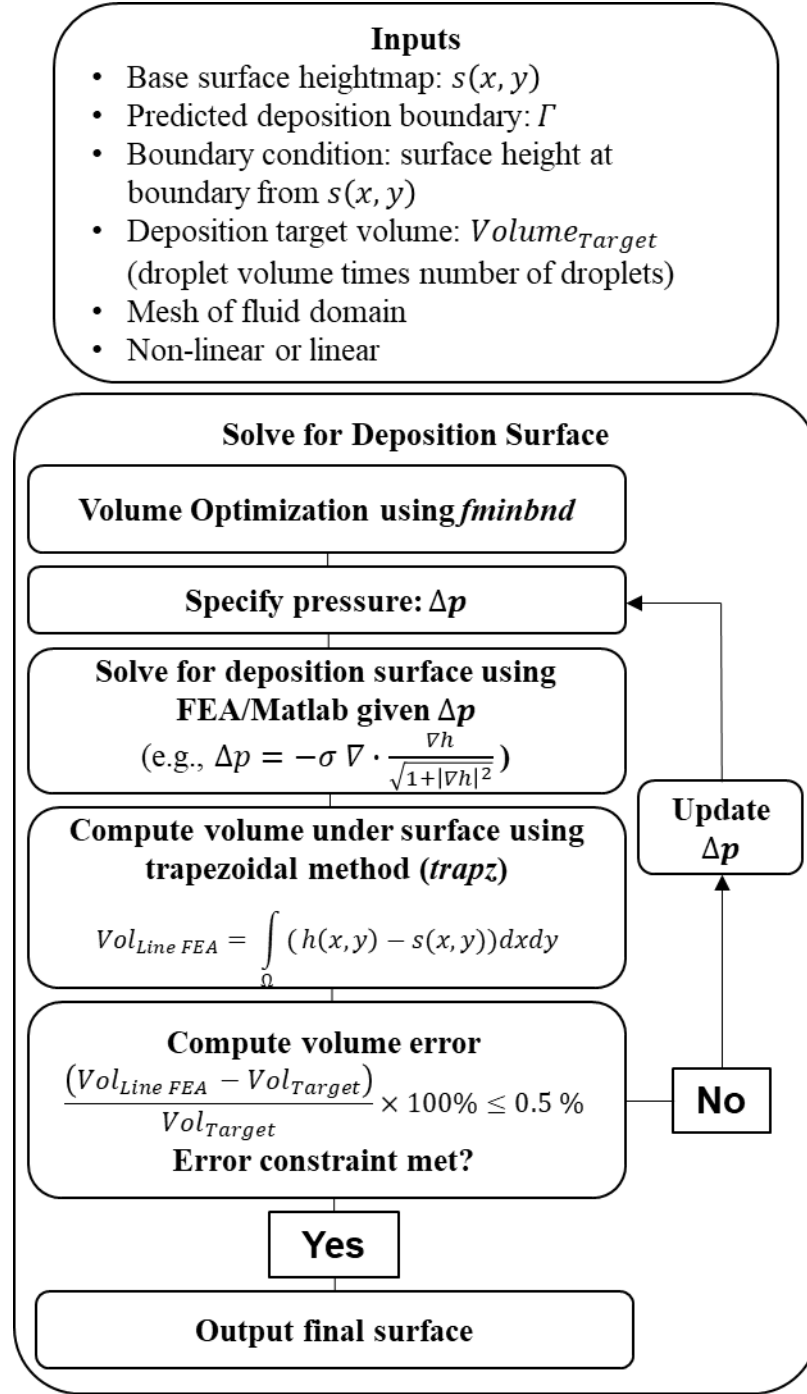


Figure 85: Process flow to solve for fluid deposition surface

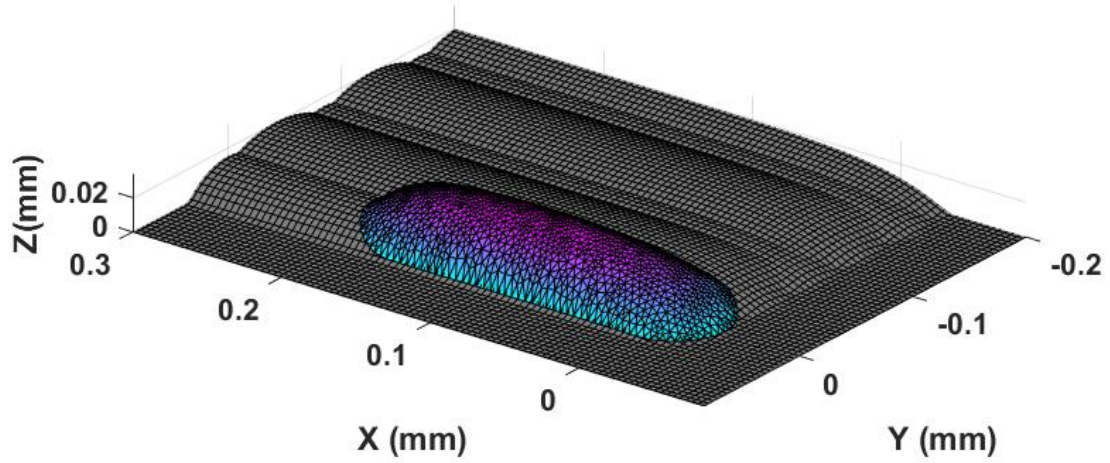


Figure 86: Solution for 3d fluid interface

5.2.4 Validation

To evaluate the boundary-based method's capacity to efficiently predict a deposited fluid surface, we compare the FEA simulation results for a single droplet on a flat surface with a spherical cap, shown in Figure 87, which is the known analytical solution to the Young-Laplace model for a micro-scale sessile drop. For this comparison, a 30pL droplet with a 45° static contact angle is used, resulting in a base radius of $35.2\ \mu\text{m}$ and center height of $14.6\ \mu\text{m}$.

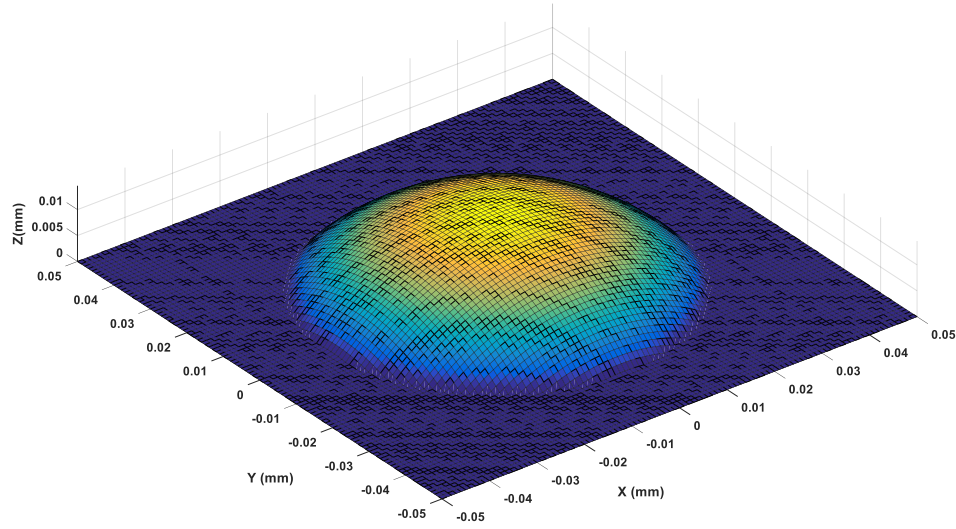


Figure 87: Spherical Cap

The numerical solution is calculated and evaluated for the mean absolute error throughout the domain and center height error compared with the spherical cap. The effect of mesh size/density and element order is evaluated, with results shown in Table 10. Overall, the numerical solution using the nonlinear formulation is quite accurate for both types of elements, as well as the coarsest mesh sizes, having a maximum average absolute error less than $0.2\mu\text{m}$ and maximum center height error less than $0.25\mu\text{m}$. Comparing the quadratic elements with the linear elements reveals a significant increase in simulation time for only a minor improvement in terms of accuracy. The linear formulation boasts an additional reduction in simulation time but has increased error. Both the nonlinear and linear formulations present orders of magnitude reduction in simulation time compared with a full 3D simulation, while still preserving acceptable accuracy. For comparison, simulation of the full droplet impingement would need several hours of simulation time using the level-set method in COMSOL running on the same computer.

Table 10: Effects of mesh size and order on simulation time and accuracy

		Nonlinear Form 2 nd Order Elements			Nonlinear Form 1 st Order Elements			Linear Form 1 st Order Elements		
<i>Elem max (μm)</i>	<i>No. Elem</i>	<i>Err_{avg} (μm)</i>	<i>Err_{cent} (μm)</i>	<i>Time (sec)</i>	<i>Err_{avg} (μm)</i>	<i>Err_{cent} (μm)</i>	<i>Time (sec)</i>	<i>Err_{avg} (μm)</i>	<i>Err_{cent} (μm)</i>	<i>Time (sec)</i>
10	136	0.082	0.104	19.01	0.177	0.230	8.78	0.273	1.012	0.99
5	504	0.102	0.175	19.23	0.114	0.209	8.33	0.305	0.945	1.19
2.5	2118	0.098	0.171	29.21	0.100	0.185	11.57	0.321	0.941	1.88

Next, to validate multiple drops in a line, the method was run using parameters from the work of Lee and Son, who studied the deposition of four sequential droplets, Figure 88a [51]. Their work used the level-set method, with contact angle hysteresis. As shown in Figure 88b, the boundary-based method showed good agreement with their work. A cross-sectional profile is shown in Figure 88c, where the nonlinear form yields a near perfect match, while the linear form has a greater error, of similar magnitude to the cap simulation, but still tracks well with the target shape. Simulation time is approximately 12 seconds for the nonlinear form and 2 seconds for the linear form.

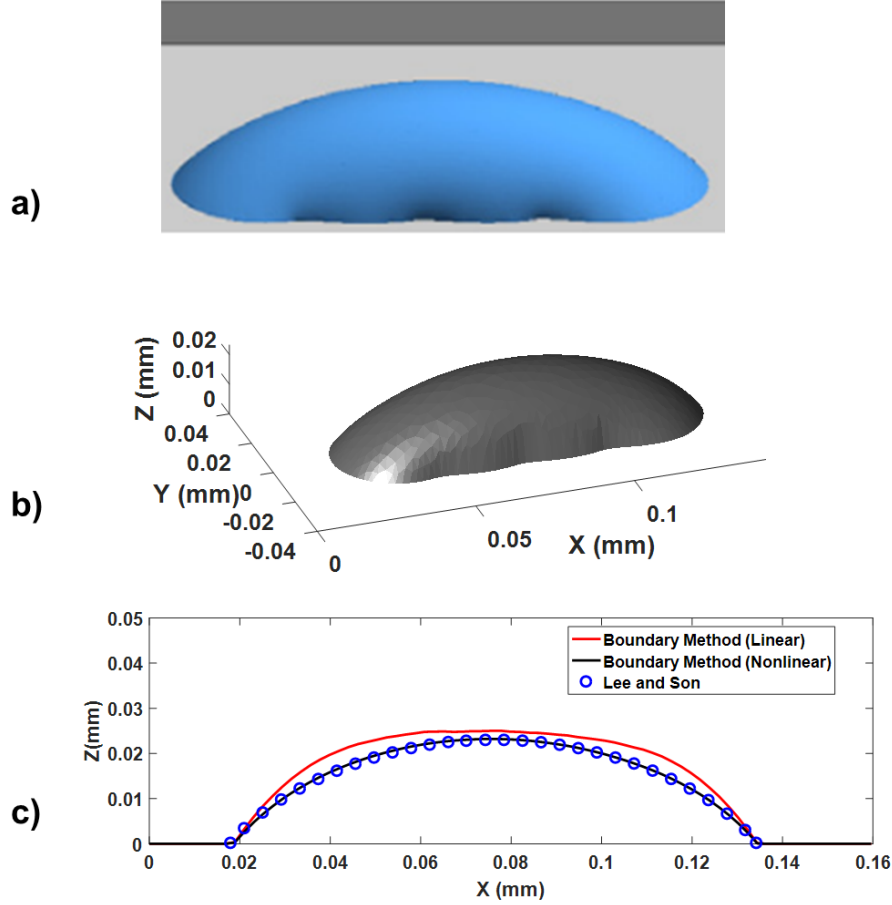


Figure 88: a) Simulation results from [51], b) Boundary-based results, c) Comparison of surface profile at $Y=0$

Finally, the case explored in Chapter 4 of a 3-layer, 9x9 square is considered. The model parameters are kept the same, based on 600 dpi resolution in the x and y axes, and a 30pL droplet with a 45° static contact angle. The simulation is set up using the same multi-pass assumption, where the system requires four deposition passes to complete a layer and the nozzle spacing is such that during any single pass, material from two adjacent nozzles does not interact. The case was run with both the linear and nonlinear formulation, taking approximately 38 seconds and 9 minutes to complete, respectively, and producing remarkably similar results. The surface profile from the linear formulation is shown in Figure 89.

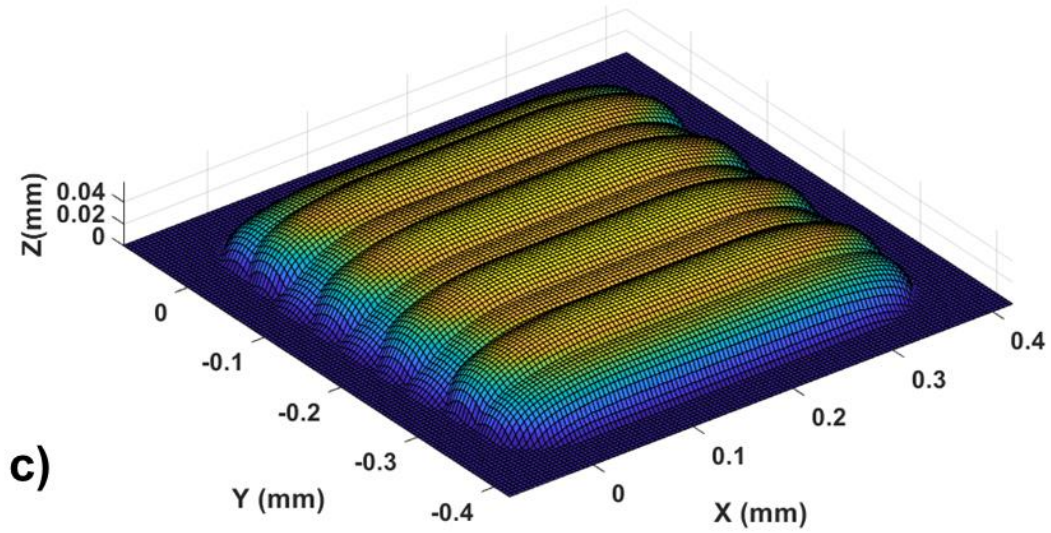
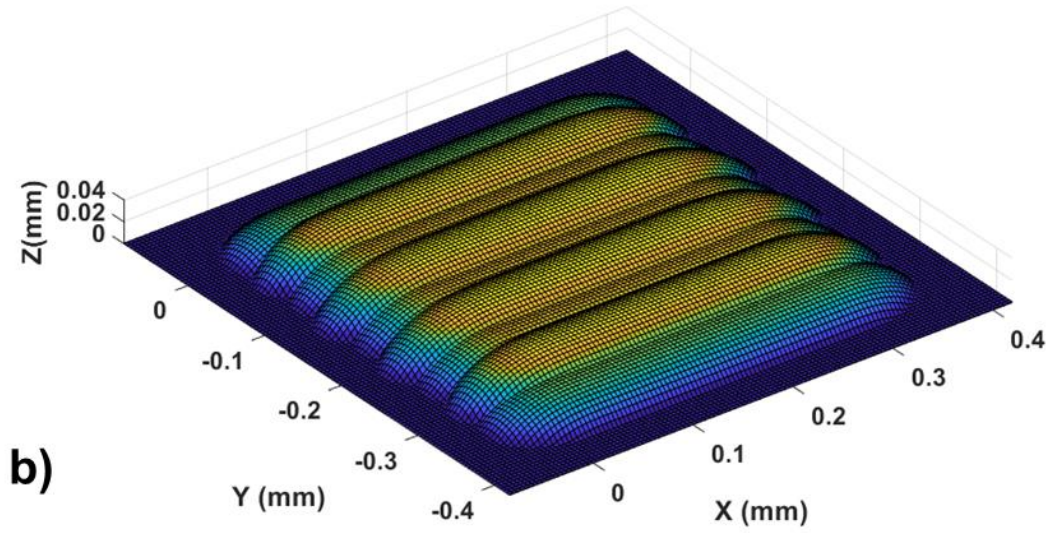
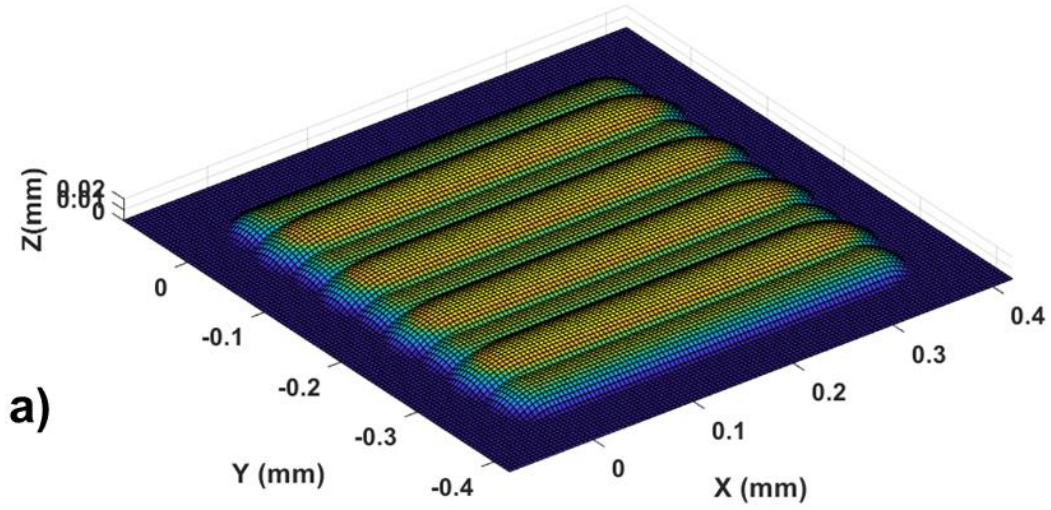


Figure 89: Simulation results for 9x9 pixel square, a) Layer 1, b) Layer 2, c) Layer 3

The overall shape tracks well with the results observed in Chapter 4, as shown in Figure 90, and the mean absolute error is $7.8\text{ }\mu\text{m}$. The main source of this error is the overflow that occurred during Layer 2 deposition, where the material flow reached the build platform, and where capillary action causes extra expansion of the layer edge. This is expected as the current implementation includes only the most basic droplet spread model, and an asymmetric spread model incorporating the surface angle will be discussed later.

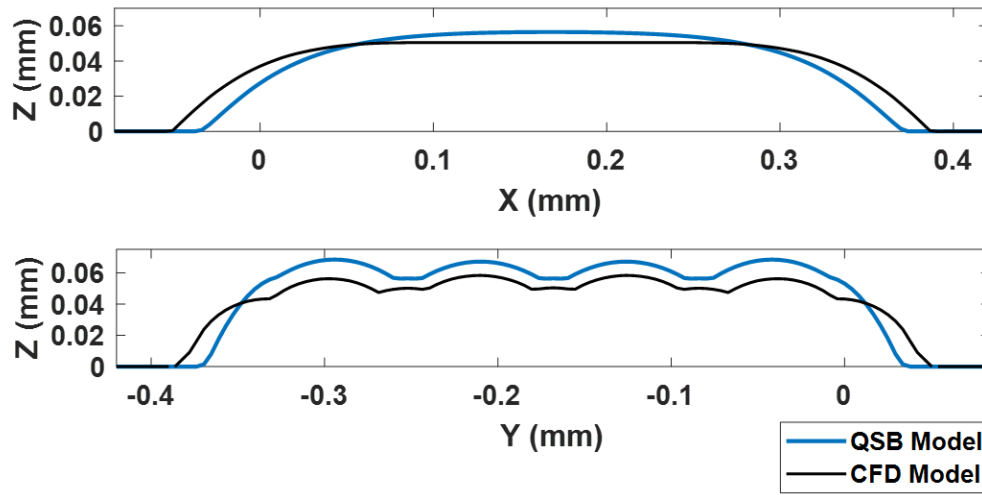


Figure 90: XZ and YZ plane cross-section through middle of feature, comparing with CFD results

Still, the current implementation is quite effective, especially under conditions where the flow does not reach the base and change directions. For instance, a second simulation was run of the third layer only, using the 2nd layer results from the CFD model as the base. The resulting cross-sectional profiles are shown in Figure 91, and they match remarkably well with the CFD simulation. The mean absolute error is now $3.4\text{ }\mu\text{m}$, with the main deviations still resulting from the spread at the edges.

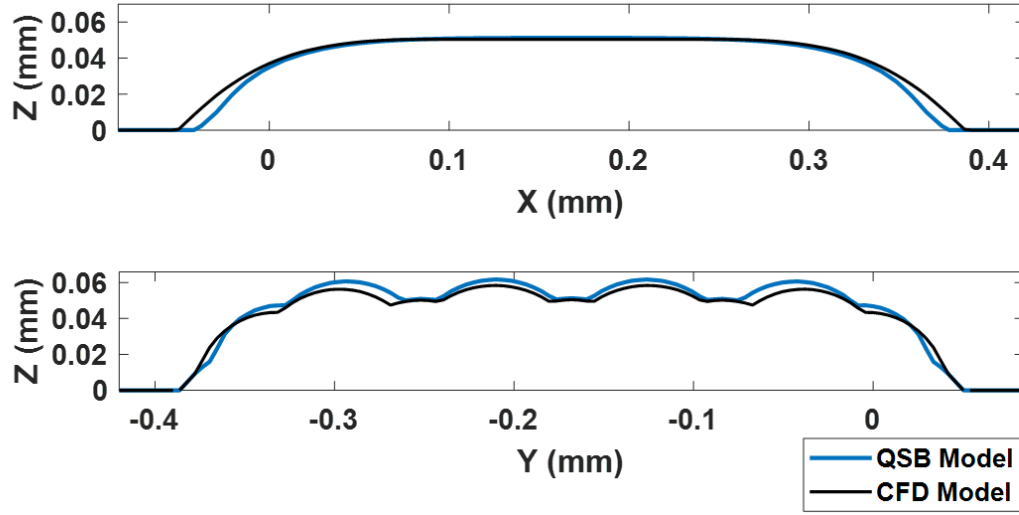


Figure 91: Simulation of 3rd layer only, using CFD results as input

The above cases show the ability of the proposed method to rapidly, and accurately, predict the material jetting process from a single droplet to a multilayer feature. This demonstrates the potential of this method to become a powerful design/manufacturing simulation tool enabling the exploration of both how a given feature design will form under given printing conditions, as well as what printing conditions are needed to achieve a desired design.

5.3 Comparison with Existing Modeling Approaches

In Chapter 3, existing modeling approaches were reviewed. Most particular to the AM material jetting process are the cap-based model of Cohen and Lipson [65], and the Flow-based and Graph-based models from the Mishra Group [66], [68], [82]. The cap-based approach determines the deposition field surface height by assuming each droplet can be approximated as a spherical cap, and the resulting height contribution of a new droplet deposition is simply a linear addition of cap height to the existing surface height, which enable height prediction but does not capture surface rounding at the edges [65]. In the

Mishra et al. models, they develop a deposition model that seek to capture such rounding by calculating the height contribution at a deposition site, as well as its nearest neighbors, as a function of the height difference between all the sites, calling this the flow-based model. Following up on this work, they developed a graph-based approach that uses a similar idea of material flow proportional to the height differences around the deposition site, but it is reported that the graph representation enables the calculations to be linear although uses a finer grid.

In evaluating their models, Mishra et al. investigated a 12-layer thick, $8\text{mm} \times 8\text{mm}$ square, comparing all three approaches (note the cap-based approach was referred to as a “Superposition Model”) with the same feature fabricated on their experimental printing setup, Figure 92a. While the authors have not implemented their methods, the surface data results from their work are available through the supplemental documents of the journal article for direct comparison. Therefore, the same feature fabrication and droplet parameters are simulated with the QSB Model to compare amongst all approaches and with their physical specimen. Their system uses a single nozzle MicroFab printhead. The deposited droplet profile is shown in Figure 92b, having a cap radius of $250\text{ }\mu\text{m}$ and height of $4\text{ }\mu\text{m}$, approximately. Droplet and line spacing are set at $250\text{ }\mu\text{m}$, respectively, where each line is deposited with an individual pass of the printhead. For better surface finish, they have implemented an offset pattern deposition scheme, as shown in Figure 92c, where four layers are needed to complete the pattern.

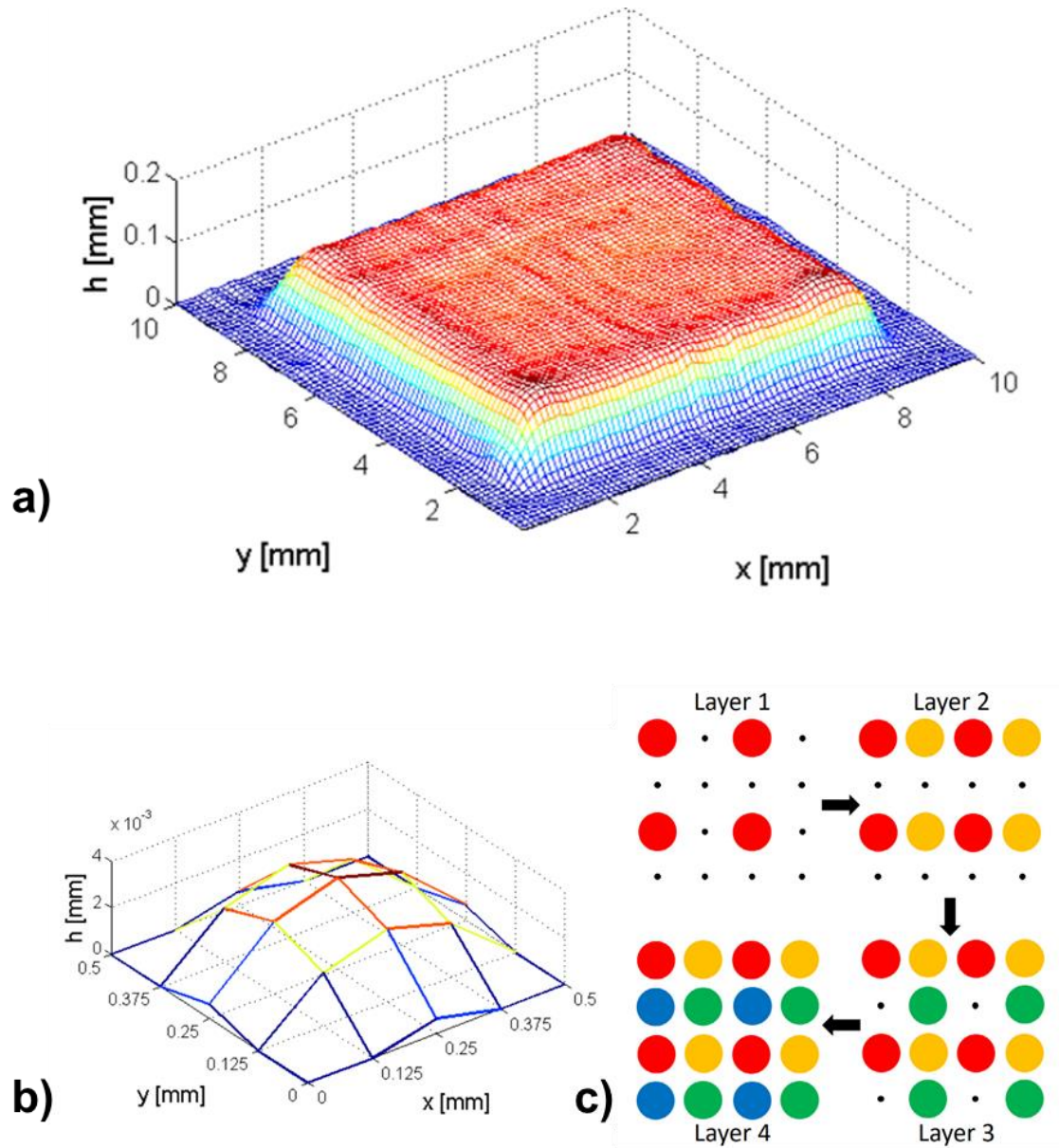


Figure 92: a) Surface profile of as fabricated 12 layer, 8mm-by-8mm square feature, b) cap profile for deposited droplet, c) four-layer deposition pattern

The results of the QSB model simulation are shown in Figure 93a, along with the surface difference between the QSB simulation and the as fabricated results shown above, Figure 93b. Table 11 reports the mean average error for the QSB model, as well as for the other three models. Overall, the QSB model does a good job of predicting the feature shape and shows accuracy improvement over the other three models (19% improvement over

Graph-based model). The greatest deviations occur at the leading and trailing edge along the X-axis. Improvements at this area can be made through a better droplet footprint prediction as well as breaking up the line deposition into smaller segments which will be discussed later.

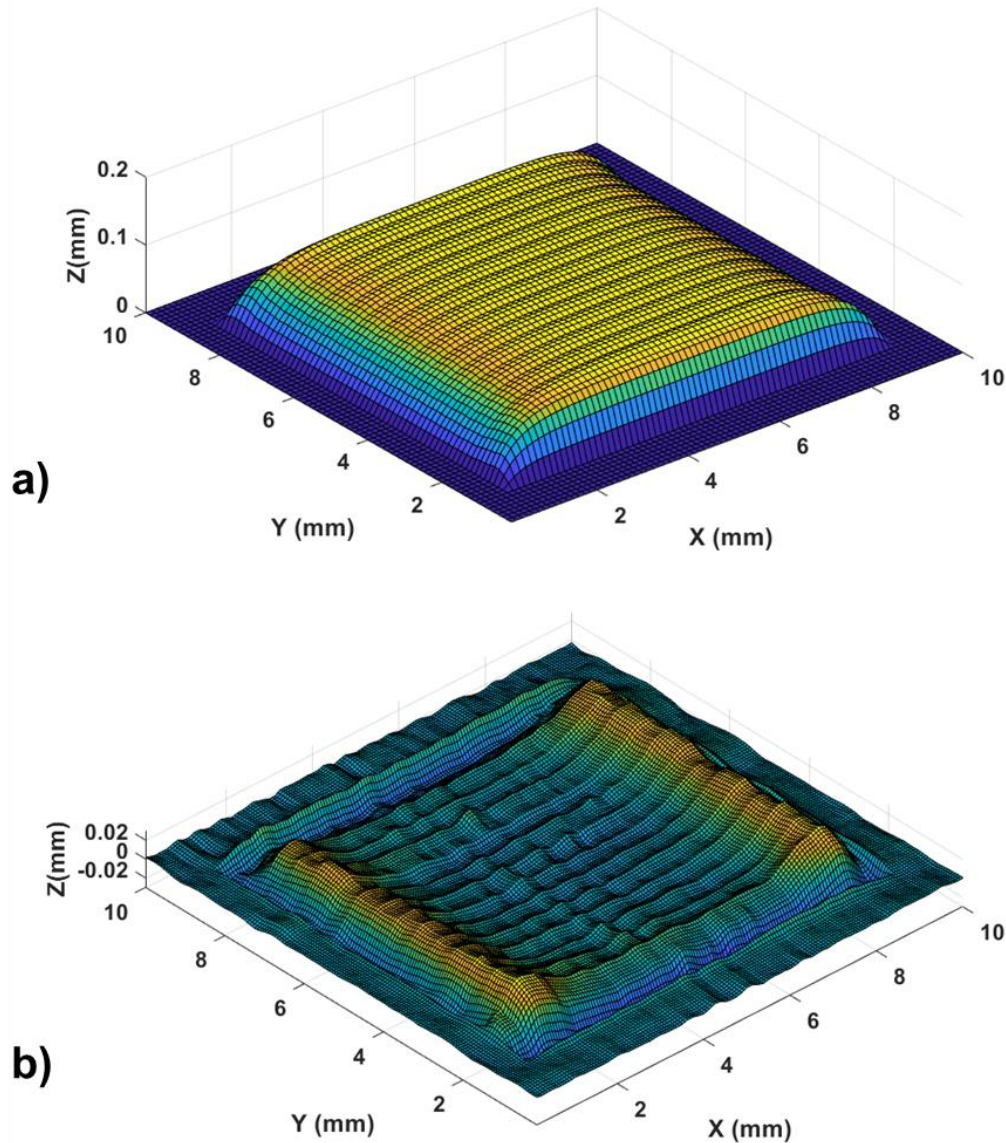


Figure 93: a) 12-layer 8mm-by-8mm square predicted feature using QSB model, b) height map of difference between QSB surface and as-fabricated feature

Table 11: Comparison of Mean average error for the different modeling methods

	QSB Model	Graph-based Model	Flow-based Model	Cap-based Model
Err_{avg} (μm)	7.6	9.4	12.4	9.5

Herein, we have further validated the QSB modeling approach through comparison with an as-fabricated feature, as well as improved surface prediction compared with existing modeling approaches. Additionally, the ability to simulate different droplet parameters and deposition patterns is demonstrated. One possible tradeoff that should be noted is the simulation time. The nonlinear QSB approach took approximately 30 minutes to run on the same desktop machine used for the CFD models in Chapter 4. This is orders of magnitude faster than traditional CFD, which considering the 12,000+ droplets would likely take years and would be unrealistic to simulate. However, while computation times were not given, the other modeling approaches would likely be even faster. Therefore, depending on the desired application, such as real-time feedback control, as targeted by Mishra et al., further consideration is required to determine the tradeoffs between an approach that more directly reflects the printing process and feature accuracy with the computation time required.

5.4 Improvements to the Model

Thus far, the model demonstrations have used a uniform spreading model that is independent from the surface angle at impact with good success. Still, from the literature and the results of Chapter 4, we know droplets impacting on a non-uniform, inclined, and curved surface produces complex and asymmetric spreading, which if better reflected in the model, can increase accuracy and usefulness.

Recognizing the many complexities of modeling, the asymmetric spread on surfaces of near infinite topology, and the fact that spread on incline and non-ideal surfaces remain an active research area, this work seeks a generalized approach in line with the reduced-order modeling of the overall method. In that vein, we adopt an approach based on the work of Amirfazli et al., who studied droplet impact on inclined and moving surfaces [38], [83]. Their work showed that after decomposing the impact velocity into normal and tangential components, the asymmetric spreading that occurs on an inclined surface can be modeled as a combination of radial spreading, modeled as if the impact occurred normal to a flat surface, and tangential translation, given by the product of the tangential velocity and the spread time, as shown in Figure 94. Then the final shape is the outer perimeter of these profiles. As discussed in Chapter 3, there is a wide variety of analytical and empirical models proposed to determine the spreading behavior of the impacting droplet. Selection of such models depends on the droplet conditions under study. Amirfazi et al. used an empirical model fitted to their experimental test data. Similar can be done using numerical simulation results as is the case in this work.

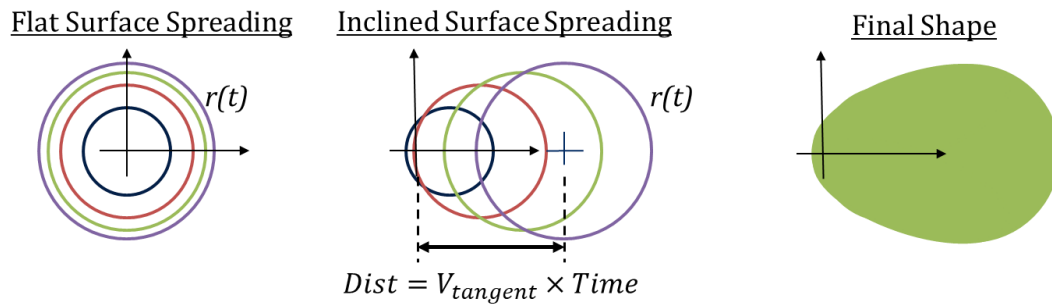


Figure 94: Asymmetric spreading as a combination of radial spreading and tangential translation

The implementation of the proposed approach is illustrated in Figure 95. To begin, we start by finding the droplet impact point and the surface normal. Next, the velocity is

decomposed into normal and tangential components. Then, the droplet profiles are drawn incorporating both the radial spreading and tangential translation. Lastly, the final droplet perimeter is calculated as the convex hull of the spreading profiles.

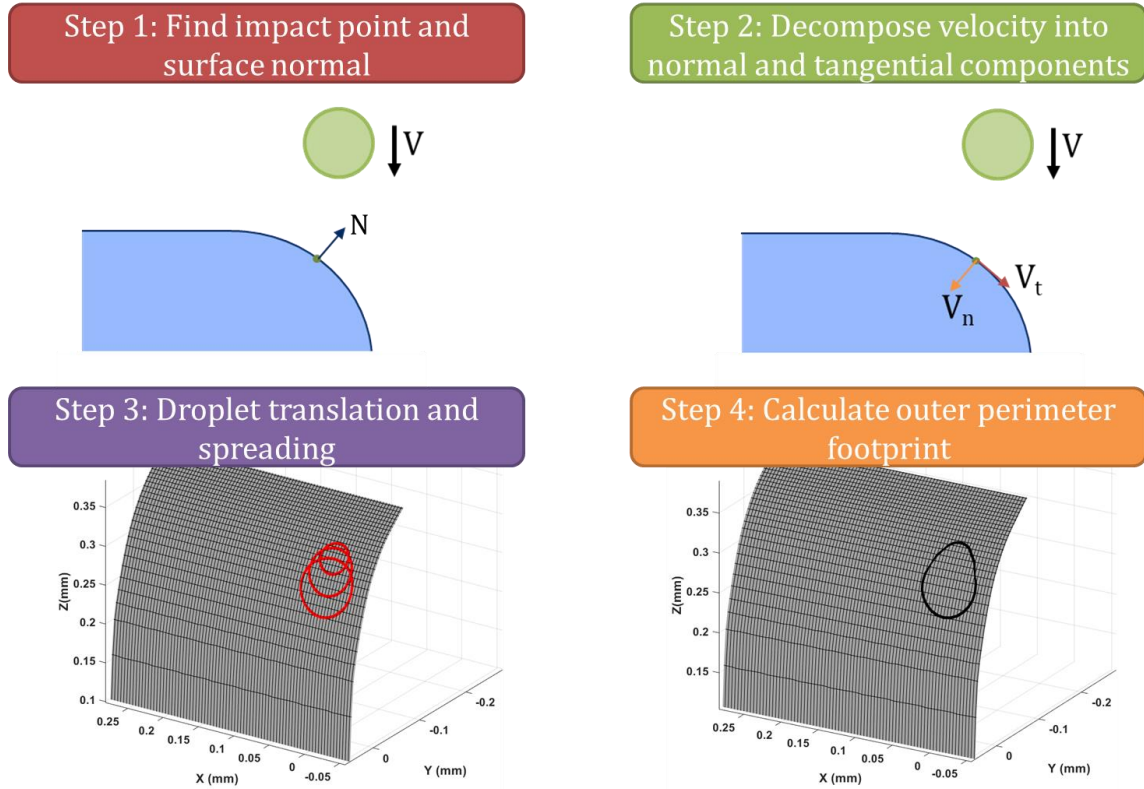


Figure 95: Implementation of asymmetric spreading and boundary determination

In addition to determining the asymmetric droplet boundary at the feature edge, a second challenge to modeling deposition near the edge is identified. For the linear thin film approximation to maintain reasonable accuracy, the solution plane and the boundary plane must keep a low angle of difference. Otherwise, at steeper angles of incline, non-physical deformations occur due to the relative plane of projection, as shown in Figure 96.

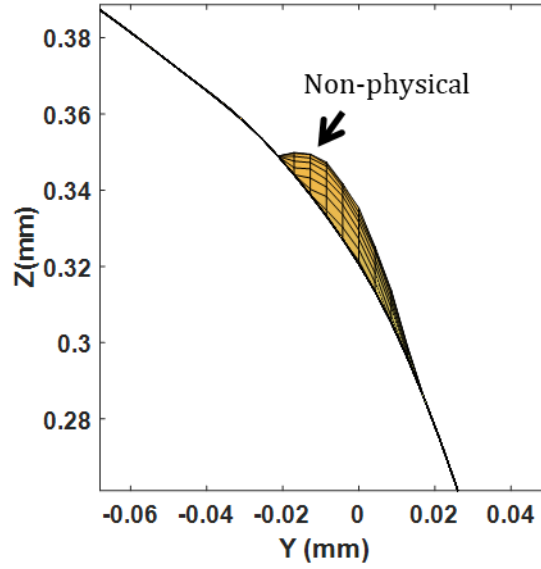


Figure 96: Non-physical solution results due to steep incline relative to solution plane

To correct for this problem, we propose a coordinate transformation to a local reference frame to solve for the surface in areas of incline then a conversion of the results back to the global reference frame. The local coordinate transformation process for the single droplet perimeter above is shown in Figure 97. First, a new local coordinate system (X' , Y' , Z') is established based on a plane of best fit with respect to the boundary. Next, the coordinates deposition boundary as well as the feature surface within the boundary region are converted to the local coordinate system. The deposition surface is then solved using the same approach as before. Lastly, the results are converted back to the global coordinate system and added to the existing surface. While illustrated here for a single droplet, the same general approach is used for multiple coalesced droplets in a line near the edge.

Define local coordinate system X', Y', Z'

Solve w.r.t X', Y', Z'

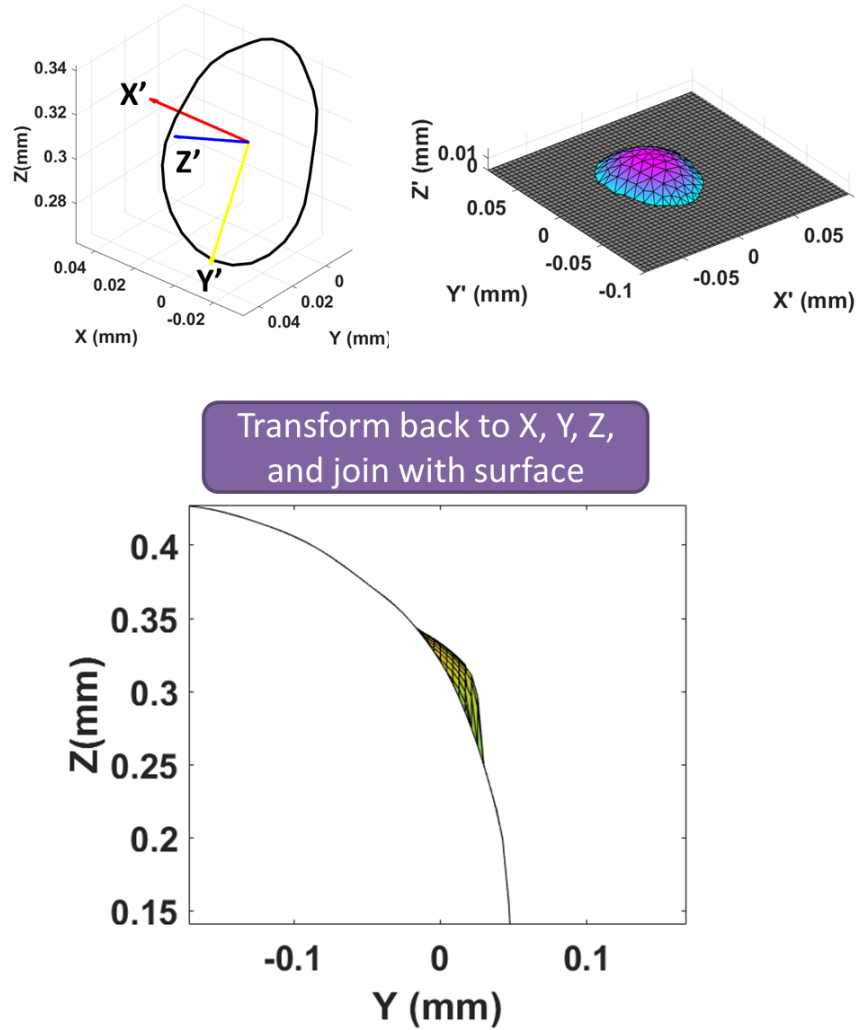


Figure 97: Process for converting to local coordinate system to solve for fluid surface

To illustrate the accuracy improvement of these approaches, the 3-layer, 9x9 pixel extruded square is revisited. Figure 98 shows the XZ and YZ cross-sections of the Improved QSB method compared with the CFD results of Chapter 4. The results show a close match to the CFD results, and a clear improvement using the asymmetric spreading, having a mean absolute error of 2.4 μm compared with 7.8 μm previously.

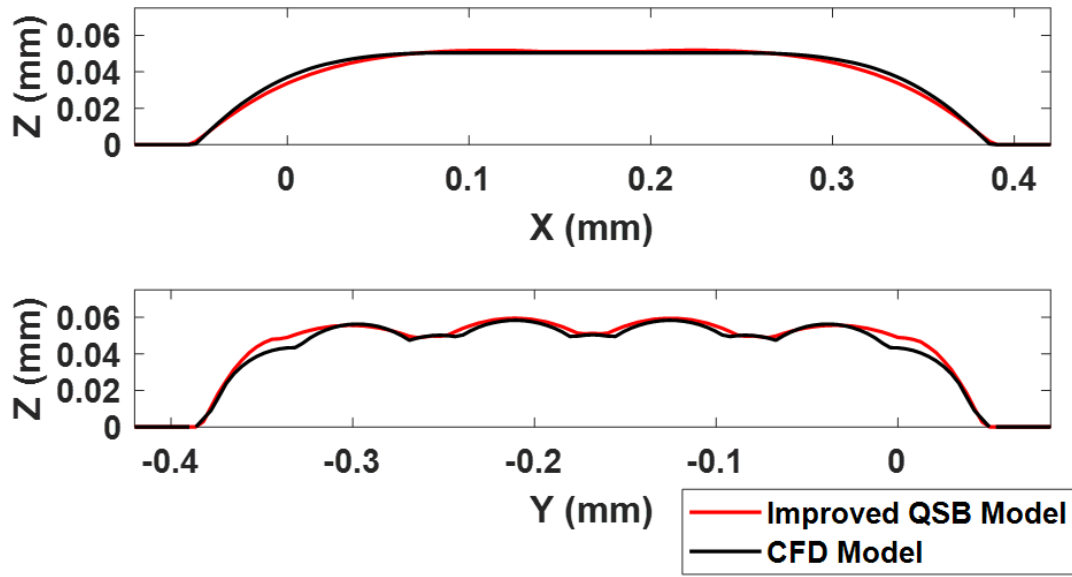


Figure 98: 9x9 pixel feature, XZ and YZ plane cross-section through middle of feature, comparing Improved QSB with CFD results

5.5 Modeling Features

Using the Quasi-static Boundary-based Method, modeling meso-scale feature fabrication is demonstrated. The model parameters are based on the Objet260 Connex printer specifications used in Chapter 4, and above in this chapter, with a reported 600 dpi resolution in the x and y axes resulting in 42.3 μm droplet and line spacing. To achieve this resolution, the system requires four deposition passes and the nozzle spacing is such that during any single pass fluid from two adjacent nozzles does not overlap or interact. For this study, a 30pL droplet with a 45° static contact angle is used.

Four features are simulated, shown in Figure 99: a 1x1mm extruded square, the extruded square with a 0.3 mm circular hole, the extruded square with a 0.3mm square hole, and a 1x2mm extruded rectangle with a 0.3x1.5mm gap. Each case is simulated for 10 layers of deposition, with no layer leveling steps.

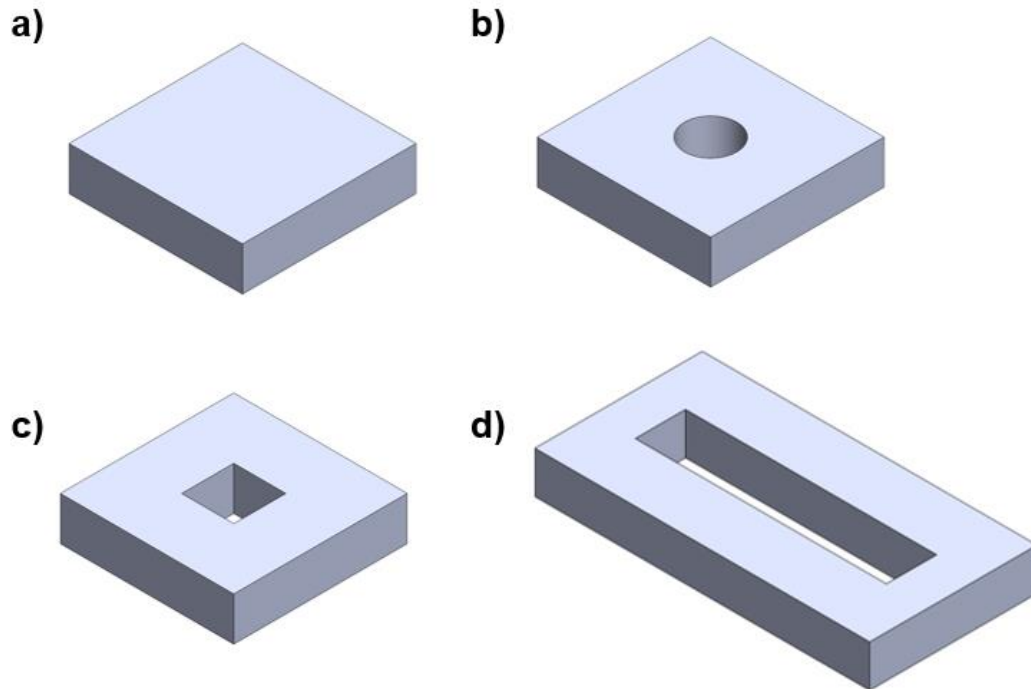


Figure 99: Illustration of features, a) extruded square, b) square with circular hole, c) square with square hole, d) rectangle with gap

The general process followed is shown in Figure 100. First the feature geometry is sliced, and the layer boundary profiles are defined. For the simple features shown herein this is a straightforward process as the boundary profile is simple and the same for all layers. For more complex shapes, there are several opensource programs, such as Slic3r, that are easy to use for layer slicing, but would require integration. The second step is to identify the deposition locations. For each layer the edge boundaries are overlaid the build area deposition grid, which is defined based on the printing resolution being simulated (here 600x600 dpi). Matlab's built-in "inpolygon" function is then used to identify the deposition sites inside the feature boundary. With the deposition sited determined, the QSB model is executed as described above, to yield the final predicted feature shape.

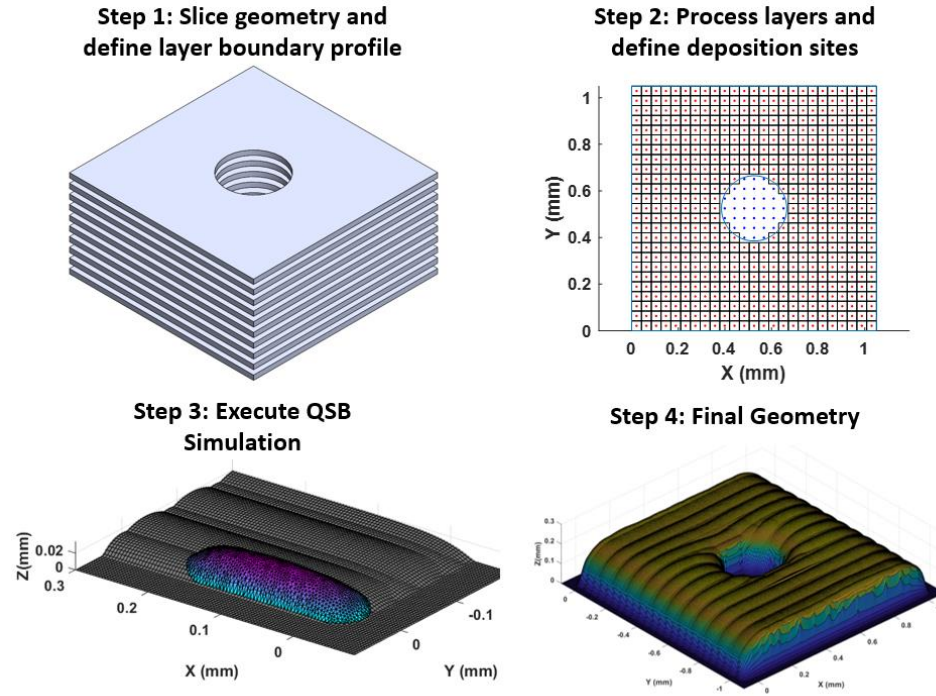


Figure 100: Feature simulation process steps

The resulting surface profiles for each simulated feature are shown below in Figure 101- Figure 104. The computational time for each feature using the linear and non-linear form is shown in Table 12 along with the time per droplet and time per discrete deposited line.

Table 12: Count of droplets and deposition line for example features and simulation times for linear and non-linear QSB method

Feature	No. Drops	No. Lines	Linear QSB			Non-linear QSB		
			Time (sec)	Time per Drop (sec)	Time per Line (sec)	Time (sec)	Time per Drop (sec)	Time per Line (sec)
Square	6250	250	569	0.09	2.28	7117	1.14	28.47
Circular Hole	5880	320	591	0.10	1.85	8172	1.39	25.53
Square Hole	5760	320	584	0.10	1.83	8148	1.41	25.46
Rectangle with Gap	9800	840	1298	0.13	1.55	16232	1.66	19.32

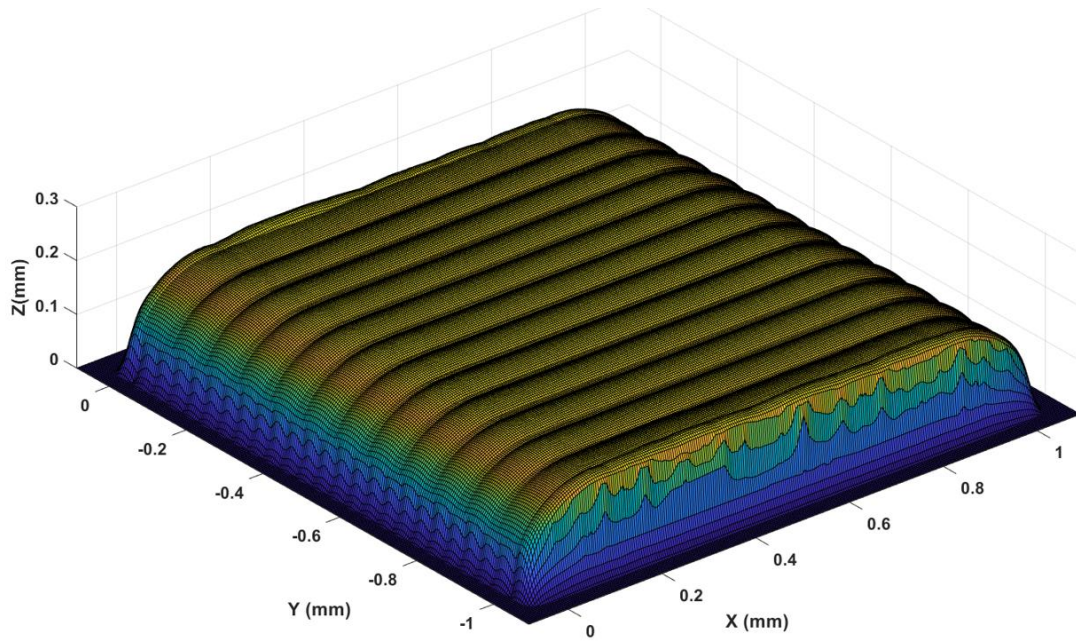


Figure 101: Simulation results for 1x1mm extruded square

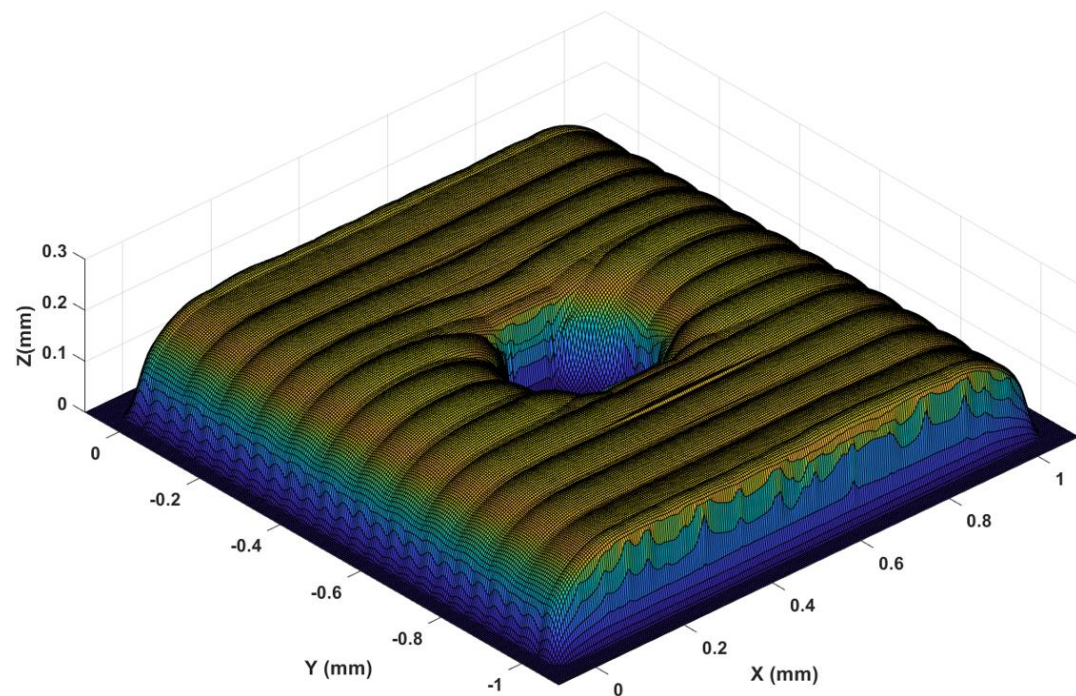


Figure 102: Simulation results for extruded square with a 0.3 mm circular hole

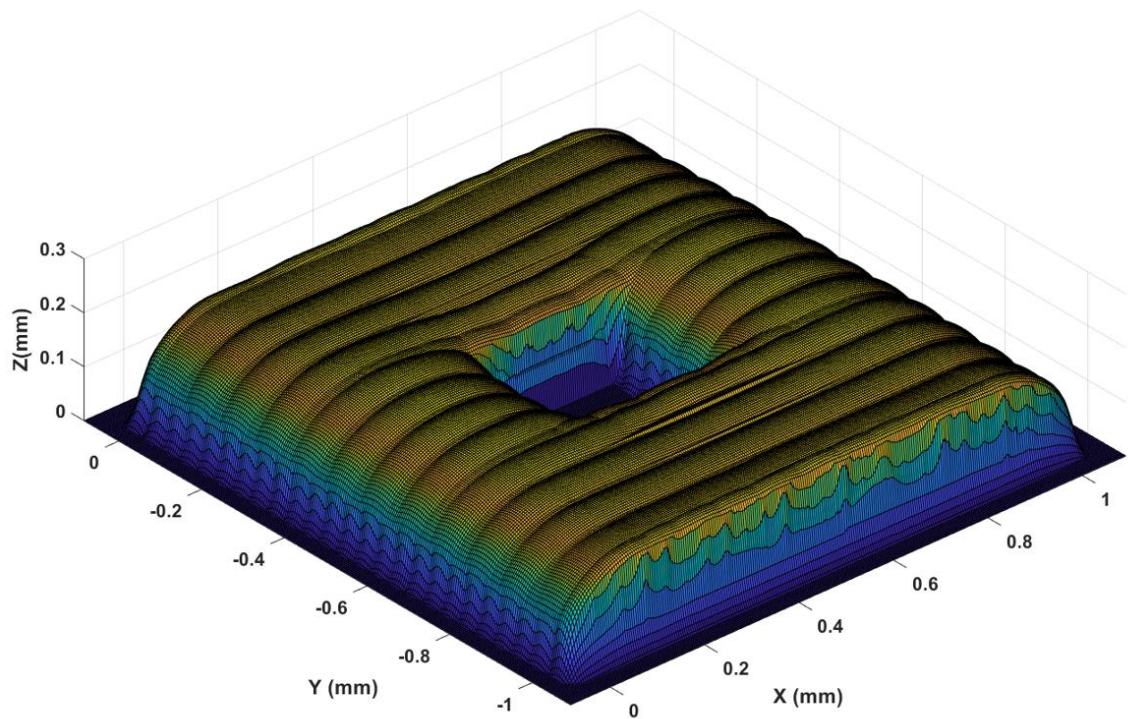


Figure 103: Simulation results for extruded square with a 0.3 mm square hole

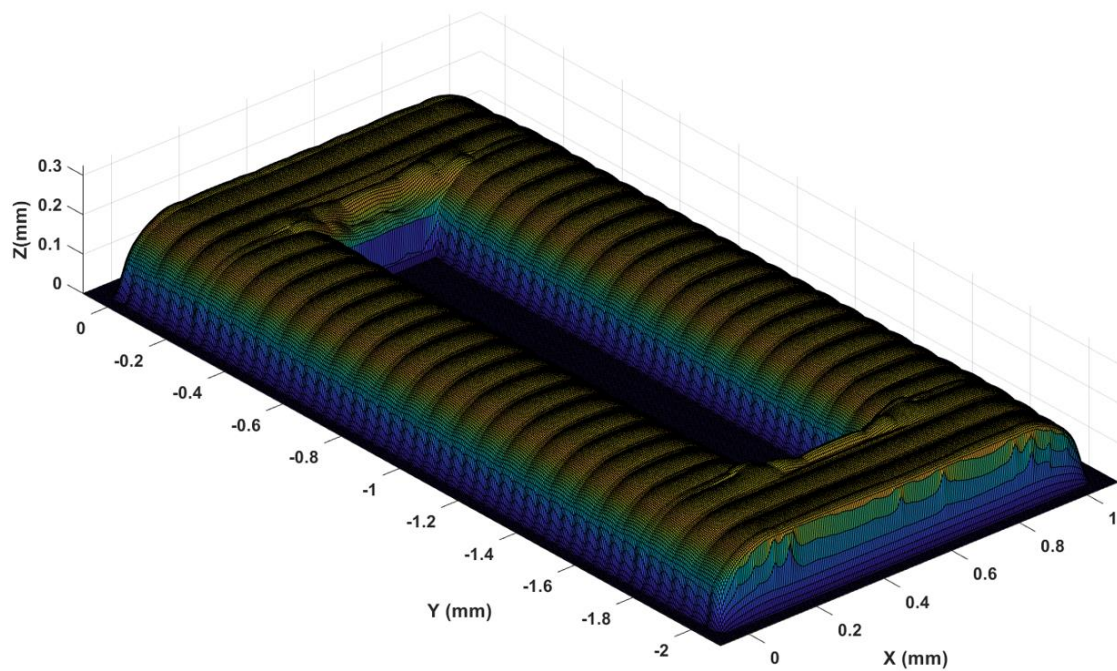


Figure 104: Simulation results for 1x2mm extruded rectangle with a 0.3x1.5mm gap

These results show similar feature deformations (i.e., edge rounding) to what was observed in Chapter 2, and further demonstrates the success of the QSB approach to model and predict material-jetting mesoscale feature fabrication. Table 12 continues to support the low computational expense of this approach with the ability to simulate thousands of droplets in minutes to hours, depending on the solution form selected (i.e. linear vs. non-linear). Table 12 also shows the influence of both the number of droplets but also the number of discrete lines on the total simulation time. For instance, the square extrusion has more simulated droplets than the two squares with holes but an overall shorter simulation time. This is due to the fact that the square has less simulated lines than the squares with holes, as in the region with a hole there are lines to be simulated on each side of the hole, and the QSB method solves for the surface at the line level.

The layer-by-layer feature evolution is shown in Figure 105, which plots the XZ-plane cross-sectional profiles through the middle of the extruded square and the gap features. We see shape deformations at the exterior and interior corners, specifically convex and concave rounding. Looking at the layer evolution, the profile starts convex for the first 3-5 layers, where layer spread overflows the previous layer edge, but then an inflection point appears as the vertical wall emerges, due to there being a finite extent of spread possible and the new layer edge recedes relative to the prior layers, matching what was seen in Figure 17 for the fabricated parts. This is significant towards our understanding of the dominant causes of the corner rounding observed in Chapter 2, as this model only includes the effects of droplet spread and quasistatic coalescence, and not the other theorized factors such as cure related shrinkage or leveling overflow.

Additionally, after the first few layers, the feature evolution becomes much more static layer after layer. This is especially true for layer height evolution on the interior flat away from the edge. For instance, consider the height increase at the center of the extruded square for each layer, Layer Height = {15.9, 16.9, 18.2, 18.4, 18.6, 18.6, 18.6, 18.6, 18.6, 18.7 μm }, where the layer height is steady after the first 4 layer. The computations could leverage this fact and only simulate the areas with proximity near the edge and then assume a fixed height increase away from the edge.

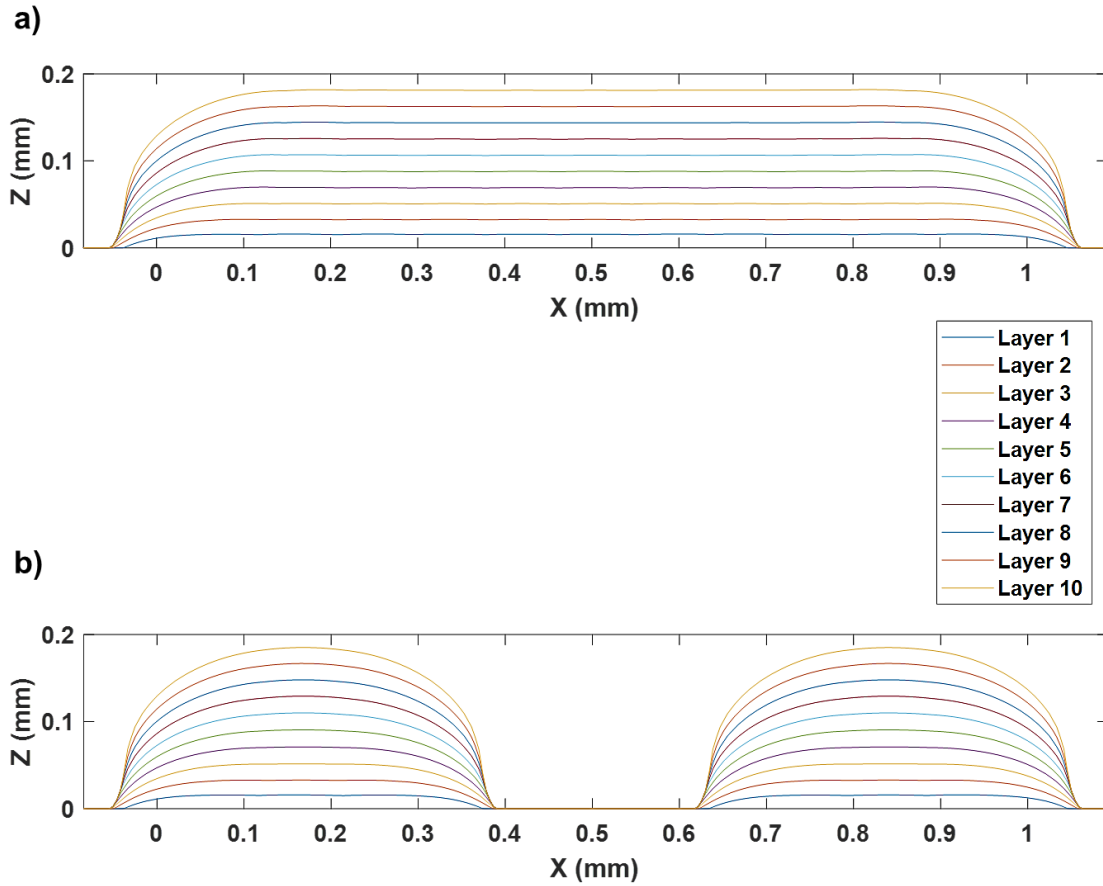


Figure 105: XZ-plane cross-sectional profiles through: a) the middle of the extruded square, b) the middle of the gap feature

In addition to the deformations at the top and bottom edges of the features, the characterization parts of Chapter 2 also showed significant rounding at interior corners of

square features. Figure 106 plots the cross-sectional profile of the square hole at the bottom and top of the modeled feature. While some rounding of the feature corner is present in the top cross-section, the middle and bottom show no rounding like the as-fabricated features, revealing a limitation of the current model. We can thus conclude that the dominant driving force for such corner rounding is more than the droplet impact driven spread. Considering this, the next most likely driver is capillary driven flow that occurs between deposition and curing. Adding such flow to the current model is possible but would require multiple time-dependent boundary evolutions. An estimate for the contact line movement relationship, such as the Hoffman-Tanner-Voinov relation, is also needed and would significantly increase the computational overhead [58]. Expanding the model in this way is recommended for future work.

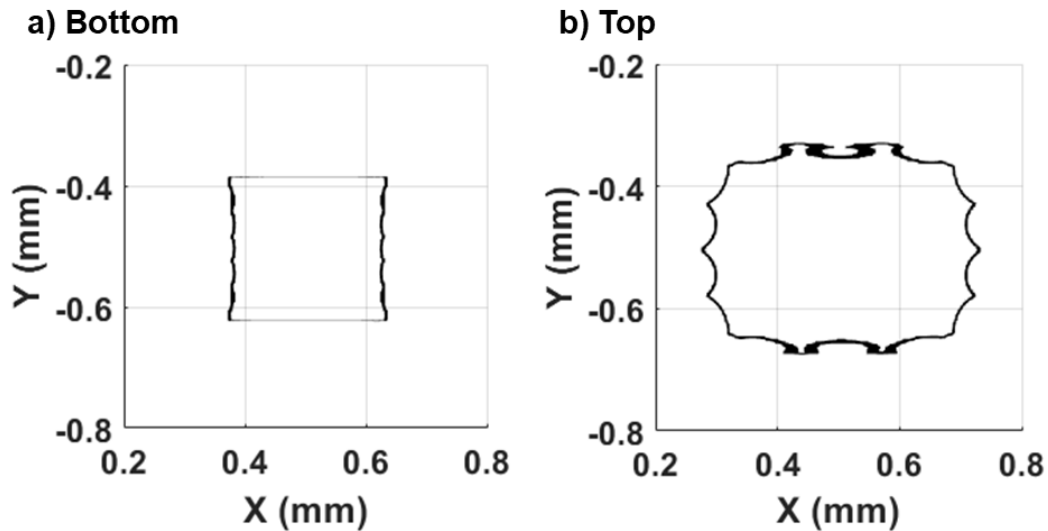


Figure 106: XY-Plane Cross-sectional profile of square hole at: a) bottom of feature (middle of layer 1), b) top of feature (middle of layer 10)

5.6 Summary

In this chapter, a novel Quasi-static Boundary-based method was developed and demonstrated, answering Research Question 2.2: How can the material jetting process be

modeled to rapidly predict the as-manufactured shape of mesoscale features? The key assumption of this approach is that for the material properties and timescales of interest for the MJ process, with a reasonable prediction of the droplet footprint after the spreading phase, the final fluid surface can be determined without having to solve the full fluid problem which is both time consuming and complex. The general framework was developed, then validated through comparison with prior literature on high-fidelity modeling as well as the modeling presented in Chapter 4. Additionally, the method was compared with other MJ modeling approaches found in literature and shown to predict the as-fabricated surface most accurately when compared to the physically printed feature, while maintaining computational costs orders of magnitude faster than the high-fidelity approaches. Since the effectiveness of the model is built on defining the deposited droplet footprint, an improved approach for predicting the asymmetric spreading phenomenon that occurs for impact on an inclined surface was presented. The model was demonstrated using representative features, like those explored in Chapter 2, which consisted of thousands of simulated droplets. These simulated mesoscale features showed similar deformations to the physical features printed, like rounded edge deformations, suggesting that the driving cause is likely the asymmetric deposition spread near the edge. Interior corner rounding was unfortunately not captured well by the current method, indicating another physical phenomenon is likely the root cause, such as capillary spreading. If predicting such deformations are critical to the application, then expanding the current approach to include a capillary boundary evolution is possible.

CHAPTER 6. DESIGN AND MANUFACTURABILITY OF NOVEL PRESS FABRIC MEMBRANES

In this penultimate chapter, we pivot away from material jetting-based additive manufacturing to highlight a separate area of research investigation, namely the design and analysis of paper machine press fabrics. While, treated independently herein, this work helped motivate the deep dive found in the preceding chapters.

6.1 Review of Paper Machine Pressing and Press Fabric Design

6.1.1 Introduction

Paper and related bio-products are ubiquitous in daily life and have played an essential role in societal development from communication to sanitary products to the current explosion of packaging to support e-commerce. To maintain this role, the industry must continue to innovate and meet the ever-increasing demands to produce economically and be more environmentally friendly. As the paper industry is the country's 3rd largest energy user, reducing energy use is a significant area for needed innovation [12].

Figure 107 shows a representative rendering of a modern paper machine, highlighting the forming, pressing, and drying sections. While highly complex, in essence, much of the paper machine's objective is the removal of water from the stock to form the fiber-based sheet. The amount of water at any stage of the process is characterized by the consistency (dry solids content): the ratio of the mass of fiber and the mass of fiber plus water. For a typical process, the initial consistency is ~0.5-1% and will finish at greater than 90%.

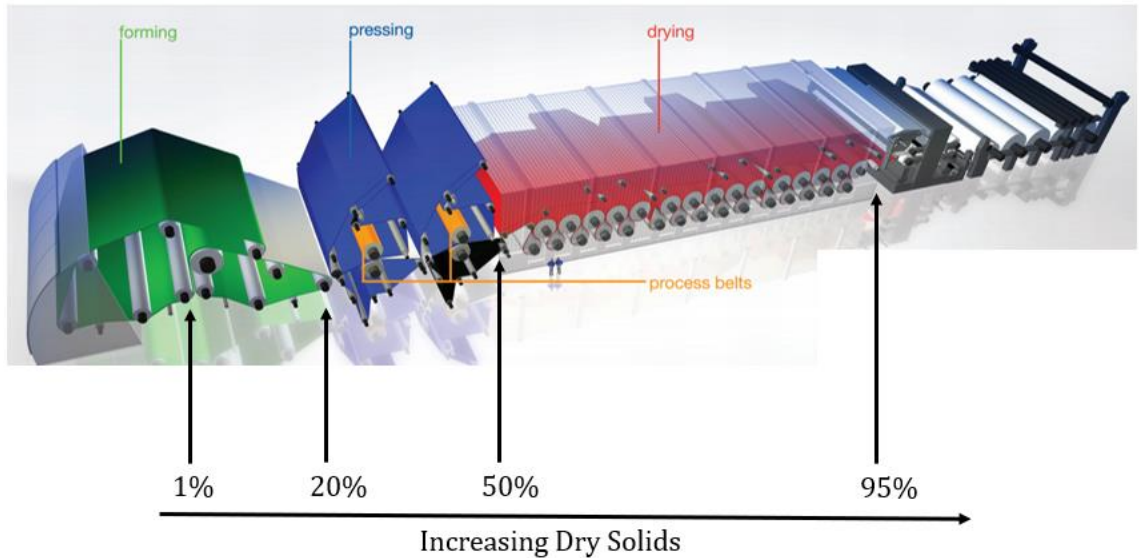


Figure 107: Overview of paper machine

Of the process steps, one of the main energy consumers is the dryer section, accounting for approximately 55% of the energy consumed in the papermaking process. This consumption is greatly influenced by dry solids content exiting the press section, where a 1% increase in outgoing press solids correlates to roughly a 4% decrease in dryer steam consumption or a corresponding increase in production speed [84]. It's estimated that enabling the exiting press section dry solids to increase from 50% to 65% would result in saving as high as \$250 million for the industry annually. For that reason, considerable development has taken place to improve dewatering efficiency in the press section. One such pursuit is the investigation into novel press fabric designs.

6.1.2 Design and Characterization of Press Fabrics

Press fabrics have an important role in the performance of the press section. Press fabrics are designed to (1) remove and receive water from the sheet, (2) build sheet properties, (3) convey the sheet through the press section and to the dryer section, and (4) power un-driven rolls in the machine position. Press fabric construction can be quite varied,

changing to accommodate different objectives related to stiffness, endurance, dewatering characteristics, and quality. Early press fabrics, referred to as felts, were constructed of wool fibers packed to form a dense sheet similar to what one might find today in a craft store under the same name. Modern fabrics have transitioned to 100% synthetic materials, commonly nylon, with the simplest variant comprising a single woven base structure with monofilament yarns in the machine and cross directions, and a denser batt layer which has been needled together. Other conventional variants build in complexity with multilayer base structures, nonwoven layers, and endless combinations of different yarn types and diameters [84]. Example fabric designs are shown in Figure 108

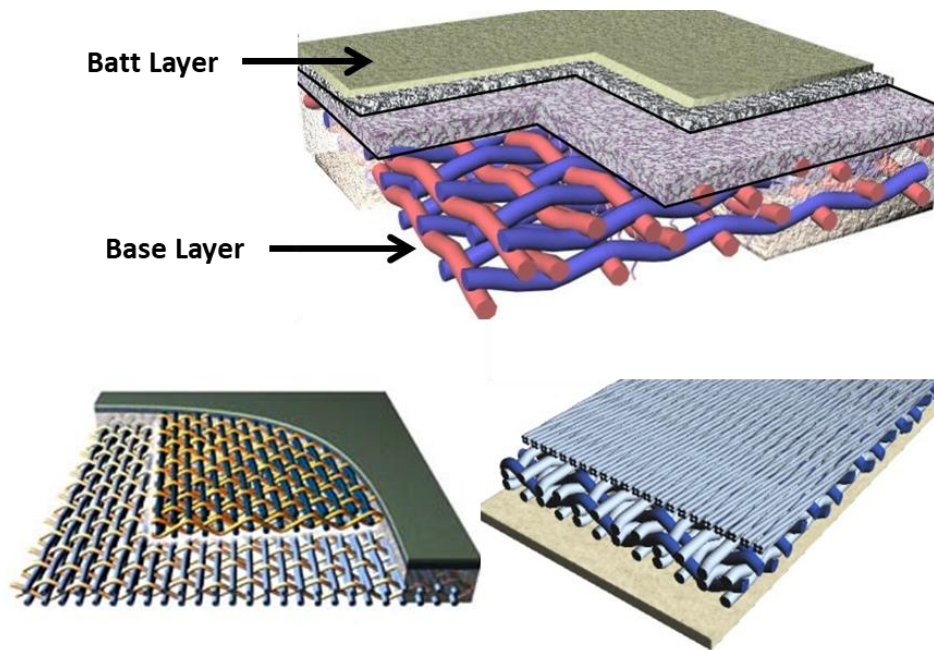


Figure 108: Examples of conventional press fabrics

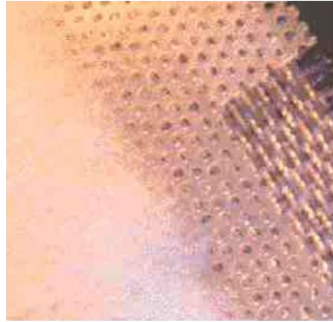
Even though many design variations exist, basic characterization of press fabrics is only based on a few properties. Tappi standard 0404-20 details the characterization of fabrics using basis weight, air permeability, void volume under loading, and pressure uniformity

[85]. There are also standards for characterization of fabric caliper (thickness) [86], as well as porosity [87].

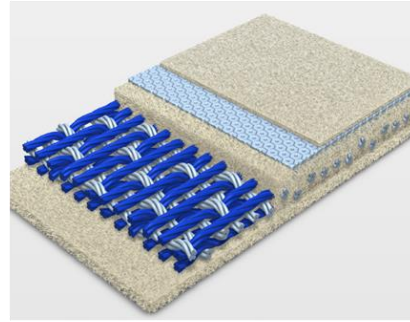
While Tappi characterization focuses only on bulk parameters, several studies investigated the press fabric structure in more detail. Helle and Forseth studied the influence of batt fiber size and layer thickness on press performance, while using an identical base [88]. They found that finer batt surface fiber and a thicker batt layer improved press solids. The improved press solids were attribute to surface pressure uniformity, which has been further studied quite extensively [11,12,13]. Xu et al. (2012) studied the effects of various base layers and found that non-woven structures resulted in better dewatering properties [92]. They attributed the results to higher pressure uniformity and reduced rewet. Based on the literature, pressure uniformity is extremely significant for press fabric performance.

Another significant challenge for press fabric design is how to prevent rewetting, which can result in a severe reduction in press solids as previously mentioned. While little research literature exists on how fabrics can be designed to combat rewet, several constructions have been proposed in patent literature, including soft polyurethane film layers with elliptical holes, as well as separate belts with conical holes on which the press fabric is placed. Table 13, summarizes the relevant patent literature on these proposed designs. Beyond these patents, no technical literature on their design or performance was found in the literature, and it appears only Albany and Voith have advertised concepts in trade magazines or marketing material, but are no longer listed on their sites [93].

a) Albany AperTech



b) Voith Evolution



c) Voith Revolution

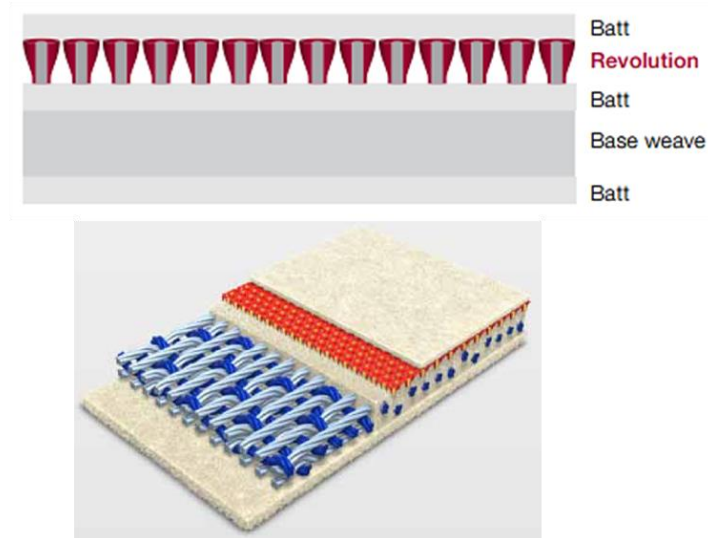


Figure 109: Press fabrics with polymer layers, a) Albany AperTech, b) Voith Evolution, c) Voith Revolution

Understanding the impact of membrane layers and how they should be designed and characterized is a critical research need for the paper community. This need is reiterated by Agenda 2020, an industry partnership tasked with identifying high priority challenges facing the pulp and paper industry. In a recently released technology roadmap, they list fabric design as one of the most critical areas for research and development, and two of the nine priority research projects focus specifically on structures and membranes that have adaptive permeability or promote unidirectional flow [12].

Table 13: Review of press fabric patent literature

Title	Description	Patent	Year
Anti-rewet membrane for an extended press nip system	High resistance layer acts as a barrier between paper and felt. Extended nip press is used to increase residence time under pressure, the expansion time is then considerably shorter than the compression time. The barrier layer inhibits flow during the expansion. Another variant includes a combination of a hydrophobic barrier layer and a hydrophilic fabric underneath	US 3,840,429 [94]	1974
Wet press fabric to be used in papermaking machine	A high resistance barrier layer is placed on the far side of the fabric away from the paper. The layer is suggested to act as a seal which causes vacuum in the fabric during expansion to counteract the vacuum in the paper sheet thus reducing rewet. The barrier layer is envisioned as very fine batt fibers, a perforated film, or sintered polymer particles.	US 5,232,768 [95]	1993
Anti-rewet felt for use in a papermaking machine	Fabric for use with an air press. A perforated layer is incorporated into the fabric to act as a barrier to resist rewet. Described as a polyester film with perforations,	US 6,616,812 [96]	2003
Papermaking Press Felt	Incorporates a rewet prevention layer near the surface of the fabric. The layer contains horn shaped perforations which are generated during the needling process. The layer is suggested to be 10-30 um thick. Patent reports comparison of fabric with and without barrier layer and suggests that rewet is present without prevention layer and inhibited with prevention layer.	US 6,716,318 [97]	2004
Anti-rewet press fabric	Barrier layer is incorporated into the fabric. The layer has cylindrical or conical holes. The conical shape is described to prevent rewet by restricting flow during expansion.	US 7,128,810 [98]	2006
Anti-rewet transfer belt	A belt with a surface permeable to air, but impermeable to water is used to inject air into the sheet during pressing. The injected air is expected to prevent suction in the sheet during expansion and inhibit rewet.	US 2008/0176690 [99]	2008

6.2 Press Fabric Design Exploration

6.2.1 Objective

The objective of this research is to investigate flow in press fabrics membrane layers and understanding how membrane hole size, shape, and pattern affect flow and dewatering potential. Simply put, this work provides a first order approximation for how hole design affects flow and what kind of designs could be beneficial in press felt membrane layers.

6.2.2 Method

Commercial CFD software (Fluent) is used to model steady-state flow through different geometries. Two-dimensional and three-dimensional CFD simulations are implemented. An example of the simulation domain and associated boundary conditions are shown in Figure 110.

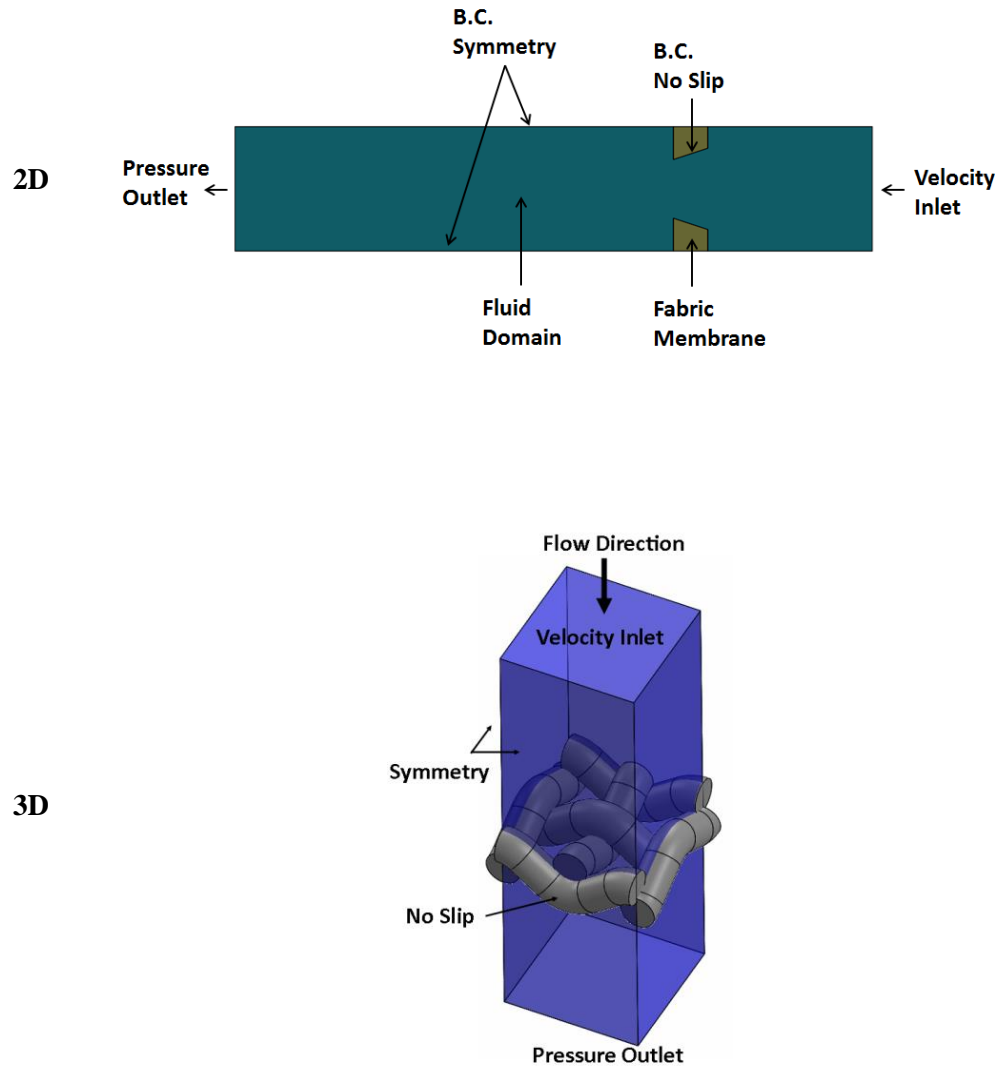


Figure 110: Simulation domain and boundary conditions

Flow in the fluid domain is assumed to be incompressible and single phase. For this study fluid, properties are that of liquid water at ambient conditions. Fluid is assumed to enter the simulation domain through a velocity-inlet boundary condition, pass through the membrane constriction, and exit from a pressure-outlet boundary condition. Symmetry boundary condition is used for the side of the computational box as the hole pattern is assumed periodic. Flow on the fabric/membrane surface is assumed to be a no-slip

boundary condition. The fluid domain is meshed with hexahedral and tetrahedral elements, along with boundary layer inflation elements. Mesh independence studies are run on both 2D and 3D geometries to ensure results are independent of meshing.

Using these constraints, different membrane holes are investigated. Most membranes envisioned are uniform patterns of a single hole; thus, only a single hole must be simulated. To evaluate different hole geometries, pressure drop through the centerline is calculated for a given inlet flow velocity. Designs are simulated in both the desired flow direction as expected during pressing and in the reverse direction representative of rewet. Ideal designs should have a lower press direction pressure drop and a higher rewet direction pressure drop, respectively.

6.2.3 Results

A wide range of possible geometries and features are considered. Figure 111 illustrates several varieties, highlighting differences in layer construction, hole shape, edge condition, and internal geometry. 2D simulations are initially run to gain a baseline understanding of the flow, then expanded to full 3D simulations. For the sake of brevity, only the 3D simulations are presented herein, as these results confirmed the results of the 2D simulations. Namely, thinner membranes and rounded entrance edges lower pressure drop in the forward flow direction; additionally, undercuts at the backside edge increase pressure drop in the reverse flow direction. These observations along with others are now discussed.





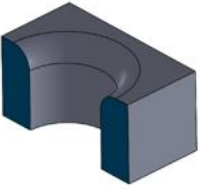

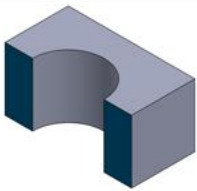
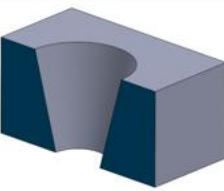

	Design Variations		
Construction			
Shape/Edge			
Internal Shape			

Figure 111: Overview of proposed design variations

The effect of membrane thickness as well as hole shape is observed in Figure 112. Cases 1 and 2 feature a circular hole ($\varnothing = 0.564\text{mm}$), while cases 3 and 4 feature a square hole ($0.5 \times 0.5\text{mm}$). Both geometries have equal open area (0.25 mm^2), and each geometry tests one case that is 1 mm thick and another that is 0.5 mm thickness. It is seen that hole shape has a minor effect on pressure drop with the circular hole having the slightly lower pressure drop of the two, regardless of thickness. Membrane thickness is more significant with both geometries showing a 10% reduction in pressure drop when the thickness is reduced from 1 mm to 0.5 mm.

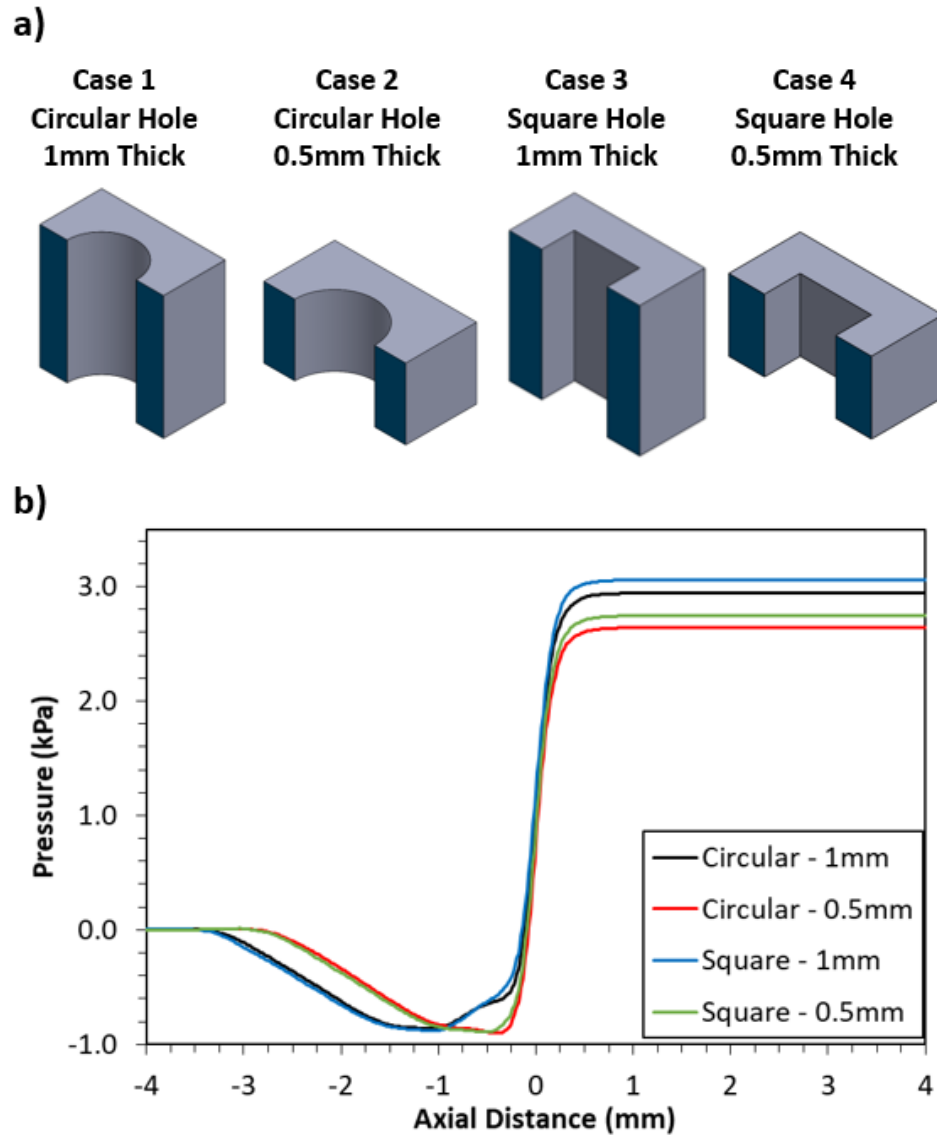


Figure 112: Simulation results for varying hole shape and membrane thickness

Cases 5 and 6 show the significance of edge features, such as rounding and undercuts, as shown in Figure 113. Such features move away from equal pressure drop in the forward and reverse direction, helping to produce a more one directional membrane where forward pressure drop is less than reverse. This can be quantified by comparing the percent increase in reverse pressure drop with the forward pressure drop. Case 5 features a rounded ingoing edge which decreases the pressure drop compared with a straight circular hole and results in a membrane with a 12% higher reverse flow resistance than

forward flow. Similarly, outgoing edge features like the undercut used in Case 6 can be significant because incorporating the undercut resulted in 13% higher resistance to reverse flow than forward flow.

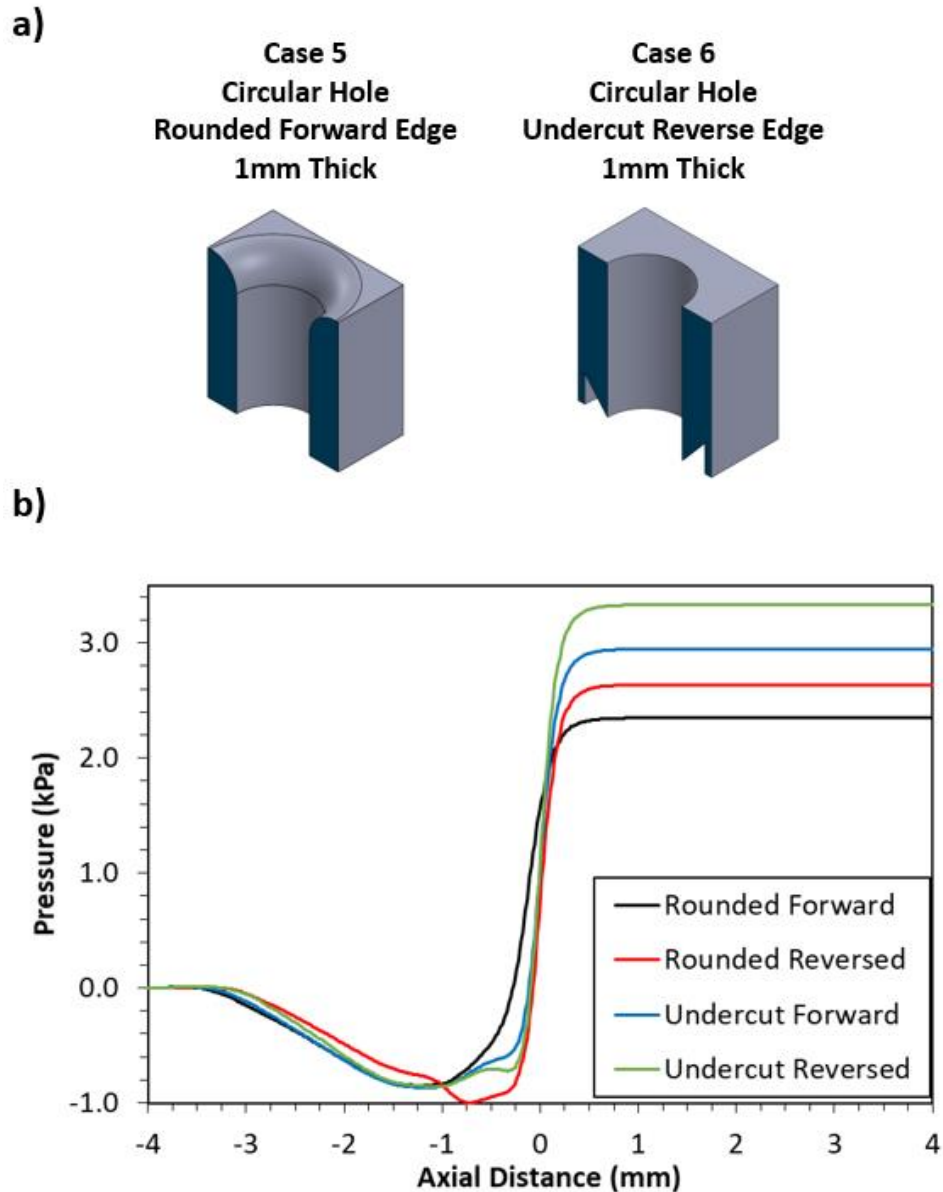


Figure 113: Investigation into effect of edge rounding and edge undercut

While such simple features show promise for the mid-layer membrane tested alone; this work recognizes that in application, a batt layer may affect their effectiveness. To test the

effect, two cases (Case 7 & 8) were run with small batt layers to determine if the benefits are still observed, see Figure 114: one featuring the Circular hole (Case 1) with batt which serves as the baseline reference, and the other a Circular Hole with Undercut (Case 6) and batt. A comparison of these two cases shows a 13% higher resistance for the undercut case which matches the increase in resistance when no batt was present. While further study is required, this result helps to validate the potential use of these designs in a composite felt.

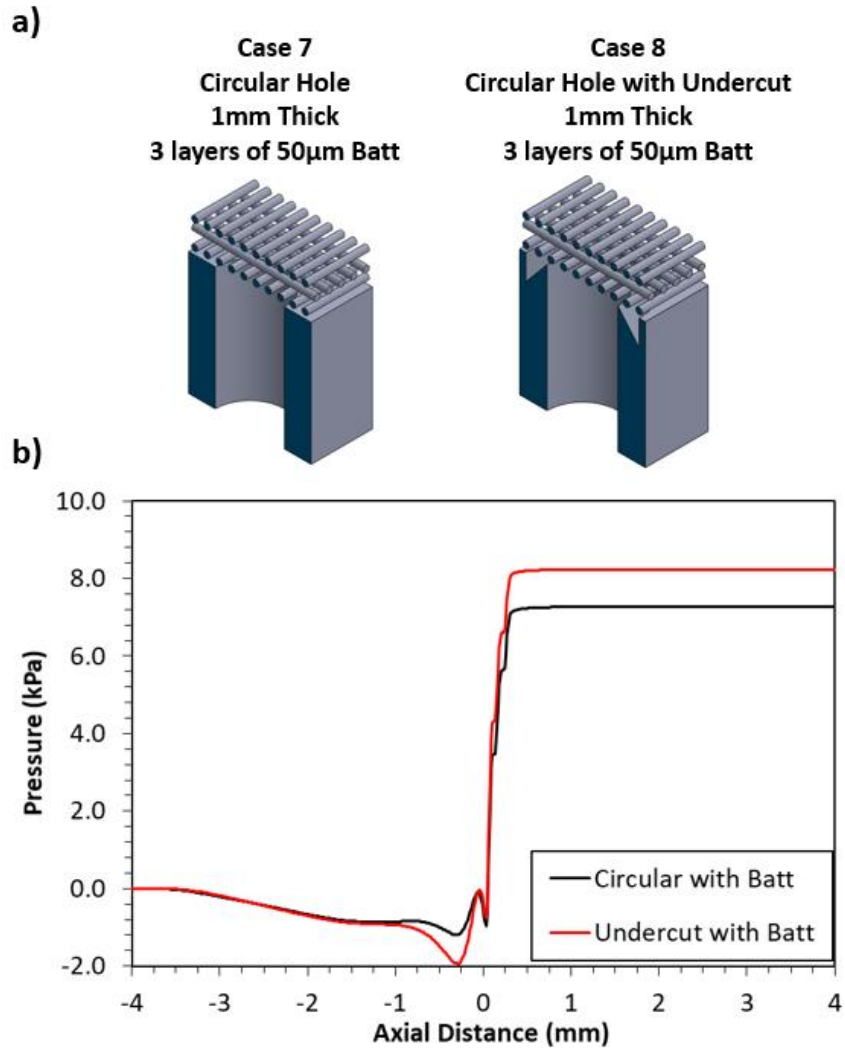


Figure 114: Investigation into effect of batt layer on membrane performance

Having seen the potential of these edge features and initially validated their use with batt, a natural extension is to combine the two features together. Several cases were tested combining a rounded edge and undercut exit. Each of these cases resulted in a combined resistance effect. As a benchmark, a representative single layer base weave is designed with 0.5mm monofilament fibers, giving the same 1x1x1mm unit cell, and the new feature is developed to match the same forward pressure drop. Cases 9 and 10 show these designs, Figure 115, with the base weave having a porosity of 55%, much lower than the proposed design with 38% porosity. The circular hole with a rounded forward edge and undercut reverse edge results in a 28% higher reverse flow resistance compared with forward flow. This increased resistance could promote one directional flow and have the potential to reduce rewet compared with the traditional base weave.

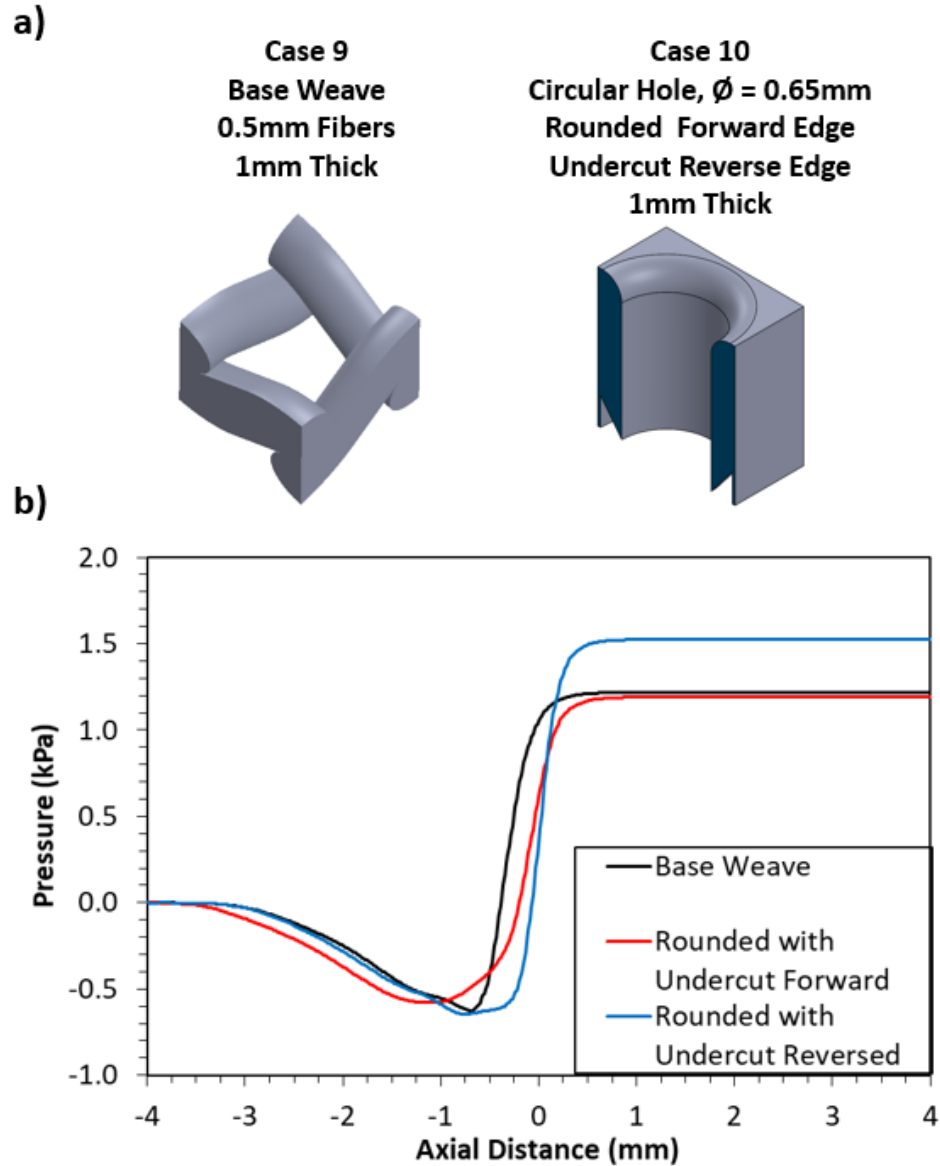


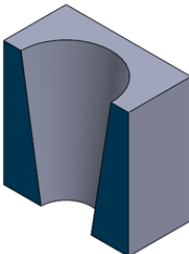
Figure 115: Simulation results comparing a traditional base weave with a tuned hole featuring a rounded forward edge and undercut reverse edge

Next, the construction is switched from a uniform circular hole to a cone shaped constriction in Cases 11 and 12, Figure 116. The cone constructions show promise of having higher resistance to reverse flow than forward flow, in the range of 18-24%, Cone 1 to Cone 2, respectively. More investigation is required to understand how the cone angle affects performance and the optimal angle. It should also be noted that equal porosity does not equate to equal pressure drop as shown by the comparison of Case 11

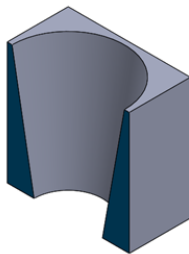
with the circular hole, Case 1, which has equal forward and reverse pressure drop. The cone as designed has more than triple the pressure drop of the circular hole, resulting from the smaller cross-section hole at the exit. Additionally, a minimum open area does not equate to equal pressure drop as shown by the comparison of Case 12 with the circular hole, Case 1. Cone 2 has a moderately lower pressure drop in the forward direct, but the advantaged higher reverse pressure drop.

a)

Case 11
Cone 1
 $\varnothing = 0.72\text{mm}$ Entrance
 $\varnothing = 0.4\text{mm}$ Exit
 1mm Thick



Case 12
Cone 2
 $\varnothing = 0.92\text{mm}$ Entrance
 $\varnothing = 0.564\text{mm}$ Exit
 1mm Thick



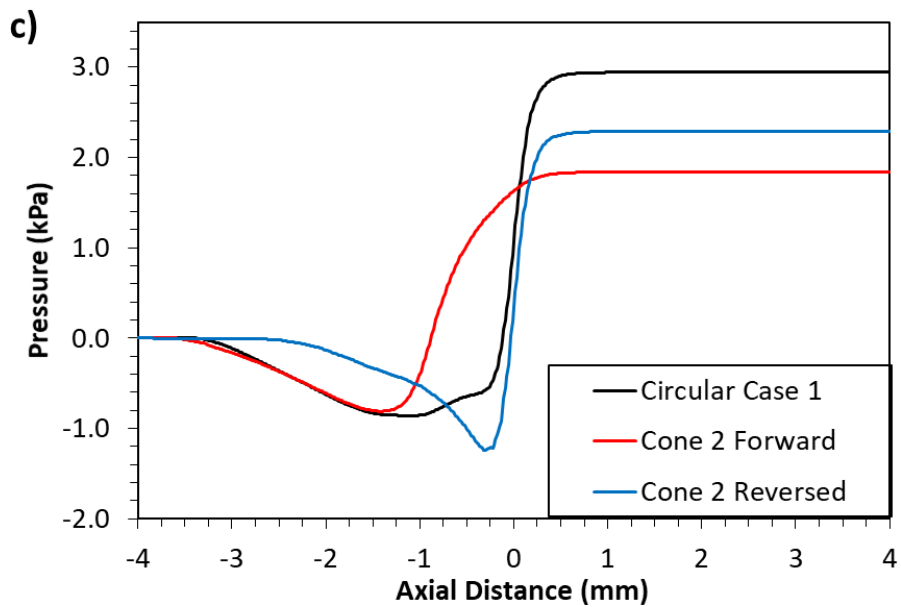
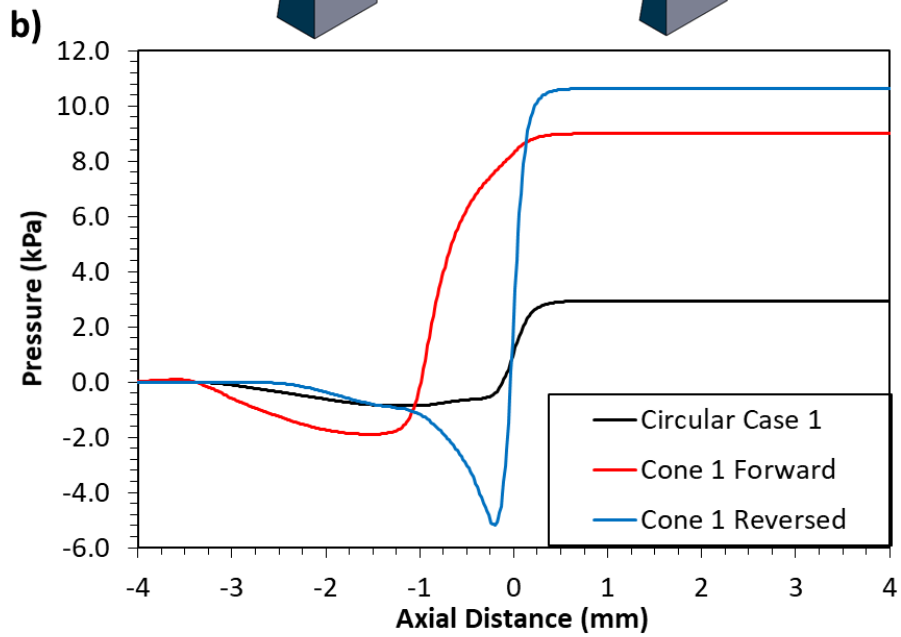


Figure 116: Effect of conical hole structure compared with circular hole

Noting the benefit of the conical shape, Cone 2 is extended to include an ingoing fillet and exit undercut as demonstrated in Cases 13, Figure 117. This design shows substantial improvement, having a 52% higher resistance to reverse flow than forward flow. The design is compared with the base weave, Case 9, and while this design's forward pressure doesn't quite reach that of the base weave, minor changes such as increasing the exit diameter or reducing the thickness would likely make that achievable.

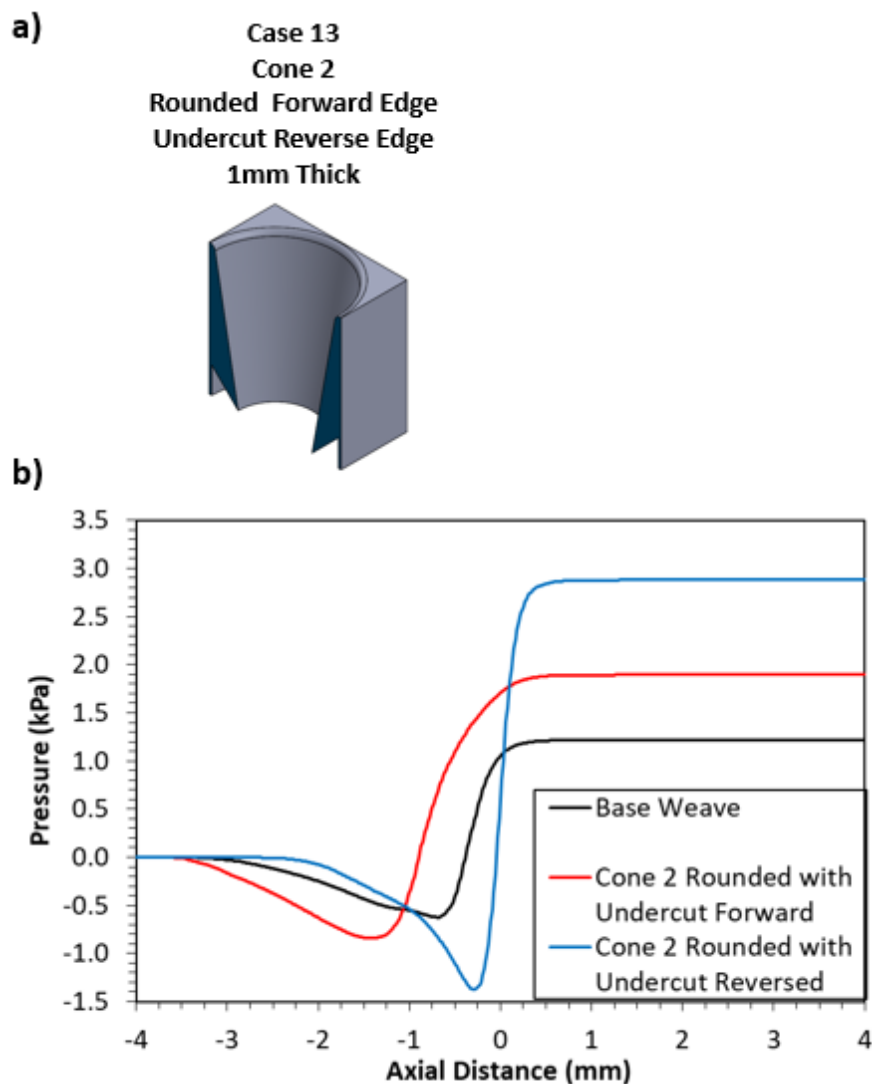


Figure 117: Investigation into conical hole with rounded forward edge and undercut reverse edge

Lastly, a design was implemented which features an internal cutback, Case 14, Figure 118. The construction is referred to as the “Tesla” design as it is inspired by Nikola Tesla’s passive valve. This design shows a 10% increase in reverse flow resistance, but it remains unknown if this was a result of the cutback or the conical shape. There is considerable design space to explore with such a geometry that could enhance the resistance to reverse flow. This work is left for future evaluation.

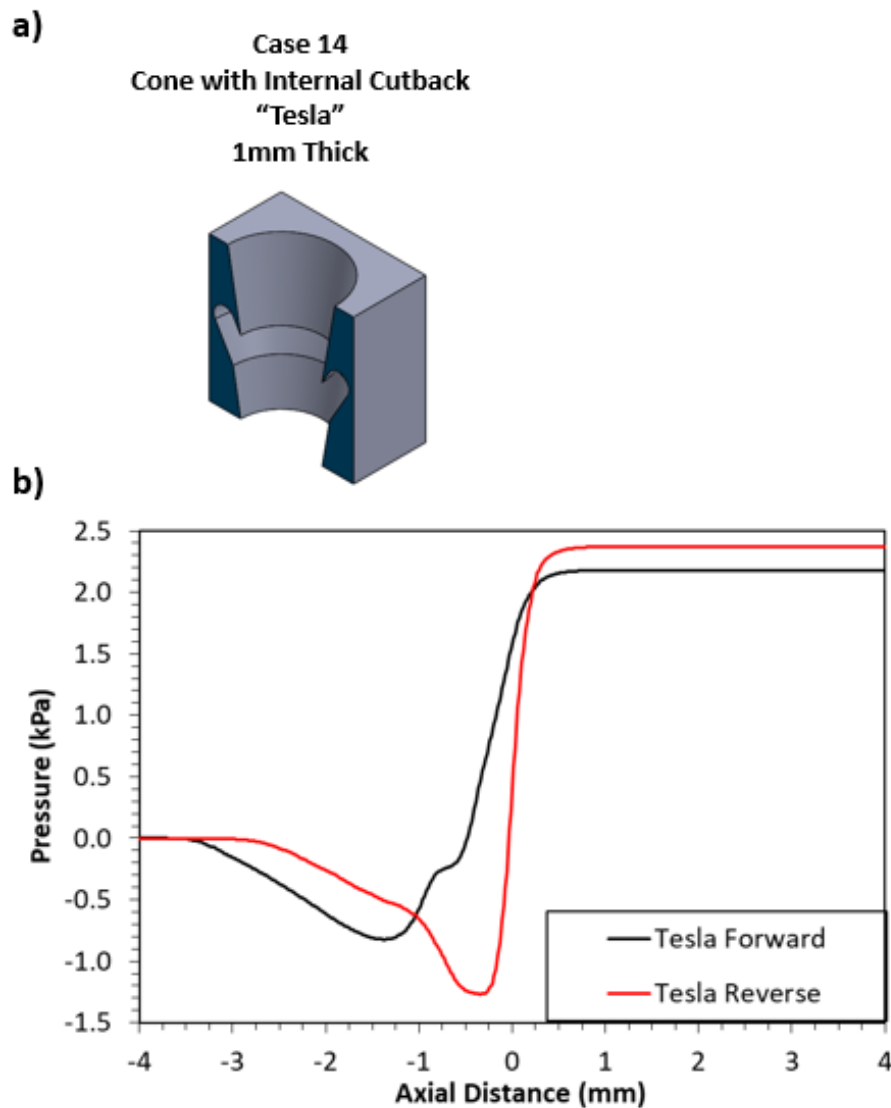


Figure 118: Tesla Design, cone with internal cutback

6.2.4 Active Press Fabrics

The geometries presented thus far are passive in construction. To improve performance, it would be advantageous to have a design that is active. An ideal “active” fabric would act dynamically during pressing, to open the flow area and reduce flow resistance at the mid nip, then close and increase resistance to back flow as you exit the nip and encounter rewet.

To test this vision, a candidate check valve design is developed, shown in Figure 119, which was inspired by the leaflet valves of a heart. To accommodate the leaflets the check valve unit cell is 2x2x1mm, compared with the 1x1x1mm of the prior designs. As the fabric is compressed, the structural and fluid pressure on the leaflets of the valve push the area open as shown Figure 120, thus lowering the resistance to flow. The opening actuation was simulated in ANSYS with a mock batt layer on top of the check valve layer and shown to successfully open under compression.

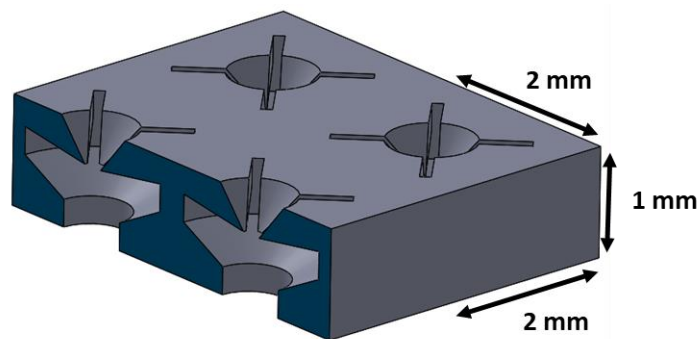


Figure 119: Active fabric design, check valves

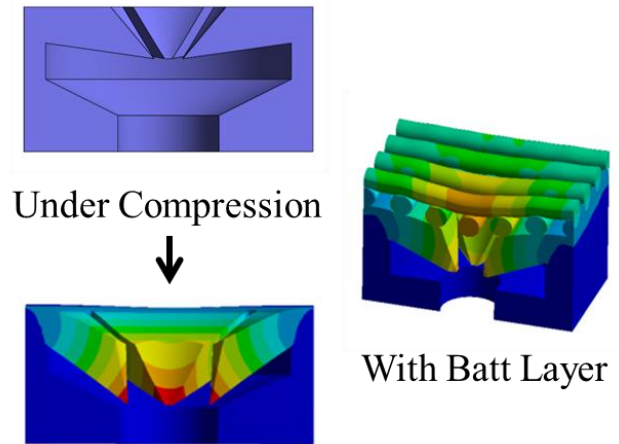


Figure 120: Actuation of the check valve, valve opens under compression.

Flow simulations are run using the same conditions as the passive geometries. For the forward flow direction, the open valve is used, whereas the closed geometry is used for the reverse flow. The resulting pressure drops are shown in Figure 121, and yield a 145% higher resistance to reverse flow than forward flow under these configurations, confirming the significant potential of an active design.

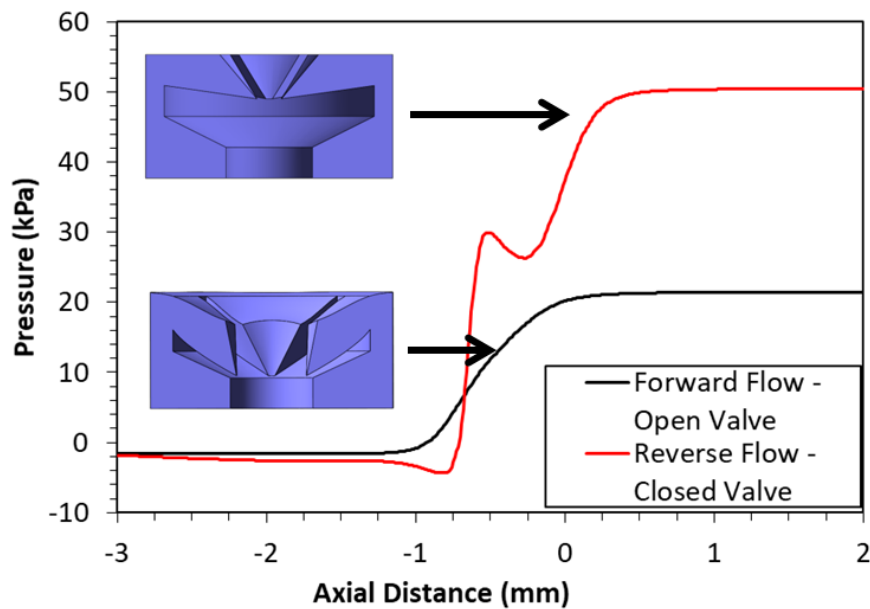


Figure 121: Simulation results for check valve design: forward flow with open valve, reverse flow with closed valve

Next the check valve design is simulated using the QSB model from Chapter 5 to show the model's applicability for simulation of target mesoscale designs. As the QSB model in its current form does not allow for overhangs or support material, the check valve design is split into two simulations. The upper region of the design is shown in Figure 122, and the lower region of the design is shown in Figure 123.

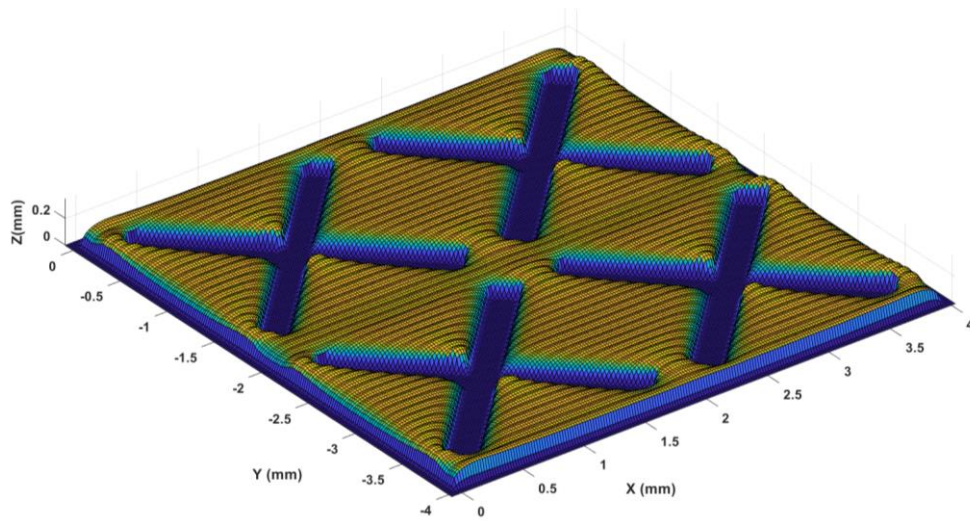


Figure 122: Simulation of the upper region of the check valve design

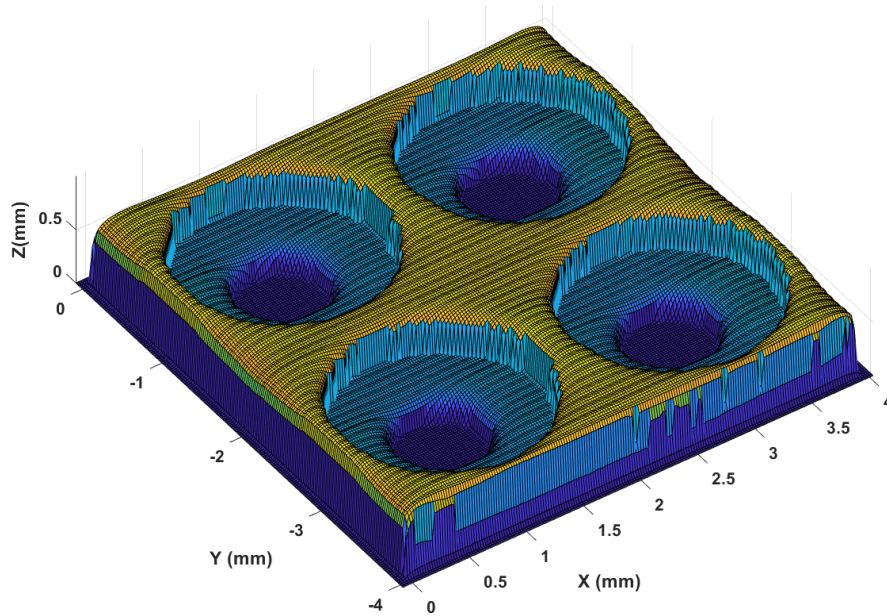


Figure 123: Simulation of the lower region of the check valve design

To bring these two simulations together the surfaces were voxelated and combined. The resulting geometry is shown in Figure 124a, and a sectional close-up of a single unit cell in Figure 124b. It is also noted that the voxel representation could be a strong direction for enabling the QSB model to be used for multi-material modeling, but this investigation is left for future work.

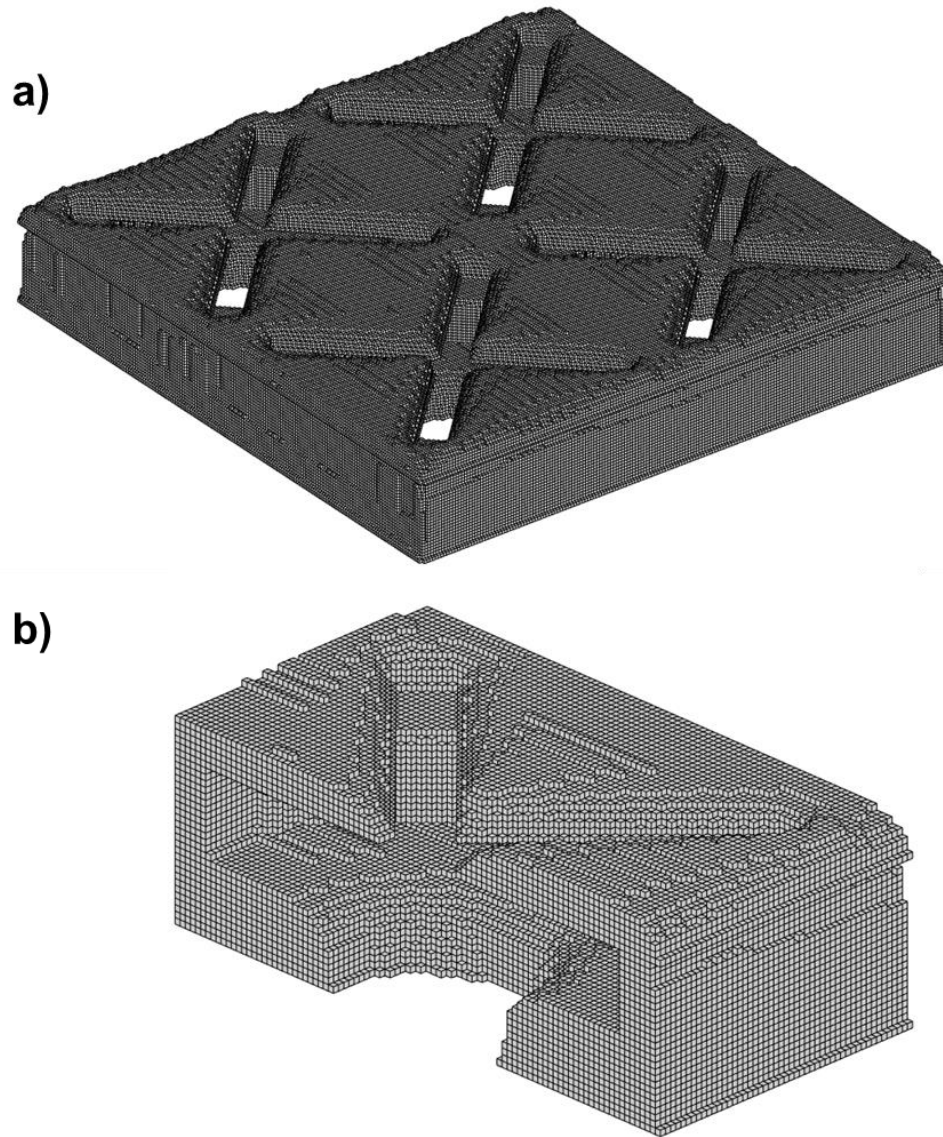


Figure 124: Voxelated representation of the QSB simulated check valve: a) full geometry, b) closeup sectional of a single cell

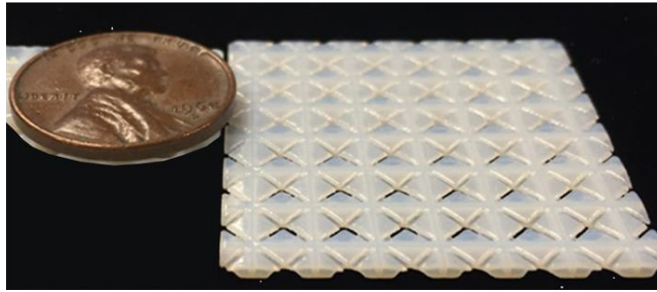
The QSB simulation times are presented in Table 14, and the results fall in line with the times per droplet and per line discussed previously. This further validates the performance of the method and the ability to simulate full features, and presents the method at a scale not seen in other material jetting simulation literature. Still, with the scale of the simulation in the hundreds of thousands of droplets the total time is not “quick”, especially if choosing to use the non-linear form. To improve on these times, and unlock even larger simulations, it is recommended that future work leverage the highly parallelizable nature QSB method formulation, to run via parallel processing.

Table 14: QSB simulation time for check valve design

Feature	No. Drops	No. Lines	Linear QSB			Non-linear QSB		
			Time (sec)	Time per Drop (sec)	Time per Line (sec)	Time (sec)	Time per Drop (sec)	Time per Line (sec)
Upper Region	85,740	4,644	9,734	0.11	2.09	105,554	1.23	22.73
Lower Region	191,672	7,422	19,178	0.10	2.58	213,597	1.11	28.78
Total	277,412	12,066	28,912	0.10	2.39	319,151	1.15	26.45

Lastly in the validation of the check valve design, a slightly modified check valve membrane was fabricated at 2X scale using the Objet 260 printer and VeroWhite material, as shown in Figure 125a. To test the valve actuation, a thin (~1mm thick) piece of felt was placed on top of the membrane and then the layers were compressed between two pieces of plexiglass. As shown in Figure 125b, the prototype valve successfully opens under load, increasing the available flow area and further validating the feasibility of the active press fabric concept.

a)



b)

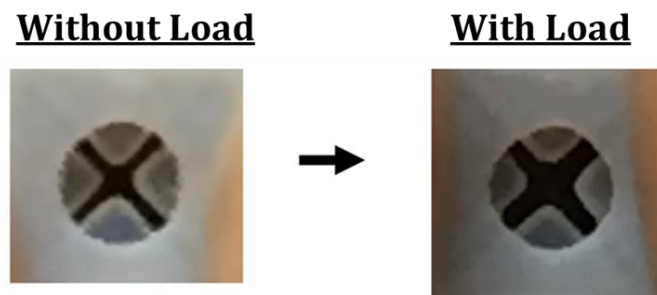


Figure 125: a) Prototype check valve membrane printed at 2X scale, b) demonstration of valve opening under compression

6.3 Summary

While paper machine press fabrics traditionally consist of a woven base layer and incorporated batt layer, more recent concepts have proposed a polymer membrane layer with the aim to improve dewatering efficiency and reduce rewet. To date, little research on such layers has been put forward on the design or evaluation of such layers. In this chapter, the design space for press fabric membrane layers was explored computationally to identify geometries which promote one directional flow and answer the third research question: How can paper machine press fabrics be designed to increase dewatering efficiency?

CFD models were developed using Fluent to explore the impact of hole construction. A wide variety of designs were evaluated comparing elements such as hole shape, edge

rounding, hole profile, and more. Designs were evaluated based on the forward and reverse pressure drop developed for a given flow condition. The target design is to have a membrane with a low forward (press direction) pressure drop, and a high reverse (rewet direction) pressure drop. Several tested design constructions were shown to achieve this aim. The key design features having the most influence was rounded forward edges and undercut reverse edges. Leveraging these features, a design was shown matching the forward pressure of a representative base weave but producing a 28% higher reverse flow resistance. Incorporating a conical profile with the rounded forward edge and undercut reverse edge further improved results, yielding a 52% higher resistance to reverse flow than forward flow. To mimic a typical fabric construction, a standard and undercut feature was run with small batt layers and shown to produce similar results to the non-batt construction.

To further explore the design domain, the final section investigated the concept of an “active” fabric. Such a fabric would ideally open under the press load allowing flow, then close as pressure releases to prevent rewet. The proposed check valve design, inspired by a leaflet heart valve, yielded tremendous results having a 145% higher resistance to reverse flow than forward flow. To validate the potential, a scaled prototype was fabricated using inkjet-based AM and shown to successfully open under load.

The results presented herein are promising and serve to validate the hypothesized potential for a membrane layer construction in paper machine press fabrics. If these concepts work as prediction, considerable energy savings could be achieved in the paper industry. Still, these results are first order approximations for how such layers will

perform, especially once integrated into a full fabric, and further development and optimization of such a concept is needed.

CHAPTER 7. CLOSING REMARKS AND CONTRIBUTIONS

The broad goal of this work is to expand the reach of additive manufacturing, specifically material jetting-based additive manufacturing, through a deeper understanding of how mesoscale features are formed, how the fabrication process can be modeled, and how a future application to paper machine press fabrics should be designed. Chapter 2 began this work with an overview of the material jetting process, then an experimental investigation into mesoscale feature fabrication using a commercially available material jetting machine from the leading manufacturer. Benchmarking parts were designed and fabricated to explore key manufacturing attributes, such as minimum manufacturable feature size, dimensional accuracy, and shape accuracy. In Chapter 3, a broad survey of the literature is performed on modeling efforts applicable to material jetting AM, from single droplet deposition to full feature fabrication. Chapter 4 studies droplet deposition near the edge of a feature using a high-fidelity 3D droplet model. The model is then used to explore multi-layer fabrication and the resulting feature formation. In Chapter 5, a novel quasi-static boundary-based approach is proposed to efficiently model the material jetting deposition and fabrication process while maintaining accuracy and physical relevance. Chapter 6 explores the design of membrane layers for paper machine press fabrics, where material jetting is a proposed fabrication method, and leverages CFD to evaluate design impacts on performance.

This chapter seeks to bring together the research activities reviewed above, and the findings presented throughout this dissertation. In the first section of this chapter, the research questions and hypotheses presented in Chapter 1 are revisited and evaluated in

the context of the work presented. The following sections will address the contributions of this research, followed by the scope and limitations. The final section looks forward, presenting recommendations for future work.

7.1 Answering the Research Questions

7.1.1 Research Question One

Research Question 1: What is the minimum size of primitive mesoscale features fabricated using commercial MJ processes, what are the effects of geometric parameters (i.e., shape, size, orientation, and feature thickness), and how does this relate to machine resolution?

Hypothesis 1: *A parametric study of representative features (square holes, circular holes, thin walls, gaps, etc.) with varying orientations, and transverse thicknesses can be used to determine minimum feature size, shape accuracy, and comparative effects.*

In Chapter 2, a series of benchmark test specimens with parametrically varying mesoscale features were designed and fabricated to explore the printing fidelity of an industry leading material jetting machine. The developed test specimens and analysis methods were shown effective at identifying minimum manufacturable feature size, dimensional accuracy, and shape accuracy, as well as any respective dependencies on design variables (i.e., feature shape, size, orientation, and thickness). For the printer and setup tested, see Chapter 2, feature sizes down to a few hundred microns were successfully fabricated. This is notably larger than the machine's reported resolution. While different feature types were shown to impact minimum manufacturable feature

size, it was concluded that feature orientation and thickness were not as significant. Geometric deformations affecting the feature accuracy as well as shape accuracy were revealed to be of significant degree. Edge rounding, sloped wall, and corner rounding were the main deviations noted. While the ultimate impact on any proposed design would depend on the application, the presented methods could be easily leveraged to define DfAM guidelines and provide clarity on expected feature outcome.

In conclusion, the test specimens and methods developed in Chapter 2 confirm the capability to characterize mesoscale features, their dependencies, and deformations. Furthermore, they are generically valuable for characterizing mesoscale fabrication using other process setting for the machine evaluated, as well as other MJ machines available or under development.

7.1.2 Research Question Two

Research Question 2.1: How can local material flow near previously jetted lines and boundary edges be modeled and how does such flow affect feature resolution?

Hypothesis 2.1: *Deposition near an existing edge can be modeled using a series of high-fidelity 3D CFD simulations that explore droplet deposition with respect to edge, or line boundaries. Additionally, these simulations can be further expanded to explore line and layer deposition.*

In Chapter 4, a high-fidelity multiphase droplet model is developed and leveraged to successfully show that material deposition near a layer edge is prone to overflow and results in reduced feature resolution. The full 3D, COMSOL-based model was first

demonstrated with single droplet deposition and validated with analytical and experimental results. The effects of ribbed and flat surface topologies were explored for single droplet deposition, with both showing impact driven overflow on the order of 20% to 40%. From single droplet deposition, the model is expanded to multi-droplet deposition and coalescence, then used to simulate a portion of a 9x9 droplet square through three layers of deposition. In these series of simulations, it is shown that droplet deposition near a prior layer edge will result in material overflow which reduces boundary resolution, reduces build height, and promotes edge. These series of simulations further demonstrated the capability of the model to predict the MJ deposition phenomenon on complex surfaces such as a layer edge which serves to improve our basic understanding of the process and answers the research question. One limitation of the proposed approach is the high computational expense of such simulations is prohibitive for full feature modeling and will be best used for local investigations as demonstrated.

Research Question 2.2: How can the material jetting process be modeled to rapidly predict the as-manufactured shape of mesoscale features?

Hypothesis 2.2: *A reduced order model based on a quasi-static boundary-based approach can accurately predict the as-fabricated feature shape with reduced computational expense.*

A novel Quasi-static Boundary-based method is developed and demonstrated in Chapter 5. To significantly reduce the computational complexity and time, compared with full 3D CFD, this approach takes a reasonable prediction of the deposited material footprint and solves for the fluid boundary using the 2D Young's-Laplace equation with quasi-static

assumptions. The QSB method is validated against prior high-fidelity simulation research as well as the CFD simulations performed in Chapter 4 to confirm accuracy. Overall, the method performed well, but tradeoffs were observed when varying element order or mesh size. The method was also compared with other MJ modeling approaches found in literature and shown to predict the as-fabricated surface most accurately when compared to a physically printed feature. After demonstrating a basic implementation, further improvements are presented to address prediction of asymmetric spreading on inclined surfaces and non-physical surface results as the angle of incline steepens.

When comparing computational time, the QSB method brings significant reductions to the time needed to solve for the deposited surface. Using the full 3D CFD models in Chapter 4 took days' worth of simulation time, where the QSB methods reduced it down to minutes or seconds, depending on the solution order. To be clear, that is not to say the full CFD models are not valuable; they most certainly are as they reveal the complex dynamics and evolutions during the deposition process. But their cost, and limited scalability, make them best suited for the fundamental studies of droplet physics. For predicting mesoscale feature fabrication, the QSB method is shown to be effective and efficient.

7.1.3 Research Question Three

Research Question 3: How can paper machine press fabrics be designed to increase dewatering efficiency? Specifically, can the traditional filament-based press fabric layout be augmented to promote unidirectional flow and resist rewet?

Hypothesis 3: *A systematic investigation of hole shapes, sizes, behaviors, can identify membrane geometries which promote one directional flow to promote dewatering flow, and restrict rewetting flow. Press fabrics which incorporate a membrane with active, one-way, structures that open under roller nip pressure and close upon exit can be designed to further increase one directional flow and dewatering efficiency.*

The main idea for answering this research question is the incorporation of an engineered membrane layer into the press fabric structure to improve dewatering performance. In Chapter 6, a simulation-based investigation is undertaken to look specifically at the ideal design for such membrane layers. The results showed that rather simple designs can promote one directional flow, representing the first steps toward answering the stated research question. A series of passive membrane structures considered the effect of different hole design parameters. It was shown that conical holes with rounded inlet edges and undercut reverse edges could result in 52% higher resistance to reverse flow than forward flow. To more closely match a true fabric construction, a representative fabric batt layer was explored with a membrane design and found to match the stand-alone membrane results. To further improve the one directional flow, an active “check-valve” design is developed. The concept intends to leverage the basic pressing mechanics to open the valve area as the fabric passes through the press nip, then close the valve as the fabric exits. Flow simulations showed significant promise for promoting one directional flow, with 145% higher resistance to reverse flow than forward flow given the simulation configurations. While all performance results were determined numerically, a physical specimen of the “check-valve” design was fabricated at 2X scale. Simulated compression of the prototype showed opening of the area as intended. These simulations

and findings should guide future development of press fabric constructions and merit physical testing to validate their performance.

7.2 Contributions

In this section, a summary of the new knowledge and scientific contributions created during this research are presented.

The first contribution of this work is deepening the understanding of mesoscale feature fabrication using material jetting additive manufacturing. The experimental investigation and identification of key MJ manufacturing constraints with respect to different design variables brought new understanding of the of the MJ process and the manufacturability of mesoscale features. Furthermore, the experimental methods developed for investigating these constraints, and the benchmarking specimens, can be leveraged for mesoscale characterization of other AM processes, or machine strategies.

Next, we leveraged high-fidelity multiphase droplet models to explore how deposition dynamics affect feature formation. While the study of droplet deposition using similar models has been explored before, most previous works looks at ideal flat surfaces. What makes this work novel is the exploration of deposition on non-uniform surfaces near a layer edge. Results showed that local deposition dynamics will result in material flow beyond the layer boundary, which will expand the layer boundary, reducing deposition height and lead to feature deformation. Additionally, the developed models were used to simulate multiple droplet deposition and coalescence, as would be seen during the printing process, to form a multi-line, 3-layer feature. In doing so, the material overflow was observed to form the edge rounding seen during physical characterization. It is thus

concluded that locally driven overflow is a main driver of such deformations. By better understanding this effect process control improvements can be made to improve feature resolution and fidelity, and a preliminary example showing an extra edge pass was demonstrated. To the best of the author's knowledge this is the first study of this effect and the first simulation to look at the deposition process for a series of line and layer depositions.

Third, the development of the Quasi-static Boundary Model for modeling the MJ fabrication process is novel in its approach, enabling efficient and accurate results. While it would be ideal to exclusively leverage the high-fidelity multiphase models discussed in Chapter 4 to simulate the full printing process, it is unrealistic due to the high-computational cost and time necessary. Others have worked to develop simplified process models, but they are generally limited by a lack of connection to the basic physics of the process. The QSB Model bridges these approaches with a reduced order model that still solves for the surface profile but reduced the impact dynamics modeling to a simplified spread model to determine the droplet boundary. The results showed significant computational savings compared with full CFD and accuracy improvements over the other modeling approaches. This approach can be leveraged to explore different process parameters and feature designs, as well as be used as a process planning tool in the future to reduce the droplet driven deformations such as corner rounding.

Lastly, the investigation into novel press fabric membranes brings a new understanding to how such membranes can be designed and analyzed. The simulation study identified key design elements, such as rounded edges and undercuts, that can facilitate one-directional flow within a passive membrane design. Furthermore, an active membrane design is

developed that has the potential to leverage the mechanics of the pressing process to drastically improve membrane performance. While the study conducted herein was solely simulation based, and therefore preliminary, the ideas presented have significant potential for further development that could greatly improve press dewatering performance.

7.3 Recommendations for Future Work

While the goal of any dissertation is to be thorough and complete, it is also natural for there to be stones left unturned and new ideas ripe for pursuit. Outlined here are several avenues for future work which will hopefully provide a jumping off point to continue deepening the understanding of additive manufacturing and its application.

The MJ models developed in this thesis, both high-fidelity and QSB, use fixed printing parameters (e.g., droplet size, viscosity, contact angle). These values were chosen to benchmark with the material and machine used during the experimental investigation of Chapter 2. To further extend these models, it would be helpful to parameterize material and printing variables and explore their impact on feature resolution, accuracy, and shape deformation. Additionally, an exploration of the impact of machine and droplet uncertainties would be natural to include.

If a dominant cause of the feature deformations lies in the local deposition phenomenon, then with the models presented, it would seem a logical next step to explore how to control the deposition planning to improve feature fidelity and resolution. One illustrative example was presented in Section 4.5 where a “corrective pass” was deposited to address the height deviation at the edge of the feature. Leveraging the QSB model to drive an

open-loop or closed-loop system would be very beneficial for existing machine process planning.

An even more novel pursuit would seek to develop alternative deposition planning strategies altogether to optimize for feature resolution and fidelity. Existing process planning appear to use a fixed deposition grid to simplify the deposition planning, constraining the printing process and increasing errors. An alternative approach could plan around critical elements like the feature boundaries, conforming to these elements, and optimize droplet location to improve feature fidelity. Leveraging the QSB model during process planning could be used to improve the planning algorithm and test different process planning approaches.

To better enable the above two ideas, an additional increase in computational speed would be desirable. The benefit of the localized droplet domain and the structure of the QSB model is that the solutions within a layer could be run separately so long as the depositions or lines are not directly adjacent. Thus, investigating a parallelization of the method implementation to utilize high performance computing would be significantly beneficial.

The QSB model at present assumes single material deposition and treats each new deposition as such. While running the model, this fact reduces complexity as we only track and store the exterior boundary surface as it grows and assume all prior material is a continuum of that single material. As multi-material deposition is a great strength of MJ AM, expansion of the model to represent multiple material deposition would unlock a

wide range of potential applications but would require a new method of representing the geometry and assigning the material type.

The final proposed area for future work is an experimental development and investigation into the press fabric membrane designs presented in Chapter 6 (passive and active). Additive manufacturing can be used to fabricate test specimens either scaled or true to design. To complete the designs for testing, batt fabrics of various calipers and basis weights can be laminated to the test specimens. Mechanical and dewatering testing could be performed using an MTS machine. Various nip pressure profiles and time durations could be tested and used to validate the simulation models.

REFERENCES

- [1] “ASTM ISO/ASTM52900-15 Standard Terminology for Additive Manufacturing – General Principles – Terminology.” ASTM International, 2015.
- [2] I. Gibson, D. W. Rosen, and B. Stucker, *Additive Manufacturing Technologies*. Boston, MA: Springer US, 2010.
- [3] “2019 Additive Manufacturing Market Outlook and Summary of Opportunities,” *SmarTech Publishing*, 2018.
- [4] C. Sulavik and T. Waller, “3D Printing comes of age in US industrial manufacturing - PWC Report.” PWC and Manufacturing Institute, 2016.
- [5] L. B. Bass, N. A. Meisel, and C. B. Williams, “Exploring Variability in Material Properties of Multi-Material Jetting Parts,” in *Proceeding of the International Solid Freeform Fabrication Symposium*, 2015.
- [6] “NanoDimension - Dragonfly Pro,” 2019. [Online]. Available: <https://www.nano-di.com/dragonfly-pro-3d-printer>.
- [7] K. Yoshihiro, S. Hodges, B. S. Cook, C. Zhang, and G. D. Abowd, “Instant inkjet circuits: Lab-based Inkjet Printing to Support Rapid Prototyping of UbiComp Devices,” *Proc. 2013 ACM Int. Jt. Conf. Pervasive Ubiquitous Comput. - UbiComp '13*, pp. 363–372, 2013.
- [8] W. Su, B. S. Cook, Y. Fang, and M. M. Tentzeris, “Fully inkjet-printed microfluidics: a solution to low-cost rapid three-dimensional microfluidics fabrication with numerous electrical and sensing applications,” *Sci. Rep.*, vol. 6, no. 1, 2016.
- [9] Z. Ding, C. Yuan, X. Peng, T. Wang, H. J. Qi, and M. L. Dunn, “Direct 4D printing via active composite materials,” *Sci. Adv.*, vol. 3, no. 4, 2017.
- [10] “Polyjet Technology,” *Stratasys*, 2016. [Online]. Available: <http://www.stratasys.com/3d-printers/technologies/polyjet-technology>. [Accessed: 20-Jun-2006].
- [11] R. Reese, “Save Energy By Optimizing Paper Machine Clothing,” *Solutions!*, vol. 89, no. 4, 2006.
- [12] “Agenda 2020 - Drier Web before Dryer Section: Research Roadmap.” Agenda 2020: Alliance for Pulp and Paper Technology Innovation, 2015.
- [13] J. M. Lee, M. Zhang, and W. Y. Yeong, “Characterization and evaluation of 3D printed microfluidic chip for cell processing,” *Microfluid. Nanofluidics*, vol. 20,

no. 1, p. 5, Jan. 2016.

- [14] S. Moylan, A. Cooke, and K. Jurens, “A Review of Test Artifacts for Additive Manufacturing. Report NISTIR 7858,” *National Institute of Standards and Technology*. Gaithersburg, MD, 2012.
- [15] M. W. Barclift and C. B. Williams, “Examining variability in the mechanical properties of parts manufactured via polyjet direct 3D printing,” in *Proceedings of the International Solid Freeform Fabrication Symposium*, 2012.
- [16] A. Cazon, P. Morer, and L. Matey, “PolyJet technology for product prototyping: Tensile strength and surface roughness properties,” *Proc. Inst. Mech. Eng. Part B J. Eng. Manuf.*, vol. 228, no. 12, pp. 1664–1675, 2014.
- [17] G. D. Kim and Y. T. Oh, “A benchmark study on rapid prototyping processes and machines: quantitative comparisons of mechanical properties, accuracy, roughness, speed, and material cost,” *Proc. Inst. Mech. Eng. Part B J. Eng. Manuf.*, vol. 222, no. 2, pp. 201–215, 2008.
- [18] L. F. Vieira, R. A. Paggi, and G. V. Salmoria, “Thermal and dynamic-mechanical behavior of Fullcure 3D printing resin post-cured by different methods,” in *Innovative Developments in Virtual and Physical Prototyping - Proceedings of the 5th International Conference on Advanced Research and Rapid Prototyping*, 2011, pp. 385–388.
- [19] D. Blanco, P. Fernandez, and A. Noriega, “Nonisotropic experimental characterization of the relaxation modulus for PolyJet manufactured parts,” *J. Mater. Res.*, vol. 29, no. 17, pp. 1876–1882, 2014.
- [20] J. P. Moore and C. B. Williams, “Fatigue properties of parts printed by PolyJet material jetting,” *Rapid Prototyp. J.*, vol. 21, no. 6, pp. 675–685, Oct. 2015.
- [21] I. Q. Vu, L. B. Bass, C. B. Williams, and D. A. Dillard, “Characterizing the effect of print orientation on interface integrity of multi-material jetting additive manufacturing,” *Addit. Manuf.*, vol. 22, pp. 447–461, 2018.
- [22] T. S. Lumpe, J. Mueller, and K. Shea, “Tensile properties of multi-material interfaces in 3D printed parts,” *Mater. Des.*, vol. 162, pp. 1–9, 2019.
- [23] R. Singh, “Process capability study of polyjet printing for plastic components,” *J. Mech. Sci. Technol.*, vol. 25, no. 4, pp. 1011–1015, 2011.
- [24] D. P. Printing, J. Kechagias, J. D. Kechagias, and S. Maropoulos, “An Investigation of Sloped Surface Roughness of An Investigation of Sloped Surface Roughness of Direct Poly-Jet 3D Printing,” in *Proceedings of the International Conference on Industrial Engineering*, 2015, pp. 150–153.
- [25] R. Udriou and L. A. Mihail, “Experimental determination of surface roughness of

- parts obtained by rapid prototyping,” *CSECS’09 Proc. 8th WSEAS Int. Conf. Circuits, Syst. Electron. Control Signal Process.*, pp. 283–286, 2009.
- [26] K. Kumar and G. S. Kumar, “An experimental and theoretical investigation of surface roughness of poly-jet printed parts,” *Virtual Phys. Prototyp.*, vol. 10, no. 1, pp. 23–34, 2015.
 - [27] N. A. Meisel, “Design for Additive Manufacturing Considerations for Self-Actuating Compliant Mechanisms Created via Multi-Material PolyJet 3D Printing,” Virginia Polytechnic Institute and State University, 2015.
 - [28] N. Meisel and C. Williams, “An Investigation of Key Design for Additive Manufacturing Constraints in Multi-Material 3D Printing,” *J. Mech. Des.*, vol. 137, 2015.
 - [29] Y. L. Yap, C. Wang, S. L. Sing, V. Dikshit, W. Y. Yeong, and J. Wei, “Material jetting additive manufacturing: An experimental study using designed metrological benchmarks,” *Precis. Eng.*, vol. 50, pp. 275–285, 2017.
 - [30] N. P. Macdonald, J. M. Cabot, P. Smejkal, R. M. Guijt, B. Paull, and M. C. Breadmore, “Comparing Microfluidic Performance of Three-Dimensional (3D) Printing Platforms,” *Anal. Chem.*, vol. 89, no. 7, pp. 3858–3866, 2017.
 - [31] “User Guide Objet260 3D Printer System.” Stratasys.
 - [32] “10 Reasons Why Multi-Material 3D Printing is Better for your Product Design & Development.” Stratasys, 2013.
 - [33] “MH1900 Datasheet - 96 Channel Print Head.” Ricoh Printing Systems America.
 - [34] J. Dilag, T. Chen, S. Li, and S. A. Bateman, “Design and direct additive manufacturing of three-dimensional surface micro-structures using material jetting technologies,” *Addit. Manuf.*, vol. 27, no. September 2018, pp. 167–174, 2019.
 - [35] C. W. Sele, T. Von Werne, R. H. Friend, and H. Sirringhaus, “Lithography-free, self-aligned inkjet printing with sub-hundred-nanometer resolution,” *Adv. Mater.*, vol. 17, no. 8, pp. 997–1001, 2005.
 - [36] Y. Y. Noh, N. Zhao, M. Caironi, and H. Sirringhaus, “Downscaling of self-aligned, all-printed polymer thin-film transistors,” *Nat. Nanotechnol.*, vol. 2, no. 12, pp. 784–789, 2007.
 - [37] J. M. Lee, M. Zhang, and W. Y. Yeong, “Characterization and evaluation of 3D printed microfluidic chip for cell processing,” *Microfluid. Nanofluidics*, vol. 20, no. 1, pp. 1–15, 2016.
 - [38] S. B. Sookran, “Drop Impact on an Inclined and Moving Surface,” York University, 2018.

- [39] Y. L. Cheng, C. H. Chang, and C. Kuo, "Experimental study on leveling mechanism for material-jetting-type color 3D printing," *Rapid Prototyp. J.*, vol. 26, no. 1, pp. 11–20, 2020.
- [40] B. Derby, "Inkjet Printing of Functional and Structural Materials: Fluid Property Requirements, Feature Stability, and Resolution," *Annu. Rev. Mater. Res.*, vol. 40, pp. 395–414, 2010.
- [41] S. D. Hoath, *Fundamentals of Inkjet Printing: The Science of Inkjet and Droplets*. Wiley-VCH Verlag GmbH & Co., 2015.
- [42] I. M. Hutchings and G. D. Martin, *Inkjet Technology for Digital Fabrication*. John Wiley & Sons, Ltd, 2012.
- [43] "MicroFab Technote 99-02: Fluid Properties Effects on Ink-Jet Device Performance." MicroFab Technologies, 1999.
- [44] S. Schiaffino and A. A. Sonin, "Molten droplet deposition and solidification at low Weber numbers," *Phys. Fluids*, vol. 9, no. 11, pp. 3172–3187, 1997.
- [45] B. Derby, "Inkjet Printing of Functional and Structural Materials: Fluid Property Requirements, Feature Stability, and Resolution," *Annu. Rev. Mater. Res.*, vol. 40, no. 1, pp. 395–414, 2010.
- [46] S. H. Davis, "Moving contact lines and rivulet instabilities. Part 1. The static rivulet," *J. Fluid Mech.*, vol. 98, no. 2, pp. 225–242, 1980.
- [47] S. Schiaffino and A. Sonin, "Formation and stability of liquid and molten beads on a solid surface," *J. Fluid Mech.*, vol. 343, 1997.
- [48] D. Soltman and V. Subramanian, "Inkjet-printed line morphologies and temperature control of the coffee ring effect," *Langmuir*, vol. 24, no. 5, pp. 2224–2231, 2008.
- [49] J. Stringer and B. Derby, "Formation and stability of lines produced by inkjet printing," *Langmuir*, vol. 26, no. 12, pp. 10365–10372, 2010.
- [50] W. K. Hsiao, G. D. Martin, and I. M. Hutchings, "Printing stable liquid tracks on a surface with finite receding contact angle," *Langmuir*, vol. 30, no. 41, pp. 12447–12455, 2014.
- [51] W. Lee and G. Son, "Numerical study of droplet impact and coalescence in a microline patterning process," *Comput. Fluids*, vol. 42, no. 1, pp. 26–36, 2011.
- [52] H. Li, P. Wang, L. Qi, H. Zuo, S. Zhong, and X. Hou, "3D numerical simulation of successive deposition of uniform molten Al droplets on a moving substrate and experimental validation," *Comput. Mater. Sci.*, vol. 65, pp. 291–301, 2012.

- [53] S. L. Li, Z. Y. Wei, J. Du, P. Wei, Z. X. Hou, and B. H. Lu, "The fusion process of successive droplets impinging onto a substrate surface," *Appl. Phys. A Mater. Sci. Process.*, vol. 120, no. 1, pp. 35–42, 2015.
- [54] W. Zhou, D. Loney, A. G. Fedorov, F. L. Degertekin, and D. W. Rosen, "Shape evolution of multiple interacting droplets in inkjet deposition," *Rapid Prototyp. J.*, vol. 21, no. 4, pp. 373–385, 2015.
- [55] W. Zhou, "Lattice Boltzmann Simulation of Multiple Droplet Interaction on Non-ideal Surfaces for Inkjet Deposition," in *Proceeding of the International Solid Freeform Fabrication Symposium*, 2015.
- [56] L. Zhang, Y. Zhu, and X. Cheng, "Numerical investigation of multi-droplets deposited lines morphology with a multiple-relaxation-time lattice Boltzmann model," *Chem. Eng. Sci.*, vol. 171, pp. 534–544, 2017.
- [57] A. B. Thompson, C. R. Tipton, A. Juel, A. L. Hazel, and M. Dowling, "Sequential deposition of overlapping droplets to form a liquid line," *J. Fluid Mech.*, vol. 761, pp. 261–281, 2014.
- [58] P. Kant, A. L. Hazel, M. Dowling, A. B. Thompson, and A. Juel, "Controlling droplet spreading with topography," *Phys. Rev. Fluids*, vol. 2, no. 9, 2017.
- [59] F. Zhang, C. Tuck, R. Hague, and Y. He, "Inkjet printing of polyimide insulators for the 3D printing of dielectric materials for microelectronic applications," *J. Appl. Polym. Sci.*, vol. 133, no. 18, 2016.
- [60] H. Kang, D. Soltman, and V. Subramanian, "Hydrostatic optimization of inkjet-printed films," *Langmuir*, vol. 26, no. 13, pp. 11568–11573, 2010.
- [61] D. Soltman, B. Smith, H. Kang, S. J. S. Morris, and V. Subramanian, "Methodology for Inkjet Printing of Partially Wetting Films," *Langmuir*, vol. 26, no. 19, pp. 15686–15693, 2010.
- [62] D. Soltman, B. Smith, S. J. S. Morris, and V. Subramanian, "Inkjet printing of precisely defined features using contact-angle hysteresis," *J. Colloid Interface Sci.*, vol. 400, pp. 135–139, 2013.
- [63] Y. Jin, S. J. Qin, and Q. Huang, "Offline Predictive Control of Out-of-Plane Geometric Errors for Additive Manufacturing," *J. Manuf. Sci. Eng.*, vol. 138, no. c, pp. 1–7, 2016.
- [64] H. Luan and Q. Huang, "Prescriptive Modeling and Compensation of In-Plane Shape Deformation for 3-D Printed Freeform Products," *IEEE Trans. Autom. Sci. Eng.*, 2016.
- [65] D. L. Cohen and H. Lipson, "Geometric feedback control of discrete-deposition SFF systems," *Rapid Prototyp. J.*, vol. 16, 2010.

- [66] L. Lu, J. Zheng, and S. Mishra, "A Layer-To-Layer Model and Feedback Control of Ink-Jet 3-D Printing," *IEEE/ASME Trans. Mechatronics*, vol. 20, no. 3, pp. 1056–1068, 2015.
- [67] Y. Guo and S. Mishra, "A predictive control algorithm for layer-to-layer ink-jet 3D printing," in *Proceedings of the American Control Conference*, 2016.
- [68] Y. Guo, J. Peters, T. Oomen, and S. Mishra, "Control-oriented models for ink-jet 3D printing," *Mechatronics*, 2018.
- [69] U. Inyang-Udoh, Y. Guo, J. Peters, T. Oomen, and S. Mishra, "Layer-to-Layer Predictive Control of Inkjet 3-D Printing," *IEEE/ASME Trans. Mechatronics*, vol. 25, no. 4, pp. 1783–1793, 2020.
- [70] U. Inyang-Udoh and S. Mishra, "A Physics-Guided Neural Network Dynamical Model for Droplet-Based Additive Manufacturing," *IEEE Trans. Control Syst. Technol.*, pp. 1–13, 2021.
- [71] Y. Wu and G. Chiu, "An Improved Height Difference Based Model of Height Profile for Drop-on-Demand 3D Printing with UV Curable Ink," in *Proceedings of the American Control Conference*, 2021.
- [72] C. Pannier, M. Wu, D. Hoelzle, and K. Barton, "LPV models for jet-printed heightmap control," in *Proceedings of the American Control Conference*, 2019.
- [73] E. Olsson and G. Kreiss, "A conservative level set method for two phase flow," *J. Comput. Phys.*, vol. 210, no. 1, pp. 225–246, 2005.
- [74] J. Hu, R. Jia, K. Wan, and X. Xiong, "Simulation of Droplet Impingement on a Solid Surface by the Level Set Method," in *Proceedings of the 2014 COMSOL Conference*, 2014.
- [75] H. Dong, W. W. Carr, D. G. Bucknall, and J. F. Morris, "Temporally-resolved inkjet drop impaction on surfaces," *AIChE J.*, vol. 53, no. 10, pp. 2606–2617, Oct. 2007.
- [76] W. Zhou, "Interface Dynamics in Inkjet Deposition," Georgia Institute of Technology, 2014.
- [77] T. Lee and L. Liu, "Lattice Boltzmann simulations of micron-scale drop impact on dry surfaces," *J. Comput. Phys.*, vol. 229, no. 20, pp. 8045–8063, 2010.
- [78] Y. L. Cheng and K. C. Huang, "Preparation and characterization of color photocurable resins for full-color material jetting additive manufacturing," *Polymers (Basel)*, vol. 12, no. 3, 2020.
- [79] A. M. Elliott, O. S. Ivanova, C. B. Williams, and T. A. Campbell, "An investigation of the effects of quantum dot nanoparticles on photopolymer resin for

use in polyjet direct 3D printing,” in *Proceedings of the International Solid Freeform Fabrication Symposium*, 2012.

- [80] S. F. Lunkad, V. V. Buwa, and K. D. P. Nigam, “Numerical simulations of drop impact and spreading on horizontal and inclined surfaces,” *Chem. Eng. Sci.*, vol. 62, no. 24, pp. 7214–7224, 2007.
- [81] M. Levi, H. Gothait, E. Kritchman, and I. Zeitun, “Rapid Prototyping Apparatus,” US 2020/0361150 A1, 2020.
- [82] Y. Guo, J. Peters, T. Oomen, and S. Mishra, “Distributed model predictive control for ink-jet 3D printing,” *2017 IEEE Int. Conf. Adv. Intell. Mechatronics*, pp. 436–441, 2017.
- [83] H. Almohammadi and A. Amirfazli, “Asymmetric Spreading of a Drop upon Impact onto a Surface,” *Langmuir*, vol. 33, no. 23, pp. 5957–5964, 2017.
- [84] S. Adanur, *Paper Machine Clothing: Key to the Paper Making Process*. CRC Press, 1997.
- [85] “TIP 0404-20: Physical characterization of press fabrics: Basis weight, air permeability, void volume under loading and pressure uniformity.” TAPPI, 2015.
- [86] “TIP 0404-28: Method for evaluating thickness of wet press fabrics.” TAPPI, 2007.
- [87] “TIP 0404-29: Porosity measurement of press felts on the paper machine.” TAPPI, 2004.
- [88] T. Helle and T. Forseth, “Influence of felt structure on water removal in a press nip,” *Tappi J.*, vol. 77, no. 6.
- [89] J. Xu, R. Phillips, and D. Hedou, “The effect of press felt non-uniformity on sheet smoothness and dewatering,” in *PaperCon 2011*, 2011.
- [90] J. Gullbrand, “The influence of stress variations in wet pressing,” Royal Institute of Technology, 2004.
- [91] Zoltan Szikla, “Role of Felt in Wet Pressing; Part II: “Movement of water during the separation of paper from felt,” *Pap. Timber*, vol. 73, no. 2, 1991.
- [92] J. Xu, R. Banks, B. Huck, D. Hedou, and R. Philips, “The Effect of Non-woven Base on Press Felt Properties and Dewatering,” in *PaperCon 2012*, 2012.
- [93] Voith, “Revolution Press Fabric.” [Online]. Available: http://voith.com/en/products-services__paper__revolution-25410.htm. [Accessed: 18-Oct-2016].

- [94] L. Busker and R. Daane, "Anti-rewet membrane for an extended press nip system," US 3,840,429, 1974.
- [95] N. Eklund and J. Olsson, "Wet press fabric to be used in papermaking machine," US 5,232,768, 1993.
- [96] D. Beck, "Anti-rewet felt for use in a papermaking machine," US 6,616,812, 2003.
- [97] K. Watanabe, "Papermaking press felt," US 6,716,318, 2004.
- [98] R. Hansen, "Anti-rewet press fabric," US 7,128,810, 2006.
- [99] L. Lefkowitz, "Anti-rewet transfer belt," US 2008/0176690, 2008.